STRESS-RELIEF DISPLACEMENTS INDUCED BY DRILLING AND THREE-DIMENSIONAL MODELING OF PLANETARY IMPACTS

Thesis by

Catherine Louise Smither

In Partial Fulfillment of the Requirements
for the Degree of
Doctor of Philosophy

California Institute of Technology
Pasadena, California
1992
(Submitted June 1992)

Acknowledgements

One can't have spent as many years as I did at the Seismo Lab and at Caltech without having a host of people to thank for their support, guidance, suggestions, and general friendliness. I would first like to thank my advisor, Tom Ahrens, for all of the above, and for the occasional push I needed to get going. I also appreciated the support of the other faculty members, particularly Rob Clayton and Dave Harkrider, who always seemed ready to lend a sympathetic ear to my complaints.

The field work gathering the holograms in Chapter 1 was done with Doug Schmidt and Bridget Jensen; Doug also contributed greatly to my understanding of the stressmeter and the practical details of holography. I would also like to thank John Smith for his help in gaining access to the field site, and for his good humor. The late Eli Sternberg of Caltech pointed me in the direction of his papers with Carl Youngdahl.

The computer work described in Chapter 2 was performed on the Cray X-MP and, later, Y-MP computer at JPL, and I would like to thank the Cray Corporation for making the free computation time available. This work would have been much more difficult (and expensive) without it.

Much of my time at Caltech was spent working on the 6-inch version of the stressmeter. I would like to thank Wayne Miller and Bill Barber for their technical expertise, and I especially thank Bob Taylor for many hours of truck driving, troubleshooting, barbecuing, and conversation both in the field and in the lab. Many people helped me out in the field at Crystalaire. Cheryl Contopulos, Doug Dreger, Sharon Kedar, Linda Rowan, and Craig Scrivner could always be counted on to cheerfully agree to spend a day in the desert, and Hong-Kie Thio could also be counted on, though perhaps less cheerfully. Other people to whom I am grateful for their help on those dusty days are: Dave Wald, Greg Holk, Phil Ihinger, Tom Duffy, Neil Humphrey, Jon Nourse, Scott King, Louise Kellogg, Brad Woods, Xiaodong Song, Rob Clayton, Joann Stock, and Dave Harkrider. I'm sure there are others, and I thank you all.

The office staff deserve thanks as well, particularly Sue Yamada, who I tried not to bother too often with things for her to do, as she is rather busy already. Whenever I did bother her, though, she was always very helpful and efficient. I also wish to thank the many other friends I made in the division: Mark Fahnestock, Phil Ihinger, Frank Webb, Jon Nourse, Ken and Lottie Herkenhoff, Marcus Bursik, Andy Gaynor, Diane Clemens Knott, and Yigal Erel for helping me keep my sanity throughout the years.

I would like to thank my parents for not losing faith that I would eventually finish my thesis. Two people who deserve more thanks that I can give in this brief acknowledgement are Cheryl Contopulos, who has given me incredible friendship and support throughout my graduate career, and, of course, my husband, John Stone, who has encouraged me to continue my work while patiently waiting for me to finish it.

Abstract

Catherine Louise Smither, Ph.D.

California Institute of Technology 1992

The holographic stressmeter uses double-exposure holographic interferometry to record the displacements induced by the drilling of a sidehole into the borehole wall. The local stresses, which are the result of the far-field stresses, concentrated at the borehole, cause deformation of the surface of the borehole wall near the sidehole. To interpret the data, it is essential to understand this deformation. The initial model used a thin infinite elastic plate subjected to plane stress at infinity. Two-dimensional finite element analysis showed that the displacement depends on the depth of the sidehole. We then developed a new model for the analysis of stress-relief displacements. For holes with a depth/diameter ratio greater than unity, the simple plane stress elastic plate solution breaks down. The revised model, which gives a more exact solution of displacements near the hole, does a better job of fitting the observed data.

A three-dimensional smoothed particle hydrodynamics code was used to model normal and oblique impacts of silicate projectiles on planetary bodies. The energy of the system is partitioned after impact into internal and kinetic energy of the both bodies. These simulations show that, unlike the case of impacts onto a half-space, up to 70% of the initial energy remains in the kinetic energy of the impactor, as parts of it travel past the main planet and escape the system. More oblique impacts retain more kinetic energy in the impactor: 6 to 75% versus 4 to 30% for the normal impacts. Higher velocity collisions also show this trend, as the kinetic energy of the impactor is 2 to 50% of the total for 5 km/s impacts, and 13 to 75% for 20 km/s impacts. Impacts at 20 km/s with an impactor 60% the size of the target completely melted both targets. Three to 4 times more vaporization of the target material occurred on the larger targets. The amount of target material ejected at velocities greater than the escape velocity is found to be higher than that predicted by studies of impact onto a half-space, and slightly less than the amount predicted by theories of catastrophic breakup of asteroids.

Table of Contents

List of Tables

List of Figures

Chapter 1

Stress-relief displacements induced by drilling – applications to holographic measurements of in situ stress

1.1 Abstract

The holographic stressmeter is an instrument which has been developed at Caltech [Bass et al. 1986] to allow determination of the complete stress tensor from in situ borehole measurements. The prototype instrument has been used to find the state of stress in a mine pillar [Smither et al. 1987]. The stressmeter uses double-exposure holographic interferometry to record the displacements induced by the drilling of a small ($\approx$ 1 centimeter) sidehole into the borehole wall. The local stresses, which are the result of the far-field stresses, concentrated at the borehole, cause deformation of the surface of the borehole wall in the vicinity of the sidehole. To interpret the data from the stressmeter, it is essential to understand in detail this deformation. The first part of this study uses a thin infinite elastic plate subjected to plane stress at infinity to model the displacements at the borehole wall. However, the existence of

some holograms which were difficult to model closely led us to examine the validity of this model. In order to investigate the problem further, we performed a two-dimensional finite element analysis for an elastic box with a terminated hole. We varied the dimensions of the hole to see what effect the radius and depth of the hole might have on the displacements. The plate model predicts that the depth of the hole should have no effect on the horizontal components of displacement, but the finite element results show that the magnitude of both components of the displacement depends on the depth of the sidehole. After considering these results, we developed a new model for the analysis of stress-relief displacements, following the work of Youngdahl and Sternberg [1965]. For holes with a depth-to-diameter ratio greater than unity, the simple plane stress elastic plate solution breaks down and does not adequately model the displacements at the surface of the body and near the hole. Since these are the areas most critical to calculate accurately with the holographic technique, the revised model does a better job of fitting the observed data.

1.2 Introduction

Detailed knowledge of the state of stress in the earth's crust is vital to the further understanding of many geophysical phenomena. Accurate in situ stress measurements may give information on plate tectonic processes such as the state of the stress acting on faults and plate boundaries or stress due to drag on the base of the lithosphere [Hickman 1991; McGarr and Gay 1978; Richardson et al. 1979; McGarr et al. 1982; Haimson 1975]. We may also wish to measure stresses associated with volcanism at mid-ocean ridges and subduction zones and in the interior of plates. Knowledge of the local in situ state of stress is also important in mining, for the design and safety of underground openings, and in the extraction of petroleum by hydrofracture [Haimson and Fairhurst 1967; Simonsen et al. 1978; Hubbert and Willis 1957].

This work presents results of in situ stress measurements made with the holographic stressmeter in a horizontal borehole in an underground mine in Garfield County, Colorado. All six stress tensor components were determined; previous work with the stressmeter in this mine [Bass et al. 1986; Schmitt 1987] and other sites [Cohn 1983; Schmitt et al. 1986] was able to determine only five of the six components. In addition, we examine the validity of the original method used to analyze the data by examining the initial predictions of the elastic plate model, the predictions of the displacements from a two-dimensional finite element model, and an analytic model for displacements on the surface of a half-space with a through-going hole.

The principles and operation of the holographic in situ stressmeter have been presented elsewhere [Bass et al. 1986, Schmitt 1987]. In brief, the stressmeter records, by holographic interferometry [Vest 1979], displacements induced by the drilling of a small hole of ≈1 cm diameter into the borehole wall. The magnitude and direction of the displacements depends on the state of stress at the borehole wall at the point where the sidehole is drilled. By measuring the stresses in several directions in the borehole, we can invert the values of the borehole wall stresses to obtain the far-field state of stress at that depth. (We use "far-field" in this study to indicate the ambient state of stress that would exist in the absence of the borehole. For the mine borehole from which the holograms in this thesis came, this is the state of stress at a given point in the mine pillar; for a conventional borehole, this might be the tectonic stress at a given depth in the crust.)

The interference holograms used for in-situ stress measurements are created by taking two exposures on a single piece of film. These two exposures interfere, and create a pattern of light and dark fringes when the hologram is reconstructed. A dark fringe is produced when the difference in the lengths of the raypath of the illuminating (object) beam reflecting off a certain point on the surface in the initial exposure and the raypath reflecting off the same point in its new location is an odd number of half-

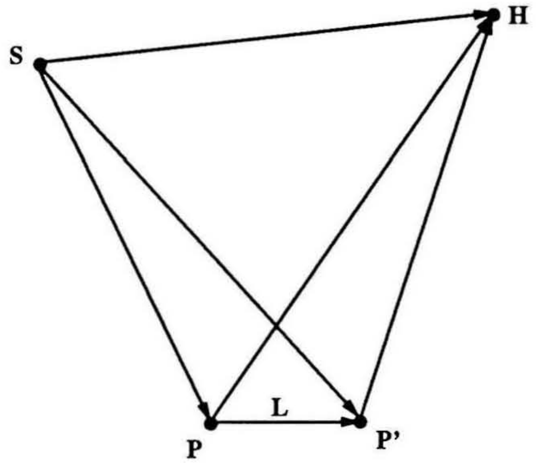

Figure 1.1: Raypaths for a double exposure hologram. Light travels from the source (S), reflecting off the point P to a point on the hologram file plane H. In the second exposure, the point P has been displaced to P′.

wavelengths of the laser light source (in this case, the wavelength of the HeNe laser beam is 632.8 nm). In figure 1.2, the light from the laser travels from the source S to a point on the borehole wall, P. It is reflected up to a point on the holographic film plane, H. For the second exposure, the point originally at P has moved to P′. The difference in the paths SPH and SP′H will determine whether there will be a dark or light fringe at the location P when the hologram is reconstructed from point H. The distance L between points P and P′ is typically quite small (microns) compared to the path SPH (centimeters).

Figure 1.2 shows a view looking down into the borehole. Once an area of the borehole, free of cracks and spallation, has been chosen, the instrument is locked into place and the first exposure is taken of the undisturbed borehole wall. After the first exposure, a drill bit advances and drills a small hole into the borehole wall. The size of the hole relative to the size of the borehole is greatly exaggerated in this figure. With the prototype instrument, the sidehole is 1 cm in diameter, while the borehole itself is 30 cm in diameter. The drill is then retracted, and, after waiting a few minutes for any thermal effects to subside, a second exposure is taken. The change in shape of the small area of the borehole wall around the stress-relief hole is recorded by this second exposure. The instrument is then either turned to face a different direction at the same depth in the borehole, or unlocked and moved to another location. Since the sensitivity of this technique is such that any displacements of more than 10 μm will be enough to cause the hologram to be unreadable due to excessive interference, it is important that motion of the camera between the time of the first and second exposures be limited as much as possible. In practice, we can use holograms in which the camera moved 5 μm or less. The pattern of the interference fringes is dependent on the borehole wall stresses, as well as the movement of the camera and the elastic properties of the rock. To analyze the data, we create "synthetic holograms" to model the displacements, and thus determine the borehole wall stresses. When these are known, we invert to find the far-field stresses.

There are several advantages in using this holographic technique to measure in situ stress. It is not limited to use in short holes, as are overcoring measurements, which are limited to boreholes only tens of meters in length [Wang and Wong 1987, Leeman 1969]. Analysis of the data does not assume that one of the principal stresses is vertical, as hydrofracture [Aggson and Kim 1987] or the USBM borehole deformation gauge [Obert et al. 1962] do. The off-axis component of the stress tensor may be significant in engineering applications, as is shown by our mine pillar results presented below, and it may be of interest as well in vertical boreholes, where the effects of topography may induce an off-vertical component. A set of three measurements at a particular depth is sufficient to determine the far-field stress tensor, unlike the flatjack method [Wareham and Skipp 1974, Rocha et al. 1966] which, since each

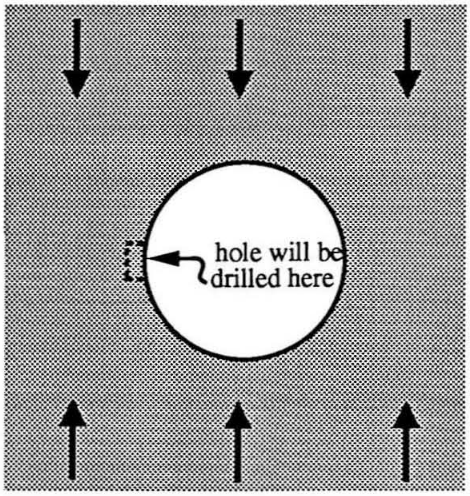

First exposure

Second exposure

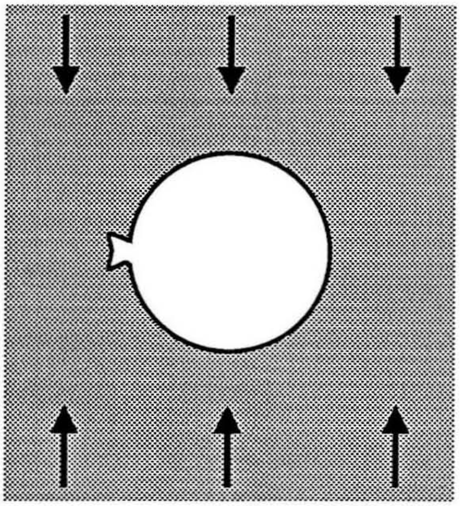

Figure 1.2: Cartoon of effect of drilling a sidehole into a stressed medium. The size of the side hole and the displacements are greatly exaggerated in this view

measurement determines stress in one direction only, requires at least six properly oriented measurements. This instrument may be used to examine changes in the state of stress at relatively closely spaced ($\approx$ 10 cm) depths in a borehole; other techniques such as hydrofracture measure stresses over a much larger interval of the borehole [Aggson and Kim 1987]. The stressmeter may also be used, with a slight modification, to measure the elastic modulus of the rock in-situ with an indention technique [Schmitt et al. 1986]. Since knowledge of the elastic properties is required in most stress-measurement techniques, it is advantageous to use an in-situ determination rather than a laboratory measurement, as the two may vary significantly. Moreover, this technique allows us to measure the elastic modulus in the same borehole as we take the stress measurements, and at the same locations, if we do the indention prior to the drilling of the stress-relief hole. The displacements induced by both the indention and the stress measurement are on the same micron scale, and so would be the most suitable means of determining the elastic parameters for each stress measurement.

Since the holograms give a picture of the area around the sidehole, we are often able to detect fine cracks and irregularities in the rock mass in the area of interest. This allows us to judge the quality of the measurements, and reject those which show a large amount of distortion by movement along cracks. Stress-measurement methods such as the slotting technique of Azzam and Bock [1987], which use strain gauges to measure the deformation, have no way of filtering out this kind of data.

The work described here was the first complete solution for the six components of far-field stress obtained by analysis of holographic stress-relief interferograms produced by this instrument. Previous work [Bass et al. 1986, Cohn 1983] had only enough data to determine five of the six components; the resulting values were not well constrained. We used the results of analysis of five stress-relief holograms taken at a distance of 4 m into a horizontal N-S oriented borehole in a pillar in a mine in

Garfield County, Colorado. The mine is approximately 180 m below the surface; the borehole is 2.0 m above the floor of the mine and is 30 cm in diameter. A sketch of the experimental set-up is shown in figure 1.3. The pillar is 15 m in height and in width.

1.3 Analysis of Holographic Data

Analysis of the interferograms begins with forward modeling of the displacement field recorded by the fringe pattern on the hologram. A typical stress relief hologram is shown in Figure 1.4. The stress relief hole is just below and to the right of the center of the figure. The long, linear fringes running from top to bottom are due to translation of the optics module of the stressmeter (the module containing the holographic camera) between the two exposures.

When considering double exposure holograms, it is important to keep two things in mind. First, the fringe patterns observed on the final product are the result of displacement arising from two distinct sources: the displacement caused by local relief of stress due to drilling the sidehole, and the rigid body translations caused by movement of the holographic camera between the two exposures. Figure 1.5 sketches the effects of the two sources of displacement. A point P is displaced to the point P_S due to the drilling of the stress-relief hole. Since the time the first exposure was taken, the camera has moved relative to the borehole wall along the vector -T. Thus the point P has been moved to P$'$. These two components of displacement are added together to produce the fringe pattern, as shown in figure 1.6. In this case the camera has moved -9.2 μm to the ϕ-direction of figure 1.9, 1.5 μm in the h-direction, and 2.7 μm in the ζ-direction, out of the page. This figure shows the fringe patterns that result from each displacement field. The second thing to remember is that the fringe pattern, while caused by the displacement that has occurred between the two

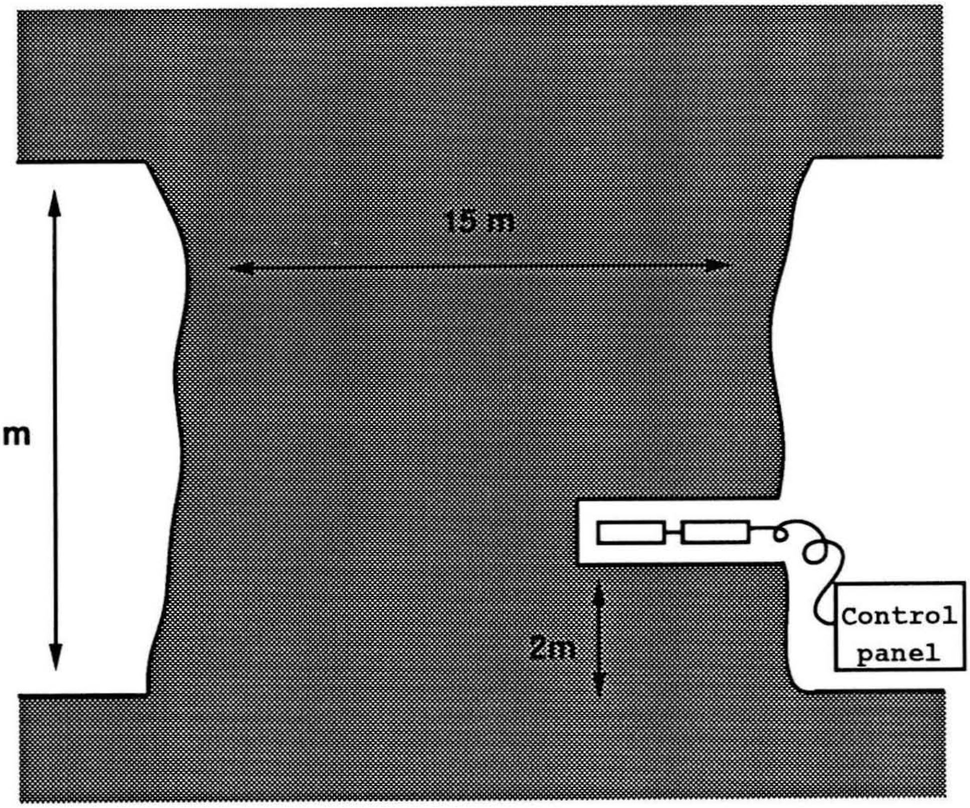

Figure 1.3: Sketch of experimental set-up for the data in this chapter. The stressmeter was placed in a horizontal borehole in a mine pillar. The size of the instrument relative to the length of the borehole is exaggerated.

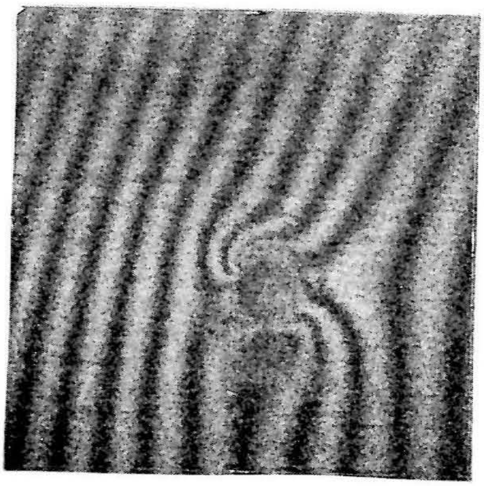

Figure 1.4: An example of a stress-relief hologram. The long, linear fringes across the picture are due to movement of the holographic camera between exposures. The curved fringes near the stress-relief hole are due to the distortion of the surface due to the hole being drilled.

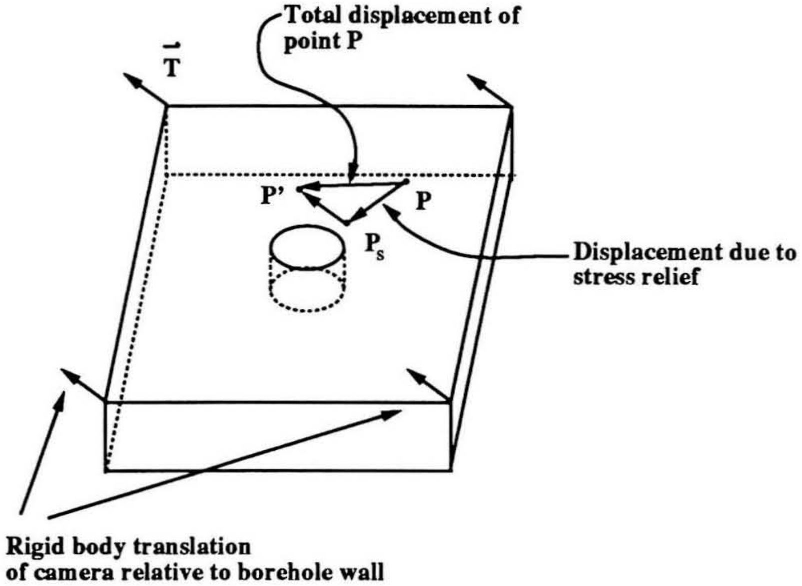

Figure 1.5: The two components of the displacement field of the borehole wall. The displacements due to camera module translation (T) and due to stress-relief (P-P′) sum to create the total displacement field.

exposures, is not a direct representation of the displacement field on the surface, but the result of change in the length of the optical path traveled by the laser light, and depends on factors such as the position of the source of the illumination and the point on the film plane from which the holographic reconstruction was made.

We model the holograms by setting the known parameters (the location of the illumination (object) beam and the reconstruction point of the film plane, as well at the elastic parameters Young's modulus and Poisson's ratio), and varying the camera module translations and the borehole wall stresses until a suitable match is made with the observed fringe pattern. As can be seen from figure 1.6, the character of the two kinds of displacement is quite different. The stress relief displacements are

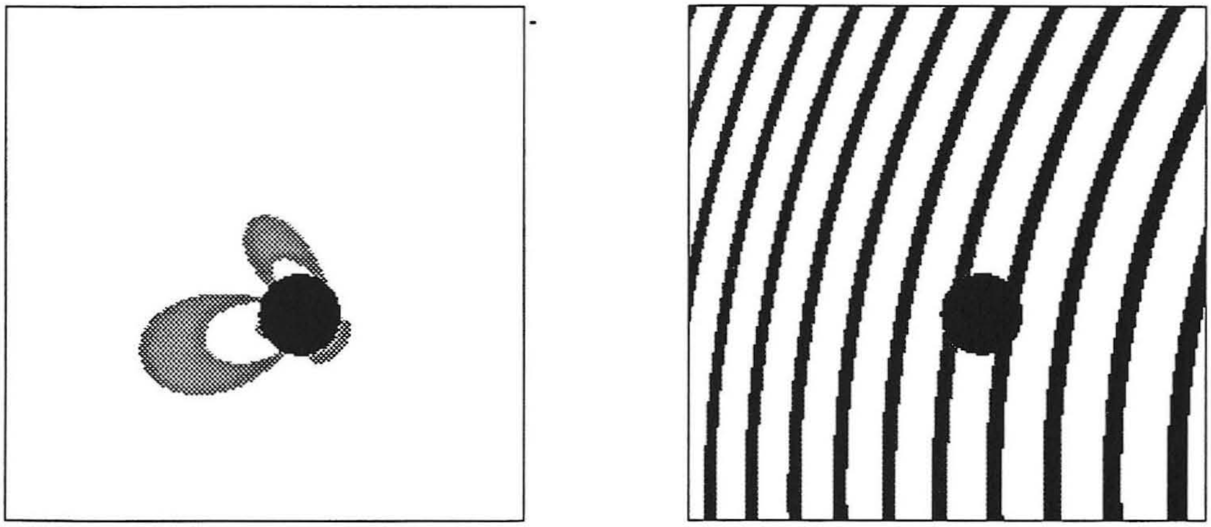

Stress relief

Rigid translations of camera

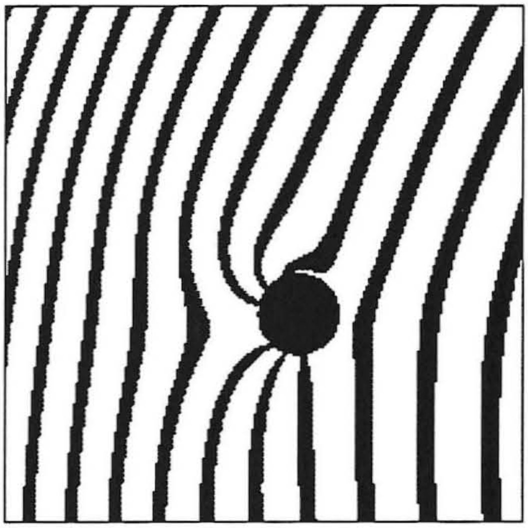

Total

Figure 1.6: The two components in the displacement field of a typical hologram. The displacements due to camera module translation and due to stress-relief sum to create the final pattern of interference fringes. The pattern also depends on the optical geometry of the holographic camera.

only significant near the sidehole, while the rigid body translations of the camera affect the entire hologram field of view. In practice, the presence of a small amount of camera movement between the two exposures can greatly aid the analysis, as the stress relief displacements perturb the regular pattern of the translations.

The model initially used to calculate stress relief displacements on the borehole wall [Bass et al. 1986] is that of a throughgoing hole in an infinite flat homogeneous elastic plate subjected to plane stress at infinity. The thickness of the plate is set at twice the depth of the sidehole that was drilled into the borehole wall, on the assumption that the displacements in the rock at the depth of the bottom of the stress relief hole are small, and would thus be similar to the plane of symmetry of a plate that is twice as thick as the stress relief hole is deep. To analyze the holograms we generate a displacement field by superposition of the displacement field induced by stressing a plate with a hole and the displacement field of a stressed plate without a hole. The difference between the two fields is the displacement due to the drilling of the stress relief hole. We assume that the flat plate is subjected to plane stress at infinity; this represents the state of stress on the borehole wall, where there are only three non-vanishing stresses: $\sigma_{\phi\phi}$, the hoop stress (the stress in the direction around the circumference of the borehole), σ_{hh}, the stress in the direction along the axis of the borehole, and $\tau_{\phi h}$, the shear stress on the borehole wall. These stresses are related to the far-field stresses $(\sigma_{xx}, \sigma_{yy}, \sigma_{zz}, \tau_{xy}, \tau_{xz}, \tau_{yz})$ by [Hiramatsu and Oka 1962, Leeman and Hayes 1966]:

$$\begin{aligned}
\sigma_{\phi\phi} &= \sigma_{xx} + \sigma_{yy} - 2(\sigma_{xx} - \sigma_{yy})\cos 2\phi - 4\tau_{xy}\sin 2\phi, && (1.1)\\
\sigma_{hh} &= -\nu[2(\sigma_{xx} - \sigma_{yy})\cos 2\phi + 4\tau_{xy}\sin 2\phi] + \sigma_{zz}, && (1.2)\\
\tau_{\phi h} &= 2(-\tau_{xz}\sin\phi + \tau_{yz}\cos\phi). && (1.3)
\end{aligned}$$

The stresses $\sigma_{\phi\phi}, \sigma_{hh}$, and $\tau_{\phi h}$ are the plane stresses applied to the edges of the plate in our model. By convention [Timoshenko and Goodier 1970], compressive normal stresses are negative, and positive shear stress is as shown in Figure 1.7. The far-field (pillar) stresses are σ_{xx}, σ_{yy}, σ_{zz}, τ_{xy}, τ_{xz}, and σ_{yz}, with the coordinate system as pictured in figure 1.7. The z-axis, which in a vertical borehole would be the vertical axis, is in the case of the mine pillar, the horizontal axis in the direction along the axis of the borehole (N-S; see Figure 1.8). These stresses may also be expressed in terms of the cylindrical coordinate system r, θ, h, as pictured in the same figure. The values of the stresses at the borehole wall depend also on Poisson's ratio (ν) and the azimuth ϕ measured from the direction of the positive x-axis.

Since the hole is small relative to the size of the borehole, and we are interested mostly in the displacements very close to the sidehole, we treat the borehole wall as locally flat and homogeneous in the vicinity of the sidehole. The displacements for an infinite, homogeneous, elastic stressed plate with no hole are, for the cylindrical coordinate system r, θ, ζ pictured in figure 1.9 [Timoshenko and Goodier 1970, Jaeger and Cook 1979]:

$$\begin{aligned} u_r &= \frac{1}{E}\left[(\sigma_2 - \nu\sigma_1) r \sin^2\omega + (\sigma_1 - \nu\sigma_2) r \cos^2\omega\right], && (1.4)\\ u_\theta &= \frac{1}{E}\left[(1+\nu)(\sigma_2 - \sigma_1) r \sin\omega \cos\omega\right], && (1.5)\\ u_\zeta &= -\frac{\nu}{E}(\sigma_1 + \sigma_2)\frac{t}{2}. && (1.6)\end{aligned}$$

Where σ_1 and σ_2 are the principal stresses, with the angle ω measured from the direction of the stress σ_1. For a stressed plate of thickness t with a hole of radius a and depth $t/2$ centered at $r = 0$:

$$\begin{aligned} u_r &= \frac{1}{2E}\left[(\sigma_1 + \sigma_2)(r + \frac{a^2}{r}) + (\sigma_1 - \sigma_2)(r - \frac{a^4}{r^3} + \frac{4a^2}{r})\cos 2\omega\right]\\ &\quad -\frac{\nu}{2E}\left[(\sigma_1 + \sigma_2)(r - \frac{a^2}{r}) - (\sigma_1 - \sigma_2)(r - \frac{a^4}{r^3})\cos 2\omega\right], && (1.7)\\ u_\theta &= \frac{1}{2E}\left[-(\sigma_1 - \sigma_2)(r + \frac{2a^2}{r} + \frac{a^4}{r^3})\sin 2\omega\right]\\ &\quad -\frac{\nu}{2E}[(\sigma_1 - \sigma_2)(r - \frac{2a^2}{r} + \frac{a^4}{r^3})\sin 2\omega], && (1.8)\\ u_\zeta &= -\frac{\nu}{E}[(\sigma_1 + \sigma_2) - (\sigma_1 - \sigma_2)\frac{2a^2}{r^2}\cos 2\omega]\frac{t}{2}. && (1.9)\end{aligned}$$

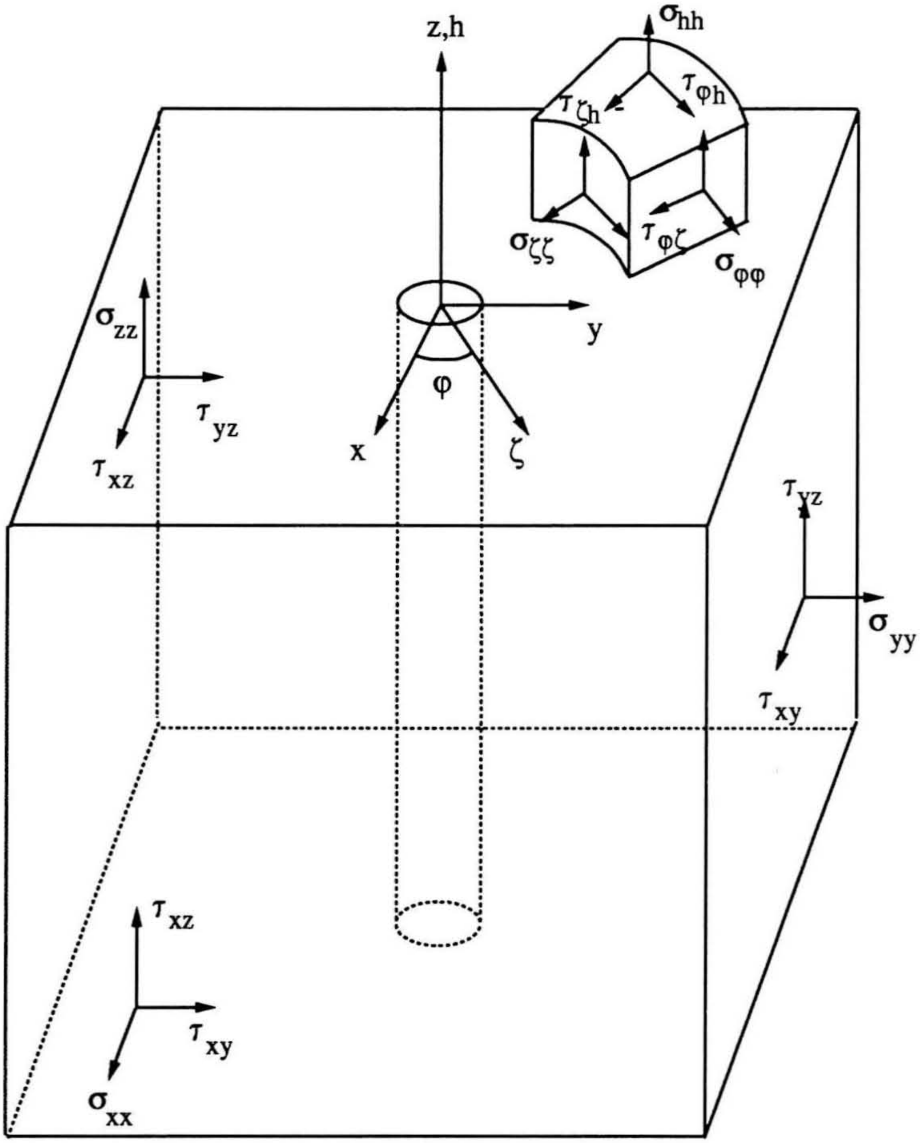

Figure 1.7: Far-field coordinate systems x, y, z and ζ, ϕ, h, centered on the axis of the borehole. Positive shear stresses are as pictured.

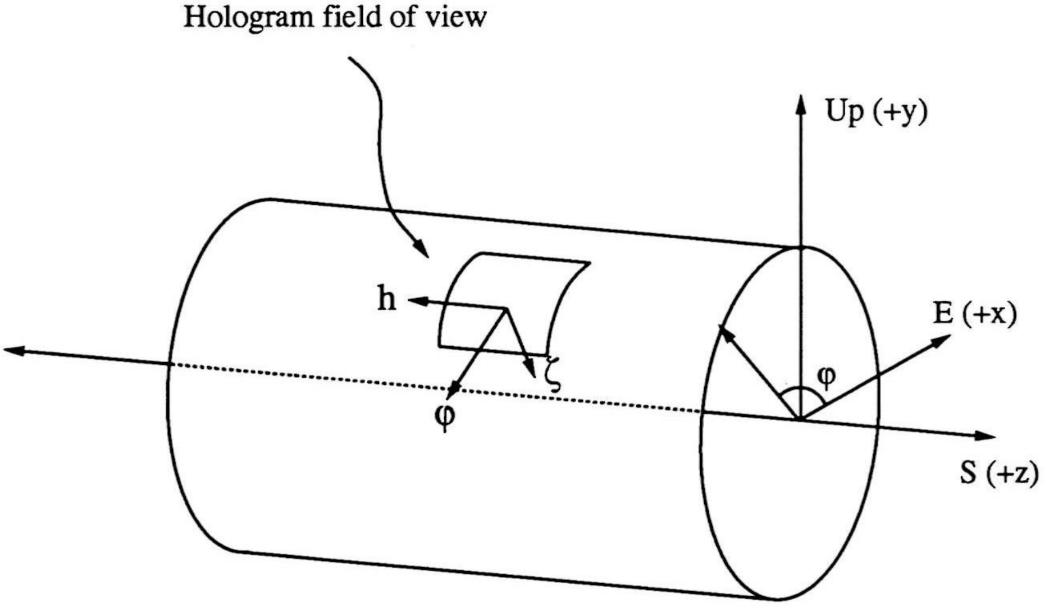

Figure 1.8: Geometry of the borehole coordinate system for these measurements. The borehole is oriented north-south, and the angle ϕ is measured from east.

Hence the displacements of the borehole wall, in terms of the borehole wall stresses $\sigma_{\phi\phi}, \sigma_{hh}$, and $\tau_{\phi h}$ are given by:

$$\begin{aligned}
u_r &= \frac{1}{2E}\left\{(\sigma_{\phi\phi}+\sigma_{hh})(1+\nu)\frac{a^2}{r}+(\sigma_{\phi\phi}-\sigma_{hh})[\frac{4a^2}{r}-(1+\nu)\frac{a^4}{r^3}]\cos 2\theta\right. \\
&+ \left. 2\tau_{\phi h}[\frac{4a^2}{r}-(1+\nu)\frac{a^4}{r^3}]\sin 2\theta\right\}, && (1.10) \\
u_\theta &= -\frac{1}{2E}\left\{[(1-\nu)\frac{2a^2}{r}+(1+\nu)\frac{a^4}{r^3}][(\sigma_{\phi\phi}-\sigma_{hh})\sin 2\theta - 2\tau_{\phi h}\cos 2\theta]\right\}, && (1.11) \\
u_\zeta &= \frac{\nu a^2 t}{E r^2}[(\sigma_{\phi\phi}-\sigma_{hh})\cos 2\theta + 2\tau_{\phi h}\sin 2\theta]. && (1.12)
\end{aligned}$$

u_r represents displacement in the radial direction, u_θ displacement in the azimuthal direction, and u_ζ displacement in the direction normal to the borehole wall. Note that only the normal displacement depends on the plate thickness. Therefore, in this theory, the depth of the hole does not affect the horizontal displacement. The modeling of the borehole wall displacements requires knowledge of Young's modulus (E) and Poisson's ratio (ν); the value of Young's modulus (25 GPa) used here was the value determined by Schmitt et al. [1986] from in situ holographic elastic modulus measurements made at the same locations in the same mine pillar borehole. Poisson's ratio, not well constrained by the borehole wall indention technique used to determine Young's modulus, was set at a value of 0.345 [Horino et al. 1982].

Ideally, only three holograms, properly oriented, are needed to determine the complete far-field stress tensor [Leeman and Hayes 1966], but five were analyzed in order to obtain a more accurate fit to the data. In the coordinate system defined in figure 1.8, where azimuths are measured from the positive x-axis (pointing east), these holograms were at azimuths of 90°, 45°, 0°, 180°, and 225°. The values of the three non-vanishing borehole wall stresses ($\sigma_{\phi\phi}$, σ_{hh}, and $\tau_{\phi h}$) were determined by forward modeling of the observed hologram interference patterns; these values are listed in Table 1.1. The rigid body translations for these holograms are given in table 1.2. The holograms are identified by a label that indicates the date, roll

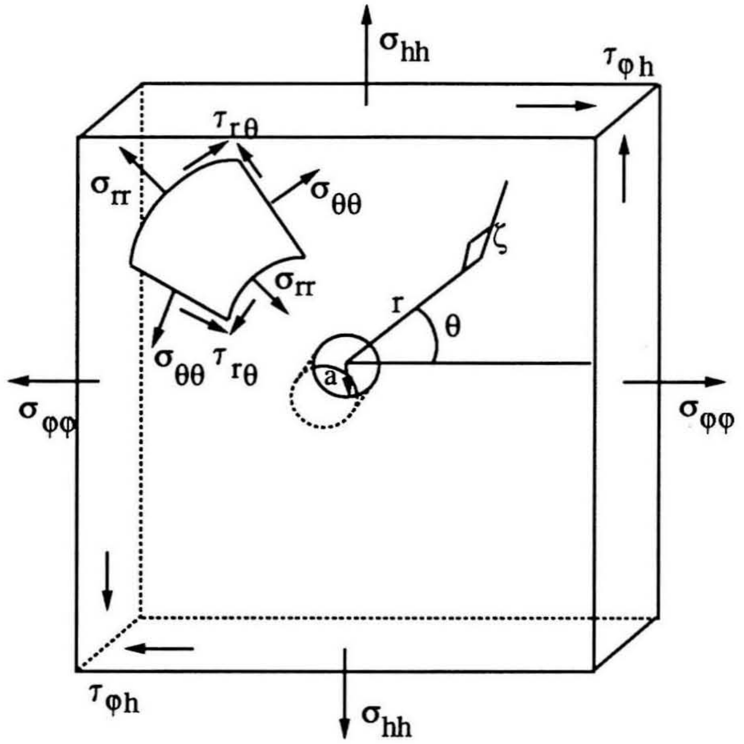

Figure 1.9: The plate coordinate system r, θ, ζ, centered on the stress-relief hole, which has radius a. The applied stresses, corresponding to the borehole wall stresses, are $\sigma_{\phi\phi}, \sigma_{hh}, \tau_{\phi h}$. The directions of positive stresses are as shown by the arrows.

Borehole wall stresses (in MPa)				
Hologram	Azimuth	$\sigma_{\phi\phi}$	σ_{hh}	$\tau_{\phi h}$
16/1/4	90°	-22.5 ± 2.5	5.0 ± 5.0	-15.0 ± 5.0
16/2/5	45°	-10.0 ± 5.0	-16.0 ± 8.0	-28.0 ± 2.0
16/3/3	0°	-20.0 ± 4.0	-7.0 ± 5.0	-10.0 ± 2.5
15/1/8	180°	-22.0 ± 4.0	0.0 ± 4.5	5.0 ± 5.0
15/1/4	225°	-22.0 ± 4.0	3.5 ± 6.5	5.0 ± 5.0

Table 1.1: Plate model solutions for the borehole wall stresses.

of film, and exposure; we have retained these labels here for ease of reference. All were 4 meters from the free surface of the pillar. The synthetic holograms are shown in figures 1.28 - 1.32. The results from this plate model analysis are the synthetic holograms on the lower left of each figure. The orientation of the holograms in the borehole is as shown in figure 1.27. Due to the geometry of the optical system, the values for the hoop stress ($\sigma_{\phi\phi}$) are the best constrained; all but one are close to -20 MPa. The uncertainties listed in the table are determined by varying the values of the borehole wall stresses until the synthetic fringe pattern is no longer similar to the observed pattern. In some cases, particularly for σ_{hh} and $\tau_{\phi h}$, the uncertainties may be quite large, since with this model, the displacement field is more sensitive to changes in $\sigma_{\phi\phi}$ than to variation of the other two stresses.

1.4 Finite Element Analysis

Since the plate model hologram analysis method described above depends on a stress-relief displacement model which may not accurately reflect the true geometry of the borehole, we developed a two-dimensional finite element model. The displacements predicted by this model were compared to the analytic solution for a hole in a stressed plate that was used in the analysis of the holograms presented above. Possible

Camera module translations (for plate module fits) (μm)			
Hologram	ϕ	h	ζ
15/1/4	3.85	2.2	2.275
15/1/8	2.0	0.8	2.05
16/1/4	3.1	2.6	1.55
16/2/5	-3.525	0.985	4.05
16/3/3	-9.2	1.5	2.7

Table 1.2: Rigid body translations of the camera module for the synthetic holograms modeled by the plate model.

inadequacies of the plate model may arise from the effects of the finite thickness and symmetry of the plate, the shape of a terminated stress-relief hole, and on the assumption of plane stress. The finite element calculations were done in part to see how large any effects might be. Another reason for doing the finite element calculations was to analyze the effects of changing the depth and diameter of the stress-relief hole on the displacements of the borehole wall. The analytic plane stress plate model predicts no change in horizontal displacements with changing hole depth (i.e., changing plate thickness); it was desired to know whether changes in depth would significantly alter the displacements. The analytic plate model uses a plate thickness that is twice the depth of the stress-relief hole, on the assumption that the vertical displacements in the rock mass are small at the depth of the stress relief hole, thus mimicking the symmetry plane of a plate of thickness twice the depth of the hole. Moreover, some holograms are difficult to analyze with the existing plate model, especially in low-stress situations. The finite element analysis was an initial attempt to discover where these problems may arise.

The finite element program used was a two-dimensional code [Hughes et al. 1987] simulating a box with dimensions large relative to the size of the hole. The sides of the box were 50 cm and 25 cm long, and the hole depth and diameter ranged from 0.25 to 1.5 cm and 0.5 to 1.5 cm respectively. (Actual holograms of the borehole wall view an area as large as 8 cm by 8 cm centered on the stress relief hole.) A stress of 20 MPa was applied to the 25 cm sides and displacements were calculated for all of the 1060 elements in the grid. This grid did not take into account the effects of curvature of the borehole wall, but the analysis presented here only considers the displacements in the area viewed by the hologram, where the effects of curvature are small. The analytic plate model also ignores the curvature of the borehole wall. The analysis was done for a material with the same elastic properties as used in the hologram analysis, with a Young's modulus of 25 GPa and a Poisson's ratio of 0.345. Three different stress configurations were tested: plane stress, plane strain, and biaxial stress (an axisymmetric calculation). The plane stress case corresponds to a case where the intermediate stress is zero; the plane strain case is one in which the intermediate stress is non-zero and smaller in magnitude than the maximum stress and the walls of the box are constrained not to move in the direction normal to the applied stress (out of the page of figure 1.10); the axisymmetric case is one in which the maximum and intermediate stresses are equal. In all three cases the minimum stress, in the direction normal to the free surface of the borehole wall, is zero. This two-dimensional finite element arrangement is unable to model shear stress on the surface of the borehole wall.

Figure 1.10 shows a cartoon of the displacements resulting from drilling a small hole into the stressed finite element box. The plane stress and plane strain cases are shown as boxes with central square cuts; this is due to the geometry of the two-dimensional calculations. The axisymmetric case is a cylinder with a hole in it subjected to a uniform stress; the situation in our experiments, a round hole in a large medium subjected to non-equal principal stresses, is in between these two extremes. In this figure, it should be noted that the magnitude of the displacements and the size of the hole are greatly exaggerated relative to the size of the finite element box. These stress-relief displacements were calculated in a manner analogous to the method used in the plate model calculations: they are the difference between the displacements of the stressed body with a hole and the stressed body without a hole. By superposition, the difference in the two displacement fields is the displacement due to the drilling of the hole in a prestressed medium. All of the displacements are about 1μm meters or less for a 20 MPa compressive stress applied to the sides of the box. In all cases, displacement is greatest near the hole. Generally, horizontal displacements are larger than vertical displacements. Surface points near the hole are displaced down and inward toward the axis of the hole when subjected to compressive stress. The vertical displacements are down toward the bottom of the box from their original location. The plane stress case shows the largest displacements, the axisymmetric case, the smallest.

Figures 1.11 - 1.13 compare the displacements predicted by the finite element calculations and the plate model, for a material with a Young's modulus of 25 GPa and Poisson's ratio of 0.345. The three plots show the displacements on the surface of the borehole wall as it varies with distance from the center of the hole. The distance scale is measured in units normalized by the hole radius, which was in these cases 0.5 cm. Thus the edge of the hole is at a distance equal to unity. For the horizontal displacements, a negative displacement is in the direction toward the center of the stress-relief hole; for the vertical displacements, a negative displacement is directed into the body, normal to the free surface. These figures show the results of calculations for the three stress states mentioned above for a hole of diameter 1.0 cm and depth 0.5 cm, a geometry which closely approximates the actual hole drilled by the stressmeter. Bold lines indicate the plate model calculations; in this case the plate would be 1.0 cm thick. Dashed lines indicate the vertical component. In the plane stress and plane strain cases, the finite element results show almost 1.5

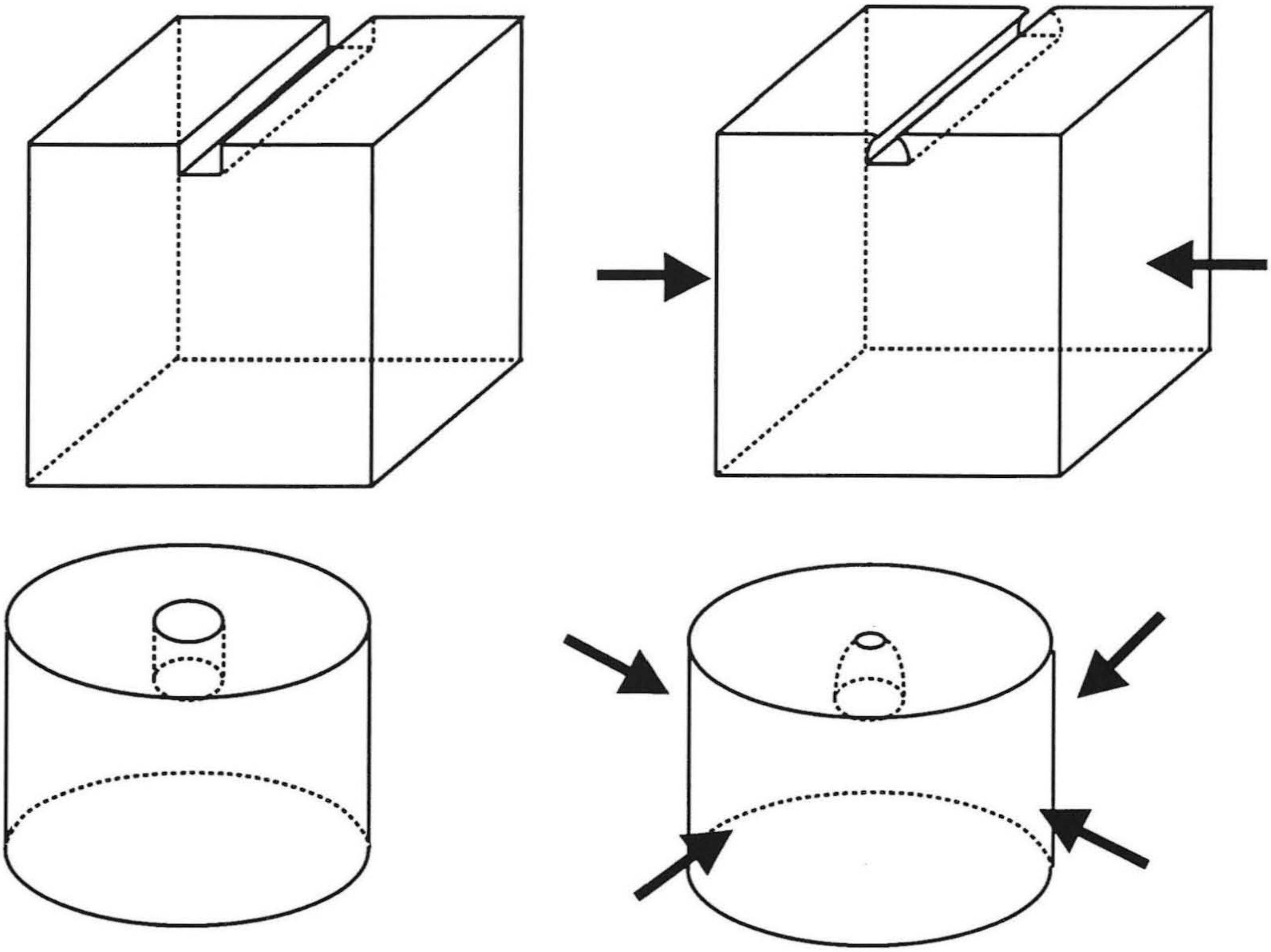

Figure 1.10: Sketch of the two-dimensional finite-element models. Top: the plane-stress and plane-strain models represent an infinite box with a square groove, with stress applied on the left and right ends of the box. The initial state is on the left; the stressed state on the right shows that the sides of the groove have moved inwards and down slightly. Bottom: the axisymmetric case represents a cylinder with a cylindrical hole, with a uniform stress around the circumference of the body.

times as much horizontal displacement as the plate model would predict. For the axisymmetric case the agreement between the two models is closer; the finite element horizontal displacements are actually slightly smaller than those of the plate model. The finite element model shows larger vertical displacements for all three cases. The plate model predicts no vertical displacements for the axisymmetric case, yet the finite element model shows some small movement of the surface. These differences in the magnitude of displacement increase near the hole, where they become large enough to affect the stress relief pattern on the hologram. This difference is enough to show up on a hologram, as is shown in figure 1.14. The fringe patterns in the figure are the result of the interaction of the displacements due to an applied stress of 20 MPa and translations of -2 μm in the ϕ-direction and 2 μm in the ζ-direction as defined by figure 1.9. While this example was chosen to highlight the possible differences, it is clear that a small change in the displacement field can have a significant effect on the final fringe pattern.

The effects of changing the depth and diameter of the stress-relief hole are shown in Figure 1.15. The light lines are for holes of depth 0.5 cm and radius varying from 0.25 to 0.75 cm; the bold lines represent holes 1.0 cm deep for the same range of radius. As in figures 1.11 - 1.13, the axis is plotted in terms of hole radius. The curves for a given hole depth are similar at the edge of the hole and at large distances from the hole, but vary in the intermediate distance. The depth of the stress-relief hole is clearly a much more important factor than its width. An increase in the depth by a factor of two yields a corresponding increase in both components of displacement, but changing the width by a factor of three will at most double the displacement at an intermediate distance, 4 radii from the center of the hole. The plate model predicts that changing the depth of the hole would have no effect on the horizontal displacements; the finite element calculations suggest that this is not the case. The analytic plate model does predict larger vertical displacements for deeper holes, as

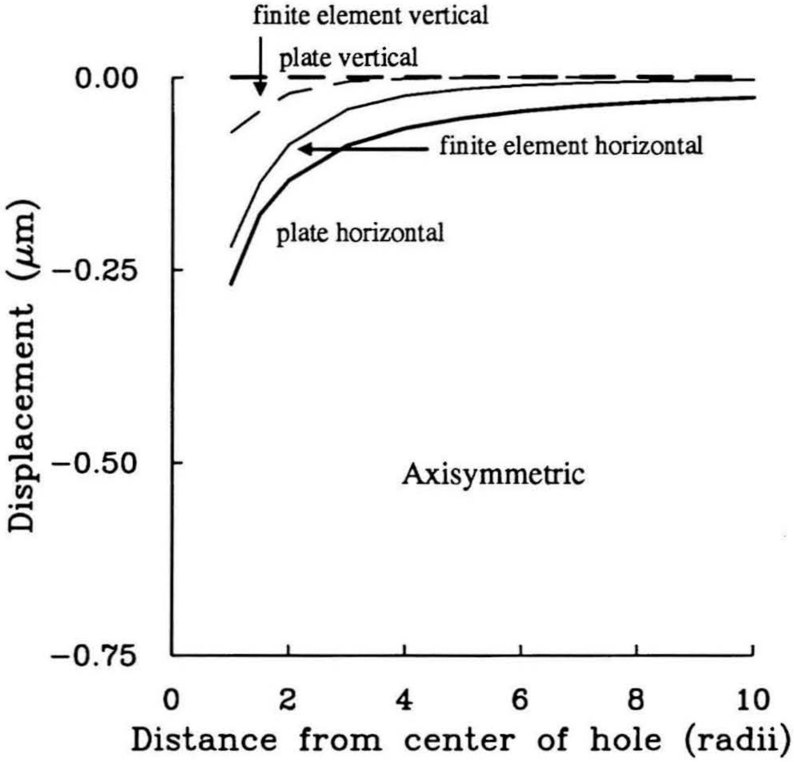

Figure 1.11: Comparison of displacements predicted by the plate model (bold lines) and the finite element model (light lines) the axisymmetric case. The horizontal displacements (solid lines) are larger in the plate model, but the finite element model predicts more vertical (dashed lines) movement.

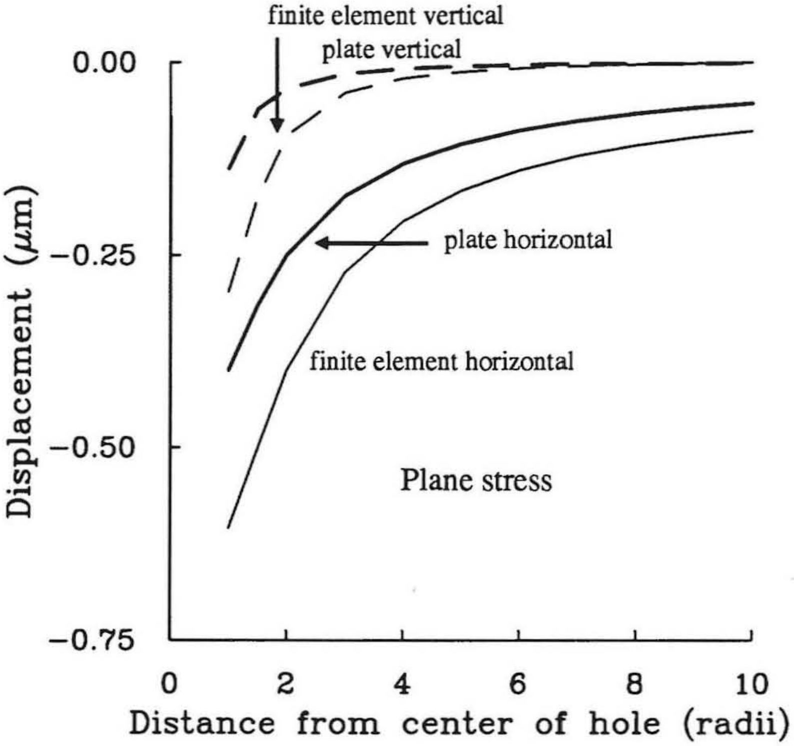

Figure 1.12: Comparison of displacements for the plane stress case. Light lines identify finite element results; dashed lines represent the vertical component.

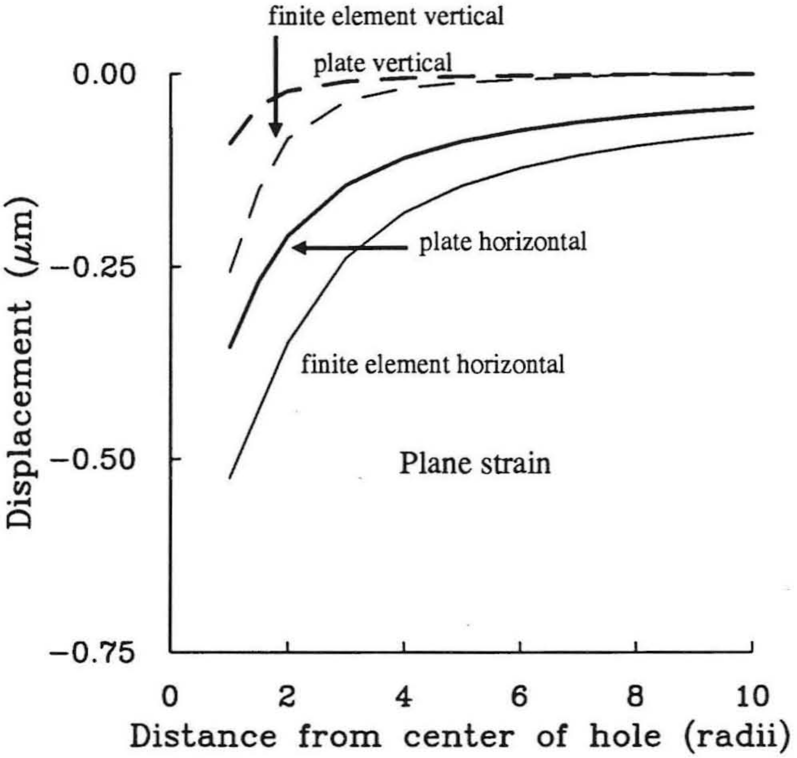

Figure 1.13: Comparison of displacements for the plane strain case. Light lines identify finite element results; dashed lines represent the vertical component.

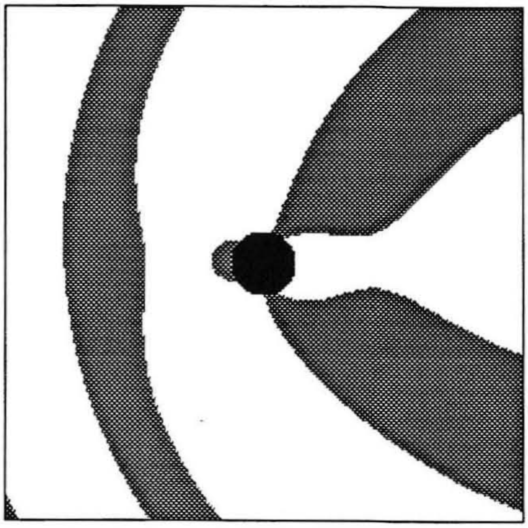

Plate model

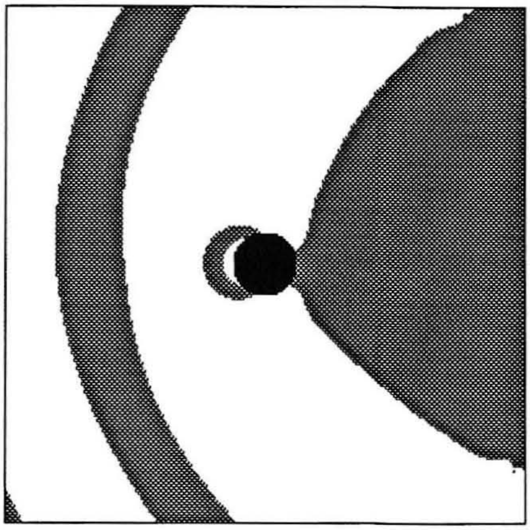

Finite element

Figure 1.14: Slight changes in the displacement can have a noticeable effect on the fringe pattern. For an applied, axisymmetric stress of -20 MPa, the fringe pattern predicted by the plate model (above) differs from that predicted by the finite element model. The camera module translations of -2 μm in the ϕ direction and 2 μm in the ζ direction were chosen to highlight this difference, but it is clear that the effect can be significant.

do the finite element calculations.

The finite element calculations suggest that the effect of hole depth on the horizontal displacements of the borehole wall is much more important than the analytic plate model indicated. This effect is most pronounced near the stress relief hole, which is in the region where stress relief displacements become large enough to create interference fringe patterns. The underestimation of total displacements due to a given set of borehole wall stresses leads to an overestimation of borehole wall stresses: more stress is put into the model in order to make up for the underestimated displacement. This in turn leads to an overestimate of the far-field state of stress. In addition, the predictions of the analytic plate model, in not accounting for as much vertical displacement near the hole as the finite element model suggests that there should be, may be the cause of the difficulty in exactly matching the observed fringe pattern by using the analytic plate model. This mismatch is most pronounced in situations where the stress field at that location on the borehole wall has a low value. Some observed fringe patterns have never adequately been modeled using the analytic plate theory.

The results of the finite element analysis may be applied to the results of the analytic plate model estimate of the components of the far-field stress presented above. For most of the holograms, the hoop stress ($\sigma_{\phi\phi}$) is much greater than the normal stress along the axis of the borehole (σ_{hh}), similar to the plane stress case. Thus the values of the borehole wall stresses may be overestimated in these cases by as much as 10%. For one hologram (taken at the azimuth 45°), the $\sigma_{\phi\phi}$ is less than or nearly equal to σ_{hh}, as in the axisymmetric case; the resulting stress values may be slightly underestimated. However, due to the use of a two-dimensional finite element code, it was not possible to take into account the effect of the shear stress ($\tau_{\phi h}$) on the displacements, so the finite element results will not directly allow us to assess the amount of error in this estimate of the state of stress in the mine pillar.

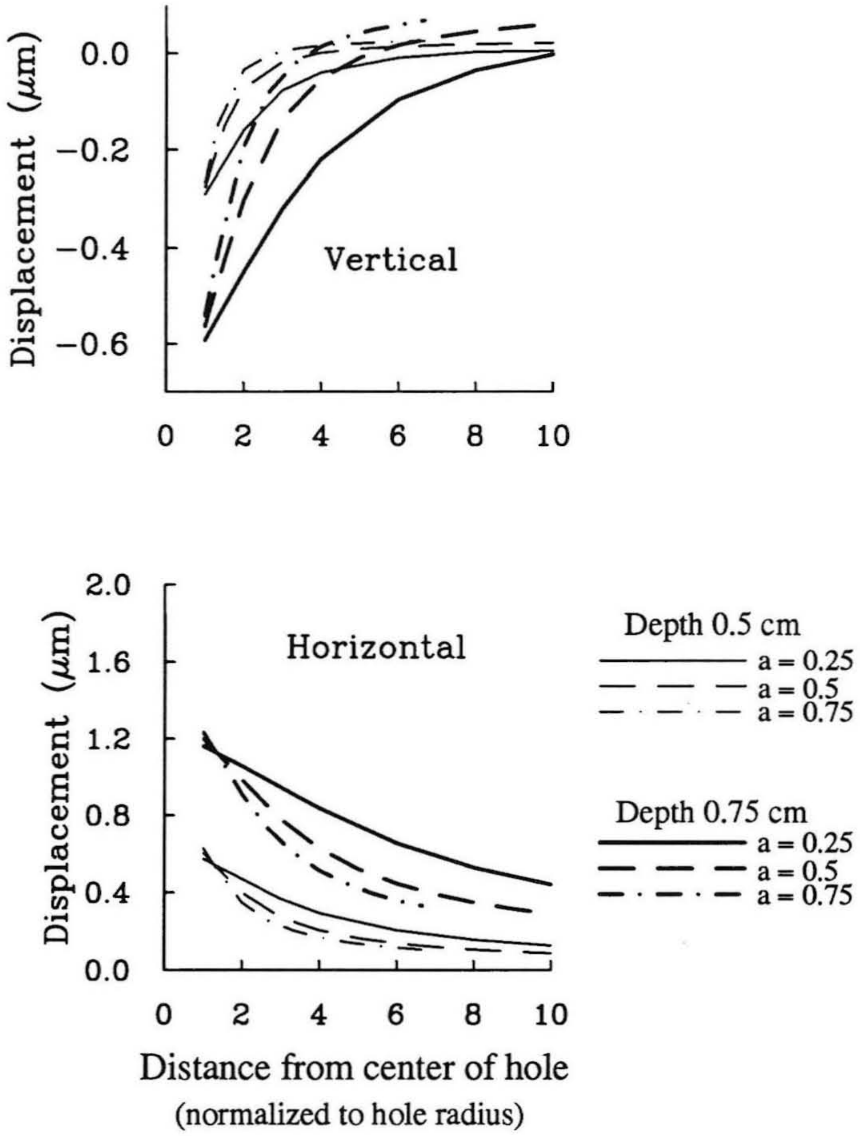

Figure 1.15: The effect of varying hole depth and diameter on the displacements in the finite element model. Results are plotted for the plane stress case. Light lines indicate curves for the case of a hole of depth 0.5 cm. The depth of the hole has a much greater effect than its width.

1.5 Revised Model

In order to determine the displacements on the surface of the borehole wall that occur due to the drilling of the stress-relief hole, we must be able to model the displacement field accurately. Previously, we have modeled the borehole wall as a flat elastic plate of thickness twice the depth of the stress relief hole. The finite element calculations presented above and the existence of holograms which cannot be matched with computed (synthetic) holograms suggest that this model is not fully adequate. Therefore, following the approach of Youngdahl and Sternberg [1965, 1966], we used the model of a cylindrical hole of radius a in an elastic, isotropic half-space. This model should more accurately represent the displacements on the surface of a body with a hole drilled in it.

Our plate model assumes plane stress within the entire plate; however, for a plate with a thickness to hole diameter ratio greater than unity, this assumption is less valid (for the stress-relief hole as drilled by the stressmeter, this ratio is approximately 1.33). Moreover, it is certainly not the case in the area near the surface of the borehole. One consequence of this is the underestimation of displacements in the ζ-direction (the direction perpendicular to the surface of the borehole wall). This effect is most pronounced near the stress-relief hole, which is the area in which these displacements become large enough to be measurable by the holographic technique. In fact, in field experiments we have collected several holograms which show only small displacements near the stress-relief hole that we have been unable to match with synthetics; this is thought to be representative of some inaccuracy in the plate model.

The approach of Youngdahl and Sternberg relaxes the assumption of plane stress within the body. An infinite isotropic elastic half-space with a throughgoing hole is loaded at infinity with plane stresses in the x and y directions (parallel to the bounding plane of the half-space). The stresses and displacements within the body and on the surface are calculated using Papkovich stress functions [Papkovich 1932, Sokolonikoff 1956] and integral transforms. The resulting integrals for the displacements and stresses can then be solved numerically. These results show the existence of a three-dimensional stress boundary layer that occurs near the edges of the hole in the related problem of a plate of finite thickness, as the ratio of the thickness of the plate to the diameter of the hole increases.

The two models are sketched in figure 1.16. Figure 1.16(c) shows the half-space model. The radius of the hole is a; any point in the half space may be described by the Cartesian coordinates x, y, z or the more convenient cylindrical coordinates r, θ, ζ. The plate model is pictured in fig 1.16(b). The hole of radius a goes all the way through the plate; the thickness of the plate is t. In the modeling of the holograms, the value of t is set at twice the depth of the stress relief hole that was drilled into the borehole wall. Figure 1.16(c) shows the actual geometry of the stress relief hole: it has radius a and depth $t/2$. Hence the real situation is intermediate to the two models – a finite depth hole in an (almost) infinite region.

This study compares the predictions of these two models in order to determine the best method for analysis of the stress relief holograms. As before, we assume plane stress, i.e., stress parallel to the bounding plane of the half-space (the surface $z = 0$). The principal stresses on the plane can be denoted $\sigma_{11} = \sigma_1$ and $\sigma_{22} = \sigma_2$. This can be decomposed into two components:

a) plane axisymmetric stress σ_H applied at infinity, and

b) plane pure shear (σ_S),

where $\sigma_H = \frac{1}{2}(\sigma_1 + \sigma_2)$ and $\sigma_S = \frac{1}{2}(\sigma_1 - \sigma_2)$. Case a) has the well known (e.g., [Jaeger and Cook 1979]) solution for the displacements:

$$\frac{2\mu u_r^H}{a\sigma_H} = \frac{1-\nu}{1+\nu}\rho + \frac{1}{\rho}, \tag{1.13}$$

$$\frac{2\mu u_\zeta^H}{a\sigma_H} = -\frac{2\nu}{1+\nu}\psi, \tag{1.14}$$

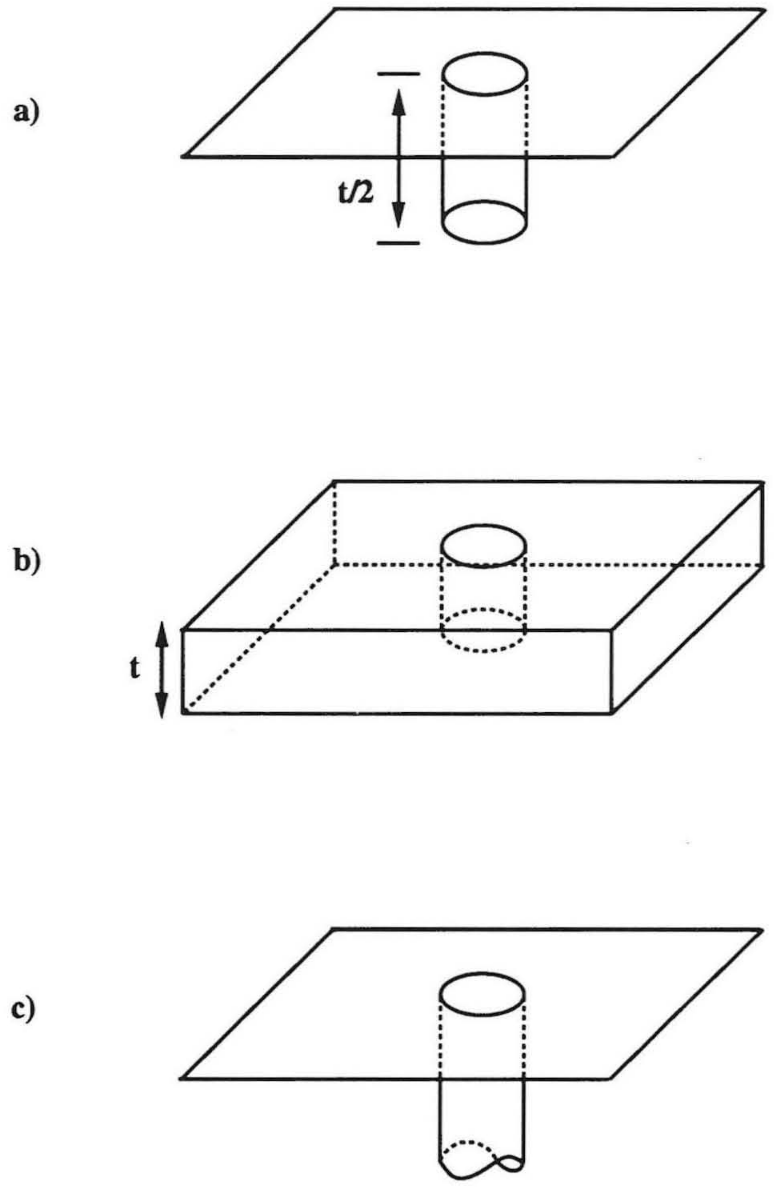

Figure 1.16: The models used for calculations of stress-relief displacements. a) the actual geometry of the stress-relief hole. b) the plate model. c) the model of Youngdahl and Sternberg (referred to in other figures as the revised model).

$$u_\theta^H \;=\; 0. \tag{1.15}$$

Where ρ and ψ are the dimensionless coordinates $\rho = r/a$ and $\psi = \zeta/a$. Note that there are no tangential displacements and that there are also no vertical displacements on the surface $\zeta = 0$.

The solution for case b), however, is not as simple. The approach taken is to consider the residual problem created by subtracting the plane strain solution associated with the pure shear problem from the exact solution. The plane strain solution satisfies the field equations as well as the boundary conditions on the surface of the cylindrical hole, but does not satisfy all of the boundary conditions on the surface of the half-space. The displacements obtained from the associated plane strain solution are:

$$\frac{2\mu u_r^P}{a\sigma_S} \;=\; (\rho + \frac{2\alpha}{\rho} - \frac{1}{\rho^3})\cos 2\theta, \tag{1.16}$$

$$\frac{2\mu u_\theta^P}{a\sigma_S} \;=\; -(\rho + \frac{2(\alpha-1)}{\rho} + \frac{1}{\rho^3})\sin 2\theta, \tag{1.17}$$

$$u_\zeta^P \;=\; 0. \tag{1.18}$$

where $\alpha = 2(1-\nu)$. Note that no ζ-displacements are predicted, since this is a plane strain solution.

The residual problem is therefore

$$u_r^R = u_r^S - u_r^P, \tag{1.19}$$

and similar equations for the other components (where the superscript S denotes the exact solution of the pure shear problem). The solution for the displacements at the surface $\zeta = 0$ is [Youngdahl and Sternberg 1966]:

$$\frac{2\mu u_r^R(\rho,\theta)}{a\sigma_S \cos 2\theta} \;=\; \int_0^\infty D(\eta)[(1-\alpha)\eta^3\Omega_2'(\eta,\rho) + U_\rho(\eta,\rho)]d\eta, \tag{1.20}$$

$$\frac{2\mu u_\theta^R(\rho,\theta)}{a\sigma_S \sin 2\theta} \;=\; \int_0^\infty D(\eta)[2(\alpha-1)\eta^2\rho^{-1}\Omega_2(\eta,\rho) + U_\theta(\eta,\rho)]d\eta, \tag{1.21}$$

$$\frac{2\mu u_\zeta^R(\rho,\theta)}{a\sigma_S \cos 2\theta} \;=\; \int_0^\infty D(\eta)[-\alpha\eta^3\Omega_2(\eta,\rho),]d\eta \tag{1.22}$$

where $D(\eta)$ satisfies the integral equation:

$$D(\eta)\eta^6 Y(\eta) = \frac{8(2-\alpha)}{\pi} + \int_0^\infty D(\xi)L(\xi,\eta)d\xi.$$

Here $Y(\eta)$ is a function of J_2' and Y_2', the derivatives of the 2nd order Bessel functions of the first and second kind, respectively [13]:

$$Y(\eta) = [J_2'(\eta)]^2 + [Y_2'(\eta)]^2, \tag{1.23}$$

and $L(\xi,\eta)$ is the kernel

$$\begin{aligned} L(\xi,\eta) \;=\; & -\frac{32}{\pi_3}\int_0^\infty \frac{\gamma^2}{\Delta(\gamma)} g(\frac{\gamma}{\xi})g(\frac{\gamma}{\eta})\Big\{\alpha f_1(\gamma) \\ & +2\alpha[g(\frac{\gamma}{\xi}) + g(\frac{\gamma}{\eta})]K(\gamma)f_2(\gamma) \\ & +g(\frac{\gamma}{\xi})g(\frac{\gamma}{\eta})K^2(\gamma)f_3(\gamma)\Big\}d\gamma. \end{aligned} \tag{1.24}$$

The functions needed to evaluate $L(\xi,\eta)$ are

$$g(x) = \frac{1}{1+x^2}, \tag{1.25}$$

$$K(\gamma) = \gamma\frac{K_2'(\gamma)}{K_2(\gamma)}, \tag{1.26}$$

$$f_1(\gamma) = \gamma^2[\gamma^2 + 4 - K^2(\gamma)] + 3\alpha K^2(\gamma), \tag{1.27}$$

$$f_2(\gamma) = \gamma^2 - (\gamma^2+3)K(\gamma), \tag{1.28}$$

$$f_3(\gamma) = (\gamma^2+2)(\gamma^2+6) - 2\gamma^2 K(\gamma), \tag{1.29}$$

$$f_4(\gamma) = (\gamma^2+3)(\gamma^2+4) - \gamma^2 K(\gamma) - \alpha f_2(\gamma) + 3\alpha K(\gamma), \tag{1.30}$$

$$\begin{aligned} \Delta(\gamma) = \; & [\gamma^2 + 4 - K^2(\gamma)]f_3(\gamma) \\ & +\gamma[-4\gamma^2 + 8(\gamma^2+3)K(\gamma) - \gamma^2 K^2(\gamma) - 6K^3(\gamma)]. \end{aligned} \tag{1.31}$$

Here K_2 and K_2' are the second order modified Bessel function and its derivative.

Also needed to evaluate equations 1.20 - 1.22 are the functions

$$\Omega_2(\gamma,\rho) = Y_2'(\gamma)J_2(\gamma\rho) - J_2'(\gamma)Y_2(\gamma\rho), \tag{1.32}$$

$$\Omega_2'(\gamma,\rho) = Y_2'(\gamma)J_2'(\gamma\rho) - J_2'(\gamma)Y_2'(\gamma\rho), \tag{1.33}$$

and

$$\begin{aligned} U_\rho(\eta,\rho) &= \frac{8}{\pi^2}\int_0^\infty \frac{1}{\rho\Delta}\Big[2\alpha g(\frac{\gamma}{\eta})\Big\{G(\gamma,\rho)[(\gamma^2\rho^2+4)f_2 - 2f_1] \\ &+ G'(\gamma,\rho)Kf_4\Big\} + g^2(\frac{\gamma}{\eta})K\Big\{G(\gamma,\rho)[(\gamma^2\rho^2+4)f_3 - 8\alpha f_2] \\ &+ G'(\gamma,\rho)[-(\gamma^2+4+\alpha K)f_3 + 4\alpha f_2]\Big\}\Big]d\gamma, \end{aligned} \tag{1.34}$$

$$\begin{aligned} U_\theta(\eta,\rho) &= \frac{16}{\pi^2}\int_0^\infty \frac{1}{\rho\Delta}\Big[\alpha g(\frac{\gamma}{\eta})\Big\{-2G(\gamma,\rho)f_4 + G'(\gamma,\rho)K(f_1 - 2f_2)\Big\} \\ &+g^2(\frac{\gamma}{\eta})\Big\{G(\gamma,\rho)[(\gamma^2+4+\alpha K)f_3 - 4\alpha f_2] \\ &+G'(\gamma,\rho)K^2[-f_3 + 2\alpha f_2]\Big\}\Big]d\gamma, \end{aligned} \tag{1.35}$$

where

$$G(\gamma,\rho) = \frac{K_2(\gamma\rho)}{K_2(\gamma)}, \tag{1.36}$$

$$G'(\gamma,\rho) = \frac{\rho K_2(\gamma\rho)}{K_2'(\gamma)}. \tag{1.37}$$

The equations 1.34 and 1.35 were integrated for the specified values of η and ρ, and are pictured in figures 1.17 - 1.20 as functions of η for ρ fixed at 1 and 1.5.

Note that the value of Poisson's ratio (ν) is involved in many of the functions through the parameter $\alpha = 2(1-\nu)$. This means that although the magnitudes of the stresses and the values of the shear modulus (μ) or Young's modulus may easily be changed to different values in equations 1.20 - 1.22, changing the value of Poisson's ratio requires recalculation of almost all of the above equations. Hence in application, we fix Poisson's ratio at an acceptable value, either from published data

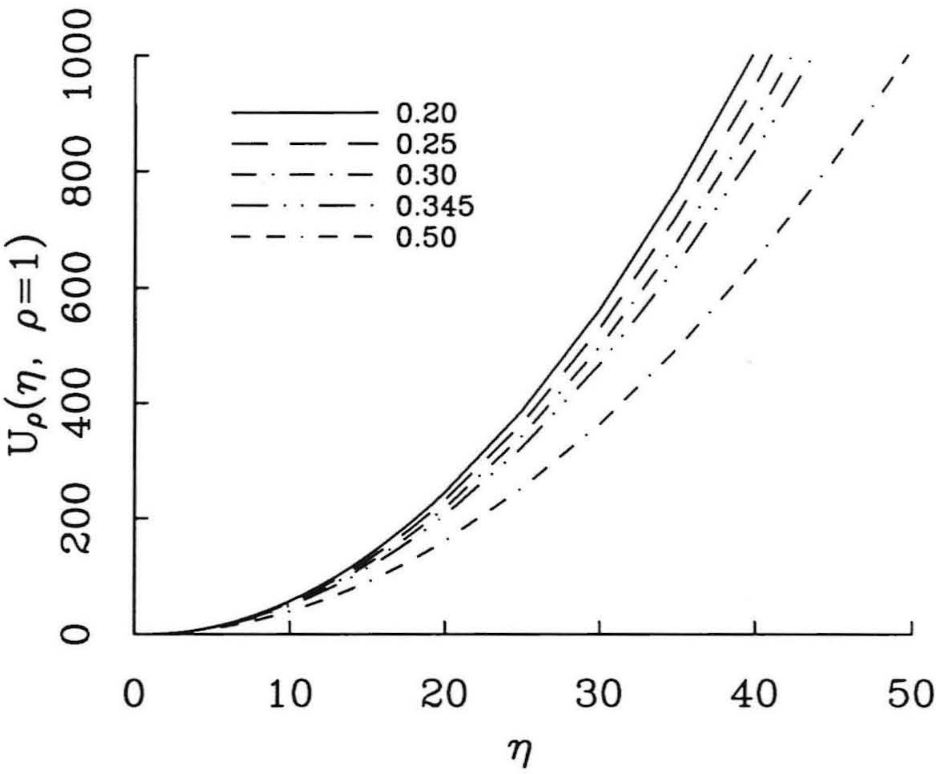

Figure 1.17: The function U_ρ for $\rho = 1$.

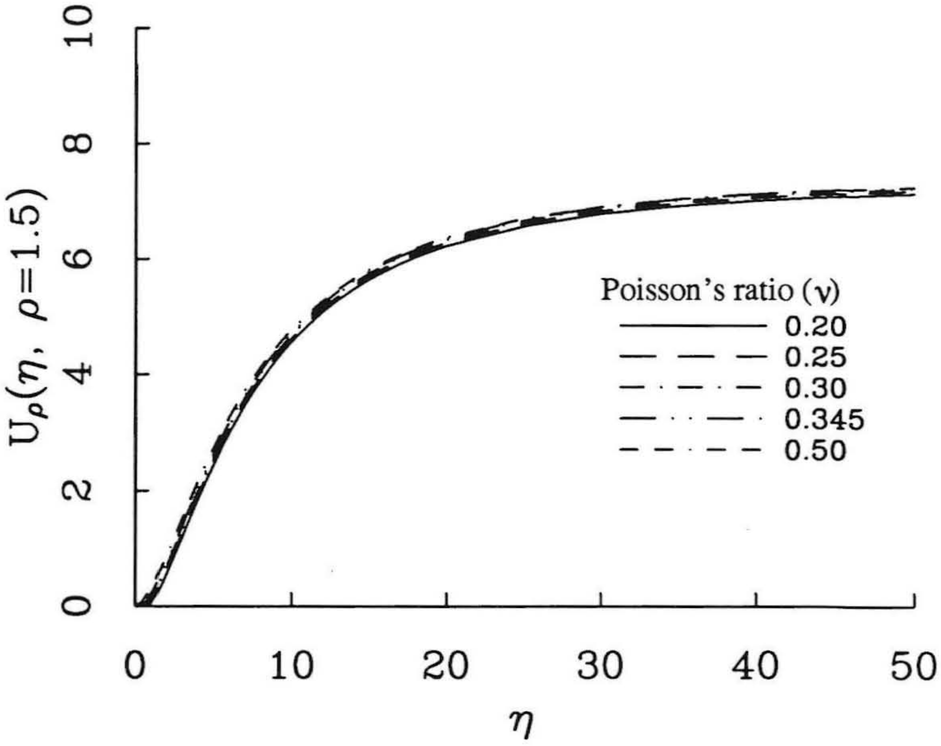

Figure 1.18: The function U_ρ for $\rho = 1.5$.

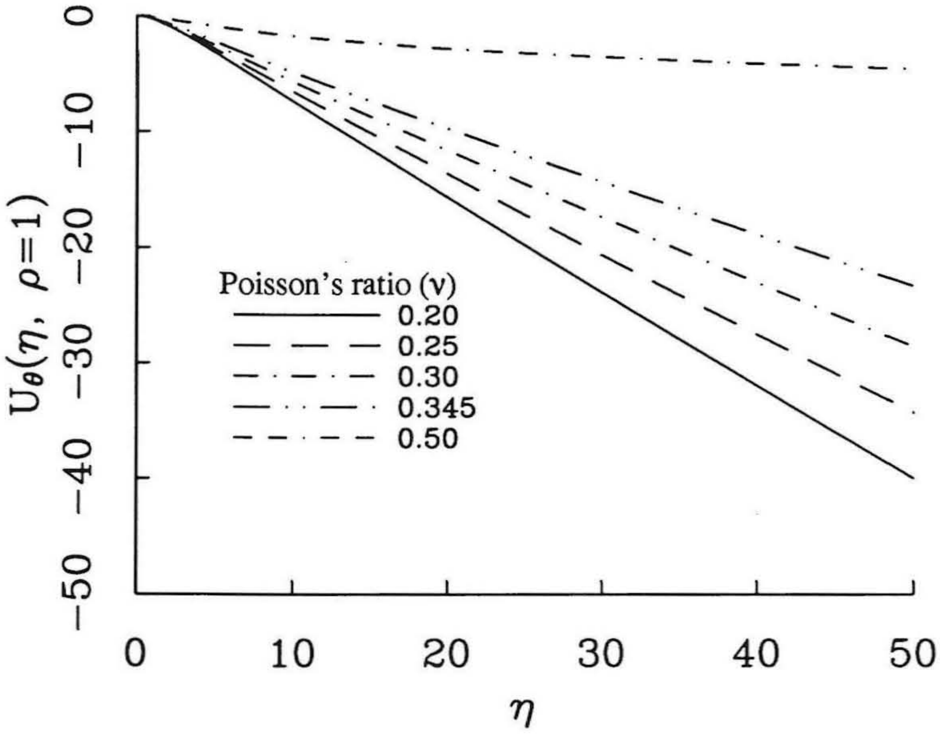

Figure 1.19: The function U_θ for $\rho = 1$.

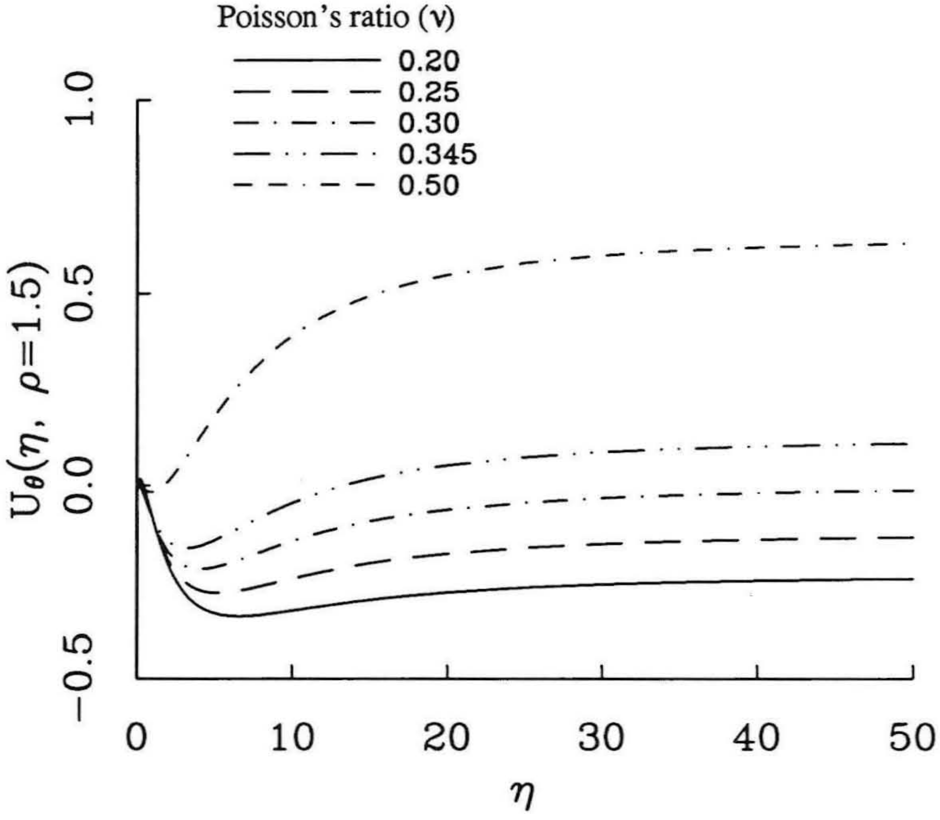

Figure 1.20: The function U_θ for $\rho = 1.5$.

or from other experiments, do the required integrations, and vary only the values of the stresses on the half-space to make our synthetic holograms. For the results presented here for the experiments in the oil shale, we set Poisson's ratio at 0.345, from the work of Horino et al. [1982]. The value of Young's modulus (E) used was that determined by in-situ holographic measurements at the site of the stress-relief measurements by Schmitt et al. [1986], a value of 25 GPa.

1.6 Numerical Analysis

Thus the bulk of the work is in evaluating the integrals for u_r^R, u_ζ^R, and u_θ^R (equations 1.20 - 1.22). To do this we need to solve the integral equation 1.5 for $D(\eta)$. First, note that

$$D(0) = \frac{(2-\alpha)\pi}{8}, \tag{1.38}$$

since at $\eta = 0$, $g(\gamma/\eta) = 0$, $L(\xi, 0) = 0$, and $\eta^6 Y(\eta) = 64/\pi^2$. Then we can determine $D(\eta)$ numerically for some discrete values of η. We will use these values of $D(\eta)$ to interpolate for all other values of η as needed. To allow for more accurate interpolation, we must choose closer spaced values of η in areas where $D(\eta)$ is rapidly varying, i.e., at small values of η, say for η between 0 and 5.

So for N values of η_j, we can approximate

$$D(\eta_j)\eta_j^6 Y(\eta_j) = \frac{8(2-\alpha)}{\pi} + \sum_{i=1}^{N} W(\xi_i) D(\xi_i) L(\xi_i, \eta_j), \tag{1.39}$$

$$j = 1, 2, ..., N. \tag{1.40}$$

Take the $\xi_i = \eta_i$ (i.e., use the same set of values). $W(\xi_i)$ are the weighting factors for the integration scheme used. Writing this in matrix form, we have:

$$\left[\eta_i^6 Y(\eta_i)\delta_{ij}\right]\{D(\eta_i)\} = \left\{\frac{8(2-\alpha)}{\pi}\right\} + \left[W(\xi_i)L(\xi_i, \eta_j)\right]\{D(\eta_i)\}, \tag{1.41}$$

where [ ] denotes a matrix of dimension N x N, and { } denotes a column vector of dimension N x 1. The expression δ_{ij} has the value 1 when $i = j$, and is equal to 0 otherwise, so the matrix on the left hand side of equation 1.42 is diagonal. We can rewrite the above equation as:

$$0 = \frac{8(2-\alpha)}{\pi} + \left([W(\xi_i)L(\xi_i,\eta_j)] - \left[\eta_i^6 Y(\eta_i)\delta_{ij}\right]\right)\{D(\eta_i)\}\,. \tag{1.42}$$

Now we have a system of N simultaneous equations that can be solved for the $D(\eta_i)$. To determine the values (the entries in the matrix to be inverted), we must obtain the values of $L(\xi,\eta)$ at the ξ_i and η_i's. We can take advantage of the symmetry $L(\xi,\eta) = L(\eta,\xi)$ to reduce our work somewhat, but the convergence of the integrand is slow; it is hard to find a value γ_0 for which $\int_0^{\gamma_0} F(\gamma)d\gamma$ is a reasonable approximation of $\int_0^{\infty} F(\gamma)d\gamma$. Therefore the technique used is as follows: We can rewrite equation 1.24 as:

$$\begin{aligned} L(\xi,\eta) &= -\frac{32}{\pi_3}\int_0^\infty g(\frac{\gamma}{\xi})g(\frac{\gamma}{\eta})\left\{F_1(\gamma) + [g(\frac{\gamma}{\xi}) + g(\frac{\gamma}{\eta})]F_2(\gamma)\right. \\ &\left. + g(\frac{\gamma}{\xi})g(\frac{\gamma}{\eta})F_3(\gamma)\right\}d\gamma, \end{aligned} \tag{1.43}$$

where

$$F_1(\gamma,\alpha) = -\alpha\gamma^2 f_1(\gamma,\alpha)/\Delta(\gamma), \tag{1.44}$$

$$F_2(\gamma,\alpha) = -2\alpha\gamma^2 K(\gamma)f_2(\gamma)/\Delta(\gamma), \tag{1.45}$$

$$F_3(\gamma,\alpha) = -\gamma^2 K^2(\gamma)f_3(\gamma)/\Delta(\gamma). \tag{1.46}$$

From the asymptotic expansions of the Bessel functions K_2, K_2', Y_2, Y_2' [Abramowitz and Stegun, 1965], we can derive asymptotic expansions for $K(\gamma)$ and the functions f_1, f_2, f_3, f_4:

$$K(\gamma) \sim -\gamma - \frac{1}{2} - \frac{15}{8\gamma} - \frac{15}{8\gamma^2} - \frac{135}{128\gamma^3} - \frac{45}{32\gamma^4} + \frac{7425}{1024\gamma^5}, \tag{1.47}$$

$$\begin{aligned} f_1(\gamma,\alpha) &\sim -\gamma^3 + 3\alpha\gamma^2 + \frac{(24\alpha+15)\gamma}{8} + \frac{48\alpha-15}{4} \\ &+ \frac{-720\alpha+405}{128\gamma} + \frac{90\alpha+45}{8\gamma^2}, \end{aligned} \tag{1.48}$$

$$
\begin{aligned}
f_2(\gamma) &\sim \gamma^3+\frac{3}{2}\gamma^2+\frac{39\gamma}{8}-\frac{3}{8}+\frac{855}{128\gamma}-\frac{135}{32\gamma^2}, && (1.49)\\
f_3(\gamma) &\sim \gamma^4+2\gamma^3+9\gamma^2+\frac{15\gamma}{4}+\frac{33}{4}+\frac{135}{64\gamma}+\frac{45}{16\gamma^2}, && (1.50)\\
f_4(\gamma,\alpha) &\sim \gamma^4+(1-\alpha)+\frac{(15-3\alpha)\gamma^2}{2}+\frac{(15-63\alpha)\gamma}{8}+\frac{81-9\alpha}{8}\\
&\quad +\frac{135-1575\alpha}{128\gamma}+\frac{45+315\alpha}{32\gamma^2}. && (1.51)
\end{aligned}
$$

Polynomial multiplication of the above equations gives the expansions for the functions F_1, F_2, F_3:

$$
\begin{aligned}
F_1(\gamma,\alpha) &= -\alpha+\frac{2\alpha(2\alpha+1)}{\gamma}+\frac{\alpha(-4\alpha^2+8\alpha+5)}{\gamma^2}+\ldots, && (1.52)\\
F_2(\gamma,\alpha) &= -2\alpha\gamma+2\alpha^2+\frac{\alpha}{4\gamma}(-8\alpha^2+8\alpha-3)+\ldots, && (1.53)\\
F_3(\gamma,\alpha) &= \gamma^3+(-\alpha+1)\gamma^2+\frac{(8\alpha^2-16\alpha+47)\gamma}{8}\\
&\quad +\frac{1}{4}(-4\alpha^3+12\alpha^2-3\alpha+15)\\
&\quad +\frac{128\alpha^4-512\alpha^3-432\alpha^2+480\alpha+1815}{128\gamma}+\ldots && (1.54)
\end{aligned}
$$

Now define the functions $F_1^0(\gamma), F_2^0(\gamma), F_3^0(\gamma)$ to contain the first terms of the asymptotic expansions above, i.e.,

$$
\begin{aligned}
F_1^0(\gamma,\alpha) &= -\alpha, && (1.55)\\
F_2^0(\gamma,\alpha) &= -2\alpha\gamma+2\alpha^2, && (1.56)\\
F_3^0(\gamma,\alpha) &= \gamma^3+(1-\alpha)\gamma^2+\frac{\gamma}{8}(8\alpha^2-16\alpha+47)\\
&\quad +\frac{1}{4}(-4\alpha^3+12\alpha^2-3\alpha+5), && (1.57)
\end{aligned}
$$

and let $\tilde{F}_i = F_i - F_i^0$ for $i = 1, 2, 3$. We can express the $\tilde{F}_i$ as power series whose coefficients depend on α:

$$
\tilde{F}_i(\gamma,\alpha) \sim \sum_{n=1}^{N} \frac{a_{in}(\alpha)}{\gamma^n}. \qquad (1.58)
$$

Youngdahl and Sternberg [1965] give coefficients for the cases of $\alpha = 1$ and 1.5 (corresponding to values of Poisson's ratio of 0.5 and 0.25, respectively). However, since we are interested in examining the solutions for a broader range of Poisson's ratio, we derived the general expressions for the coefficients $a_{in}(\alpha)$:

$$a_{11} = 2(2\alpha + 1), \tag{1.59}$$

$$a_{12} = -4\alpha^2 - 4\alpha + 5, \tag{1.60}$$

$$a_{13} = (16\alpha^3 - 66\alpha - 91)/4, \tag{1.61}$$

$$a_{14} = (-16\alpha^4 + 16\alpha^3 + 180\alpha^2 + 172\alpha + 17)/4, \tag{1.62}$$

$$\begin{aligned} a_{15} = {} & \Big(256\alpha^5 - 512\alpha^4 - 4448\alpha^3 - 3328\alpha^2 \\ & +8366\alpha + 11303\Big)/64, \end{aligned} \tag{1.63}$$

$$\begin{aligned} a_{16} = {} & \Big(-64\alpha^6 + 192\alpha^5 + 1440\alpha^4 + \\ & 128\alpha^3 - 7176\alpha^2 - 11484\alpha - 5491\Big)/16, \end{aligned} \tag{1.64}$$

$$\begin{aligned} a_{17} = {} & \Big(2048\alpha^7 - 8192\alpha^6 - 54528\alpha^5 + 43520\alpha^4 \\ & 4 + 486832\alpha^3 + 701952\alpha^2 + 70334\alpha - 383825\Big)/512, \end{aligned} \tag{1.65}$$

$$\begin{aligned} a_{18} = {} & \Big(-64\alpha^8 + 320\alpha^7 + 1904\alpha^6 - 3568\alpha^5 - 24964\alpha^4 \\ & -25504\alpha^3 + 38399\alpha^2 + 105122\alpha + 63983\alpha\Big)/16, \end{aligned} \tag{1.66}$$

$$a_{21} = (-8\alpha^2 + 8\alpha - 3)/4, \tag{1.67}$$

$$a_{22} = (4 - \alpha^3 - \alpha^2 - 23\alpha + 6)/2, \tag{1.68}$$

$$a_{23} = (-128\alpha^4 + 384\alpha^3 + 1392\alpha^2 - 112\alpha - 2367)/64, \tag{1.69}$$

$$a_{24} = (16\alpha^5 - 64\alpha^4 - 240\alpha^3 + 200\alpha^2 + 934\alpha + 837)/8, \tag{1.70}$$

$$\begin{aligned} a_{25} = {} & \Big(-1024\alpha^6 + 5120\alpha^5 + 18560\alpha^4 - 36224\alpha^3 \\ & -139928\alpha^2 - 112616\alpha + 11061\Big)/512, \end{aligned} \tag{1.71}$$

$$\begin{aligned} a_{26} = {} & \Big(64\alpha^7 - 384\alpha^6 - 1296\alpha^5 + 4384\alpha^4 + 15036\alpha^3 \\ & +5724\alpha^2 - 20675\alpha - 27891\Big)/32, \end{aligned} \tag{1.72}$$

$$a_{31} = (128\alpha^4 - 512\alpha^3 - 432\alpha^2 + 480\alpha + 1815)/(128\alpha), \tag{1.73}$$

$$a_{32} = (-16\alpha^5 + 80\alpha^4 + 104\alpha^3 - 240\alpha^2 - 294\alpha - 375)/(16\alpha), \tag{1.74}$$

$$\begin{aligned} a_{33} &= \Big(1024\alpha^6 - 6144\alpha^5 - 8832\alpha^4 + 37376\alpha^3 \\ &\quad +55512\alpha^2 + 27216\alpha + 23535\Big)/(1024\alpha), \qquad (1.75) \\ a_{34} &= \Big(-64\alpha^7 + 446\alpha^6 + 624\alpha^5 - 4304\alpha^4 - 6676\alpha^3 \\ &\quad +1080\alpha^2 + 5103\alpha + 3240\Big)/(64\alpha). \qquad (1.76) \end{aligned}$$

Now we can recast equation 1.24 as:

$$L(\xi,\eta) = \frac{32}{\pi^3}[L^0(\xi,\eta,) + \tilde{L}(\xi,\eta,\gamma_0) + \tilde{\tilde{L}}(\xi,\eta,\gamma_0)], \qquad (1.77)$$

where

$$\begin{aligned} L^0(\xi,\eta) &= \int_0^\infty g(\frac{\gamma}{\eta})g(\frac{\gamma}{\xi})\Big\{F_1^0(\gamma,\alpha) + [g(\frac{\gamma}{\eta}) + g(\frac{\gamma}{\xi})]F_2^0(\gamma,\alpha) \\ &\quad + g(\frac{\gamma}{\eta})g(\frac{\gamma}{\xi})F_3^0(\gamma,\alpha)\Big\}\,d\gamma, \qquad (1.78) \end{aligned}$$

$$\begin{aligned} \tilde{L}(\xi,\eta,\gamma_0) &= \int_0^{\gamma_0} g(\frac{\gamma}{\eta})g(\frac{\gamma}{\xi})\Big\{\tilde{F}_1(\gamma,\alpha) + [g(\frac{\gamma}{\eta}) + g(\frac{\gamma}{\xi})]\tilde{F}_2(\gamma,\alpha) \\ &\quad + g(\frac{\gamma}{\eta})g(\frac{\gamma}{\xi})\tilde{F}_3(\gamma,\alpha)\Big\}\,d\gamma, \qquad (1.79) \end{aligned}$$

$$\begin{aligned} \tilde{\tilde{L}}(\xi,\eta,\gamma_0) &= \int_{\gamma_0}^\infty g(\frac{\gamma}{\eta})g(\frac{\gamma}{\xi})\Big\{\tilde{\tilde{F}}_1(\gamma,\alpha) + [g(\frac{\gamma}{\eta}) + g(\frac{\gamma}{\xi})]\tilde{\tilde{F}}_2(\gamma,\alpha) \\ &\quad + g(\frac{\gamma}{\eta})g(\frac{\gamma}{\xi})\tilde{\tilde{F}}_3(\gamma,\alpha)\Big\}\,d\gamma. \qquad (1.80) \end{aligned}$$

The equation 1.78 is integrable in closed form, yielding, for $\xi \neq \eta$,

$$\begin{aligned} L^0(\xi,\eta) &= \frac{\pi}{16}(-4\alpha^3 + 36\alpha^2 - 11\alpha - 15)\frac{\xi\eta}{\xi+\eta} \\ &\quad +\frac{\pi}{16}(-4\alpha^3 + 12\alpha^2 - 3\alpha - 15)\frac{\xi^2\eta^2}{(\xi+\eta)^2} \\ &\quad +\frac{\pi}{4}(1-\alpha)\frac{\xi^3\eta^3}{(\xi+\eta)^3} - 2\alpha Q(\xi,\eta) \qquad (1.81) \\ &\quad +\frac{1}{16}(8\alpha^2 - 16\alpha + 47)\frac{\xi^2\eta^2}{(\xi^2-\eta^2)^2}[\xi^2 + \eta^2 - 4Q(\xi,\eta)] \\ &\quad +\frac{\xi^2\eta^2}{\xi^2-\eta^2)^2}[(\xi^2+\eta^2)Q(\xi,\eta) - \xi^2\eta^2], \qquad (1.82) \end{aligned}$$

where

$$Q(\xi,\eta) = \frac{\xi^2\eta^2}{\xi^2-\eta^2}\log(\frac{\xi}{\eta}). \tag{1.83}$$

For the case $\xi = \eta$, we have

$$\begin{aligned} L^0(\eta,\eta) &= \frac{\pi}{128}(-20\alpha^3 + 156\alpha^2 - 47\alpha - 75)\eta \\ &\quad + \frac{1}{48}(8\alpha^2 - 64\alpha + 47)\eta^2 \\ &\quad \frac{\pi}{32}(1-\alpha)\eta^3 + \frac{1}{12}\eta^4. \end{aligned} \tag{1.84}$$

Equation 1.80 may be approximated by substitution of the asymptotic expansions for the $\tilde{F}_i$, equation 1.58, and integrating the resulting power series. This gives, for $\xi \neq \eta$:

$$\begin{aligned} \tilde{\tilde{L}}(\xi,\eta,\gamma_0) &= \frac{\xi^2\eta^2}{\xi^2-\eta^2}\left\{\sum_{n=1}^{8}\frac{a_{1n}(\alpha)}{\gamma_0^{n+1}}[-H_n(\frac{\xi}{\gamma_0}) + H_n(\frac{\eta}{\gamma_0})]\right. \\ &\quad + \frac{1}{2\gamma_0}\tilde{F}_2(\gamma_0,\alpha)[g(\frac{\xi}{\gamma_0}) - g(\frac{\eta}{\gamma_0})] \\ &\quad \left. + \sum_{n=1}^{6}\frac{(n+3)a_{2n}(\alpha)}{2\gamma_0^{n+1}}[-H_n(\frac{\xi}{\gamma_0}) + H_n(\frac{\eta}{\gamma_0})]\right\} \\ &\quad + \frac{\xi^4\eta^4}{(\xi^2-\eta^2)^3}\sum_{n=1}^{4}\frac{2a_{3n}(\alpha)}{\gamma_0^{n+1}}[H_n(\frac{\xi}{\gamma_0}) - H_n(\frac{\eta}{\gamma_0})] \\ &\quad + \frac{\xi^2\eta^2}{(\xi^2-\eta^2)^2}\left\{-\frac{1}{2\gamma_0}\tilde{F}_3(\gamma_0,\alpha)[\eta^2 g(\frac{\xi}{\gamma_0}) + \xi^2 g(\frac{\eta}{\gamma_0})]\right. \\ &\quad \left. + \sum_{n=1}^{4}\frac{(n+1)a_{3n}(\alpha)}{2\gamma_0^{n+1}}[\eta^2 H_n(\frac{\xi}{\gamma_0}) + \xi^2 H_n(\frac{\eta}{\gamma_0})]\right\}. \end{aligned} \tag{1.85}$$

For the case $\xi = \eta$, we have

$$\begin{aligned} \tilde{\tilde{L}}(\eta,\eta,\gamma_0) &= -\frac{\gamma_0}{2}\tilde{F}_1(\gamma_0,\alpha)g(\frac{\gamma_0}{\eta}) + \eta^2\sum_{n=1}^{8}\frac{(n+1)a_{1n}(\alpha)}{2\gamma_0^{n+1}}H_n(\frac{\eta}{\gamma_0}) \\ &\quad -\frac{\gamma_0}{2}\tilde{F}_2(\gamma_0,\alpha)g^2(\frac{\gamma_0}{\eta}) - g(\frac{\gamma_0}{\eta})\sum_{n=1}^{6}\frac{(n+3)a_{2n}(\alpha)}{4\gamma_0^{n-1}} \\ &\quad +\eta^2\sum_{n=1}^{6}\frac{(n+1)(n+3)a_{2n}(\alpha)}{4\gamma_0^{n+1}}H_n(\frac{\eta}{\gamma_0}) \end{aligned}$$

$$\begin{aligned}
&-\frac{\gamma_0}{6}\tilde{F}_3(\gamma_0,\alpha)\sum_{n=1}^{4}\frac{(n+3)(n+5)a_{3n}(\alpha)}{48\gamma_0^{n-1}} \\
&-g(\frac{\gamma_0}{\eta})\sum_{n=1}^{4}\frac{(n+3)(n+5)a_{3n}(\alpha)}{48\gamma_0^{n-1}} \\
&+\eta^2\sum_{n=1}^{4}\frac{(n+1)(n+3)(n+5)a_{3n}(\alpha)}{48\gamma_0^{n+1}}H_n(\frac{\eta}{\gamma_0}),
\end{aligned} \tag{1.86}$$

where

$$H_{2j+1}(x) = -\frac{(-1)_j}{x^{2j+2}}\left[\frac{1}{2}\log(1+x^2)+\sum_{i=1}^{j}\frac{(-1)^i x^{2i}}{2i}\right], \tag{1.87}$$
$$j = 0,1,2,\ldots,$$
$$H_{2j}(x) = \frac{(-1)^j)}{x^{2j+1}}\left[\arctan x+\sum_{i=1}^{j}\frac{(-1)^i x^{2i-1}}{2i-1}\right], \tag{1.88}$$
$$j = 1,2,3,\ldots,$$

$$\int_0^\infty F(\gamma)d\gamma = \int_0^\infty F^0(\gamma)d\gamma + \int_0^\infty \tilde{F}(\gamma)d\gamma. \tag{1.89}$$

The function $\tilde{L}(\xi,\eta,\gamma_0)$ (equation 1.79) was integrated numerically for values of ξ from 0.25 to 2000. (Since $g(\gamma/\eta) = 0$ when $\eta = 0$, $L(\xi,0) = 0$.) Figures 1.22 and 1.23 show $L(0.25,\eta)$ and $L(1.0,\eta)$ respectively. The sum of $L, \tilde{L}, \tilde{\tilde{L}}$ was then used in the matrix equation 1.42 to determine the vector $D(\eta_i)$. The solution was checked against the original equation 1.42 to check its precision. Figure 1.21 shows the function $D(\eta)$ for various values of Poisson's ratio.

Next the functions U_ρ and U_θ (equations 1.34 and 1.35) were evaluated numerically. For large values of the variable of integration γ, the functions $f_1, f_2, f_3, f_4, \Delta$, and Ω were represented by their asymptotic expansions. Near the lower limit of integration $\gamma = 0$, the integrand must be replaced by its limit as $\gamma \to 0$, since individual terms in the expression blow up. For the integrand of U_ρ, the limit as $\gamma \to 0$ is $(2-\alpha)\alpha/\rho$; for U_θ, the limit is $(1-\alpha)(2-\alpha)/(2\rho)$.

Once we have the residual displacements $u_r^R, u_\theta^R, u_\zeta^R$ the total displacements may be calculated by adding in the contributions from the plane axisymmetric component

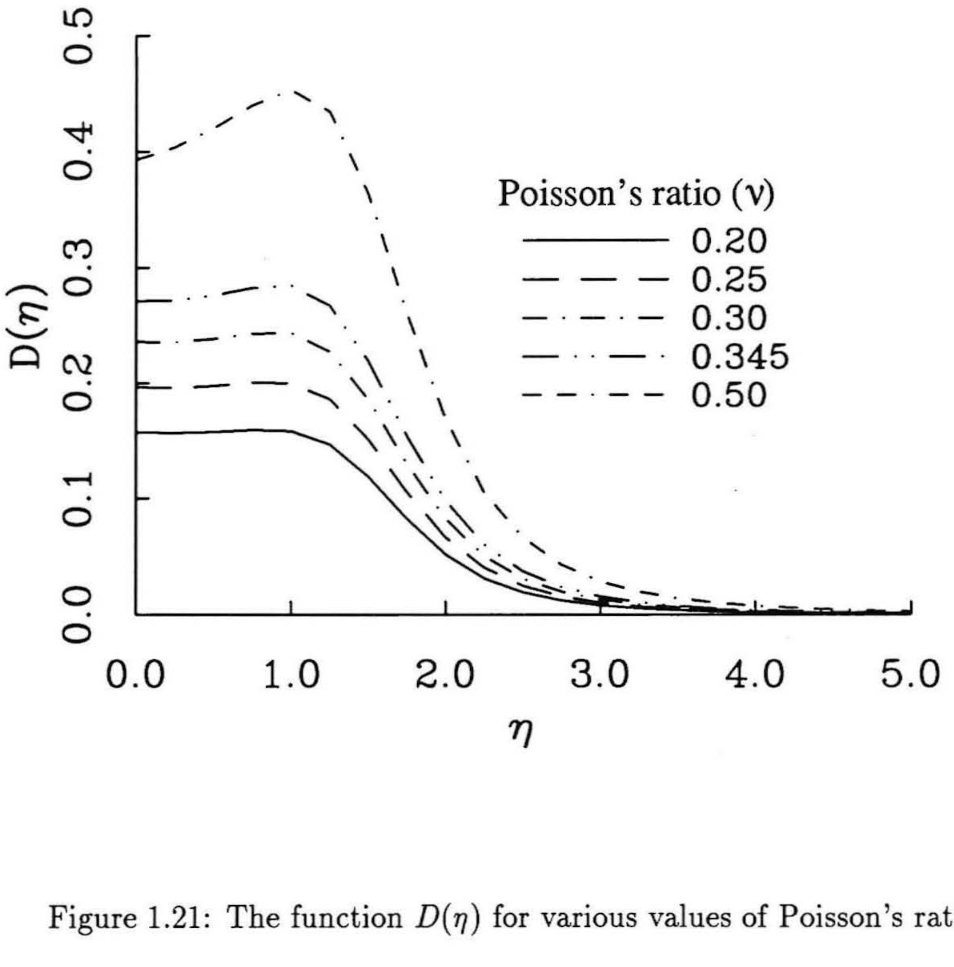

Figure 1.21: The function $D(\eta)$ for various values of Poisson's ratio.

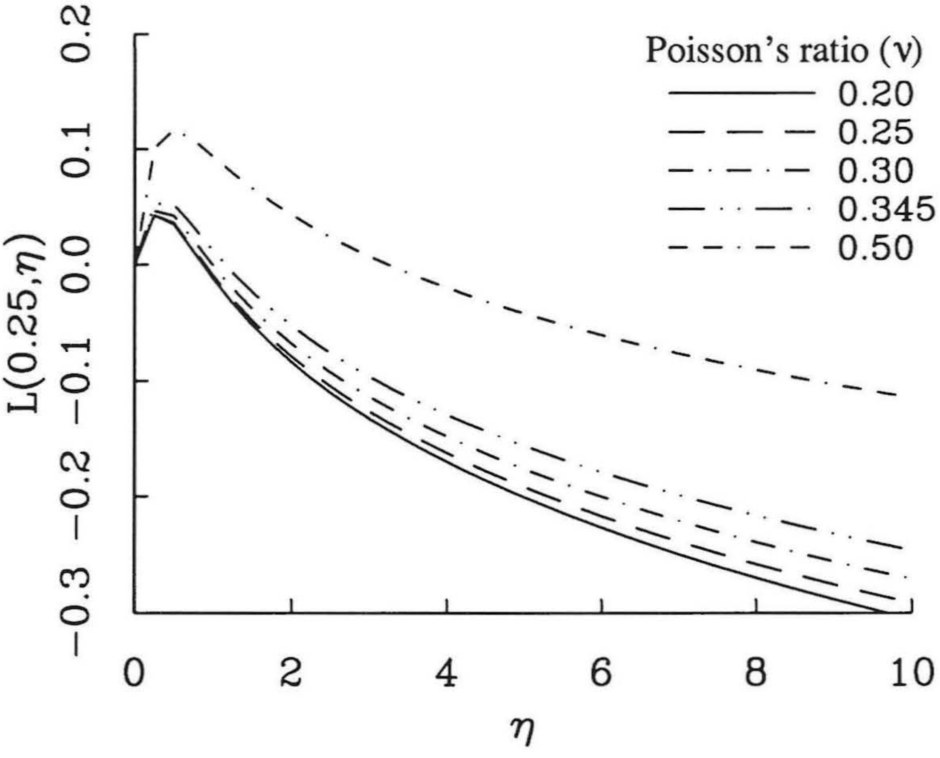

Figure 1.22: The function $L(\xi, \eta)$ for $\xi = 0.25$ for Poisson's ratios from 0.2 to 0.5

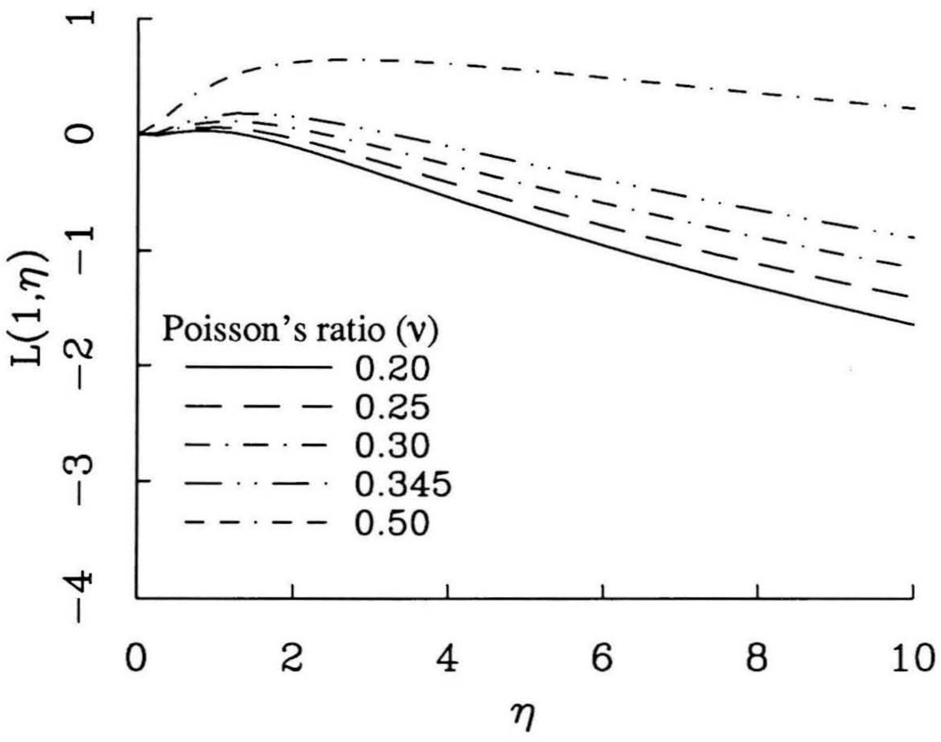

Figure 1.23: The function $L(\xi, \eta)$ for $\xi = 1.0$ for Poisson's ratios from 0.2 to 0.5

(equations 1.13 - 1.15) and the pure shear plane strain solution (equations 1.16 - 1.18). Then, subtracting the displacements due to the stressing of an elastic half-space without a hole, we arrive, as before, with the displacements due to the drilling of the stress-relief hole:

$$
\begin{aligned}
u_r &= \frac{(1+\nu)a}{E}\left\{\frac{\sigma_H}{\rho} + \sigma_S \cos 2\phi \left[u_r^R + \frac{2\alpha}{\rho} - \frac{1}{\rho^3}\right]\right\} && (1.90) \\
u_\theta &= -\frac{(1+\nu)a}{E}\left[-u_\theta^R + \frac{2(\alpha-1)}{\rho} + \frac{1}{\rho^3}\right] \sin 2\phi\sigma_S && (1.91) \\
u_\zeta &= \frac{(1+\nu)a}{E}\sigma_S u_\zeta^R \cos 2\phi && (1.92)
\end{aligned}
$$

where u_r^R, u_θ^R, and u_ζ^R are the residual components of the solution to the pure shear problem, as defined in equations (1.20 - 1.22), and ϕ is measured from the σ_1 direction. Figures 1.24 - 1.26 show the values of u_r^R, u_θ^R, and u_ζ^R for several values of Poisson's ratio. The importance of the residual term u_ρ^R, etc. is greater for larger Poisson's ratios; in fact, for a Poisson's ratio of 0, all three components of the residual displacements are exactly 0. Thus we would expect to see a greater difference in the fringe patterns of the synthetic holograms from places where the rocks have larger values of this parameter.

1.7 Application

To determine the utility of this technique, it is necessary to know whether using this model will yield any significant improvement in the analysis of the data. To this end, we re-analyzed the holograms that had previously been modeled using the plate theory. For this rock, a dolomitic marlstone, we set the value of Young's modulus at 25 GPa, and used a Poisson's ratio of 0.345 [Horino et al. 1982]. The new model proved to give a better fit to the observed holograms; the results may be seen in figures 1.28 - 1.32. In most cases, the actual values of the stresses obtained by matching the synthetic holograms with the data are not significantly changed;

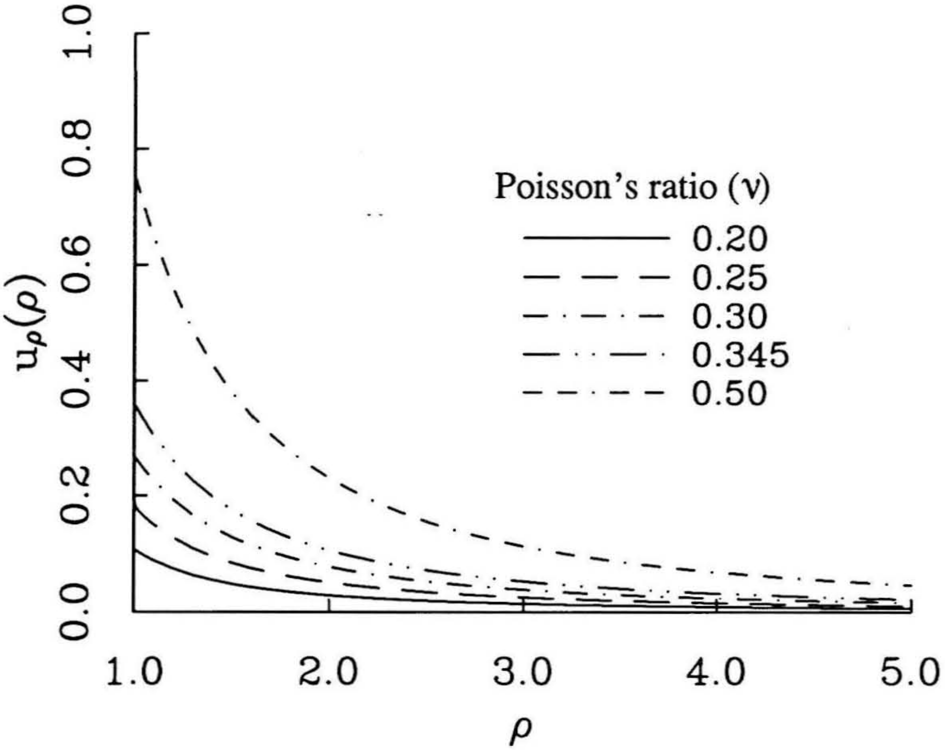

Figure 1.24: The solution to the residual displacement u_ρ^R for various values of Poisson's ratio. The dimensionless values are plotted against the distance from the center of the hole, normalized to the hole radius.

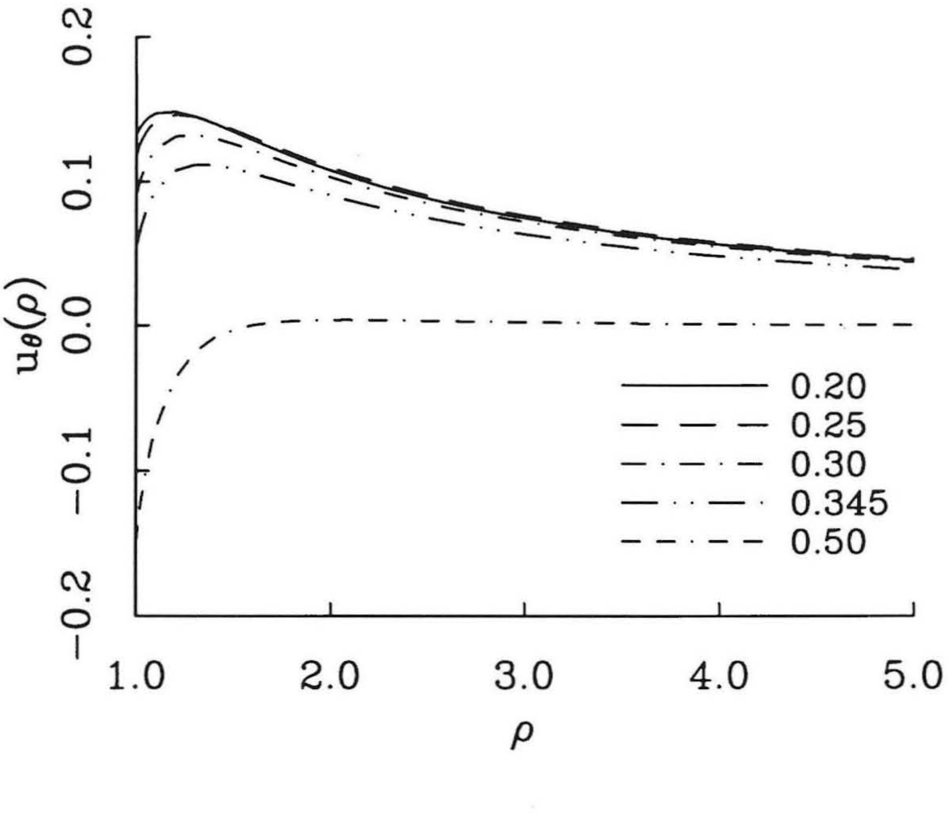

Figure 1.25: The solution to the residual displacement u_θ^R for various values of Poisson's ratio. The dimensionless values are plotted against the distance from the center of the hole, normalized to the hole radius.

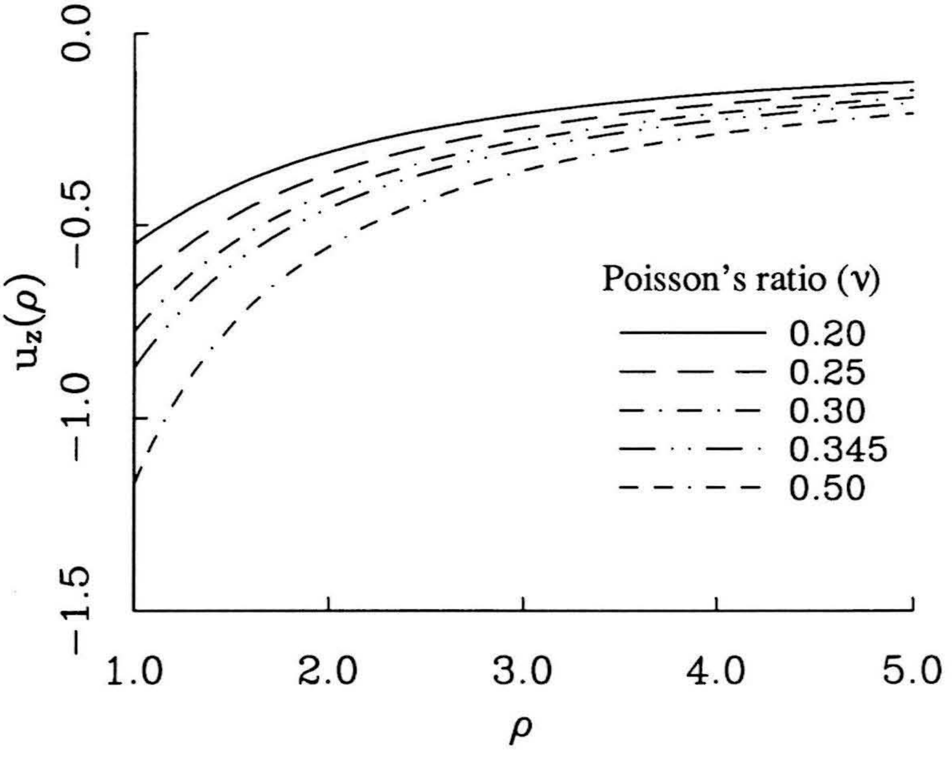

Figure 1.26: The solution to the residual displacement u_ζ^R for various values of Poisson's ratio. The dimensionless values are plotted against the distance from the center of the hole, normalized to the hole radius.

however, the errors associated with each stress determination have been reduced. Figures 1.33 - 1.35 show the magnitude of the stress-relief displacements around the hole, the radial, tangential, and vertical components for both the plate model solution from section 1.3 and for the revised solution from this work. The hologram being modeled here figure is the hologram 16/3/3 of figure 1.32. Figures 1.36 - 1.38 show the displacements predicted by both models for the holograms of figure 1.32. The upper plot in each figure shows the variation of the displacements with radius; distance from the center of the stress-relief hole is here normalized to the radius of the hole. The displacements are those that occur along a line from the center of the hole along the x-axis to the right of the hologram. The diameter of the hole is 0.5 cm. Figure 1.36 shows the radial component of displacement (u_ρ), which is quite similar in the two models. The real difference between the two models is in the magnitudes of the tangential and vertical components, as can be seen in figures 1.37 and 1.38, respectively. The values of the tangential displacement predicted by the plate model are generally larger than those predicted by the revised model; however, the situation is reversed for the vertical component, which is significantly greater in the revised model. Since, as can be seen in figures 1.33 - 1.35, the azimuthal variation of displacement is different for the tangential and vertical components, any change in the relative magnitude of these components will result in different fringe patterns. Thus a decrease in the magnitude of the tangential component will not be offset directly by an increase in the magnitude of the vertical component.

1.8 Inversion of Data to Obtain Far-field Stresses

The results of both models were inverted to obtain the far-field stresses using equations 1.1 - 1.3. Since the problem is overdetermined, a least squares scheme was used to solve for the six stress components. Equations 1.1 - 1.3 determine the borehole

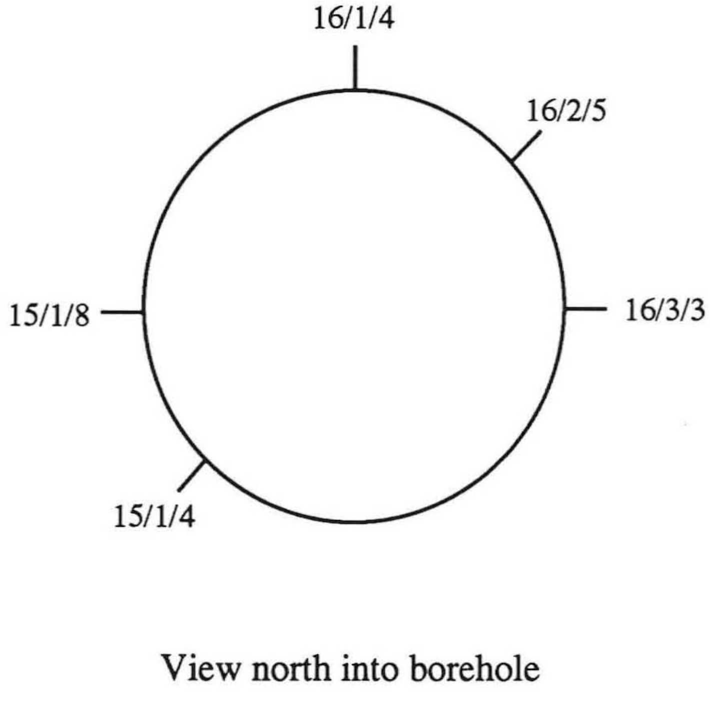

Figure 1.27: Orientation of holograms in the pillar borehole. The view into the page is due north.

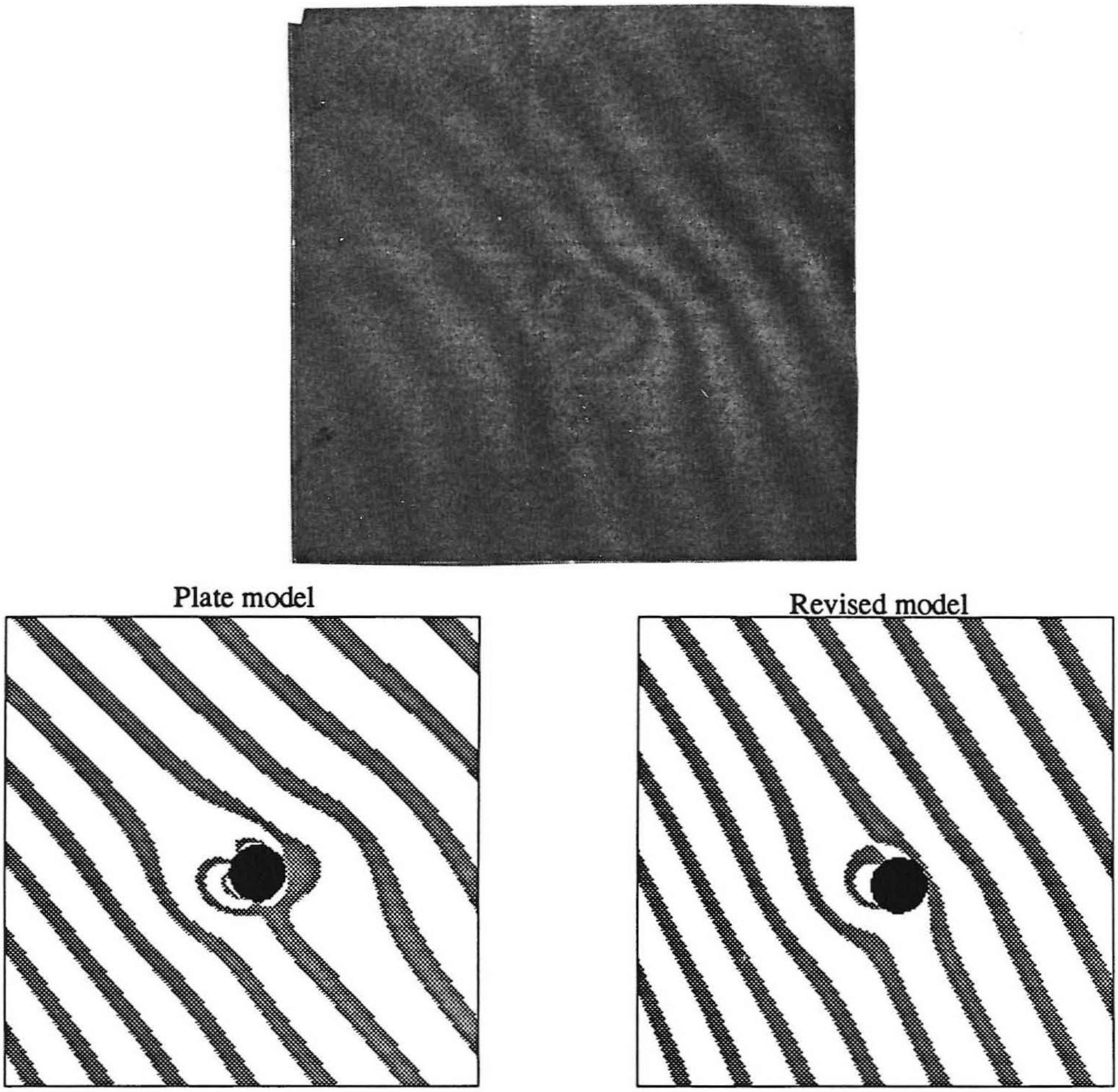

Plate model

Revised model

Hologram 15/1/4 225 degrees

Figure 1.28: Plate model (left) and revised synthetic holograms for the hologram 15/1/4.

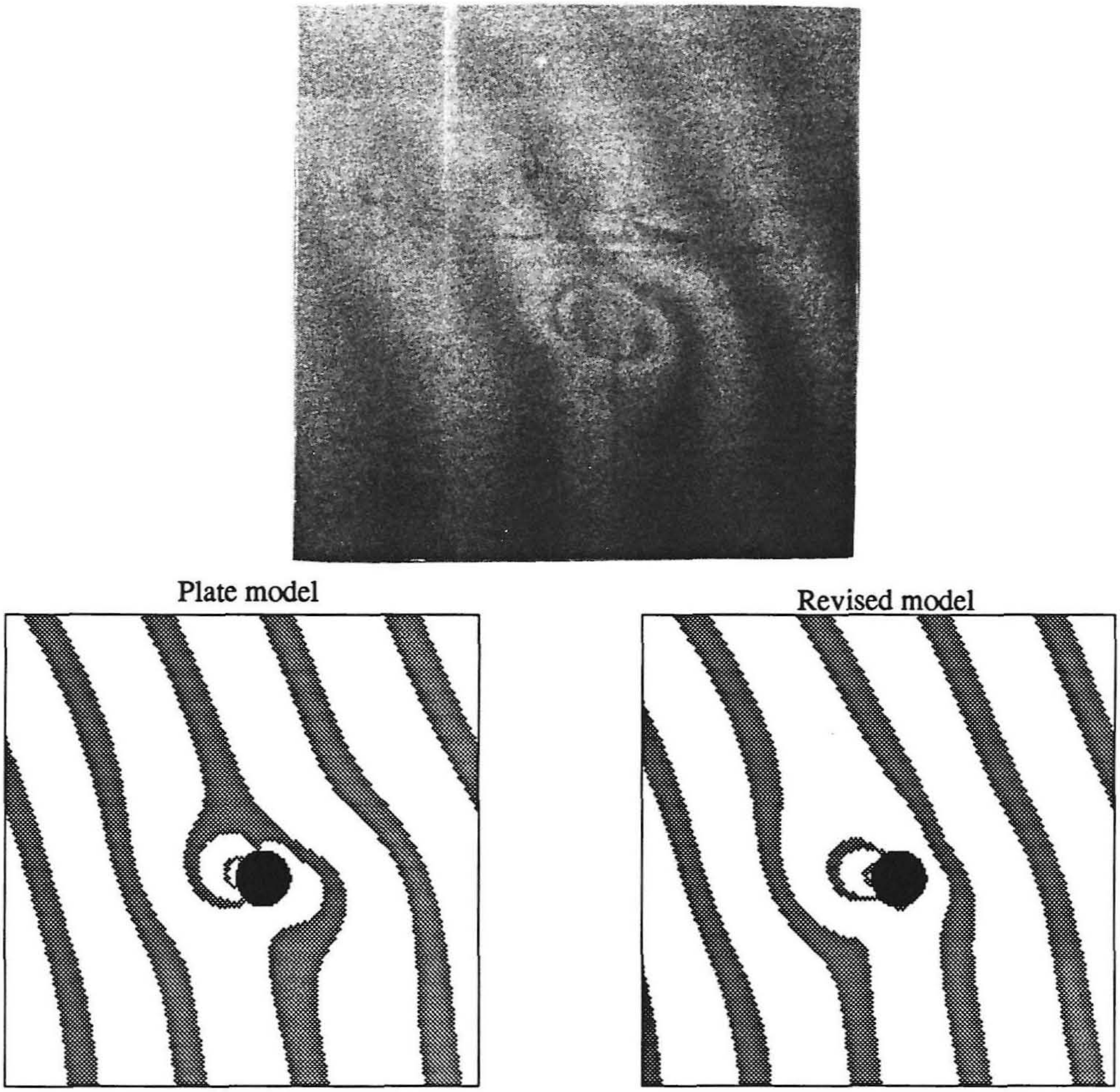

Plate model

Revised model

-20, 0,5 Hologram 15/1/8 180 degrees - 20, 0, 2

Figure 1.29: Plate model (left) and revised synthetic holograms for the hologram 15/1/8.

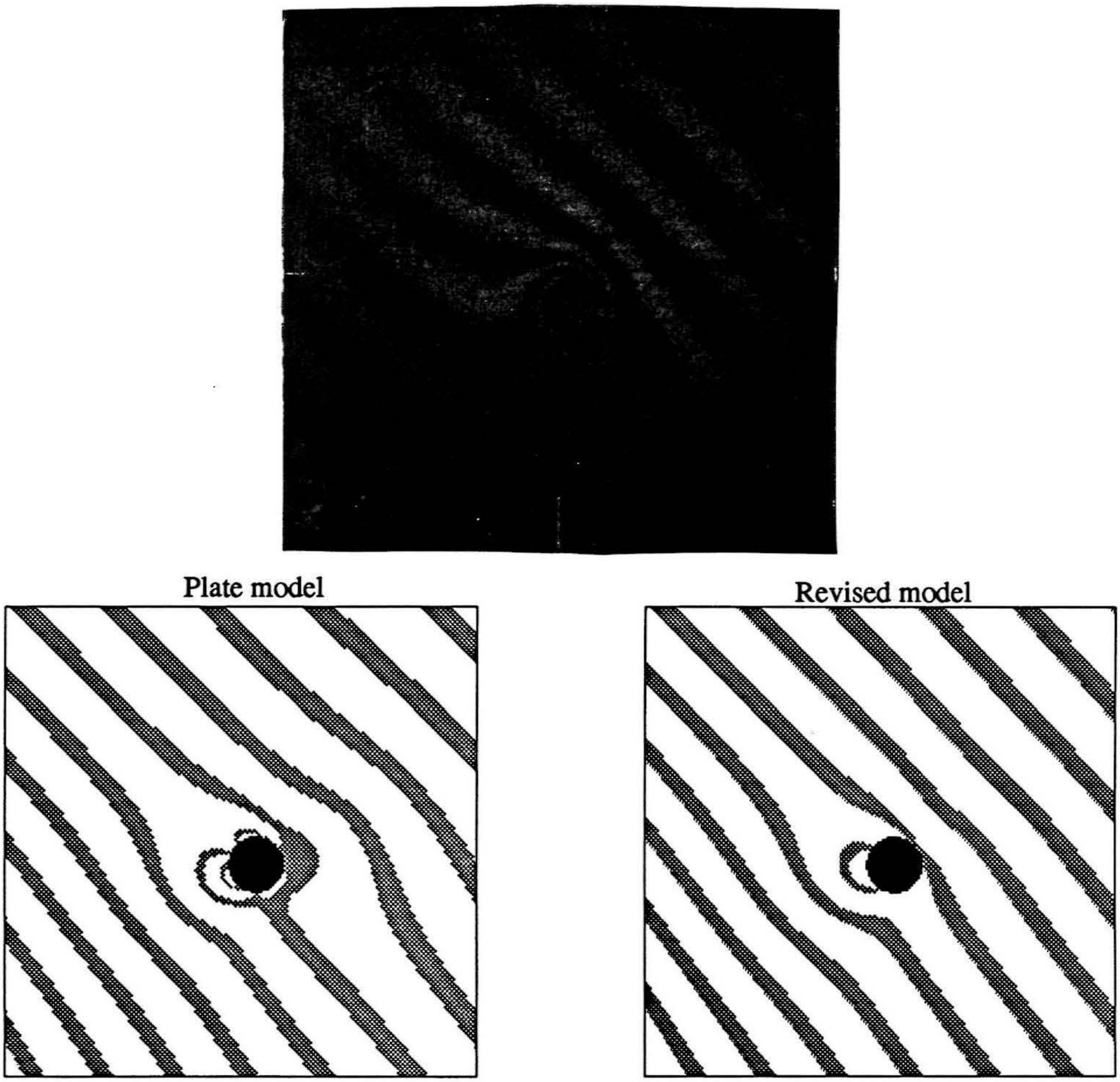

-22.5, 5, -15 Hologram 16/1/4 90 degrees -20, -5, 2

Figure 1.30: Plate model (left) and revised synthetic holograms for the hologram 16/1/4.

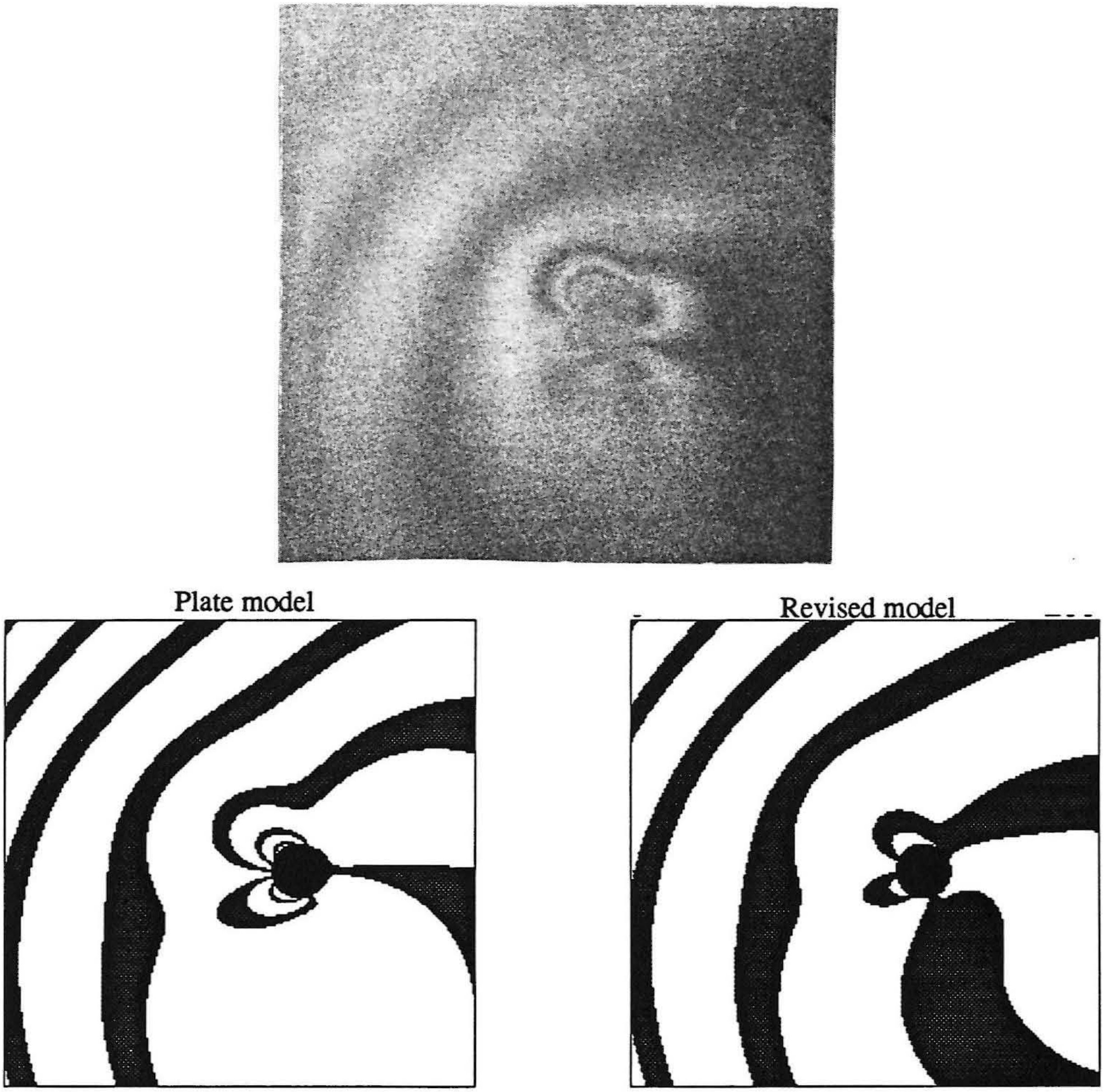

Hologram 16/2/5 45 degrees

Figure 1.31: Plate model (left) and revised synthetic holograms for the hologram 16/2/5.

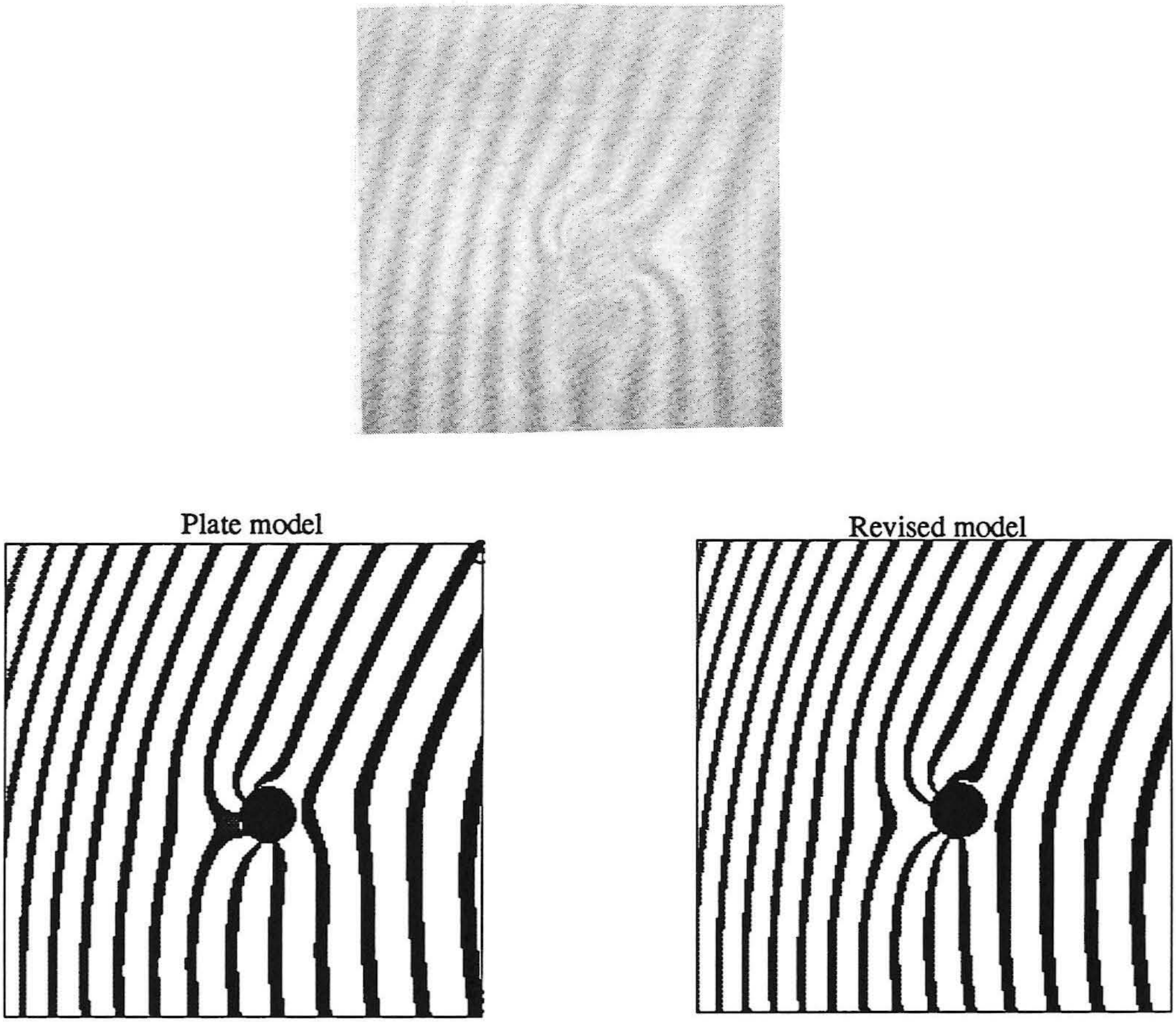

Figure 1.32: Plate model (left) and revised synthetic holograms for the hologram 16/3/3.

Plate model

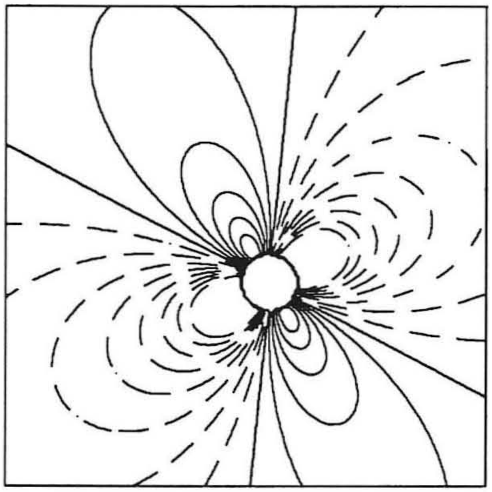

Revised model

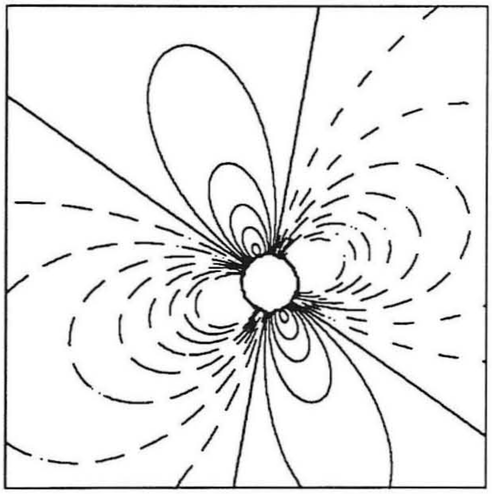

Figure 1.33: Comparison of the displacement fields for the two models (radial component u_r). The contour interval is .05 μm and dashed lines indicate negative displacements. For this component, contours for displacements greater than .4 μm have been suppressed.

Plate model

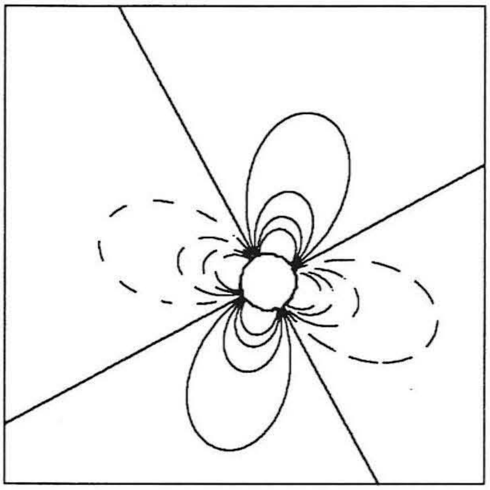

Revised model

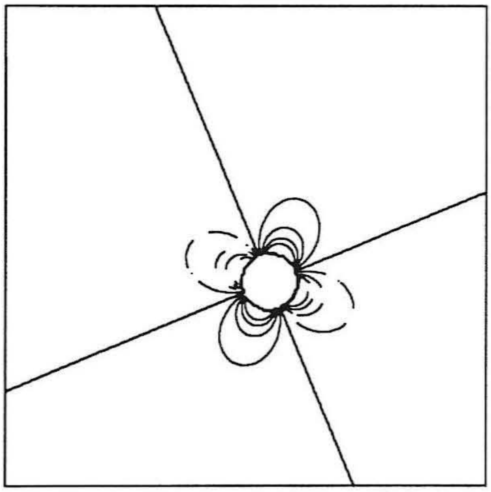

Figure 1.34: Comparison of the displacement fields for the two models (tangential component u_θ). The contour interval is .05 μm and dashed lines indicate negative displacements.

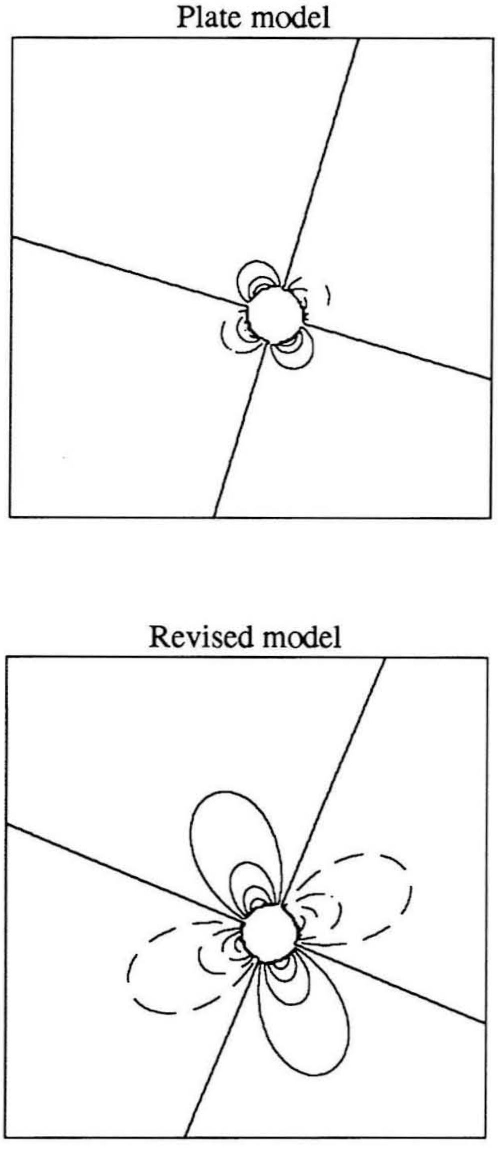

Figure 1.35: Comparison of the displacement fields for the two models (vertical component u_ζ). The contour interval is .05 μm and dashed lines indicate negative displacements.

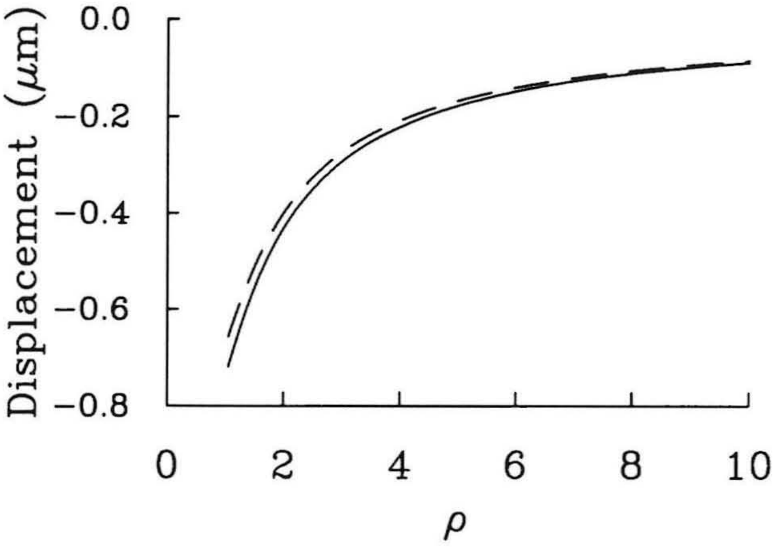

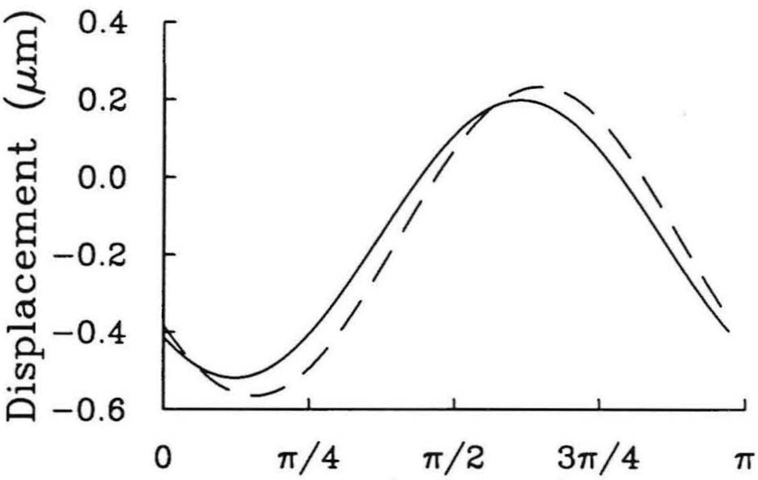

Figure 1.36: Radial component of displacements for the plate model (dashed line) and the revised model (solid line). The upper figure shows the displacements along a line from the center of the hole out to a distance of 10 radii at azimuth 0. The lower figure shows the azimuthal variation of the displacements at a distance of two radii from the center of the stress-relief hole. The results are from the hologram 16/3/3.

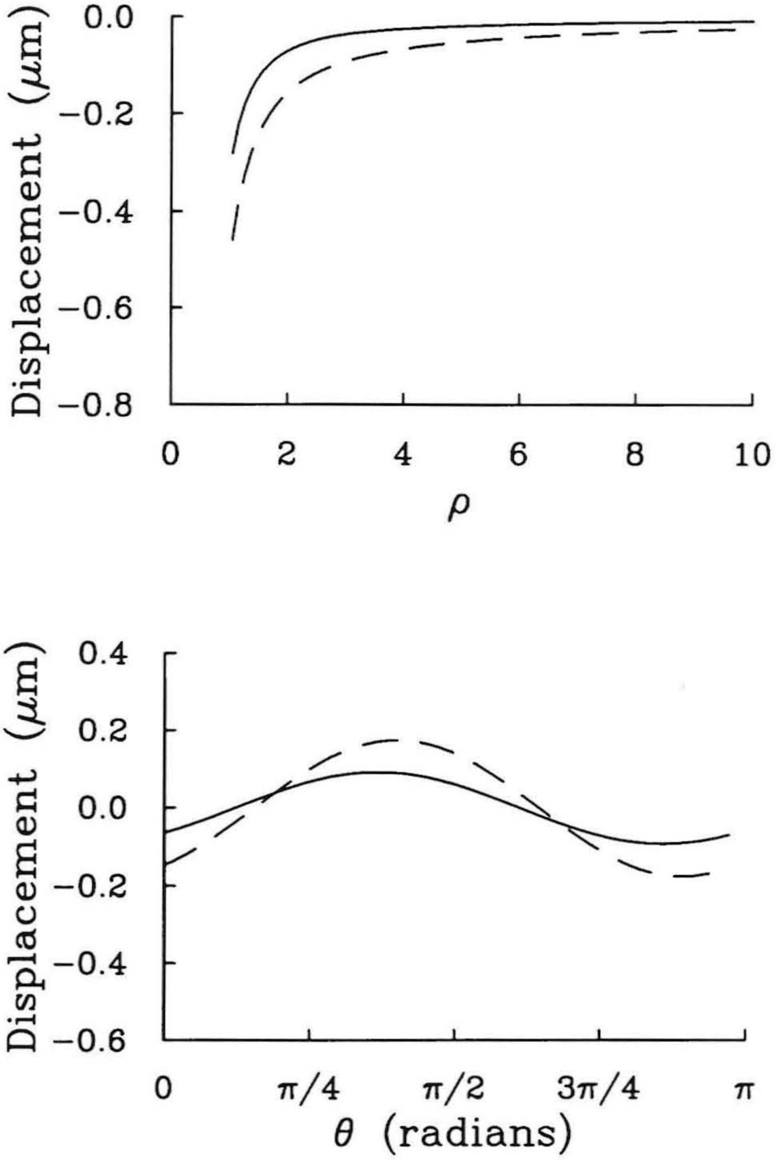

Figure 1.37: Tangential component of displacements for the plate model (dashed line) and the revised model. The results are from the hologram 16/3/3.

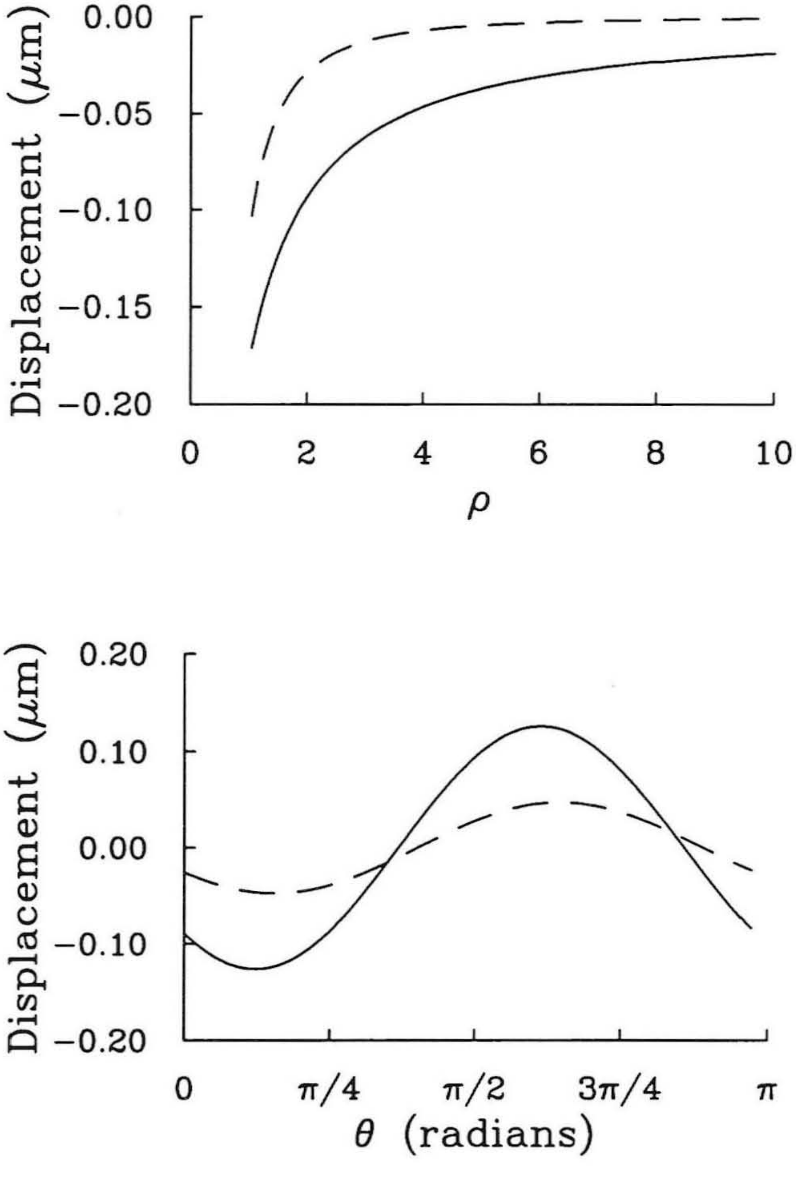

Figure 1.38: Vertical component of displacements for the plate model (dashed line) and the revised model. The results are from the hologram 16/3/3.

wall stresses in terms of the far-field stresses. In matrix form, we can write

$$Ax = b \tag{1.93}$$

Where A is the matrix of coefficients in equations 1.1 - 1.3, x is the 6-component vector containing the values of the far-field stresses, and b is the vector containing the modeled borehole wall stress values. The dimensions of A and b depend on the number of observations. In this case, we had 5 holograms, each with values of the three borehole wall stresses, so A is a 15 x 6 matrix and b is a 15-component vector. We know the values of the components of A and b; we need to find the best fit x to this overdetermined system. The least squares solution gives us this best fit:

$$x = (A^T A)^{-1} A^T b \tag{1.94}$$

Here A^T is the transpose of the A matrix and A^{-1} is the inverse of A. This solution minimizes the error [Strang 1980]:

$$E^2 = \|Ax - b\|^2 = \sum_{i=1}^{n} \left\{ \sum_{j=1}^{m} (A_{ij} x_j) - b_i \right\}^2 \tag{1.95}$$

Due to uncertainties in the borehole wall stresses, a set of calculations were made, varying the borehole wall stresses within the range of their uncertainties; the results are presented in Table 1.8. Of the six components, five are well constrained: four of these have uncertainties of less than 20%; the fifth, the shear stress in the E-W - vertical plane, is shown to be small. Only the normal stress in the N-S direction, parallel to the axis of the borehole, is poorly determined due to wide variations in the observed values of σ_{hh}, the normal stress in the direction along the borehole wall axis. The results show values of about -10 MPa (compressive) in both the vertical and E-W (perpendicular to the axis of the borehole) directions. This vertical normal stress is close to the value -11.2 MPa predicted by the relation

$$\sigma_p = \sigma_v s \tag{1.96}$$

Pillar stresses (in MPa) (plate model)	
σ_{EW}	-10.06 ± 0.765
σ_{Vert}	-10.23 ± 0.966
σ_{NS}	-2.51 ± 2.48
$\tau_{EW-Vert}$	-0.64 ± 0.54
τ_{EW-NS}	7.76 ± 1.05
$\tau_{NS-Vert}$	-3.64 ± 0.71

Table 1.3: Pillar stresses calculated from the values of the borehole wall stresses calculated from the plate model.

where σ_p is the load on the pillar induced by excavations of span s and σ_v is the vertical stress before mine excavation, estimated by mine depth and overburden mass [Brady and Brown 1985, Obert and Duvall 1967]. The values of σ_p predicted by equation 1.96 is, however, an upper bound on the vertical stress in a mine pillar. Rock anisotropy and proximity to the unmined areas can reduce the actual vertical stress in mine pillars [Coates and Ignatieff 1966, Salamon 1974]. This pillar was within 15 meters of the wall of the mine.

The principal stresses and their orientations for these stress components are given in Table 1.4. The maximum principal stress is a compressive stress of -15.35 MPa and is approximately horizontal and in an E-W direction, in the direction perpendicular to the borehole axis. The intermediate stress is nearly vertical, with magnitude -10.68 MPa. The least principal stress is tensile, oriented approximately N-S, along the axis of the borehole. Its magnitude is +3.22 MPa. The small, tensile value of the least principal stress is not surprising, since its orientation is along the axis of the borehole, and since the stress measurements were made near the edge of the pillar face. Measurements in pillars at another mine in the same formation show similar stress regimes, including the presence of a small horizontal tensile stress along the

Principal stresses (in MPa) (Plate model)		
Magnitude	Orientation	Plunge
-15.35	N54°E	17°
-10.68	N83°W	67°
3.22	N31°W	−14°

Table 1.4: Principal stresses, derived from the borehole wall stresses as determined from the plate model.

axis of the borehole in regions near the pillar face [USBM 1973].

The better fit of revised model synthetics to the observed holograms allows for increased precision of the solution for the state of stress acting on the borehole wall at the point of each stress-relief measurement. Tables 1.6 - 1.8 summarize the results of the new analysis. The rigid body translations of the camera module used in these fits are given in table 1.5. The largest principal stress has a magnitude of -11.34 MPa (compressive), close to the predicted value of -11.2 MPa for a pillar of this geometry [Obert and Duvall 1967, Brady and Brown 1985].

The stresses at the five different azimuths at this station, 4 m into the pillar face, may now be used in conjunction with equations (1.1 - 1.3) to obtain the solution for the far-field (in this case, the pillar) state of stress. These results are summarized in Table 1.8. The x-, y-, and z- directions are, respectively, East-West, Up-Down, and North-South. Again, the end result is similar to that obtained with the plate model, but the errors associated with each component of the stress tensor are greatly reduced. This solution yields the principal stresses shown in Table 1.8. Note that there exists a significant off-axis orientation to the stresses, i.e., they are not in-line with the borehole coordinate system. The ability to detect such phenomena is one of the strengths of the holographic method.

Camera module translations (for revised module fits) (μm)			
Hologram	ϕ	h	ζ
15/1/4	3.85	2.2	2.275
15/1/8	1.95	0.9	2.45
16/1/4	3.25	2.85	1.95
16/2/5	-3.525	0.985	4.05
16/3/3	-10.6	1.72	3.5

Table 1.5: Rigid body translations of the camera module for the synthetic holograms modeled by the revised model.

Revised borehole wall stresses (in MPa)				
Hologram	Azimuth	$\sigma_{\phi\phi}$	σ_{hh}	$\tau_{\phi h}$
16/1/4	90°	-20.0 ± 2.0	-5.0 ± 4.0	2.0 ± 1.5
16/2/5	45°	-12.0 ± 2.0	-7.5 ± 2.0	-8.5 ± 2.0
16/3/3	0°	-21.0 ± 1.0	-5.0 ± 2.0	-8.0 ± 2.0
15/1/8	180°	-20.0 ± 2.0	0.0 ± 5.0	2.0 ± 2.0
15/1/4	225°	-20.0 ± 2.0	-5.0 ± 4.5	2.0 ± 1.5

Table 1.6: Borehole wall stresses as fit by the revised model.

Revised pillar stresses (in MPa)	
σ_{EW}	-10.21 ± 0.414
σ_{Vert}	-10.70 ± 0.33
σ_{NS}	3.48 ± 0.99
$\tau_{EW-Vert}$	0.203 ± 0.22
τ_{EW-NS}	0.898 ± 0.43
$\tau_{NS-Vert}$	-3.05 ± 0.91

Table 1.7: Pillar stresses determined by the revised model.

Principal stresses (in MPa) (revised)		
Magnitude	Orientation	Plunge
-11.45	N55°E	68°
-10.14	E	−18°
4.16	N3°E	12°

Table 1.8: Principal stresses determined by the revised pillar stresses.

1.9 Conclusions

The initial model used to calculate the displacements on the free surface of the borehole wall underestimates the magnitude of the vertical component of displacement and overestimates the tangential component. These two components, while not as significant as the radial component in determining the final fringe pattern, make the accurate modeling of the borehole wall stresses difficult. A two-dimensional finite element analysis suggested that the simple model needed revision. Substitution of the half-space model of Youngdahl and Sternberg for the plate model improved the precision of the determination of the state of stress on the borehole wall and the inversion of these stresses for the far-field state of stress. The greatest part of the work in this new analysis is the numerical calculation of the residual components of displacement u_r^R, u_θ^R, and u_ζ^R for the appropriate value of Poisson's ratio. These having been obtained, it is easy to generate the displacement field for any state of stress desired, i.e., the new model is no more difficult to use than the old one was. The new model still does not exactly fit the observed fringe patterns, but seems to come closer to the observed state. Therefore in the future, holographic stress analysis will be better served by using the new model.

This method may be applied to techniques other than the holographic stressmeter described above. Any application which involves the measurement of deformation after drilling a hole into a free surface under stress could use this analysis, assuming the depth of the hole relative to the diameter is greater than unity. Strain gauges could be placed on the surface of a wall or rock face before a hole was drilled. Careful consideration of the placement of the gauges would result in improved estimations of the stresses on the wall or rock face.

Bibliography

Abramowitz, M. and Stegun, I. *Handbook of Mathematical Functions*, Dover, New York (1965).

Aggson, J. R. and Kim, K. Analysis of hydraulic fracturing pressure histories: a comparison of five methods used to identify shut-in pressure. *Int. J. Rock Mech. Min. Sci. & Geomech. Abstr.* **24**, 75-80 (1987).

Azzam, R. and Bock, H. A new modified borehole jack for stiff rock, *Rock Mechanics and Rock Engineering* **20**, 191-211 (1987).

Bass, J., Schmitt, D. R., and Ahrens, T. J. Holographic in situ stress measurements, *Geophys. J. R. Astr. Soc.* **85**, 13-41 (1986).

Brady, B. G. H. and Brown, E. T. *Rock Mechanics for Underground Mining*, Allen and Unwin, London (1985).

Cohn, S. N. Holographic in-situ stress measurement in geophysics, *Ph.D. Thesis*, California Institute of Technology (1983).

Coates, D. F. and Ignatieff, A. Prediction and measurement of pillar stresses. *Can. Min. J.* **87**, 50-56 (1966).

Haimson, B. C. The state of stress in the earth's crust. *Rev. Geophys. Space Phys.* **13**, 350-362 (1975).

Haimson, B. C. and Fairhurst, C. Initiation and extension of hydraulic fractures in rock. *Soc. Petrol. Engrs. J.* **7**, 310-318 (1967).

Hickman, S. Stress in the lithosphere and the strength of active faults. *Rev. of Geophysics, Supplement*, 759-775 (1991).

Hiramatsu, Y. and Oka, Y. Stress around a shaft or level excavated in ground with a three-dimensional stress state, *Mem. Fac. Engng, Kyoto*, **24**, 56-76 (1962).

Horino, F., Dolinar, D. and Tadolini, S. *Mechanical properties of the mahogany zone shale, Garfield County, Colorado*, U.S. Bureau of Mines Internal Report, United States Department of the Interior, Bureau of Mines, Denver (1982).

Hubbert, M. K. and Willis, D. G. Mechanics of hydraulic fracture. *AIME Trans.* **210**, 153-168 (1957).

Hughes, T. J. R., Ferencz, R. M. and Raefsky, A. M. DLEARN: A linear static and dynamic finite element analysis program, in *The Finite Element Method: Linear Static and Dynamic Finite Element Analysis*, by Hughes T. J. R. Prentice-Hall, Englewood Cliffs NJ, 631-796 (1987).

Jaeger, J. C. and Cook, N. G. W. *Fundamentals of Rock Mechanics* Chapman and Hall, London (1979).

Leeman, E. R. The CSIR doorstopper and triaxial rock stress measuring instruments. *Proc. ISRM Symp. on the Determination of Stresses in Rock Masses*, 578-616, L. N. E. C., Lisbon (1969).

Leeman, E. and Hayes, D. A technique for determining the complete state of stress in rock using a single borehole, *Proc. 1st Cong. Int. Soc. Rock Mech. Lisbon*, **2**, 17-24 (1966).

McGarr, A. and Gay, N. C. State of stress in the earth's crust. *A. Rev. Earth Plan. Sci.* **6**, 405-436 (1978).

McGarr, A., Zoback, M. D. and Hanks, T. C. Implications of an elastic analysis of in situ stress measurements near the San Andreas fault. *J. Geophys. Res.* **87**, 7797-7806 (1982).

Obert, L. and Duvall, W. I. *Rock Mechanics and the Design of Structures in Rock.* John Wiley & Sons, New York (1967).

Obert, L., Merrill, R. H. and Morgan, T. A. Borehole deformation for determining the stress in mine rock. *USBM RI 5978* (1962).

Papkovich, P. F. *Compte rendus hebdomadaires des seances de l'academie des sciences*, Paris **195**, 513-515, 754-756 (1932).

Richardson, R. M., Solomon, S. C. and Sleep, N. H. Tectonic stress in the plates. *Rev. Geophys. Space Phys.* **17**, 981-1019 (1979).

Rocha, M., Baptista, Lopes J. and DaSilva, J. A new technique for applying the method of the flatjack in determination of stresses inside rock masses. *Proc. 1st Int. Congr. on Rock Mechanics*, **2**, 57-65, Lisbon (1966).

Salamon, M. D. G. Rock mechanics of underground excavations, in *Advances in Rock Mechanics, Proc. 3rd Cong. Int. Soc. Rock Mech.* **IB**, National Academy of Sciences, Washington DC, 951-1099 (1974).

Schmitt, D. R. Applications of double-exposure holography to the measurement of in situ stress and the elastic moduli of rock from boreholes, *Ph.D. Thesis*, California Institute of Technology (1987).

Schmitt, D. R., Smither, C. L., Ahrens, T. J., and Jensen, B. Borehole in-situ holographic stress and elastic moduli measurements, *Proc., The Society of Exploration Geophysicists, 56th Annual Meeting*, Houston, 9-12 (1986).

Schmitt, D. R., Smither, C. L., Ahrens, T. J. and Jensen, B. Holographic measurement of elastic moduli, *Rock Mechanics: Key to Energy Production, Proc. 27th US Symp. Rock Mechanics*, Society of Mining Engineers, Littleton, CO, 185-191 (1986).

Simonsen, E. R., Abou-Sayed, A. S. and Clifton, R. J. Containment of massive hydraulic fractures. *Soc. Petrol. Eng.* **18** (1978).

Smither, C. L., Schmitt, D. R., and Ahrens, T. J. Holographic in situ measurements I: Borehole measurements of in situ stress, *EOS, Trans. Am. Geophys. Un.* **68**, 1460 (1987).

Smither, C. L., Schmitt, D. R. and Ahrens, T. J. Analysis and modelling of holographic measurements of in situ stress, *Int. J. Rock Mech. Min. Sci. & Geomech. Abstr.* **25**, 353-362 (1988).

Sokolonikoff, I. S. *Mathematical Theory of Elasticity*, McGraw Hill, New York p. 331 (1956).

Strang, G. *Linear Algebra and Its Applications*, Academic Press, New York (1980).

Timoshenko, S. and Goodier, J. *Theory of Elasticity*, McGraw-Hill, New York (1970).

U. S. Bureau of Mines. Rock Mechanics instrumentation for mine design; *Proceedings: Bureau of Mines Technology Transfer Seminar*, Washington, DC. USBM IC 8585 (1973).

Vest, C. M. *Holographic Interferometry* John Wiley & Sons, New York (1979).

Wang, Y. and Wong, T.-F. Finite element analysis of two overcoring techniques for in situ stress measurement. *Int. J. Rock Mech. Min. Sci. & Geomech. Abstr.* **24**, 41-52 (1987).

Wareham, B. F. and Skipp, V. O. The use of the flatjack installed in a saw-cut slot in the measurement of in situ stress. *Proc. 3rd Int. Cong. on Rock Mechanics*, **2A**, 481-488, Denver (1974).

Youngdahl, C. K. and Sternberg, E. Three-dimensional stress concentration around a cylindrical hole in a semi-infinite elastic body, *Research and Development Report*, Argonne National Laboratory, Argonne, IL ANL 7097 (1965).

Youngdahl, C. K. and Sternberg, E. Three-dimensional stress concentration around a cylindrical hole in a semi-infinite elastic body, *J. Appl. Mech.* **33**, 855-865 (1966).

Chapter 2

Three-dimensional modeling of planetary impacts

2.1 Abstract

A three-dimensional smoothed particle hydrodynamics code was used to model normal and oblique impacts of silicate projectiles on asteroidal and planetary bodies. The kinetic energy of the impactor is partitioned after impact into internal and kinetic energy of the impactor and the target body. These simulations show that, unlike the case of impacts onto a half-space, as much as 70% of the initial kinetic energy remains in the kinetic energy of the impacting body, as parts of it travel past the main planet and escapes the system. More oblique impacts retain much more kinetic energy in the impactor material: 6 to 75% as compared to 4 to 30% for the normal impacts. Higher velocity collisions also show this trend, as the kinetic energy of the impactor material is 2 to 50% of the total kinetic and internal energy for 5 km/s impacts, and 13 to 75% for 20 km/s impacts. Melting and vaporization were also examined. Impacts with the 60% impactor at 10 km/s melt 20 to 60% of the target, and melt 10 to 30% of the target at 5 km/s. The smaller impactor melts less of the

target material: 10 to 50% at 10 km/s and 2 to 6% at 5 km/s. Impacts at 20 km/s with an impactor 60% the size of the target were sufficient to completely melt both targets. A factor of 3 to 4 times more vaporization of the target material occurred on the larger targets. The amount of material completely vaporized in impacts at 5 and 10 km/s on the 1700 km target is less than 1% of the target, while on the 6400 km target, 2 to 4% is vaporized. For impacts at 20 km/s with the larger impactor, 3 to 9% of the 1700 km target is vaporized, while 10 to 20% of the 6400 km target is vaporized. The total amount of target material ejected at velocities greater than the escape velocity is found to be as much as that predicted for impacts at twice the impact velocity by earlier studies of impact onto a half-space. The amount of this ejected material that is ejected above the plane tangent to the target at the point of impact is consistent with the half-space studies for the 1700 km targets. Impacts at 20 km/s with the 60% impactor cause catastrophic fragmentation of the 1700 km target, where less than half of the target material remains together after the impact. Impacts with the 40% impactor at 20 km/s on the smaller target eject 4 to 53% of the target material. No ejecta is produced in impacts with the 40% impactor on the 6400 km target, and the 60% impactor ejects 5 to 9% of the target mass after impacts at 20 km/s. The degree of fragmentation of the target is slightly lower than that predicted by the model of Housen et al. [1991], due to the effect of gravity in re-accumulating dislodged material.

2.2 Introduction

Smoothed particle hydrodynamics (SPH) [Gingold and Monaghan 1977, Lucy 1977] is a technique which allows fully three-dimensional modeling of impact processes. In this study, we have used an SPH code developed at Caltech to examine the effects of impacts of silicate projectiles on planetary and asteroidal bodies to determine the extent of melting and vaporization of the impact, as well as the partitioning of the system's energy and the amount of ejecta thrown off the target due to the impact. The objects are modeled as a collection of particles, each representing a mass distribution in space, described as a function of a characteristic length scale. For each particle, the position, velocity, density, internal energy, pressure and bulk sound speed are calculated at each time step in the simulation. The system is self-gravitating, and energy and momentum are conserved throughout the run. The material properties are determined by an equation of state. For these simulations, we used the Tillotson equation of state [Tillotson 1962] for anorthosite [Ahrens and O'Keefe 1977] for both the targets and the impactors.

We modeled impacts on three different target sizes: 1700 and 6400 km in radius, corresponding approximately to the size of the moon and the earth, respectively, and 25 km in radius to examine impacts on asteroids. Each of the larger targets was hit with impactors of 40% and 60% of its radius (6% and 22% of its mass) at speeds of 5, 10 and 20 km/s. In order to investigate the effects of oblique impacts, we varied the angle of incidence of the collision from 0° to 90°, where this angle is measured from the axis of the plane parallel to the impact trajectory to the line from the center of the target to the center of the impactor at the time of impact (see figure 2.1). Thus a normal impact corresponds to an angle of 0°, and a 90° impact is a glancing blow. The angular momentum of these impacts ranged from 2.5×10^{25} to 1.4×10^{33} g/cm^{2}s for impacts on the 1700 km target to 1.2×10^{28} to 1.2×10^{35} g/cm^{2}s for impacts on the 6400 km target. In all cases, the angular momentum of these collisions is far below that of the earth-moon system (3.5×10^{41} g/cm^{2}s).

Initially, the kinetic and internal energy of the system resides entirely in the kinetic energy of the impactor. Upon impact, some of the energy goes into ejection of material from the target, and some into heating (internal energy) of both bodies. Studies of impact onto a half-space [e.g., O'Keefe and Ahrens 1977a] show that little

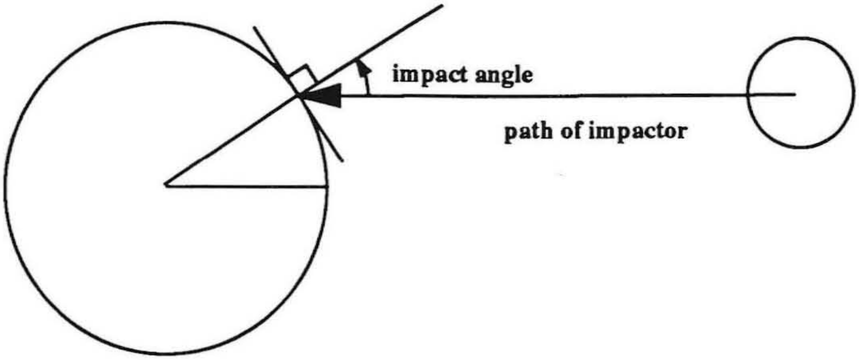

Figure 2.1: The impact angle is the angle between the path of the center of the impactor and the normal to the surface of the target at the point of impact.

to none of the total initial kinetic energy remains in the kinetic energy of the impactor after the impact. This is as expected, since, for an impact onto a planet of effectively infinite radius, very little of the impactor material will be able to get past the target. However, for our cases of impacts on finite-sized bodies, we find that a significant portion of the total kinetic and internal energy of the system remains in the kinetic energy of the impactor. This is especially pronounced in the more oblique, and higher velocity, collisions.

The impact causes melting of both the target and the impactor. For all but the most oblique collisions, all of the impactor is shocked to a state sufficient to cause complete melting. Normal impacts, which transfer more kinetic energy to the target, melt 1 to 2 times more material than the oblique impacts do. For normal and low-angle impacts, the larger impactor melts 3 to 6 times more of the target.

We also studied the formation of ejecta, material thrown off the target body at velocities greater than the escape velocity of the target, and the amount of impactor material accreted to the target. For all cases of impact onto the 6400 km body, very little material was ejected; the greatest amount of ejecta generated was 9% of the total mass of the target. The smaller targets lost much more mass. The larger and faster impacts at low angles were sufficient to cause catastrophic breakup of the smaller target, where the largest fragment remaining has less than half the original mass of the target. Normal impacts at 20 km/s caused complete destruction of the smaller target.

For the larger targets, much of the impactor mass was accreted. Except for the most oblique collisions, all of the smaller impactor remained with the target after impact. The 6400 km target, when hit by the 60% impactor at 10 km/s (a velocity lower than the escape velocity at its surface), caused 90 to 100% of the impactor material to be accreted. The only material from the impactor to escape was that which was on the side opposite the point of impact in the oblique cases. The higher velocity impacts accreted between 70% (normal impact) and 25% (90° impact) of the impactor material. The 1700 km targets, due to the lower escape velocity relative to the impact velocity, accreted much less of the impactor.

We compared the SPH ejecta results with the two-dimensional normal-impact models of O'Keefe and Ahrens [1977b]. Our simulations of impacts of the 60% impactor produced more ejecta than predicted by the O'Keefe and Ahrens results. The normal impact onto our smaller target produced as much ejecta as would have been produced by an impact of twice the velocity onto the half-space. The ejecta predicted for the larger targets, while not as great in terms of total projectile masses as that of the smaller targets, was still more than predicted by the half-space model. The smaller impacts produce no ejecta on the 6400 km target; on the 1700 km target, the total ejecta production from impacts at 10 and 20 km/s is close to that predicted by O'Keefe and Ahrens for impacts at velocities between 7.5 and 15 km/s. When we consider only the ejecta with trajectories that take the particles above the plane tangent to the target at the point of impacts (see figure 2.1, the 1700 km target results are consistent with the half-space model, but the results from the 6400 km target are still higher than predicted by O'Keefe and Ahrens. The larger amount of ejecta produced in the larger impacts may be a consequence of the finite size of the target.

2.3 Smoothed Particle Hydrodynamics (SPH)

2.3.1 Method

Smoothed Particle Hydrodynamics (SPH), developed independently by Lucy [1977] and Gingold and Monaghan [1977] is a method that represents a continuum by a collection of masses in space, the trajectories of which are followed through time. The method is fully Lagrangian, and is particularly well suited for the study of highly distorted flows, since there is no grid. Each mass is distributed in space; the exact distribution is described by a kernel function. At each time step, we calculate the position and velocity of each particle from the equations of motion. Once these are known, we can calculate the internal energy, density, and pressure at each point. The density at a point in the medium is related to the number of mass points per unit volume, and may be treated statistically as the probability [Gingold and Monaghan 1982] that a particle will be found in a unit volume. The positions of the particles are considered as a random sample from a probability density, which is proportional to the mass density. Then known statistical methods may be applied to interpolate from the known parameters of each point to obtain densities and gradients.

A function $f(r)$ may be interpolated as

$$< f(r) >= \int_D f(r')W(r-r',h)dr' \tag{2.1}$$

where D is the domain, and W is an interpolating kernel such that

$$\int_D W(r-r',h)dr' = 1 \tag{2.2}$$

Here h is the smoothing length, which has the effect of limiting the domain of influence of the kernel to small values of $|r-r'|$. If we have N points where we know the value of the function f, and these points are distributed with the number density n(r), we can approximate equation 2.1 as

$$f(r) \approx f_N(r) = \sum_{i=1}^{N} \frac{f(r_i)}{n(r_i)} W(r-r_i,h) \tag{2.3}$$

From which we can determine the number density to be

$$n(r) = \sum_{j=1}^{N} W(r-r',h) \tag{2.4}$$

We can estimate the derivative of f by

$$\frac{\partial f}{\partial x} = \int \frac{\partial f}{\partial x} W(r-r',h)dr' \tag{2.5}$$

Integration by parts of the above gives:

$$\frac{\partial f}{\partial x} = -\int f \frac{\partial}{\partial x} W(r - r', h) dr' \tag{2.6}$$

The equation of motion of the i^{th} particle is [Monaghan and Gingold 1983, Benz et al. 1986]:

$$\frac{d\mathbf{v}_i}{dt} = -m_i \sum_{j=1}^{N} \left(\frac{P_j}{\rho_j^2} - \frac{P_i}{\rho_i^2} \right) \nabla_i W(r_{ij}, h) - G \sum_{j=1}^{N} \frac{M(r_{ij})}{r_{ij}^2} \hat{\mathbf{r}}_{ij} + \mathbf{F}_i^{visc} \tag{2.7}$$

where m_i, P_i and ρ_i are the mass, pressure and density, respectively, of the i^{th} particle, G is the gravitational constant, r_{ij} is the distance between particles r_i and r_j $(= |r_i - r_j|)$, and

$$\hat{\mathbf{r}}_{ij} = \frac{\mathbf{r_i} - \mathbf{r_j}}{\mathbf{r}_{ij}} \tag{2.8}$$

The function $M(r_{ij})$ in the gravitational term is the mass of particle j within a sphere of radius r_{ij} about particle i:

$$M(r_{ij}) = \int_0^{r_{ij}} r^2 W(r, h) dr \tag{2.9}$$

$\mathbf{F}_i^{visc}$ is the force due to artificial viscosity. The artificial viscosity is introduced into the system to dampen excessive oscillation of the particles [Monaghan and Gingold 1983], and to discourage interpenetration of the impactor and the target. In this work, we have used the artificial viscosity of Benz et al. [1986], which is composed of a bulk and a drag viscosity:

$$\mathbf{F}_i^{visc} = \mathbf{F}_i^{bulk} + \mathbf{F}_i^{drag} \tag{2.10}$$

where

$$\begin{aligned} \mathbf{F}_i^{bulk} &= -\textstyle\sum_{j=1}^{N} \Pi_{ij} \nabla_i W(r_{ij}, h), \quad \mathbf{v}_{ij} \cdot \mathbf{r}_{ij} < 0 \\ &= 0, \qquad\qquad \mathbf{v}_{ij} \cdot \mathbf{r}_{ij} \geq 0 \end{aligned} \tag{2.11}$$

where $\mathbf{v}_{ij} = \mathbf{v}_i - \mathbf{v}_j$, and [Monaghan and Gingold 1983]:

$$\Pi_{ij} = -\frac{\alpha h \bar{c}_{ij}}{\bar{\rho}_{ij}} \frac{\mathbf{v}_{ij} \cdot \mathbf{r}_{ij}}{r_{ij}^2 + \varepsilon h^2} \tag{2.12}$$

Here $\bar{c}_{ij}$ and $\bar{\rho}_{ij}$ are the averaged sound speeds and densities of particles i and j, and ε and α are arbitrary numerical constants, for these runs set to 0.1 and 1 respectively.

The drag term is:

$$\mathbf{F}_i^{drag} = -K \frac{\sum_{j=1}^{N} \mathbf{v}_{ij} p_{ij} \hat{\mathbf{r}}_{ij}}{\sum_{j=1}^{N} p_{ij}} \tag{2.13}$$

with

$$\begin{aligned} p_{ij} &= W(r_{ij}, h) \quad r_{ij}/h < 4 \\ &= 0 \qquad\qquad r_{ij}/h \geq 4 \end{aligned} \tag{2.14}$$

and where K is another arbitrary constant, set to 0.01 in our simulations.

The equation for the internal energy is:

$$\frac{du}{dt} = -P\frac{dV}{dt} + \frac{dQ}{dt} \tag{2.15}$$

where dQ is the amount of energy absorbed by the system from its surroundings. For the i^{th} particle we have:

$$-\left(P\frac{dV}{dt}\right)_i = -0.5 \sum_{j=1}^{N} \left(\frac{P_j}{\rho_j^2} + \frac{P_i}{\rho_i^2}\right) \mathbf{v}_{ij} \nabla_i W(r_{ij}, h) \tag{2.16}$$

and

$$\left(\frac{dQ}{dt}\right)_i = 0.5 \sum_{j=1}^{N} \Pi_{ij} \mathbf{v}_{ij} \nabla_i W(r_{ij}, h) + \sum_{j=1}^{N} \mathbf{v}_{ij} \mathbf{F}_i^{drag} \tag{2.17}$$

The values of P and c, the pressure and sound speed, are determined by the equation of state. In this work we used the Tillotson equation of state [Tillotson 1962], which has three regimes:

1. The cold, condensed state (where $\rho > \rho_0$, or $U < U_s$, where ρ and U_s are the reference density and internal energy for the material)

$$P = \left(a + \frac{b}{U/(U_s \eta^2) + 1}\right) \rho U + A\mu + B\mu^2 \tag{2.18}$$

where $\eta = \rho/\rho_0$, $\mu = \eta - 1$, and a, b, A, B, and U_s are parameters specific to the material being studied.

2. The expanded state, where $\rho < \rho_0$ and $U > U_{cv}$

$$P = a\rho U + \left[\frac{b\rho U}{U/(U_s\eta^2)+1} + A\mu e^{-\beta(\rho_0/\rho-1)}\right] e^{-\alpha(\rho_0/\rho-1)^2} \tag{2.19}$$

where α and β are constants, and

3. The intermediate regime, where $U_s < U < U_{cv}$ and $\rho > \rho_0$

$$P = \frac{(U - U_s)P_E + (U_{cv} - U)P_c}{U_{cv} - U_s} \tag{2.20}$$

where P_C is the pressure from equation 2.18 and P_E is the pressure from equation 2.19.

Note that this α is distinct from the α in the viscosity equation 2.12.

For these simulations, we used the equation of state for gabbroic anorthosite [Ahrens and O'Keefe 1977], which assigns the following values to the constants:

$$\begin{aligned}
A &= 7.1 \text{ x } 10^{11} \text{ dyne/cm}^2 \\
B &= 7.5 \text{ x } 10^{11} \text{ dyne/cm}^2 \\
a &= 0.5 \\
b &= 1.5 \\
\alpha &= 5 \\
\beta &= 5 \\
\rho_0 &= 2.94 \text{ gm/cm}^3 \\
U_s &= 4.85 \text{ x} 10^{12} \text{ erg/gm} \\
U_{cv} &= 1.82 \text{ x } 10^{11} \text{ erg/gm}
\end{aligned}$$

Other parameters for anorthosite used in this work are the specific energies required for incipient melting (U_{im}), complete melting (U_{cm}), and incipient vaporization (U_{iv}),

Kernel parameters for targets			
Target size	m (g)	h (cm)	Spacing
1700 km	6.45 x 10^{22}	1.42 x 10^{7}	2.0
6400 km	6.9 x 10^{24}	6.75 x 10^{7}	1.6

Table 2.1: Parameters of the kernel W used in the construction of the 1700 and 6400 km targets.

which are:

$$\begin{aligned} U_{im} &= 1.76 \text{ x } 10^{10} \text{ erg/gm} \\ U_{cm} &= 2.065 \text{ x } 10^{10} \text{ erg/gm} \\ U_{iv} &= 4.72 \text{ x } 10^{10} \text{ erg/gm} \end{aligned}$$

The smoothing kernel W for a particle is a function of the smoothing length h and the mass of the particle m. The kernel we used for these simulations is the exponential kernel of Wood [1981]:

$$W(r,h) = \frac{m}{8\pi^3 h^3} e^{-r/h} \tag{2.21}$$

Changing the smoothing length and the spacing between the particles changes the density structure of the object. To assemble our targets and impactors, we varied the structures until a reasonable density distribution was found. The targets were composed of 925 particles, with the parameters given in table 2.1. Parameters for the impactors, which were constructed of 257 particles, are given in table 2.2. With this configuration, energy was conserved in our simulations to within 5%. Figure 2.2 shows energy conservation results for impacts with the 40% and 60% impactor on the 1700 km target for impact angles of 50° and 90°. The total energy is the sum of the kinetic, internal, and gravitational potential energies.

The initial density distributions for both targets are shown in figure 2.3. The central densities are 3.25 g/cm^3 in the 1700 km target, and 6.16 g/cm^3 in the 6400

Kernel parameters for impactors				
Target size	Impactor	m (g)	h (cm)	Spacing
1700 km	40%	1.4 x 10^{22}	1.1 x 10^{7}	1.6
1700 km	60%	5.1 x 10^{22}	1.0 x 10^{7}	2.4
6400 km	40%	1.5 x 10^{24}	6 x 10^{7}	1.0
6400 km	60%	5.3 x 10^{24}	8 x 10^{7}	2.25

Table 2.2: Parameters of the kernel W used in the construction of the 40% and 60% impactors for the 1700 and 6400 km targets.

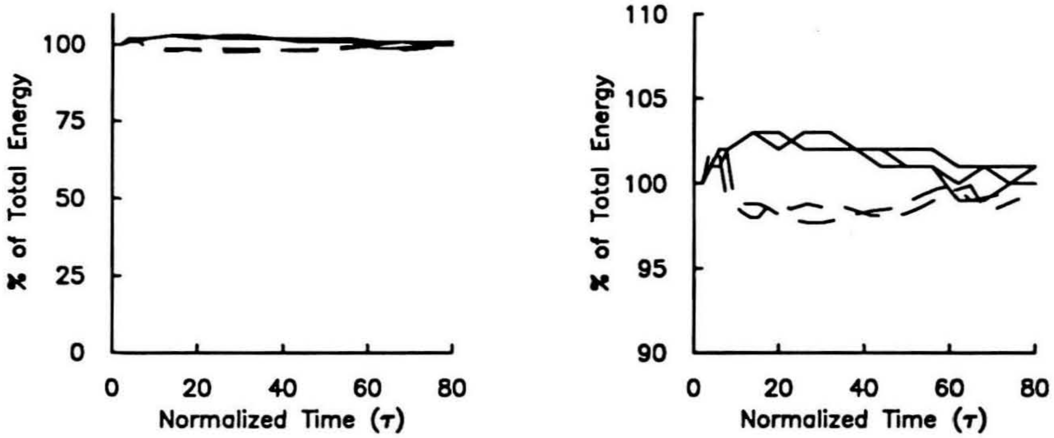

Figure 2.2: Energy conservation for impacts on the 1700 km target with the 60% (solid line) and 40% impactors at 50° and 90°. The total energy (internal, kinetic, and gravitational potential) in the system is plotted against time dimensionless time τ described in the text.

km target. To check the SPH model, we may approximate the pressure variation with depth by the relation

$$\frac{dP}{dr} = -\rho g, \tag{2.22}$$

where $g(r)$ is the gravitational acceleration at radius r within the target, and

$$\begin{aligned} g(r) &= \frac{GM(r)}{r^2} && (2.23) \\ M(r) &= \int_0^r 4\pi a^2 \rho(a) da && (2.24) \end{aligned}$$

Figure 2.4 shows the pressures that would be predicted by the density structure of figure 2.3, and the SPH results. The 6400 km target shows a close agreement with the predicted values, but the 1700 km target has pressures which are approximately twice that predicted by equation 2.22.

2.3.2 Previous applications of SPH to planetary impacts

There have been several previous studies using SPH to model impacts on terrestrial planets. Perhaps the best-known are the papers by Benz and his co-workers [Benz et al. 1986, 1987, 1989, and Cameron et al. 1991], in which they examine the theory that the moon was formed as a result of a hypervelocity giant impact of a Mars-sized body with the proto-earth. They initially modeled both bodies as undifferentiated granite spheres, using the Tillotson equation of state. The simulations run after 1987 use the ANEOS equation of state [Thompson and Lauson 1984], and include iron cores in both the impactor and the target. The relative sizes of the impactor and target are similar to the ones we used for this study (their impactors are 0.1 to 0.25 the size of the target by mass, ours are 0.06 to 0.22), and the range of impact velocities is similar (11 to 15 km/s) to our values of 5 to 20 km/s, since they want to minimize the amount of destruction of the target, and maximize the amount of impactor material that would remain in earth orbit after the impact. Velocities that are too high tend to cause too much target material to be ejected, and too many

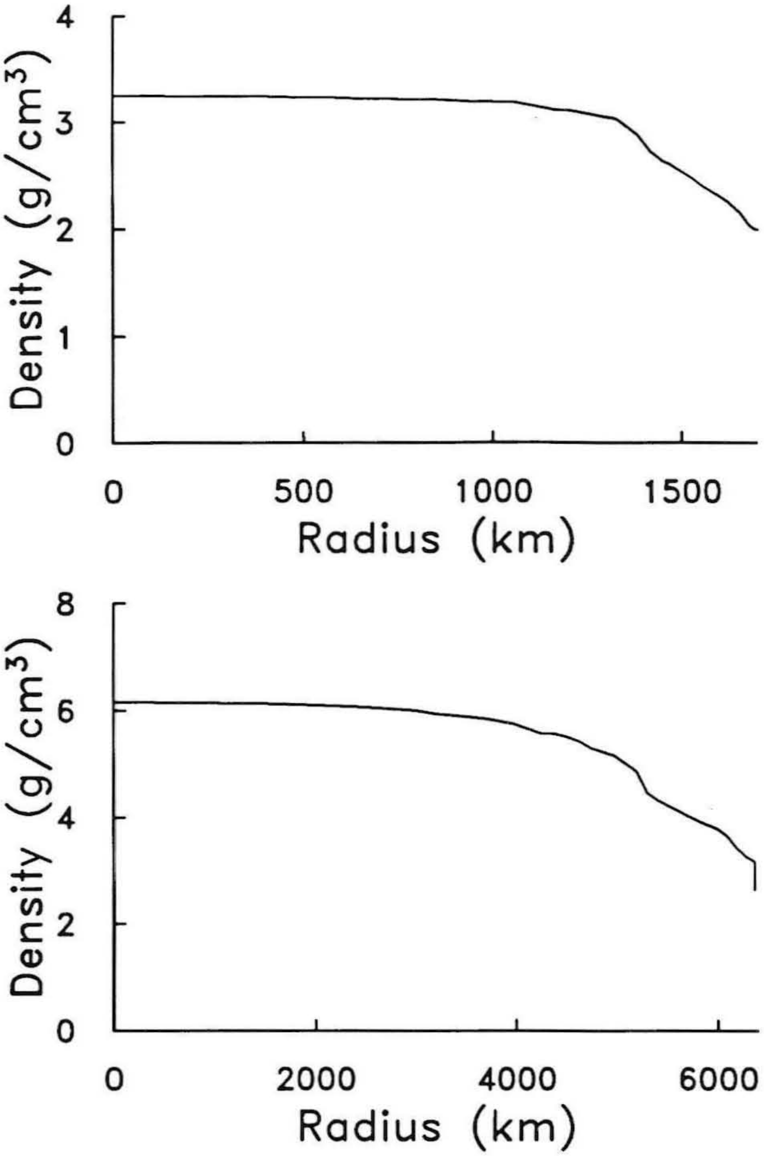

Figure 2.3: Initial density structure for the 1700 km (top) and 6400 km target.

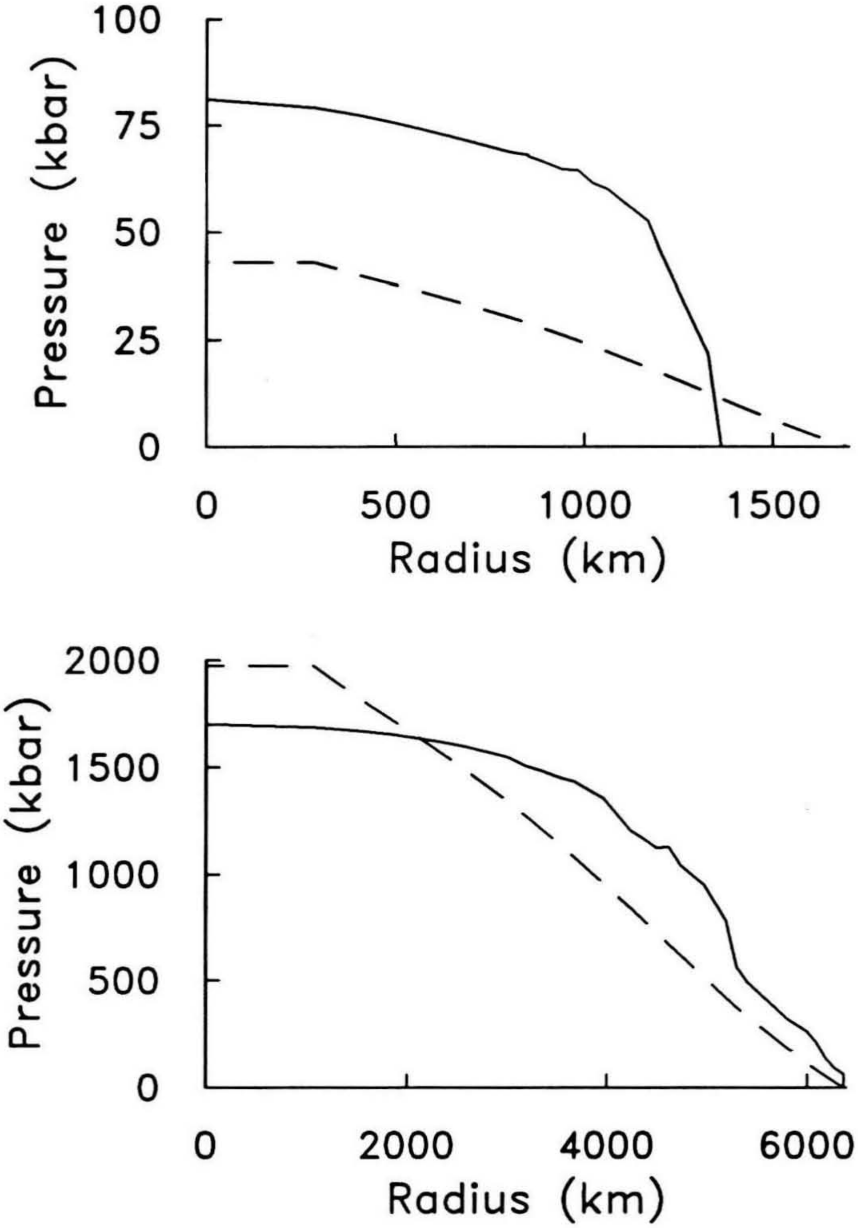

Figure 2.4: Initial pressure profile for the 1700 km (top) and 6400 km target. The SPH result is shown by the solid line; the dashed line is the pressure predicted for the density structure of the preceding figure.

of the impactor particles to retain post-impact velocities that are higher than the escape velocity of the earth. For very low velocities, most of the impactor material is accreted to the earth, and too much remains in orbit within the Roche limit, and so would be broken up by the earth's tidal forces.

The impact parameter (or impact angle) was varied as well. For low impact parameters (low angles) the impactor was completely destroyed and spread out into space. Higher impact parameters were therefore more favorable for forming a moon. In grazing impacts, clumps of impactor material remain in elliptical orbits around the target. These clumps are molten. This implies (though they do not state this directly) that the impactor is completely melted in the collision, which agrees with our findings, except for in the very slowest, high angle, collisions. These clumps, which are less highly shocked than the material that is spread out after impact, generally come from the side of the impactor that is farthest from the interface at the time of maximum compression.

Benz et al. also applied SPH to study the question of the early history of Mercury [Benz et al. 1987]. The anomalously high density of Mercury as it exists today is proposed by them to be the result of a large collision which stripped off most of the planet's mantle, leaving mostly the core material behind. For these simulations, the impact velocities are higher than in the moon-forming impact scenarios, between 10 and 38 km/s. The target radius is 2400 km, which is intermediate to our two large targets, and the impact angle ranged from 0° and 36°. The impactor is 6% by mass of the target. Several combinations of impact velocity and angle were shown to yield a target that had been stripped of most of its mantle, leaving behind an iron core.

Pongracic [1988] modeled impacts of silicate projectiles onto a semi-infinite body, much like the earlier two-dimensional finite-difference work of O'Keefe and Ahrens [1977a,b]. She varied the topography of the impact site, as well as the impact velocity (10 to 49 km/s) and impact angle (0° to 75°). Since the impactor is small compared to the size of the target (which is essentially of infinite radius), gravitational effects were not considered. She found more material ejected at velocities greater than the surface escape velocity than predicted by the finite-difference model. This is in agreement with our results, which will be presented below.

2.4 Results

In this study, we modeled impacts on planetary scale targets (1700 and 6400 km radius) at impact velocities from 5 to 20 km/s and impact angles ranging from 0° to 90°. Thus an angle of 0° corresponds to a normal impact, and an impact angle of 90° is a grazing impact. Both target and impactor were modeled as gabbroic anorthosite, using the Tillotson equation of state outlined above, with the parameters from the work of Ahrens and O'Keefe [1977]. Only the early stages of the impacts were followed, out to about 2 hours of real elapsed time after the impact occurred. Thus, unlike the work of Benz et al., we did not seek to answer questions about the ultimate fate of the ejected material, i.e., whether the particles that did not achieve escape velocity would orbit around the target, land back on the surface, or form a disk around the planet. The calculations are sufficient, however, to estimate the amount of melting and vaporization of the material, the energy partitioning, and the production of ejecta at velocities sufficient for it to escape the pull of the target's gravity.

For each target, we used two sizes of impactors. The larger one was 60% of the radius of the target (22% of the mass), and the smaller one was 40% by radius, 6% by mass. Each impactor was sent toward the target at 5, 10, and 20 km/s, at impact angles of 0°, 5°, 15°, 30°, 50°, and 90°. The velocity at infinity of the impacts ranged from 3.6 to 18.6 km/s for the 1700 km targets, and -2.5 to 12.5 km/s for the 6400 km targets. Early work on scaling laws for impacts [e.g., Gault and Wedekind 1969] suggested that the amount of ejecta produced in a given impact was related to the specific energy (the ratio of the impactor kinetic energy to the target mass). If this were the case, the outcomes of, for instance, the impacts of the 40% impactors at 10 km/s on the two different targets would be similar. Yet, as will be shown below, there are significant differences in the aftermaths of collisions on the two bodies.

Figures A.1 - A.54 show the results of some representative runs. Figures A.31 - A.50 show three cases of 10 km/s impacts on the 6400 km target with the 60% impactor at 15°, 50° and 90°. The velocities of the individual particles are represented by arrows; the position of a particle is at the origin of the arrow. Boxes at the end of arrows indicate particles from the impactor. Some impactor particles have traveled out of the frame and thus are not evident in the later pictures. The view is from the z-axis, and the impactor came in from the top of the page. All particles are shown; however, due to the initial geometry of the bodies, some are hidden behind others. Particles nearest the impact point are shocked the hardest, and travel fastest. In the 15° and 50° impacts, only 0.6% of the target (6 particles) are traveling fast enough to escape the target. Other particles are affected by the target's gravity, and eventually curve back around toward the target instead of traveling straight out from it. The target suffers significant damage during the impacts, as nearly an entire hemisphere is blown away, and the remaining part is highly deformed. Much of the impactor is accreted to the target, and may be seen at the edge of the deformed side of the target. Normal and near-normal impacts send particles in directions nearly perpendicular to the impact direction, while the more oblique impacts send material into trajectories which are generally closer to the impact direction. In the most oblique impact in this series, much of the impactor material remains in a clump following the bulk of the disturbed target particles.

The same range of impact angles for impacts at 20 km/s is shown in figures A.35 - A.54. Notice that more particles are moved away from the target, and that more of them are scattered back with a component of velocity in the opposite direction of the impact. More of the disturbed particles are ejected at velocities high enough to escape the target, and less of the impactor material is accreted. Most of the particles moved from the target have trajectories that do not curve back around towards the main mass of the remaining target.

Figures A.16 - A.30 show the results of the 15°, 50° and 90° impacts at 5 km/s on the 1700 km target with the 60% impactor. These impacts are much more destructive than the corresponding impacts on the 6400 km target. Two to 3% of the target material is ejected at velocities sufficient for escape from the target, and only 20 to 60% of the impactor material is accreted, even at this relatively low impact velocity. Similar impacts (5 km/s, 60% impactor) on the 6400 km target produce no ejecta, and accrete all of the impactor to the target.

The effects of increasing the impact velocity are shown in figures A.1 - A.15 for impacts at 15° by the 40% impactor on the 1700 km target. The impact at 5 km/s does very little damage to the target, and manages to dislodge only a few particles (the total amount of ejecta is 0.4% of the target mass). An impact at 10 km/s is much more destructive, and causes 1.7% of the target to be ejected at velocities greater than the escape velocity (2.4 km/s). The impactor particles are scattered widely. The 20 km/s case disrupts the target greatly. The entire target feels the effects of the impact, and 24% of the target is ejected. Only 33% of the impactor material is accreted to the target, as opposed to 55% in the 10 km/s case, and 95% in the 5 km/s case.

2.4.1 Melting and vaporization

Figures 2.5 - 2.9 and tables 2.3 - 2.6 show the amount of melting and vaporization resulting from these impacts. By "melted" and "vaporized" we mean the material which was shocked to an internal energy sufficient to cause complete melting or vaporization of the particle. Thus these figures do not include regions of partial melt or partial vaporization. In figure 2.5, the results of impacts onto the 6400 km target are plotted in the lower half of the figure, and those of the 1700 km target are shown in the upper half. Impacts by the 40% impactor are on the left, the 60% impactor on the right. All melt and vapor production is plotted normalized to the impactor mass. In the case of the impacts by the 60% impactor, the maximum amount of melting of the target possible is 4.55 projectile masses, since the mass of the impactor is 22% of the target. Thus the curves for the impacts at 20 km/s flatten out for the strongest (lowest impact angle) impacts, in which the entire target was melted. The amount of vaporization is shown by a bar below the plotted point. In most of the impacts, the amount of complete vaporization of the target material is quite small. In all cases, the amount of target material vaporized is significantly higher on the 6400 km target than in the corresponding impacts on the 1700 km target, by a factor of 2 to 3 for the 60% impactors, and 10 to 20 for the 40% impactors.

Figures 2.6 - 2.9 show the dependence of melt and vapor production on impact velocity for normal and the most oblique impacts. The amount of melt, measured in units of impactor mass, shows a clear dependence on the squared impact velocity in the case of the normal (0°) impacts (figure 2.6). (As in figure 2.5, the curves for the impacts with the 60% impactor are limited in the 20 km/s impacts by the fact that not more than 4.55 impactor masses can be melted.) The 90° impacts (figure 2.7) do not show as strong a dependence. This implies that the effects of increasing the impact velocity (and thus increasing the energy of the impact) are weaker for more oblique impacts. The corresponding plots of vaporization against impact velocity (figures 2.8 and 2.9) show a somewhat different relationship. Points are plotted only for those cases where some material was completely vaporized. The change in impact velocity from 5 to 10 km/s does not produce as large an increase in the amount of material vaporized as does the change from 10 to 20 km/s. This suggests that there is a threshold velocity (or energy) that must be exceeded before significant vaporization of target material can occur.

The amount of target material melted, when measured relative to the impactor mass, is quite similar for the 5 and 10 km/s impacts with both impactor sizes. A normal impact at 10 km/s melts 2.3 to 2.7 impactor masses in all cases. Since the amount of melt produced in the 20 km/s impacts is quite high, and for the larger impactor tends to melt the entire target for impacts at angles of 30° or less, it is difficult to compare the outcomes directly. However, it is clear that the impacts of the 40% impactor on the 1700 km target at 20 km/s produce 1.4 to 1.6 times as much melt as the impacts on the 6400 km target. This trend is not seen for impacts with the 60% impactor, where the melt output on the 1700 km target is 0.8 to 1.1 times that of the 6400 km target, for the most oblique (50° to 90°) impacts, where the entire target was not melted.

The effect of the obliquity of the impact seems to be strongest for higher velocity impacts. For the 5 km/s impacts on the 6400 km target, the amount of melt produced is 1.5 projectile masses for impacts at both 0° and 90° for the 60% impactor and is 1 projectile mass at 0° and 0.8 at 90° for the 40% impactor. The smaller targets show more variation in melt production with impact angle compared to the same mass ratio impact on the larger target in all cases. For the 5 km/s impact, the amount of melt produced ranges from 0.25 to 0.67 projectile masses for the 40% impactor, and 0.47 to 0.91 projectile masses for the 60% impactor.

Appendix B contains more tables detailing the melt and vapor produced in our simulations. Tables B.1 - B.8 show the amount of partial melt, in terms of the fraction of the target mass melted (tables B.1 - B.4), and measured relative to the mass of the impactor (tables B.5 - B.8). These tables list the mass that was shocked to an internal energy high enough to cause 1%, 10%, 50%, 90% and 100% melting. At all levels of partial melting, the impacts with the 60% impactor at 5 km/s melt 5

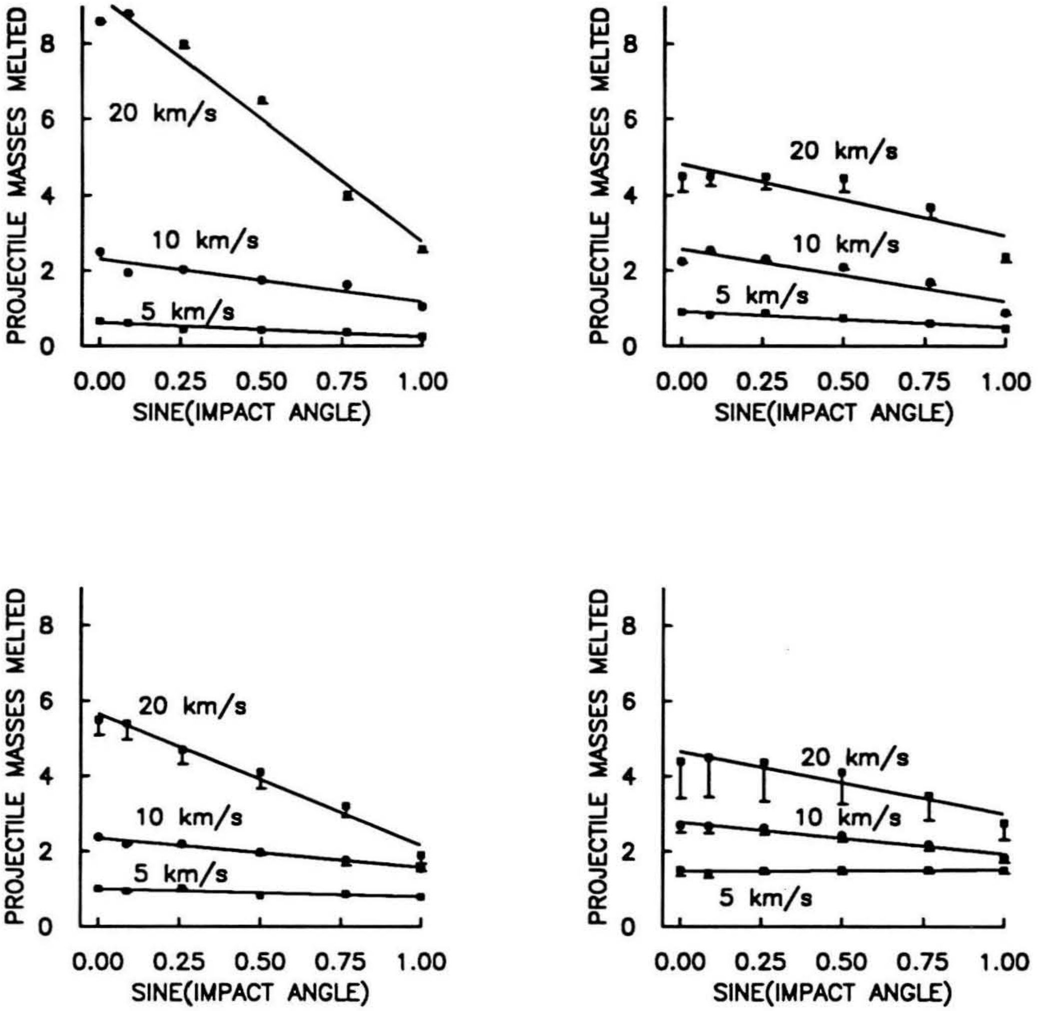

Figure 2.5: Effect of impact angle on melt and vapor production. The mass of material melted and vaporized, in terms of number of projectile masses is plotted for all impacts. Impacts on the 1700 km target are above, and on the 6400 km target below. Impacts with an impactor that is 40% by radius of the target are shown on the left, with the 60% impactor on the right. The amount of vaporization is shown by the bars.

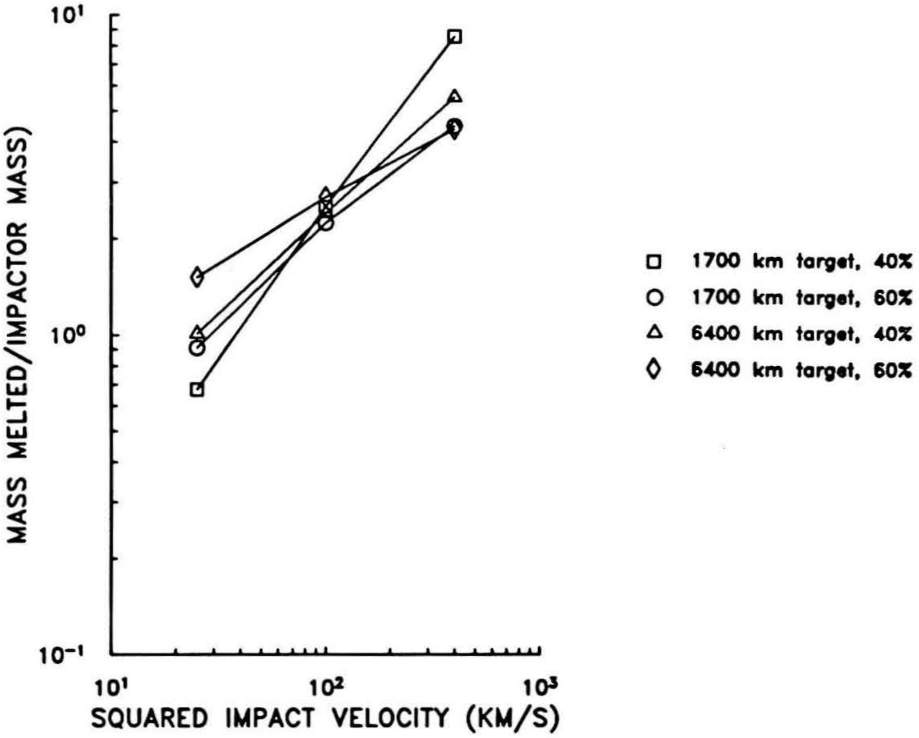

Figure 2.6: Amount of material melted, in terms of number of projectile masses, plotted against impact velocity for normal impacts.

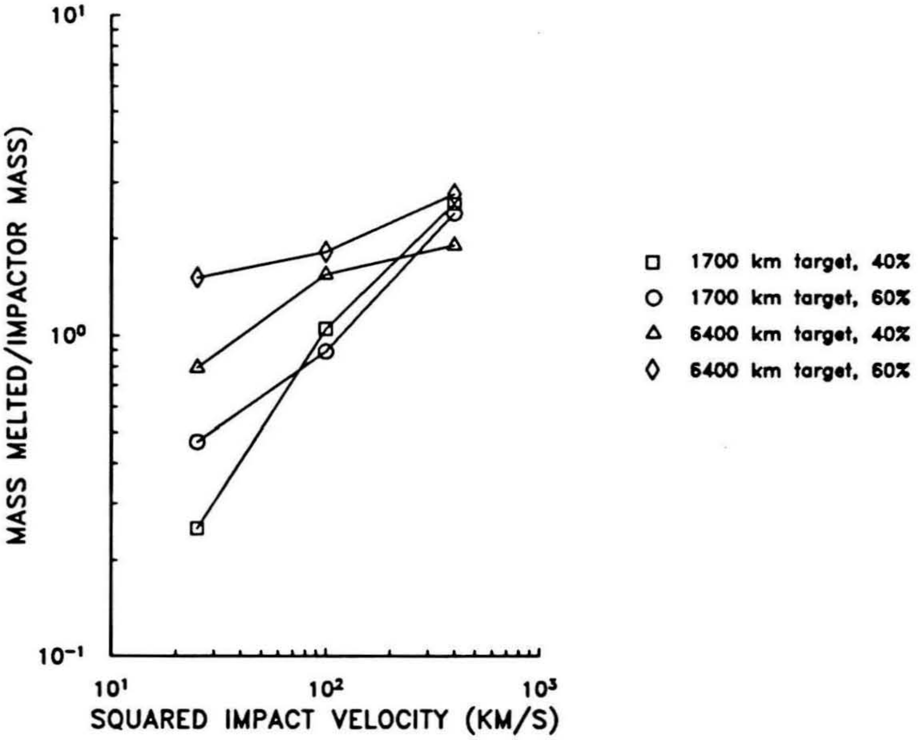

Figure 2.7: Amount of material melted, in terms of number of projectile masses, plotted against impact velocity for oblique (90°) impacts.

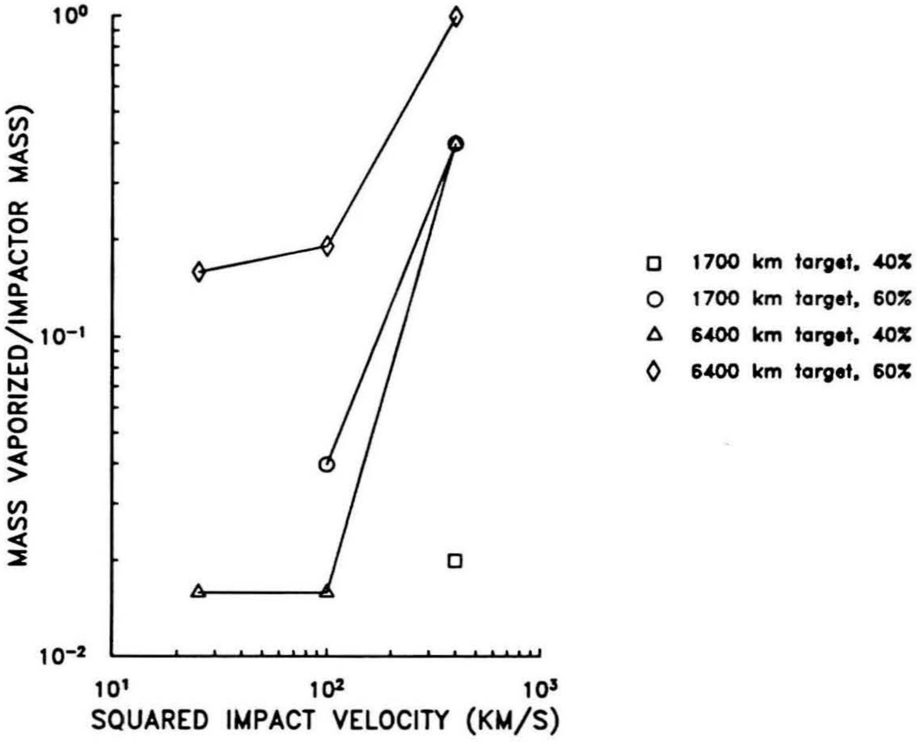

Figure 2.8: Amount of material vaporized, in terms of number of projectile masses, plotted against impact velocity for normal impacts.

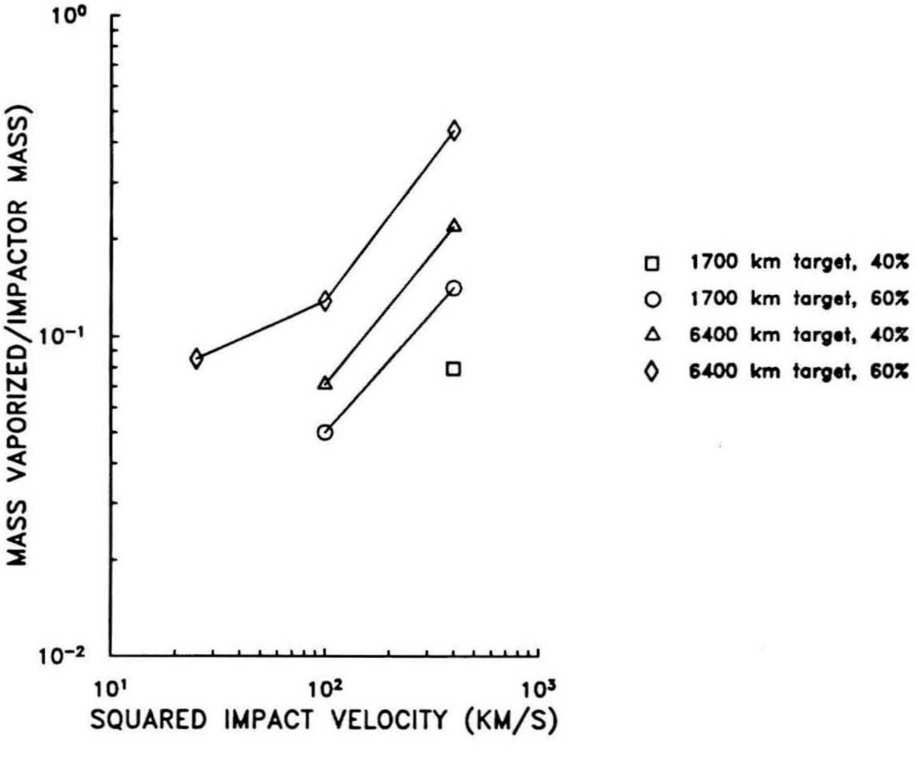

Figure 2.9: Amount of material vaporized, in terms of number of projectile masses, plotted against impact velocity for oblique (90°) impacts.

to 6 times as much of the target material as the impacts with the 40% impactor on both the 1700 and 6400 km targets. At 10 km/s, the ratio of target material melted with the 40% impactor to that melted with the 60% impactor is 3 to 4. Since the 20 km/s impacts with the larger impactor melt the target completely at impact angles of 30° or less, we can only compare the impacts at 50° and 90°. The impacts on the 1700 km target with the larger impactor melt 3 to 3.5 times as much material as do the impacts with the smaller impactor. For the 6400 km target, the ratio is larger: 3 to 5.5.

Impacts with equivalent impactor on the different targets vary in terms of the amount of target material melted. Approximately 50% to 100% more of the target is melted in the 5 km/s impacts on the 6400 km target than on the 1700 km target at all levels of partial melting and for all impact angles. For the 10 km/s impacts, the difference in the amount of target material melted is smaller: at most 20% more is melted in the less oblique collisions (impact angle less than 30°) on the 6400 target compared with the 1700 km target. The more oblique impacts show more variation in melt production, with 20 to 30% more target material melted in the 50° impacts, and 80 to 100% more melted in the 90° impacts. The corresponding figures for the 40% impactor are: 60 to 200% more melt on the larger target for impacts at 5 km/s; 10 to 70% more at 10 km/s, while the 20 km/s impacts actually produce less melt on the larger targets than on the 1700 km target, by a factor of 1.5 to 2.

When considered normalized to the mass of the impactor (tables B.5 - B.8), the amount of melt produced in the impact still shows some variation with impactor size. If melt production scaled simply with the mass of the impactor, we should see the same amount of melt, in terms of the number of impactor masses melted, in the case of impact with either impactor at the same impact velocity and angle. However, our results show that for most cases, more melt is produced after impacts by the 60% impactor than the 40% impactor for both targets. On the larger target, impacts with the 60% impactor at 5 km/s yield 20 to 90% more melt than impacts with the smaller impactor. This effect is more pronounced for more oblique impacts, where the melt production in the case of the 60% impactor is 60 to 90% higher than in the case of the 40% impactor. At 10 km/s, the agreement is much closer, and the amount of melt is at most 20% higher for the larger impactor, and is in some cases actually a few percent lower than the amount melted by the smaller impactor. Again, for the 20 km/s impacts we can only directly compare the most oblique collisions. For an impact at 50°, 6 to 9% more melt is produced by the 60% impactor; at 90°, the figures are 35 to 50%.

On the smaller target, the melt production at 5 km/s is similar to what we see on the 6400 km target: 35 to 95% more impactor masses are melted after impact by the larger impactor. At 10 km/s, the melt amounts are much closer to each other, 4 to 20% higher after the 60% impact. The 20 km/s impacts show the opposite trend: both the 50° and 90° impacts produce 10 to 20% less melt in the case of the 60% impactor than in the 40% case.

The amount of target mass partially and completely vaporized is shown in tables B.9 - B.12 as the fraction of the total target mass, and in tables B.13 - B.16 in units of impactor mass. The fraction of the total target mass vaporized is much greater in the collisions with the larger impactors. For the 1700 km target, collisions at 5 km/s produce only small amounts of partial vaporization, at the limit of our resolution in the 40% impactor cases. At 10 km/s, the amount of target material brought to 1% partial vaporization is 5 to 10 times higher in the 60% impacts, and at 20 km/s, 4 to 8 times higher than in the 40% case. The amount of material that is 50% vaporized after the 20 km/s impacts with the 60% impactor is 5 to 12 times higher than what is seen in the smaller impacts. On 6400 km targets, 5 to 8 times more target material is shocked to the 1% vaporization state for impacts with the 60% impactor at all impact velocities. For 20 km/s impacts, the amount of target material completely vaporized is 8 to 10 times higher in the 60% impacts.

When measured normalized to the impactor mass, we again see that the amount of partial or complete vaporization of target material generated after an impact does not scale linearly with impactor size. For impacts on the 1700 km target at 10 and 20 km/s, the 60% impactor shocks 1.5 to 3 times as many impactor masses to the 1% vaporization state; at 20 km/s the same ratio holds for material completely vaporized. The results for impacts on the 6400 km target are similar: 1.5 to 2.3 times as much target material is 1% vaporized in the 60% collisions at all angles and velocities, and 2 to 3 times as much material is completely vaporized in the 20 km/s impacts.

Comparing the results of equivalent impacts on the two targets in figure 2.10, we see that impacts on the larger target produce more vaporization in all cases. In this figure, the cumulative vaporized mass fraction of target particles is plotted in units of projectile masses. Impacts on the 1700 km targets are in the upper half of the diagram, and impacts with the 40% impactor are on the left. Only the results from the normal impacts are plotted. For a normal impact at 20 km/s with the 60% impactor on the 1700 km target, 3.1 projectile masses (68% of the total mass of the target) are brought to an internal energy sufficient to cause 1% of the particle to be vaporized. Of that 3.1 projectile masses, 2.3 are 10% vaporized, 0.84 50% vaporized, and 0.4 completely vaporized. For impacts at 20 km/s with the 40% impactor, 2 to 5 times as many impactor masses were completely vaporized on the 6400 km target as on the 1700 km target. For impacts at 10 and 20 km/s, 1 to 2.4 times as many impactor masses were 1% vaporized. For impacts with the 60% impactor, the normalized amount of target material 1% vaporized was 3 to 5 times as much on the 6400 km target for impacts at 5 km/s, 1.5 to 2.5 times for the 10 km/s impacts, and 1 to 2 times as much for the 20 km/s impacts. The amount completely vaporized in impacts at 20 km/s was 2.5 to 3 times as much on the 6400 km target as on the

1700 km target.

These values for the amount of melt and vapor produced are generally lower than those reported by O'Keefe and Ahrens [1977a]. For impacts at 7.5 km/s, they found that 1.6 impactor masses were melted, intermediate to our values of 0.7 to 1.5 projectile masses for impacts at 5 km/s and 2.25 to 2.7 impactor masses for impacts at 10 km/s. At 15 km/s, 9.5 impactor masses were melted, which is much higher than the 4.4 to 8.6 impactor masses we find for impacts at 20 km/s. They found no vaporization at 7.5 or 15 km/s, but 3.6 projectile masses were vaporized at an impact velocity of 30 km/s, while 42 impactor masses were melted. Our results show only minor amounts of vaporization at 5 and 10 km/s, and at most 1.1 impactor mass completely vaporized in the 20 km/s impacts. In our runs, it would be impossible to melt more than 4.55 projectile masses in the cases of the 60% impactor, and 16.7 projectile masses in the cases of the 40% impactor, so the highest velocity impacts are obviously not directly comparable in terms of melt production. The relatively large size of the impactor to the target may have some effect on the relative amounts of melt produced.

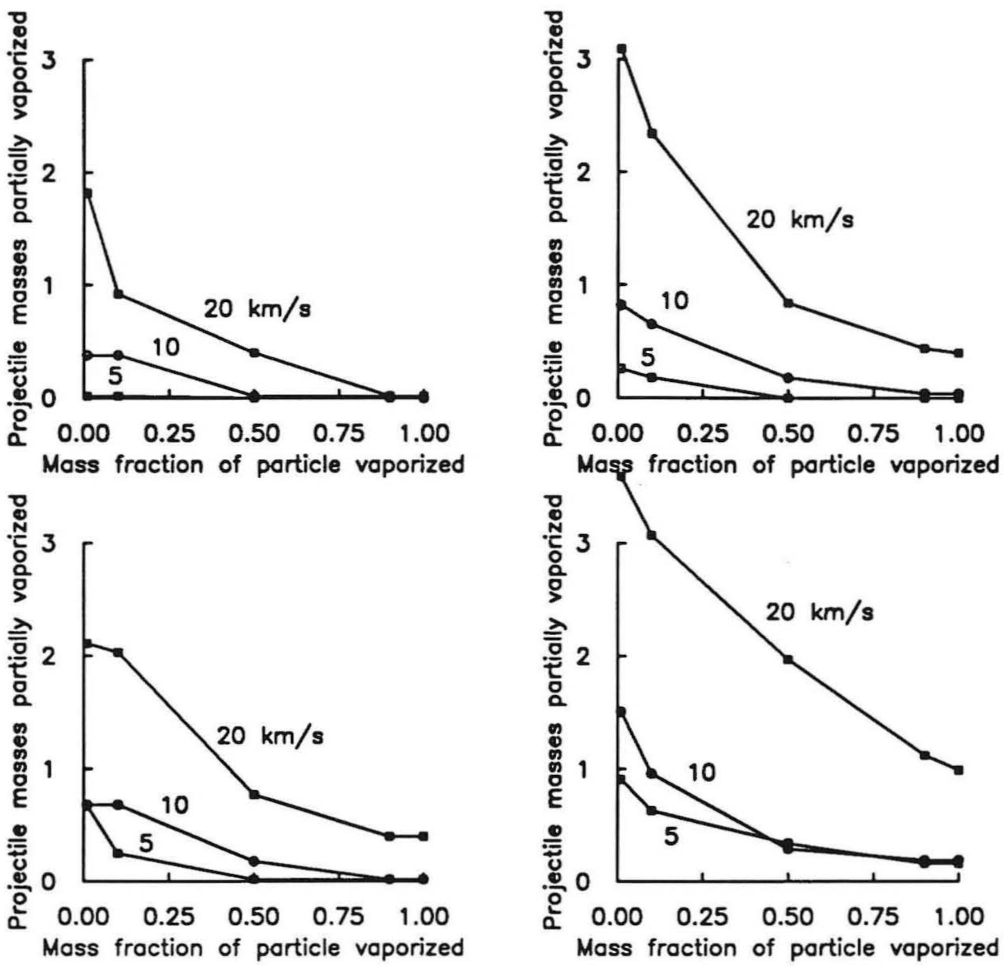

Figure 2.10: Cumulative vaporized mass fraction of target particles partially vaporized, in terms of projectile masses. Impacts on the 1700 km target are above, and on the 6400 km target below. Impacts with an impactor that is 40% by radius of the target are shown on the left, with the 60% impactor on the right.

Melting and vaporization for 1700 km targets 40% impactor					
Impact velocity	Impact angle	Melting		Vaporization	
		M_{melt}/M_{imp}	M_{melt}/M_{target}	M_{vap}/M_{imp}	M_{vap}/M_{target}
5 km/s	0°	0.67	0.04	0	0
	5°	0.61	0.03	0	0
	15°	0.45	0.03	0	0
	30°	0.43	0.03	0	0
	50°	0.36	0.02	0	0
	90°	0.25	0.02	0	0
10 km/s	0°	2.5	0.15	0	0
	5°	1.95	0.12	0	0
	15°	2.03	0.12	0	0
	30°	1.75	0.11	0	0
	50°	1.63	0.10	0	0
	90°	1.05	0.06	0	0
20 km/s	0°	8.6	0.51	0.02	0.001
	5°	8.8	0.53	0.02	0.001
	15°	8.0	0.48	0.11	0.007
	30°	6.5	0.39	0.09	0.005
	50°	4.0	0.24	0.14	0.009
	90°	2.6	0.15	0.07	0.004

Table 2.3: Mass melted and vaporized for impacts of the 40% impactor on the 1700 km radius target. M_{melt} and M_{vap} are the mass of target material melted or vaporized. The values are reported normalized to the mass of the impactor (M_{imp}) and the mass of the target (M_{target}).

Melting and vaporization for 1700 km targets 60% impactor					
Impact velocity	Impact angle	Melting		Vaporization	
		M_{melt}/M_{imp}	M_{melt}/M_{target}	M_{vap}/M_{imp}	M_{vap}/M_{target}
5 km/s	0°	0.91	0.20	0	0
	5°	0.83	0.18	0	0
	15°	0.88	0.19	0	0
	30°	0.75	0.17	0	0
	50°	0.61	0.14	0	0
	90°	0.47	0.10	0	0
10 km/s	0°	2.25	0.49	0.04	0.01
	5°	2.54	0.56	0.04	0.01
	15°	2.31	0.51	0.05	0.01
	30°	2.1	0.46	0.06	0.01
	50°	1.7	0.36	0.06	0.01
	90°	0.9	0.20	0.05	0.01
20 km/s	0°	4.5	1.00	0.4	0.09
	5°	4.5	0.99	0.25	0.06
	15°	4.5	0.99	0.32	0.07
	30°	4.5	0.98	0.35	0.08
	50°	3.68	0.81	0.28	0.06
	90°	2.36	0.52	0.14	0.03

Table 2.4: Mass melted and vaporized for impacts of the 60% impactor on the 1700 km radius target. M_{melt} and M_{vap} are the mass of target material melted or vaporized. The values are reported normalized to the mass of the impactor (M_{imp}) and the mass of the target (M_{target}).

Melting and vaporization for 6400 km targets 40% impactor					
Impact velocity	Impact angle	Melting		Vaporization	
		M_{melt}/M_{imp}	M_{melt}/M_{target}	M_{vap}/M_{imp}	M_{vap}/M_{target}
5 km/s	0°	1.01	0.061	0.02	0.001
	5°	0.94	0.056	0.02	0.001
	15°	1.03	0.062	0.02	0.001
	30°	0.83	0.050	0	0
	50°	0.87	0.052	0.03	0.002
	90°	0.79	0.048	0	0
10 km/s	0°	2.4	0.14	0.02	0.001
	5°	2.2	0.13	0.02	0.001
	15°	2.2	0.13	0.07	0.004
	30°	2.0	0.12	0.07	0.004
	50°	1.8	0.11	0.13	0.008
	90°	1.6	0.09	0.10	0.006
20 km/s	0°	5.5	0.33	0.4	0.024
	5°	5.4	0.33	0.42	0.025
	15°	4.7	0.31	0.38	0.023
	30°	4.1	0.25	0.43	0.023
	50°	3.2	0.19	0.29	0.017
	90°	1.9	0.11	0.22	0.013

Table 2.5: Mass melted and vaporized for impacts of the 40% impactor on the 6400 km radius target. M_{melt} and M_{vap} are the mass of target material melted or vaporized. The values are reported normalized to the mass of the impactor (M_{imp}) and the mass of the target (M_{target}).

<table>
<tr><th colspan="6">Melting and vaporization for 6400 km targets
60% impactor</th></tr>
<tr><th>Impact velocity</th><th>Impact angle</th><th colspan="2">Melting</th><th colspan="2">Vaporization</th></tr>
<tr><th></th><th></th><th>M_{melt}/M_{imp}</th><th>M_{melt}/M_{target}</th><th>M_{vap}/M_{imp}</th><th>M_{vap}/M_{target}</th></tr>
<tr><td>5 km/s</td><td>0°</td><td>1.51</td><td>0.33</td><td>0.16</td><td>0.036</td></tr>
<tr><td></td><td>5°</td><td>1.43</td><td>0.32</td><td>0.11</td><td>0.025</td></tr>
<tr><td></td><td>15°</td><td>1.48</td><td>0.33</td><td>0.07</td><td>0.015</td></tr>
<tr><td></td><td>30°</td><td>1.5</td><td>0.33</td><td>0.09</td><td>0.021</td></tr>
<tr><td></td><td>50°</td><td>1.5</td><td>0.33</td><td>0.07</td><td>0.017</td></tr>
<tr><td></td><td>90°</td><td>1.5</td><td>0.33</td><td>0.09</td><td>0.021</td></tr>
<tr><td>10 km/s</td><td>0°</td><td>2.7</td><td>0.60</td><td>0.19</td><td>0.04</td></tr>
<tr><td></td><td>5°</td><td>2.67</td><td>0.59</td><td>0.18</td><td>0.04</td></tr>
<tr><td></td><td>15°</td><td>2.62</td><td>0.58</td><td>0.17</td><td>0.04</td></tr>
<tr><td></td><td>30°</td><td>2.43</td><td>0.53</td><td>0.17</td><td>0.04</td></tr>
<tr><td></td><td>50°</td><td>2.18</td><td>0.48</td><td>0.16</td><td>0.04</td></tr>
<tr><td></td><td>90°</td><td>1.84</td><td>0.41</td><td>0.13</td><td>0.03</td></tr>
<tr><td>20 km/s</td><td>0°</td><td>4.4</td><td>0.97</td><td>0.99</td><td>0.22</td></tr>
<tr><td></td><td>5°</td><td>4.5</td><td>0.98</td><td>1.1</td><td>0.23</td></tr>
<tr><td></td><td>15°</td><td>4.4</td><td>0.96</td><td>1.1</td><td>0.23</td></tr>
<tr><td></td><td>30°</td><td>4.1</td><td>0.91</td><td>0.85</td><td>0.19</td></tr>
<tr><td></td><td>50°</td><td>3.5</td><td>0.77</td><td>0.66</td><td>0.14</td></tr>
<tr><td></td><td>90°</td><td>2.8</td><td>0.61</td><td>0.44</td><td>0.10</td></tr>
</table>

Table 2.6: Mass melted and vaporized for impacts of the 60% impactor on the 6400 km radius target. M_{melt} and M_{vap} are the mass of target material melted or vaporized. The values are reported normalized to the mass of the impactor (M_{imp}) and the mass of the target (M_{target}).

2.4.2 Pressure and internal energy

With the onset of the impact, material in the target experiences increased pressure, internal energy, and density as a result of the shock. This effect is transmitted into the interior of the target at successive time steps. For the largest impacts, the entire target feels some perturbation due to the collision with the impactor. For the smaller and lower velocity impacts, however, the far side of the target may not see any increase in these parameters.

Figures 2.11 - 2.14 show the variation of pressure with time as a function of the initial position of the particles relative to the point of impact. The points plotted represent the average pressure at all points at a given distance from the point of the target where the impact is first felt. Thus the figures for areas away from the impact point include the pressures at points that were initially in the interior and on the sides of the target. The curves representing the states at later times still consider the particles as a function of their initial position in the target, regardless of whether they have been ejected or remain in place. Due to the limited number of points along any path running directly through the target from the impact point, we have used this averaging to attempt to get a general overview of the internal state of the target during and after the target. Figure 2.11 shows the pressure after a 20 km/s normal impact with the 60% impactor in the 6400 km target. Pressure is plotted against the dimensionless time τ, where

$$\tau = tV_{imp}/R_{imp}, \tag{2.25}$$

and R_{imp} and V_{imp} are the impactor radius and impact velocity, and t is the elapsed time since the start of the run. The initial contact occurred at time τ=1.7. Before the impact (at τ=1), the target has a pressure profile that shows a higher pressure in the center of the body, and low pressure at the edges. As the shock moves through the target, the highest pressures are seen nearest the point of impact. Here the pressure increases until τ=3.5, and then falls back down. The points farther away from the initial point of impact feel the effects later; the pressure increase is lower at the opposite end of the body. Pressures remain high on the side of the target nearest the impact point even after the initial shock has passed into the body, since the impactor is still trying to move through the target, and material is compressed.

The arrow on the left side of the plot is the maximum pressure predicted by a one-dimensional impedance match solution for impacts of two anorthosite bodies at 20 km/s [Ahrens and O'Keefe 1977]. The predicted maximum pressure at the impact point is 5 Mbar, approximately half the actual maximum pressure of 10.9 Mbar. This is an example of one of the strongest impacts on the 6400 km target; for smaller impacts, little to no change in pressure is felt on the other side. Figure 2.12 shows the effects on pressure of impacts of the 40% impactor at 10 km/s and 0° and 90° on the 6400 km target. In the 0° case, the initial contact occurred at time τ=2.5; in the 90° case, it happened slightly later, at time τ=5. The impedance match solutions (marked by arrows on the axis) for impacts at 10 km/s predict a maximum pressure of 1.5 Mbar; these simulations yield maximum pressures of 3.8 Mbar for the normal impact and 2.9 Mbar for the 90° impact. The oblique impact does not bring the pressures in the target near the impact point to as high a state as the normal impact. At the later stages (τ=10), the particles nearest the impact point have been dislodged from the surface and melted, and hence have low pressures. This occurs more noticeably in the normal impact, as more material has been disrupted.

Two impacts with the 40% impactor at 15° on the 6400 km target at 5 and 10 km/s are shown in figure 2.13. In the 5 km/s case, impact started at time τ=2.5 and the maximum pressures nearest the impact point are over by τ=5. At late time (τ=17), the target has come back to nearly the same pressure profile as it had before the impact. The 20 km/s impact initiated at time τ=4.5. Again, the maximum effects are seen 2.5 time units later, at τ=7. The pressures near the impact point are

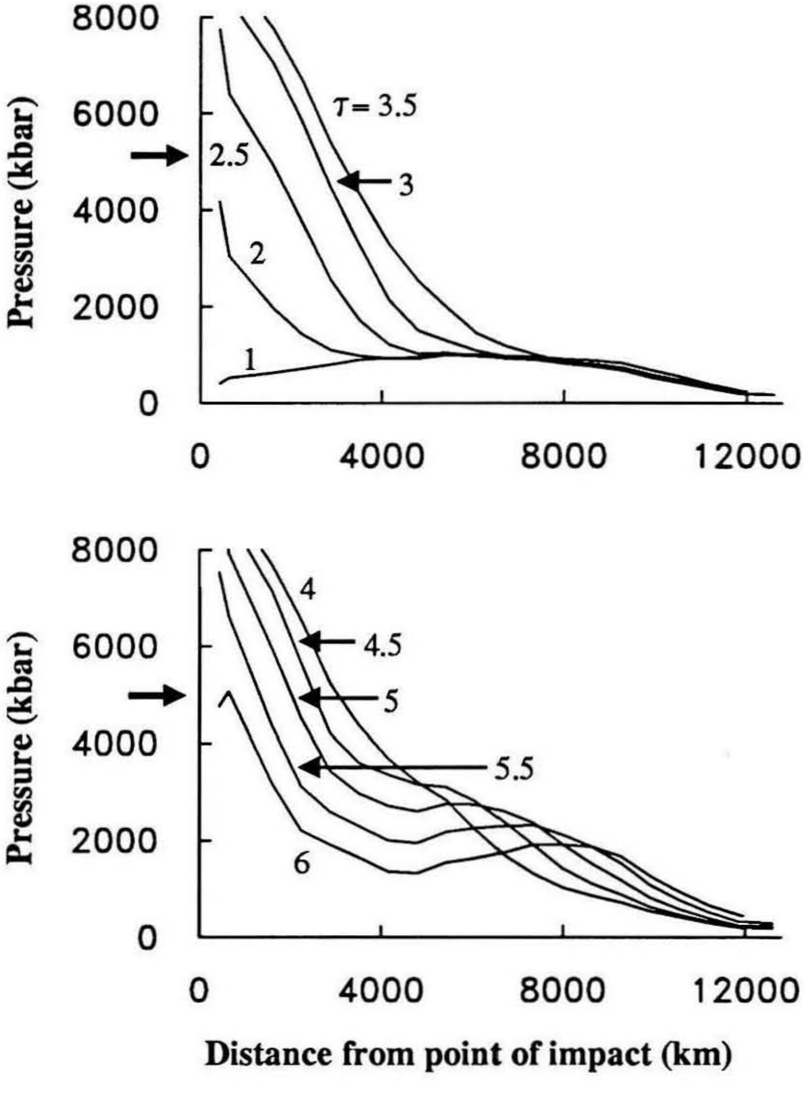

Figure 2.11: Pressure as a function of distance from the point of impact for an impact of the 60% impactor on the 6400 km target at 0° and 20 km/s. Curves are plotted to show the state at several values of the non-dimensional time τ. The pressure increases from the beginning of the run until the time τ=3.5 and then decays. The effects are felt farther back in the target at each timestep. The one-dimensional impedance solution for the maximum pressure in a 20 km/s impact is 5 Mbar, marked by an arrow on the pressure axis.

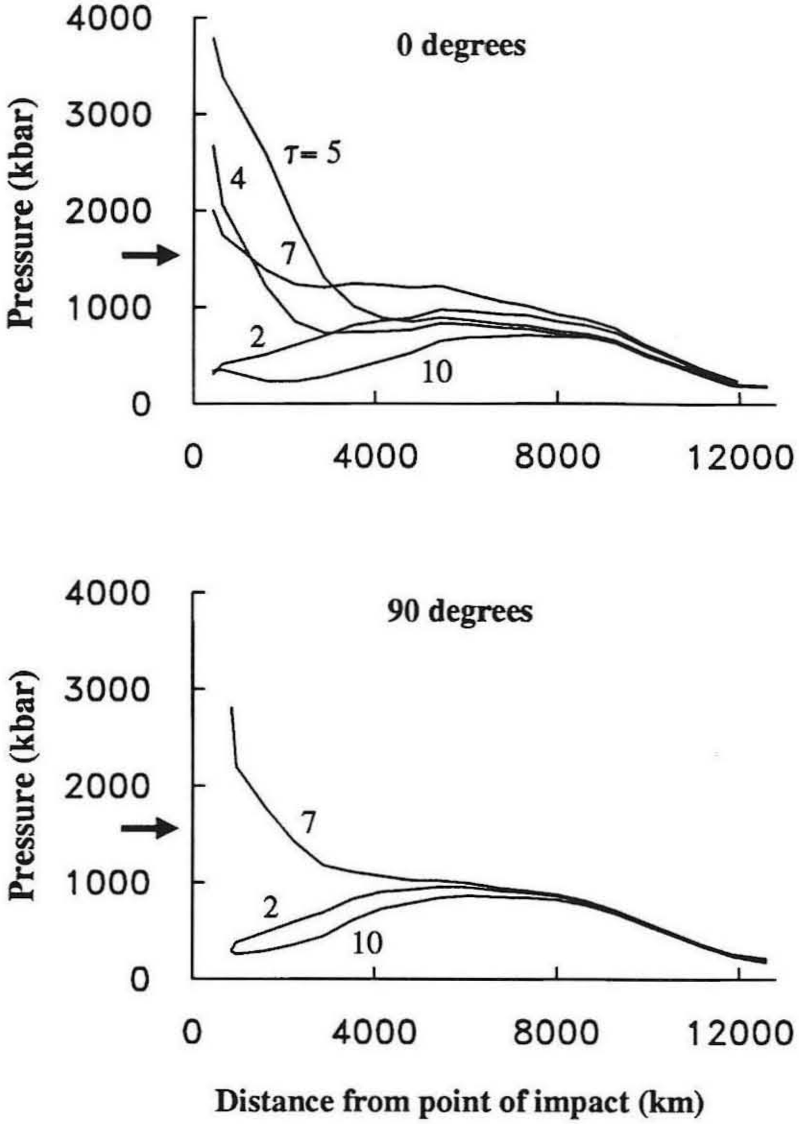

Figure 2.12: Pressure as a function of distance from the point of impact for impacts of the 40% impactor on the 6400 km target at 10 km/s and 0° and 90°. The impedance match solution for pressure in a 10 km/s impact is 1.5 Mbar, and is marked with an arrow on the pressure axis.

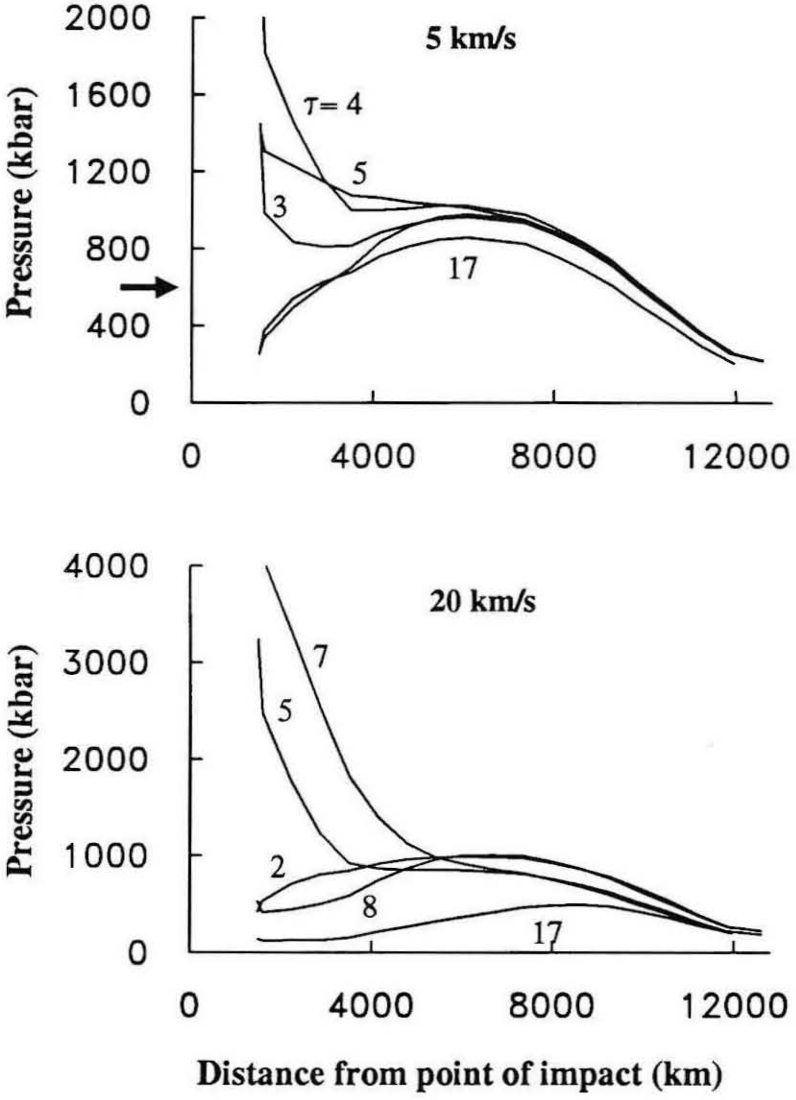

Figure 2.13: Pressure as a function of distance from the point of impact for impacts of the 40% impactor on the 6400 km target at 15° and 5 and 20 km/s. Note the difference in the vertical scales. The impedance match solution for pressure in a 5 km/s impact is 0.6 Mbar, and is marked with an arrow on the pressure axis of the upper graph. The corresponding pressure for the 20 km/s case is 5 Mbar.

higher than in the 5 km/s case by a factor of 2. The final (τ=17) pressure profile is significantly lower than the initial state, due to the fact that a large amount of material was dislodged and vaporized. This impact melted 33% of the target and vaporized 2.3%, compared with the 6% melted in the 5 km/s impact. The impedance match solution for the 5 km/s case is 0.6 Mbar. Our pressures are a factor of four higher in this case, with a maximum pressure of 2.3 Mbar.

Impacts on the 1700 km target do not generate pressures as high as those seen on the 6400 km target, but the pressure effects are seen throughout the target. Figure 2.14 shows the effects of impacts with the 60% impactor at 0° and 5 and 20 km/s. In both cases, the initial impact occurred at time τ=1.7. As is seen in the impacts on the larger targets, the pressure increase is felt farther back into the target at successive time steps. The 20 km/s impact has destroyed the target and completely melted it; the final (τ=80) pressure profile is nearly flat, and all pressures are low. The pressures are closer to the impedance match solutions of 0.6 and 5 Mbars for impacts at 5 and 20 km/s. We find pressures of 0.4 Mbar in the 5 km/s case, and 7.4 Mbar in the 20 km/s case.

The maximum values of pressure and density achieved during the simulations of impacts at 5° and 50° at all impact velocities are shown in figures 2.15 - 2.22. For impact on the 1700 km target with the 40% (figure 2.15) and the 60% (figure 2.16) impactor, we see that the pressure increase at distances away from the point of impact is greater with increasing impact velocity and at lower impact angles. Impacts at 5° and 5 and 10 km/s have similar maximum pressure profiles near the impact point and at more than one target radius away, but differ in the intermediate range, where higher pressures are seen after the 60% impact. The curves for 20 km/s impacts show a stronger difference. In the 50° impacts, the 5 and 10 km/s pressures near the impact point are larger by a factor of 2 in the 60% impacts; for the 20 km/s impacts, the pressures are higher still, three times as high as in the 40% impacts.

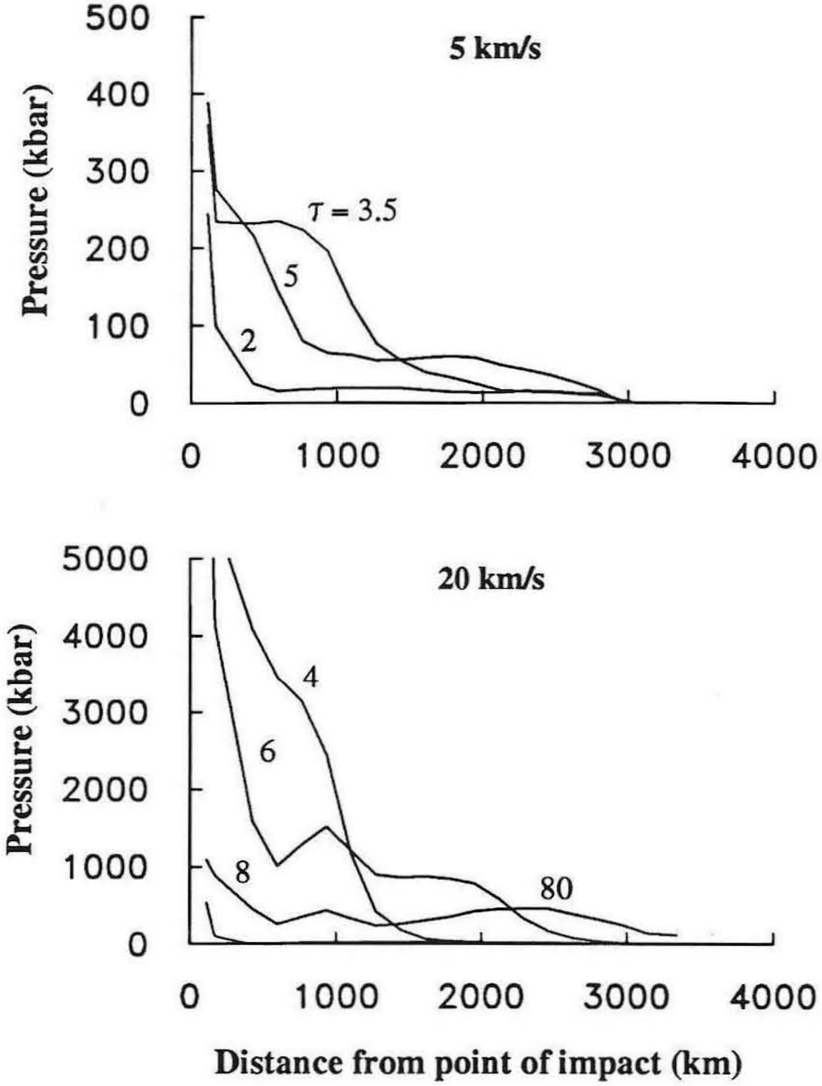

Figure 2.14: Pressure as a function of distance from the point of impact for impacts of the 60% impactor on the 1700 km target at 0° and 5 and 20 km/s. Note the difference in the vertical scales.

The difference between the 5° and 50° impacts with the larger impactor are much smaller; peak pressures are only 30% higher in the less oblique impact. With the 40% impactor, there is a more pronounced change in the maximum pressure near the impact point with impact angle: the 5° impacts yield pressures which are twice as high as the 50° impacts. The maximum pressures in our simulations on the 1700 km target were generally lower than the one-dimensional impedance solutions, indicated by the arrows. For the 5° impacts, the maximum pressures were 0.2, 1.3, and 3.8 Mbar, compared to the predicted values of 0.6, 1.5, and 5.0 Mbar. In the 50° case, the maximum pressures were 0.4, 0.9, and 3.2 Mbar.

The variation in the maximum internal energy with distance from the point of impact on the 1700 km target is shown in figures 2.17 for the 40% impactor and 2.18 for the 60% impactor. The difference between a near-normal impact (5°) and an oblique impact (50°) is much more noticeable in the case of the smaller impactor, where the 5° impact produces internal energies near the point of impact which are 1.5 times greater than those seen in the 60% impact. In contrast, the impacts with the 60% impactor seem to be insensitive to the impact angle in terms of the maximum energy seen at a given distance from the point of impact. Comparing the collisions with the different impactors, we see that the difference in maximum internal energy is dependent on the impact velocity: for the 5 km/s impacts, the maximum internal energy near the point of impact is 1.3 times higher in the 60% impactor case, 1.5 times higher for the 10 km/s impacts, and 2.2 times higher for the 20 km/s impacts.

Maximum pressure profiles for impact on the 6400 km target are shown in figures 2.19 and 2.20. For both of the impactors, the maximum pressures near the point of impact in the 5° impact are 20% greater than those seen in the 50° impact. For both impact angles, the impacts with the 60% impactor produce maximum pressures which are 50% greater for the 5 km/s impacts, 60% greater for the 10 km/s impacts, and 110% greater for the 20 km/s impacts. However, the increase in pressure as a

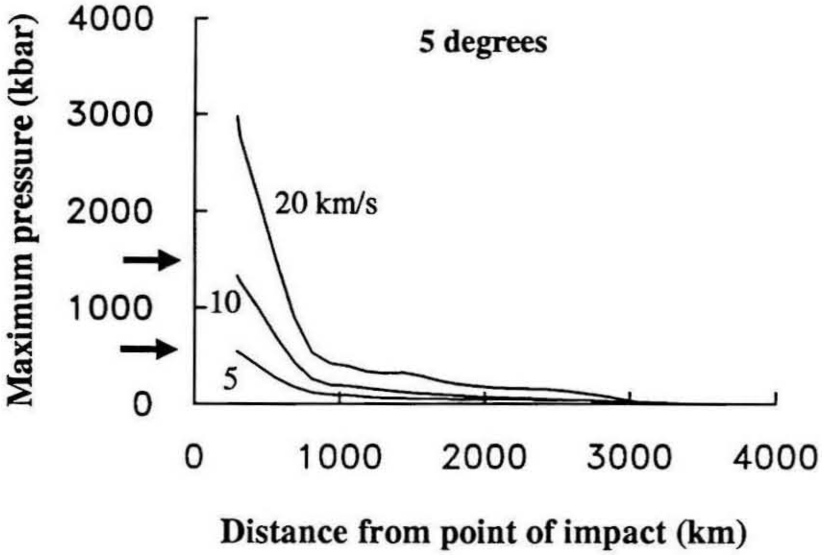

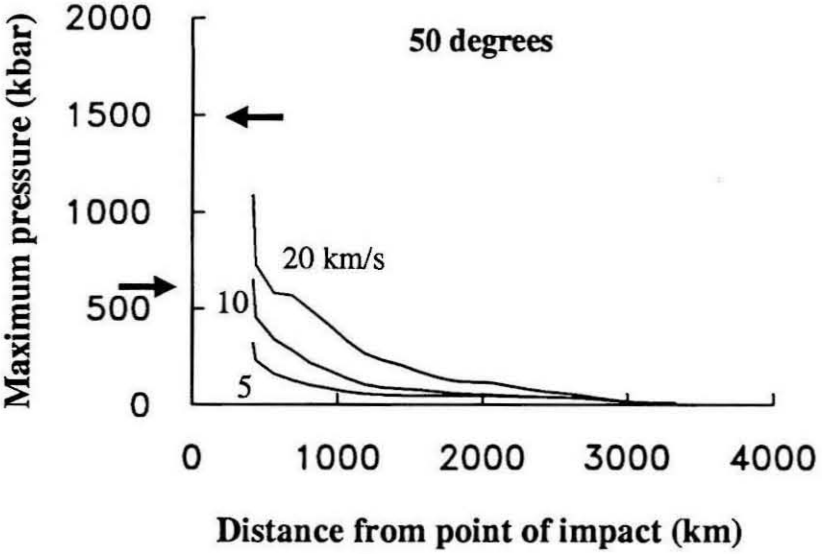

Figure 2.15: The maximum pressure felt as a function of distance from the point of impact for impacts of the 40% impactor on the 1700 km target at 5° and and 50° and 5, 10, and 20 km/s. The impedance match solutions for 5 and 10 km/s impacts are indicated with arrows. The impedance match solution for 20 km/s is 5 Mbar.

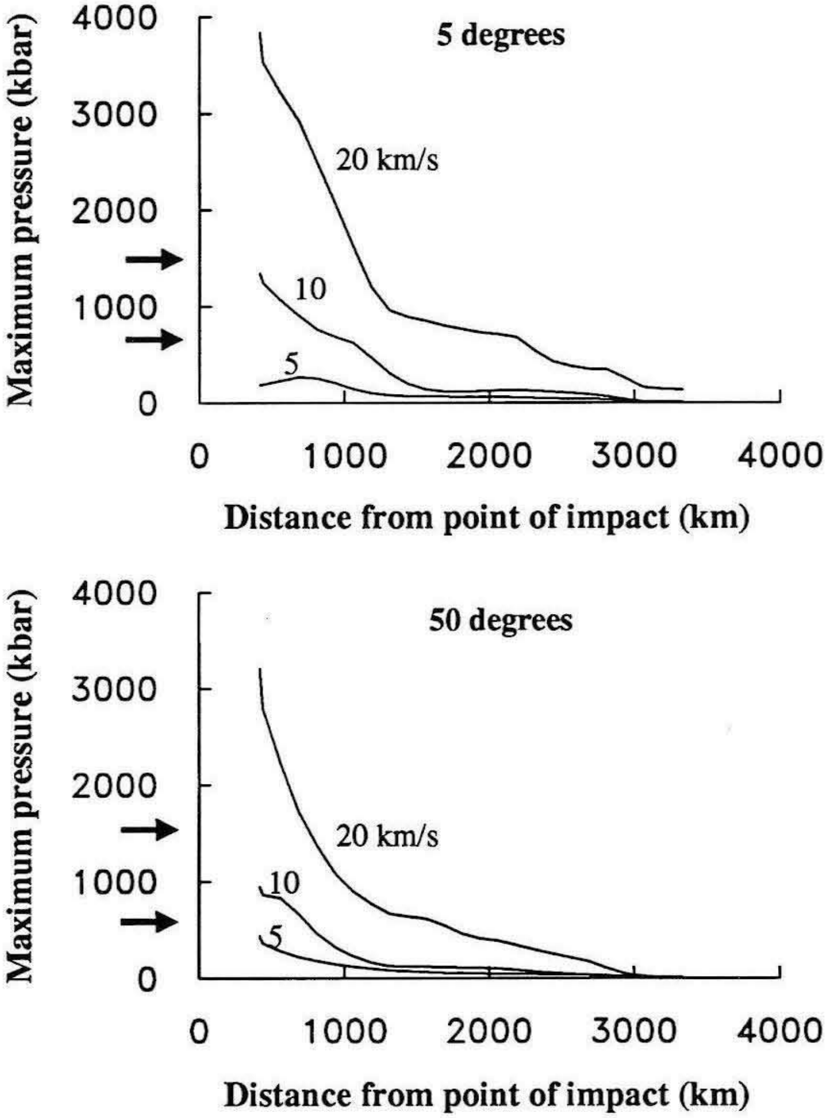

Figure 2.16: The maximum pressure felt as a function of distance from the point of impact for impacts of the 60% impactor on the 1700 km target at 5° and and 50° and 5, 10, and 20 km/s. Impedance match solutions designated by arrows.

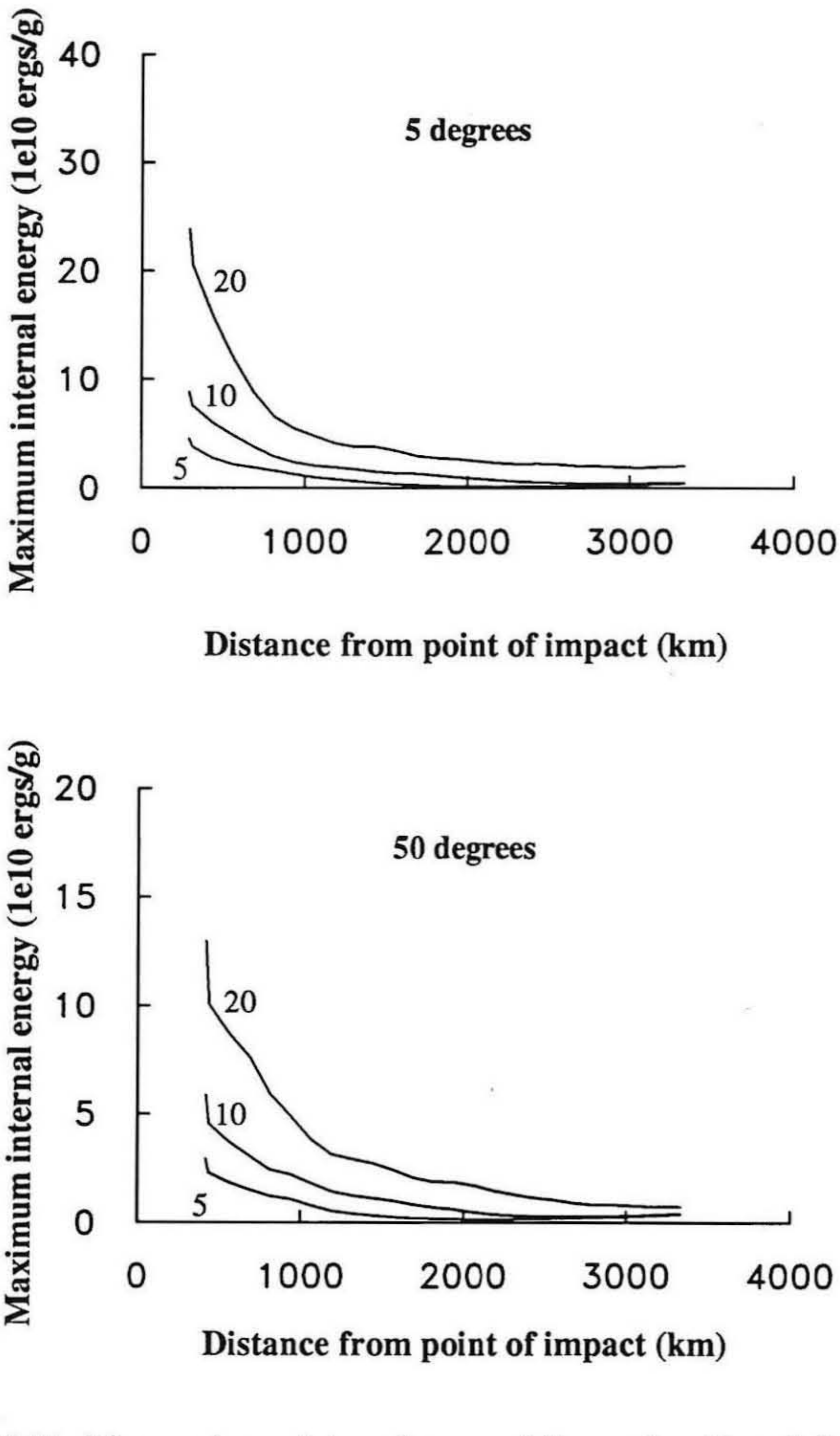

Figure 2.17: The maximum internal energy felt as a function of distance from the point of impact for impacts of the 40% impactor on the 1700 km target at 5° and and 50° and 5, 10, and 20 km/s.

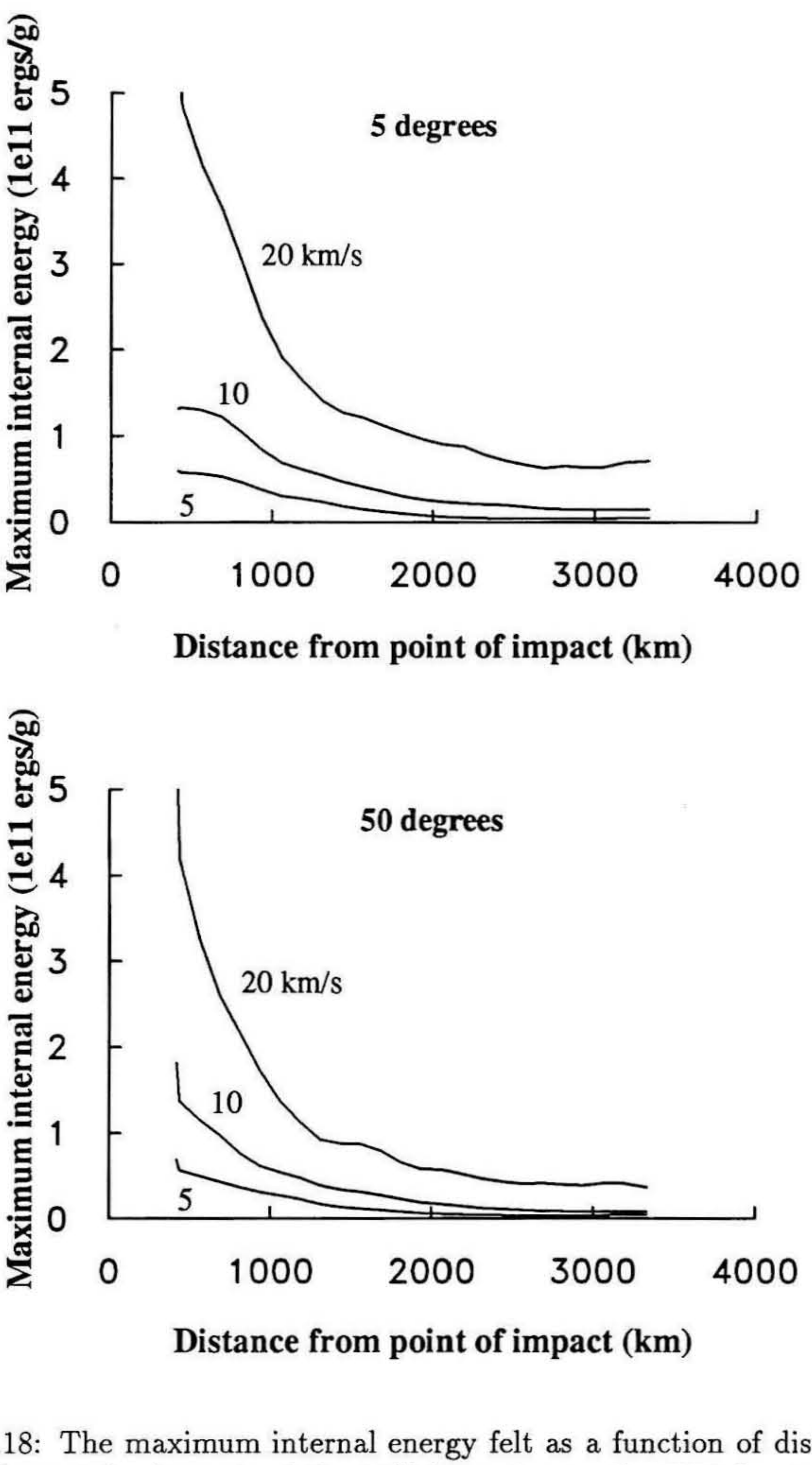

Figure 2.18: The maximum internal energy felt as a function of distance from the point of impact for impacts of the 60% impactor on the 1700 km target at 5° and and 50° and 5, 10, and 20 km/s.

function of impact velocity differs with impactor size. In the case of the 40% impactor, the 10 km/s impacts produce pressures which are 1.2 times greater than the 5 km/s impacts, and the impacts at 20 km/s produce pressures which are a factor of 1.5 times higher. For the 60% impactor, the changes are larger: 1.5 times for impacts at 10 km/s relative to 5 km/s, and 1.9 times for 20 km/s versus 10 km/s. The pressures seen in these simulations for impacts on the 6400 km target are higher than the impedance match solutions. The maximum pressures in the 5° impacts were 2.9, 3.9, and 5.8 Mbar in the 40% impacts, and 4.2, 6.4, and 12.1 Mbar in the 60% impacts for velocities of 5, 10, and 20 km/s. For the 50° impacts, the pressures were 2.6, 3.2, and 4.7 Mbar for the 40% impacts, and 3.7, 5.2, and 10.4 Mbar for the 60% impacts.

Comparing the maximum internal energy profiles for the 6400 km target (figures 2.21 and 2.22), we again see that a change in impact angle has less effect on the maximum internal energy at a given point than does a change in the impact velocity or impactor size. For the 40% impactor, the energies reached after an impact at 5° are 1.4 times as large as an impact at the same velocity at an impact angle of 50°, while changing the velocity from 10 to 20 km/s increases the maximum energy by a factor of two. For collisions with the larger impactor, the difference is somewhat greater. The 5° impacts only bring energies up to a level 1.2 times higher than that reached after the 50° impacts, while increasing the impact velocity from 10 to 20 km/s increases the energy by a factor of 2.5. The larger impactor shocks the target harder; the differences are larger than those seen in corresponding impacts on the 1700 km target. At 5°, the 5 km/s impacts with the 60% impactor bring the maximum energy near the point of impact to a level two times higher than the same impact with the 40% impactor. The 10 km/s case gives energies 2.8 times as high, and for the 20 km/s impacts, the factor is 3.2.

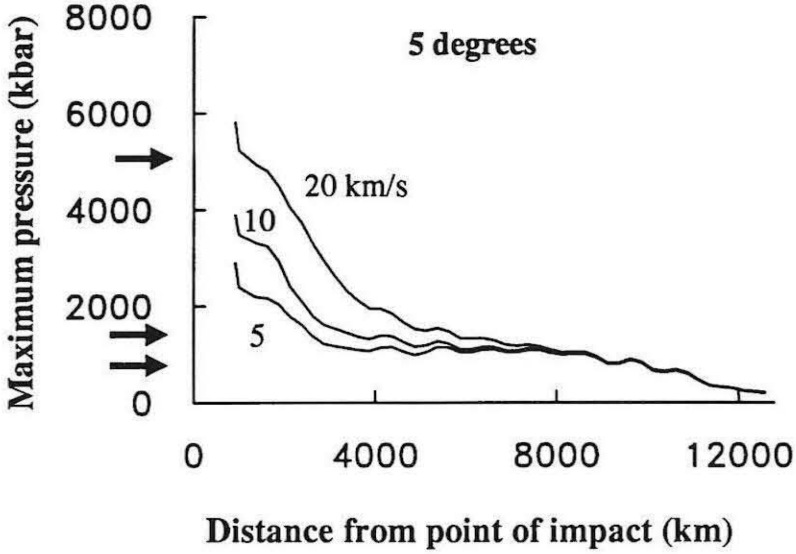

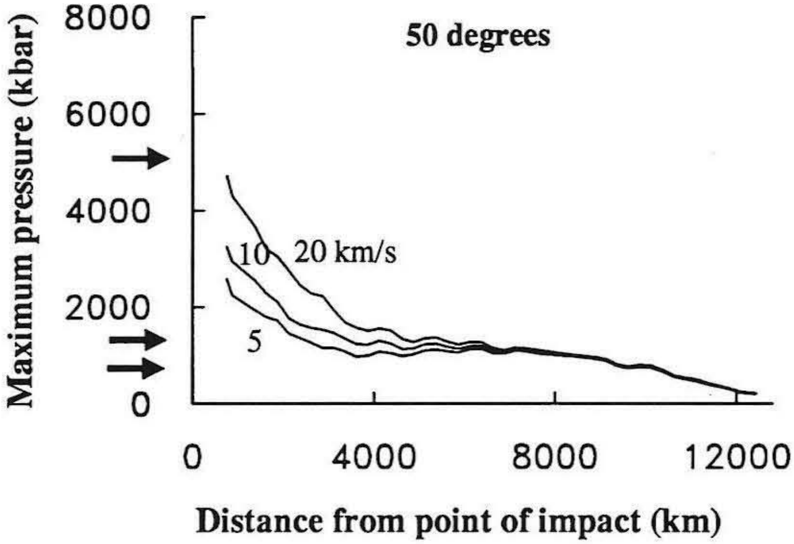

Figure 2.19: The maximum pressure felt as a function of distance from the point of impact for impacts of the 40% impactor on the 6400 km target at 5° and and 50° and 5, 10, and 20 km/s. The impedance match solutions are indicated by arrows.

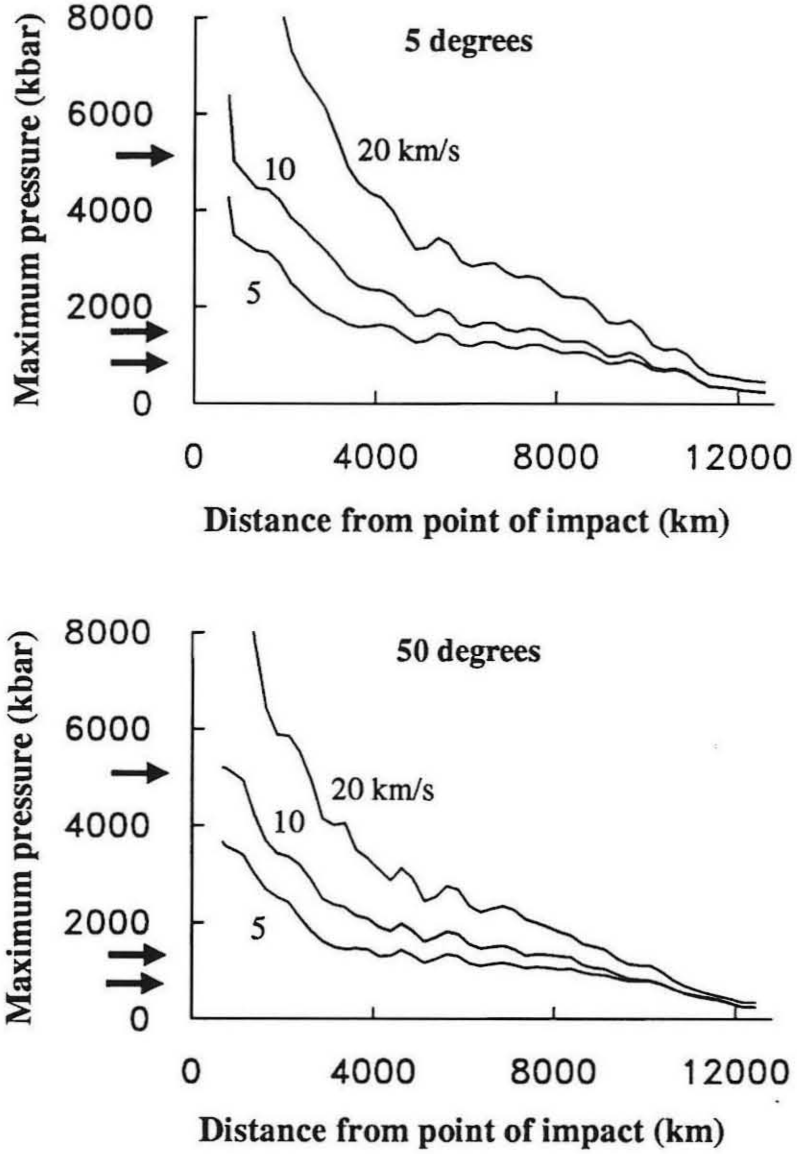

Figure 2.20: The maximum pressure felt as a function of distance from the point of impact for impacts of the 60% impactor on the 6400 km target at 5° and and 50° and 5, 10, and 20 km/s. The impedance match solutions are indicated by arrows.

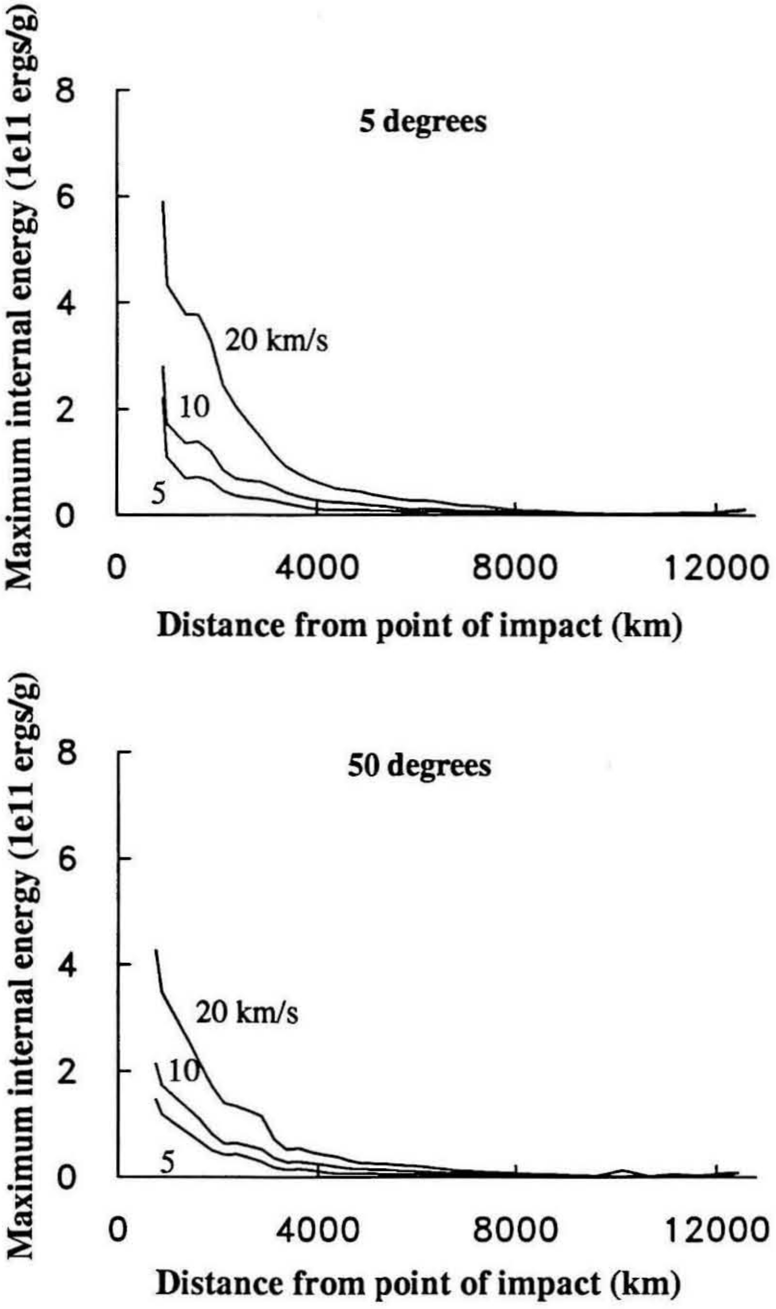

Figure 2.21: The maximum internal energy felt as a function of distance from the point of impact for impacts of the 40% impactor on the 6400 km target at 5° and and 50° and 5, 10, and 20 km/s.

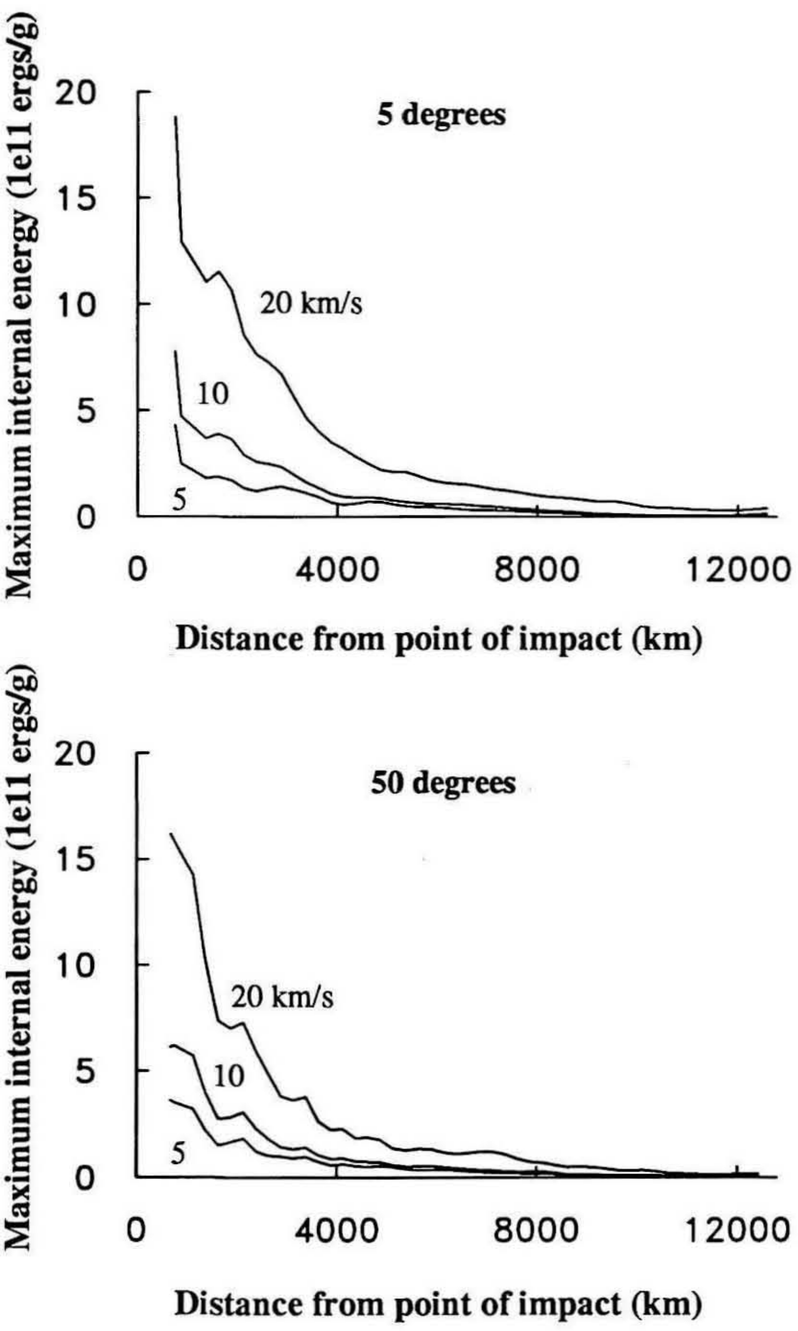

Figure 2.22: The maximum internal energy felt as a function of distance from the point of impact for impacts of the 60% impactor on the 6400 km target at 5° and and 50° and 5, 10, and 20 km/s.

2.4.3 Energy partitioning

Simulations of normal impacts onto semi-infinite bodies [O'Keefe and Ahrens 1977a, Ahrens et al. 1989] predict that very little of the kinetic energy of the impactor will remain after the impact; it will be partitioned into kinetic and internal energy of the target material, and internal energy of the impactor material. This is not surprising, since the path of the impactor is effectively blocked by the target. For more oblique impacts, and for cases where the size of the impactor relative to the target is large, one would expect that some of the initial kinetic energy would remain as kinetic energy in the portion of the impactor material that had not been accreted to the target body.

In our work, we find that the impact angle and velocity have a great effect on the final energy partitioning of the system. Tables 2.7 - 2.10 show the percent of the total kinetic and internal energy residing in the internal and kinetic energy of the target and impactor. For the 1700 km target, the impacts by the 60% impactor result in significantly more of the energy remaining in the kinetic energy of the impactor. For normal impacts at 5 km/s, 2.5% of the total internal and kinetic energy is taken up by the kinetic energy of the impactor in the 40% impacts, while the value is 17.4% for the 60% impacts. Generally, the amount of kinetic energy of the impactor as a fraction of the total internal and kinetic energy increases with impact angle, since much of the impactor material passes freely beyond the target. The most oblique impacts on the 1700 km target result in as much as 75% of the energy being accounted for by the impactor kinetic energy.

The impacts on the 6400 km targets show the same general trend of increasing amounts of kinetic energy remaining in the impactor particles after impact, but the amounts are in general lower than for the corresponding impacts on the 1700 km targets. For normal impacts, 2 to 20% of the total energy is in the kinetic energy of the impactor. For the most oblique impacts, the figure ranges from 6 to 57%.

Energy partitioning for 1700 km targets 40% impactor					
Impact velocity	Impact angle	Target		Impactor	
		IE	KE	IE	KE
5 km/s	0°	49.9	3.5	44.2	2.5
	5°	48.3	2.6	46.9	2.1
	15°	47.7	2.7	46.7	2.9
	50°	40.9	2.3	43.0	13.8
	90°	31.8	0.84	31.3	36.1
10 km/s	0°	44.0	5.3	42.5	8.2
	5°	41.3	4.9	45.3	8.5
	15°	39.9	4.9	44.4	10.9
	30°	36.8	5.2	40.3	17.7
	50°	28.1	4.6	31.5	35.8
	90°	17.9	1.7	20.2	60.2
20 km/s	0°	27.4	14.5	44.5	13.6
	5°	25.9	11.3	47.3	15.4
	15°	25.5	10.8	45.8	18.0
	30°	24.3	10.1	39.9	25.7
	50°	17.3	6.0	26.3	50.3
	90°	10.1	2.0	14.5	73.4

Table 2.7: Energy partitioning for impacts of the 40% impactor on the 1700 km radius target. IE and KE refer to the internal and kinetic energy, respectively, of the particles comprising the target or impactor. The values are listed as the percent of the total internal and kinetic energy, which, at the start of the run, is comprised entirely of the kinetic energy of the impactor.

Energy partitioning for 1700 km targets 60% impactor					
Impact velocity	Impact angle	Target		Impactor	
		IE	KE	IE	KE
5 km/s	0°	50.0	11.2	21.4	17.4
	5°	49.3	10.0	22.4	18.3
	15°	51.4	9.6	20.5	18.6
	30°	45.6	7.8	18.8	27.8
	50°	39.3	7.2	16.4	37.1
	90°	30.6	3.5	14.9	51
10 km/s	0°	32.9	29.2	13.7	24.2
	5°	33.4	26.4	16.2	24.0
	15°	33.1	24.9	15.6	26.4
	30°	30.7	20.4	13.7	35.2
	50°	25.0	14.3	11.3	49.3
	90°	16.7	8.1	8.0	67.1
20 km/s	0°	18.8	39.7	11.9	29.6
	5°	18.2	33.5	14.2	34.0
	15°	18.1	32.4	13.6	36.0
	30°	17.6	30.8	11.5	40.1
	50°	14.8	20.4	9.2	55.6
	90°	10.3	9.0	5.4	75.3

Table 2.8: Energy partitioning for impacts of the 60% impactor on the 1700 km radius target. IE and KE refer to internal and kinetic energy.

Energy partitioning for 6400 km targets
40% impactor

Impact velocity	Impact angle	Target		Impactor	
		IE	KE	IE	KE
5 km/s	0°	32.7	1.7	63.7	1.9
	5°	31.8	1.6	64.6	2.1
	15°	32.0	1.6	64.2	2.1
	30°	30.0	1.8	65.1	3.0
	50°	26.9	1.8	67.2	4.1
	90°	23.3	1.7	68.8	6.1
10 km/s	0°	16.7	9.2	51.8	22.2
	5°	16.2	8.7	52.2	22.8
	15°	8.1	5	50.5	25.5
	30°	15.1	7.2	46.5	31.2
	50°	11.2	4.6	36.9	47.3
	90°	5.9	2.5	24.9	66.7
20 km/s	0°	13.6	10.3	55.4	20.6
	5°	13.3	11.9	58.7	16.0
	15°	12.9	11.4	57.6	18.2
	30°	12.0	10.7	53.3	24.1
	50°	9.5	8.1	45.7	36.7
	90°	5.8	4.9	32.2	57.1

Table 2.9: Energy partitioning for impacts of the 40% impactor on the 6400 km radius target. IE and KE refer to internal and kinetic energy.

Energy partitioning for 6400 km targets 60% impactor					
Impact velocity	Impact angle	Target		Impactor	
		IE	KE	IE	KE
5 km/s	0°	33.9	26.3	35.7	4.2
	5°	31.9	26.0	37.3	4.9
	15°	32.0	25.8	37.4	4.8
	30°	32.1	25.0	38.1	4.7
	50°	32.4	24.5	38.5	4.6
	90°	31.8	21.7	40.2	6.3
10 km/s	0°	23.9	28.5	38.9	8.6
	5°	23.5	26.8	40.5	9.2
	15°	23.0	25.4	40.5	11
	30°	21.9	24.1	40.0	14.1
	50°	20.8	20.3	37.0	21.9
	90°	18.1	15.4	35.0	31.5
20 km/s	0°	11.5	41.7	26.6	20.2
	5°	11.6	40.6	27.0	20.7
	15°	11.5	39.7	26.7	22.2
	30°	10.8	37.1	25.0	27.1
	50°	8.8	28.1	23.0	40.1
	90°	6.8	20.5	19.6	53.1

Table 2.10: Energy partitioning for impacts of the 60% impactor on the 6400 km radius target. IE and KE refer to internal and kinetic energy.

As the late stage kinetic energy of the impactor rises as a function of the impact angle, the other components fall. For 20 km/s impacts, the kinetic energy of the target falls from 10 to 40% at 0° to 2 to 20% for 90° impacts. The internal energy of the target falls from 12 to 27% at 0° to 6 to 10% at 90°, and the internal energy of the impactor falls from 12 to 55% at 0° to 5 to 32% at 90°. As the impact velocity increases, the amount of energy in the internal energy of the target and impactor both decrease, and the kinetic energies increase.

The partitioning of energy as a function of time may be shown graphically, as in figures 2.23 - 2.25. Figure 2.23 shows the energy partitioning for impacts at 15° and 90° and 20 km/s of the 60% impactor on the 6400 km target. The energy values are plotted against the normalized time τ described in equation 2.25. The impact at 15° shows the kinetic energy of the impactor comprising a much smaller percentage of the total internal and kinetic energy than in the 90° impact (22% versus 53%). When one considers the trajectory plots shown in figures A.1 - A.54, where we see that much of the impactor material travels past the target in the oblique impacts, this is not surprising.

Another example of energy partitioning is shown in figure 2.24, which gives the results of impacts on the 1700 km target at 5 km/s with the 60% impactor at angles of 15° and 90°. As before, the 90° case has much more energy in the kinetic energy of the impactor (51% versus 19%). These results differ from those on the 6400 km target, however, in that the internal energy of the target (and thus the degree of melting and vaporization) is a greater proportion of the total (30 to 50% as opposed to 30%). The kinetic energy of the target material is quite small, only 3 to 8%. Figure 2.25 shows two cases of impact at 15° of the 40% impactor on the 1700 km target, at 5 and 20 km/s to illustrate the effect of increasing the impact velocity. In the 5 km/s case, 3% of the initial energy is left in the kinetic energy of the impactor after the impact. The internal energy of the target and the impactor make up 94% of

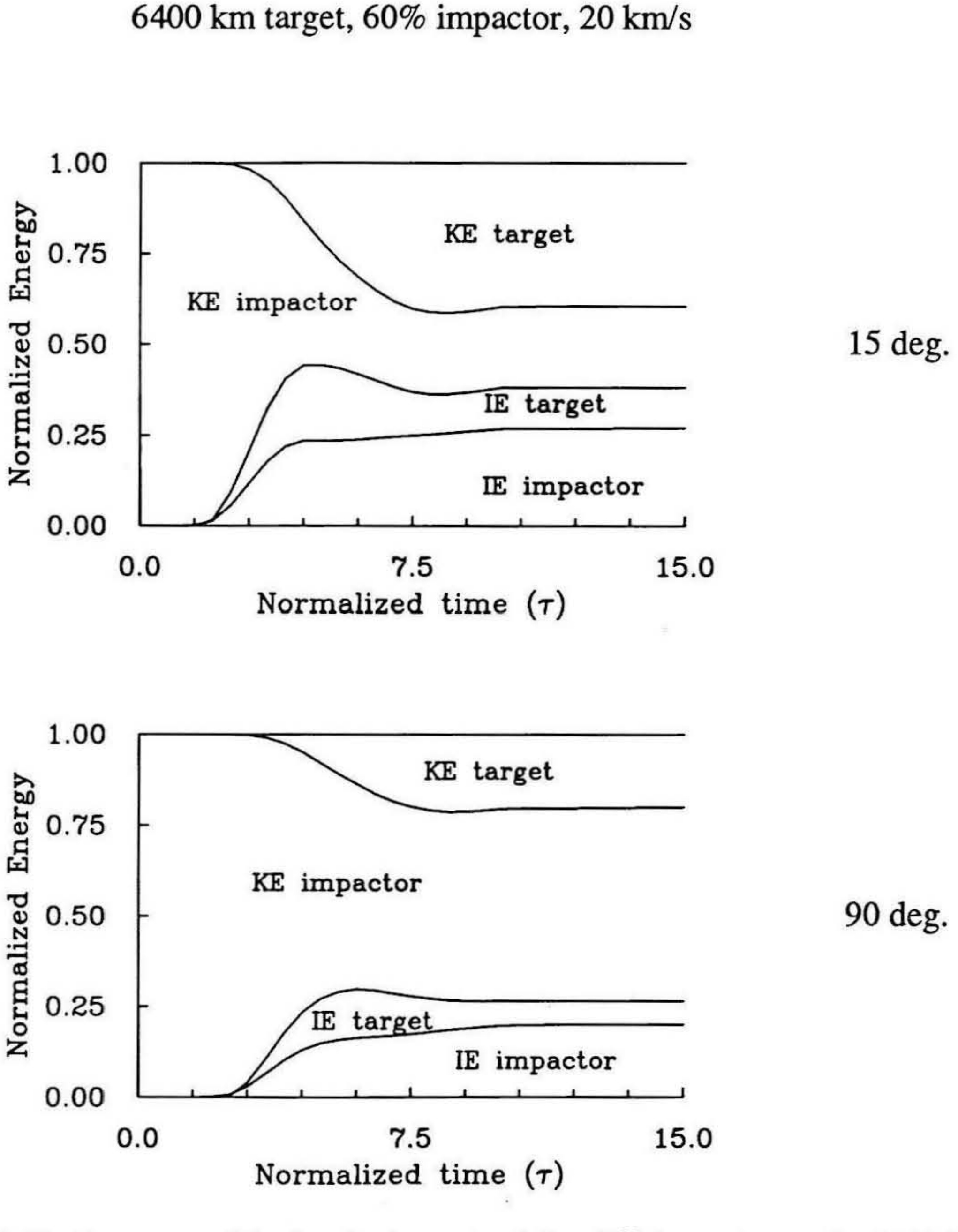

Figure 2.23: Energy partitioning for impacts of the 60% impactor on the 6400 km target at 20 km/s and 15° and 90°.

the total internal and kinetic energy. At an impact velocity of 20 km/s, the internal energies of the two bodies take up 70% of the total, and the kinetic energy of the impactor material is 18% of the total.

Figure 2.26 summarizes the partitioning of energy at the end of the runs for impacts at 0° and 90°. The portion of the energy taken up by the kinetic energy of the target and impactor material increases with impact velocity from 20% at 5 km/s to 40% at 20 km/s in the normal impacts, and from 30% to 70% in the oblique impacts. We can compare these results with those of Ahrens et al. [1989], as shown in figure 2.27 for impacts onto a half space. The amount of energy taken up by the target internal and kinetic energy varies from 85% in the 7.5 km/s case to 95% in the 45 km/s case. The amount of kinetic energy of the impactor material is negligible, since the infinite size of the target restricts the forward motion of any impactor material. Pongracic [1988] finds 90% of the system energy partitioned into the internal and kinetic energy of the target after a normal impact at 25 km/s. For more oblique impacts, the amount of energy in the kinetic energy of the impactor increases from 4% at normal impact to 78% for an impact angle of 70°.

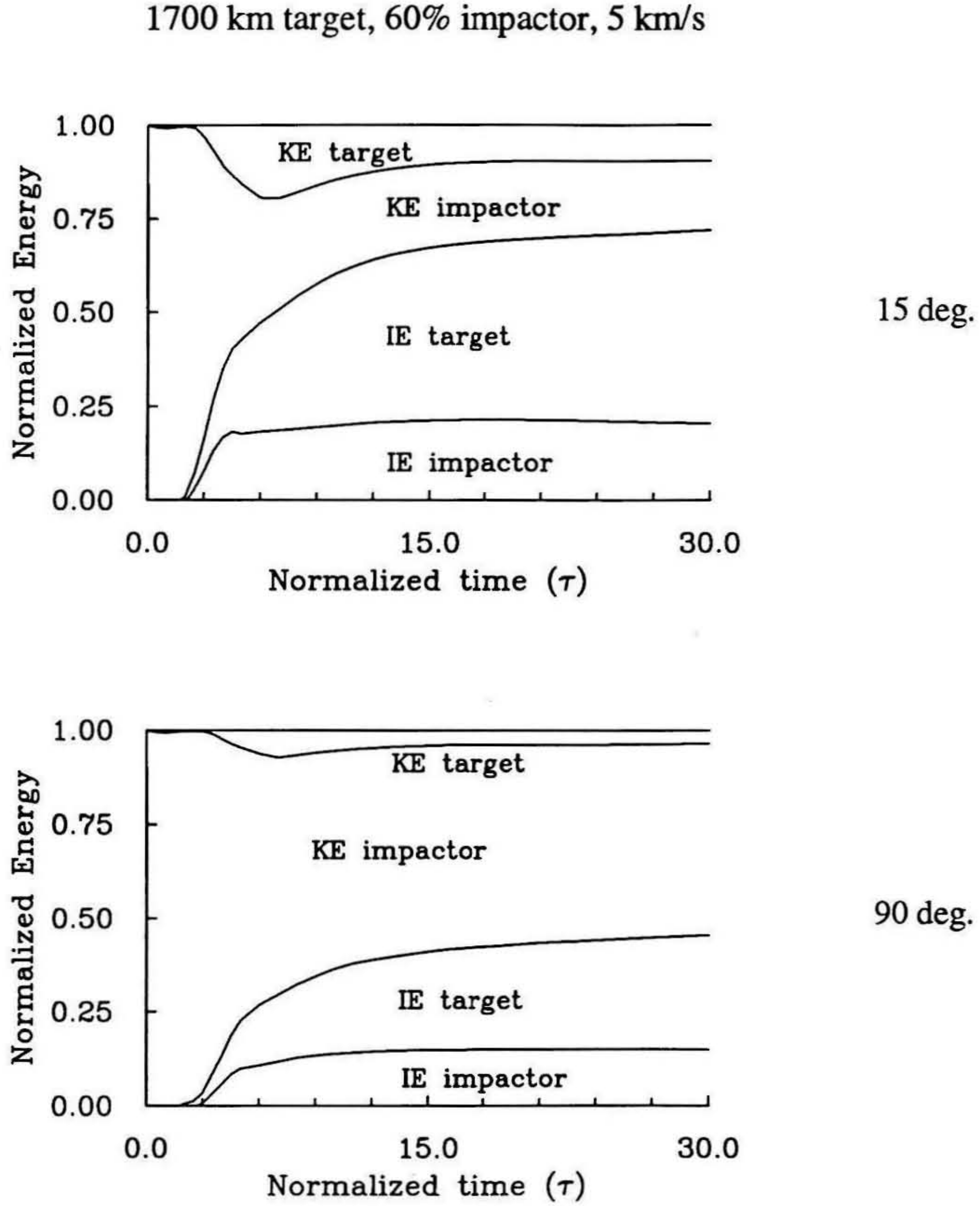

Figure 2.24: Energy partitioning for impacts of the 60% impactor on the 1700 km target at 5 km/s and 15° and 90°.

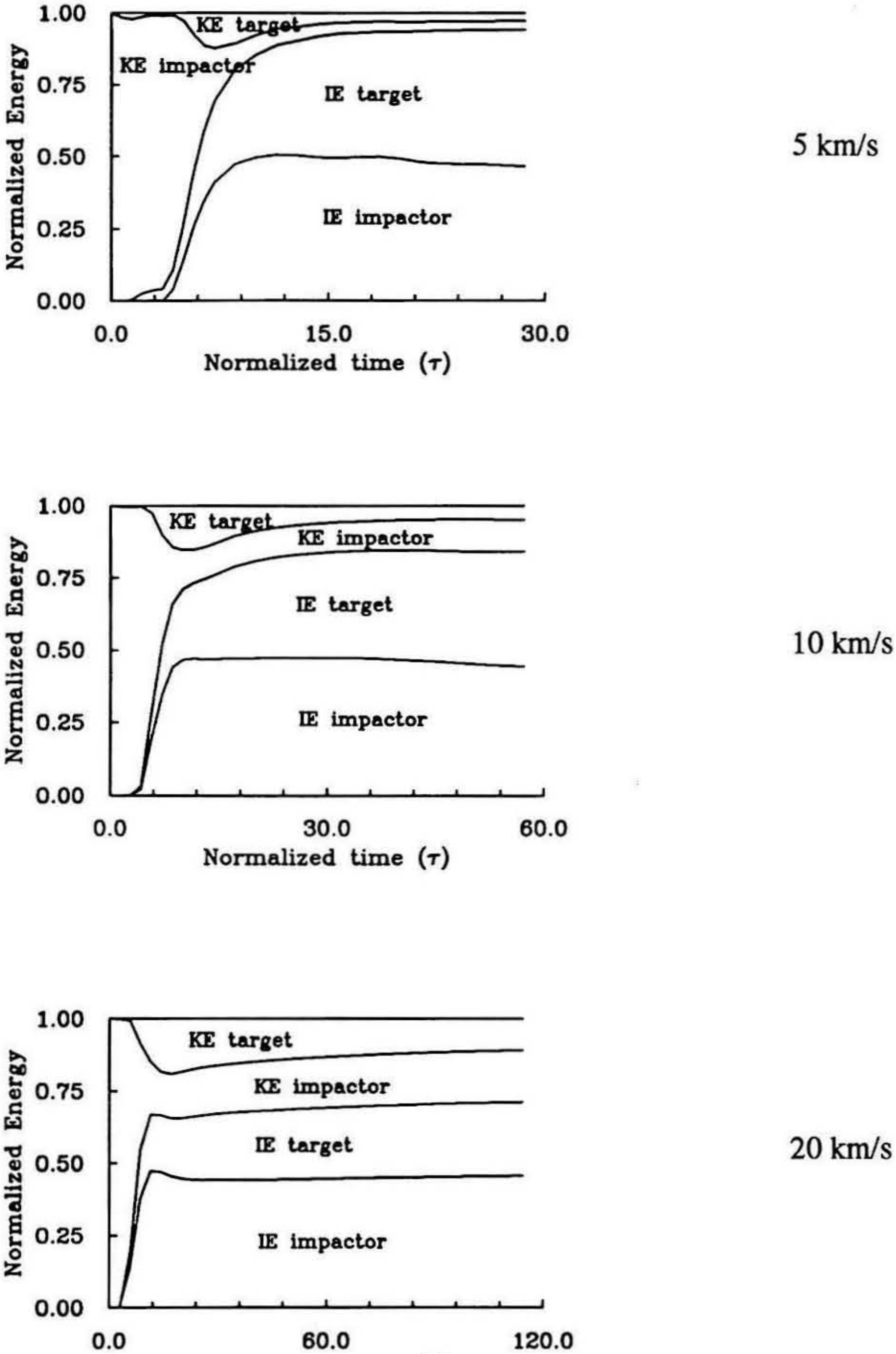

Figure 2.25: Energy partitioning for impacts of the 40% impactor on the 1700 km target at 15° and 5, 10, and 20 km/s.

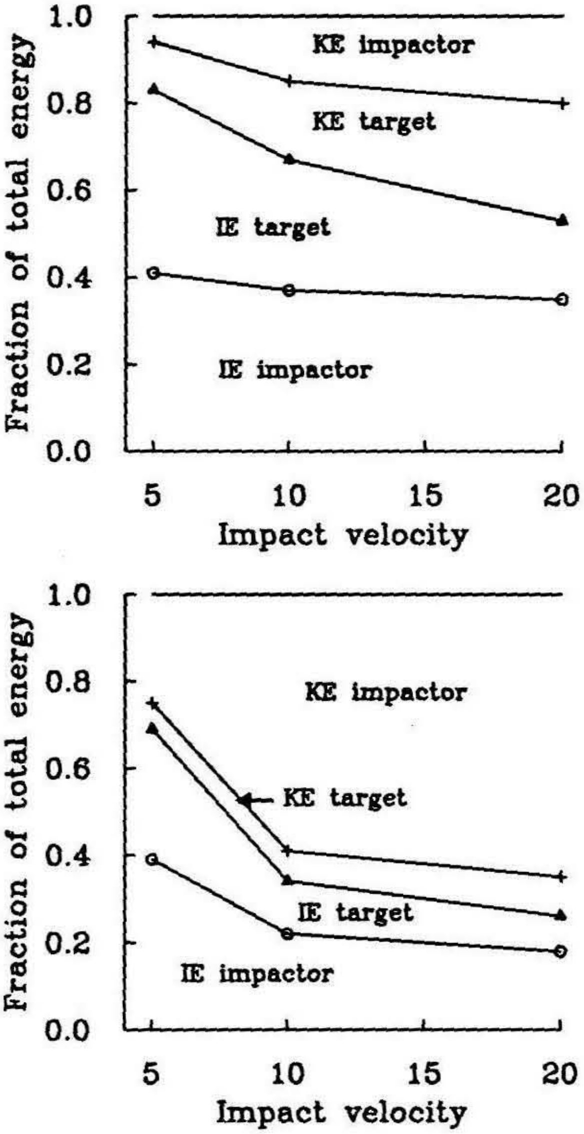

Figure 2.26: Average energy partitioning for all impacts at 0° (top) and 90° (bottom).

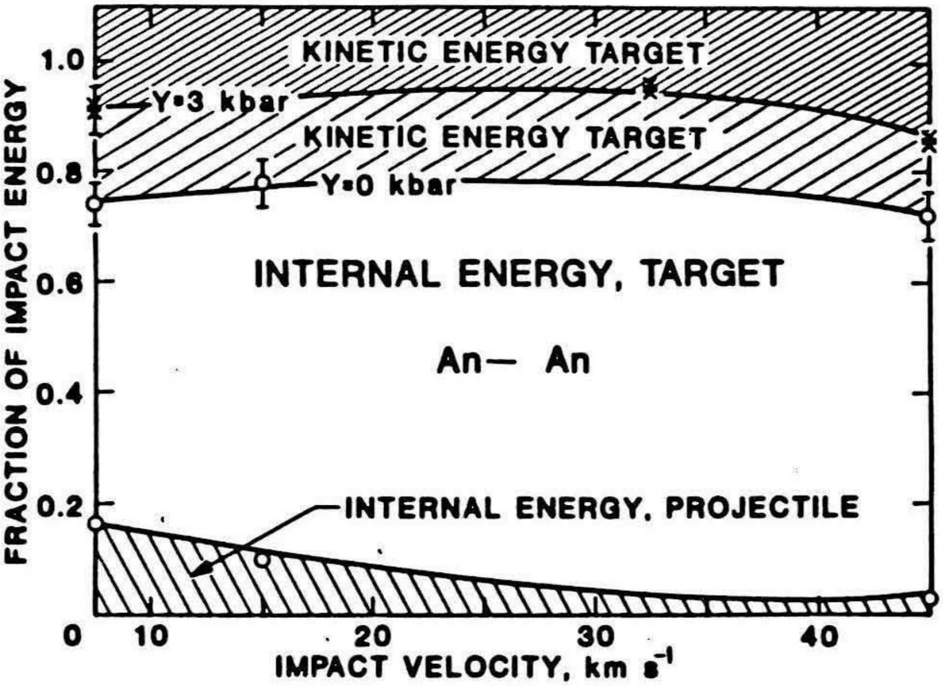

Figure 2.27: Energy partitioning for impacts from 5 to 45 km/s from the work of O'Keefe and Ahrens [1977a].

2.4.4 Ejecta production

The ejecta production for these impacts is shown in tables 2.11 - 2.13. Here, ejecta is classified as the material which is dislodged from the target at velocities higher than the escape velocity, and includes material scattered both forward and backward relative to the impact velocity. Material which is removed from its original position but is not traveling fast enough to escape the target body's gravitational field is not counted. The 1700 km targets, which have an escape velocity at their surface of 2.4 km/s, lose much more of their material than the larger targets do. Impacts at 5 km/s on the smaller targets eject only minor amounts of material in the case of the 40% impactor (0.3 to 0.4% of the target mass, or 0.05 to 0.07 projectile masses), and impacts with the 60% impactor are not much more effective at removing material, ejecting only 2 to 3% of the target, or 0.07 to 0.12 projectile masses. The higher velocity impacts, however, are quite destructive. The 60% impactor, colliding with the target at 20 km/s, completely destroys the target for all but the most oblique impacts. The smaller impactor is, of course, less destructive; a 20 km/s normal impact is still sufficient to cause more than half of the original target material to be ejected. More oblique impacts are much less effective at producing ejecta, and yield only a third to a tenth as much ejecta.

For the 6400 km target, we find that the 40% impactor is too small to produce ejecta, even after the 20 km/s impacts. The 60% impactor, however, launches a small amount of target material (0.3 to 1.3% of its mass, or 0.02 to 0.06 projectile masses) as a result of a 10 km/s impact, and 5 to 9% of its mass (0.2 to 0.4 projectile masses) after a 20 km/s impact. The ejected particles, for both the 1700 and 6400 km targets, are generally the most highly shocked of the target particles, and are the particles which were originally situated near the point of impact.

We can plot the amount of ejecta produced as a function of the escape velocity (which is essentially the same as plotting against target size) to compare with the

Ejecta production for 1700 km targets 40% impactor					
		Mass of ejecta			
Impact velocity	Impact angle	Total ejected		Scattered back	
		M_{ej}/M_{imp}	M_{ej}/M_{target}	M_{ej}/M_{imp}	M_{ej}/M_{target}
5 km/s	0°	0	0	0	0
	5°	0	0	0	0
	15°	0.07	0.0043	0	0
	30°	0	0	0	0
	50°	0.05	0.0032	0	0
	90°	0	0	0	0
10 km/s	0°	0.38	0.023	0.38	0.023
	5°	0.30	0.018	0.31	0.018
	15°	0.28	0.017	0.2	0.012
	30°	0.27	0.016	0.22	0.013
	50°	0.45	0.027	0.25	0.015
	90°	0.14	0.009	0.09	0.005
20 km/s	0°	8.8	0.53	7.6	0.456
	5°	5.3	0.32	4.8	0.286
	15°	4.0	0.24	2.95	0.177
	30°	1.4	0.084	1.17	0.07
	50°	1.1	0.066	0.54	0.032
	90°	0.67	0.04	0.38	0.023

Table 2.11: Ejecta production for impacts of the 40% impactor on the 1700 km radius target. The mass of ejecta produced by the impact (M_{ej}) is listed normalized to the impactor mass (M_{imp}) and the target mass (M_{target}). Ejecta labeled "Scattered back" is the material which has a trajectory that takes it back above the plane tangent to the target at the point of impact.

Ejecta production for 1700 km targets 60% impactor					
		Mass of ejecta			
		Total ejected		Scattered back	
Impact velocity	Impact angle	M_{ej}/M_{imp}	M_{ej}/M_{target}	M_{ej}/M_{imp}	M_{ej}/M_{target}
5 km/s	0°	0.12	0.026	0	0
	5°	0.14	0.031	0.1	0.002
	15°	0.15	0.032	0.1	0.002
	30°	0.08	0.017	0	0
	50°	0.08	0.018	0.1	0.002
	90°	0.07	0.016	0	0
10 km/s	0°	1.97	0.41	0.57	0.125
	5°	1.7	0.37	1.7	0.373
	15°	1.6	0.35	0.62	0.136
	30°	1.2	0.26	0.51	0.112
	50°	0.72	0.16	0.20	0.044
	90°	0.30	0.067	0.03	0.006
20 km/s	0°	4.45	0.98	2.25	0.495
	5°	4.48	0.99	1.8	0.39
	15°	4.44	0.98	1.85	0.408
	30°	4.51	0.99	2.18	0.479
	50°	4.31	0.95	2.46	0.54
	90°	1.4	0.31	0.63	0.14

Table 2.12: Ejecta production for impacts of the 60% impactor on the 1700 km radius target. The mass of ejecta produced by the impact (M_{ej}) is listed normalized to the impactor mass (M_{imp}) and the target mass (M_{target}).

Ejecta production for 6400 km targets 60% impactor					
		Mass of ejecta			
Impact velocity	Impact angle	Total ejected		Scattered back	
		M_{ej}/M_{imp}	M_{ej}/M_{target}	M_{ej}/M_{imp}	M_{ej}/M_{target}
5 km/s	0°	0	0	0	0
	5°	0	0	0	0
	15°	0	0	0	0
	30°	0	0	0	0
	50°	0	0	0	0
	90°	0	0	0	0
10 km/s	0°	0.06	0.013	0.06	0.013
	5°	0.02	0.005	0.02	0.005
	15°	0.03	0.006	0.03 0.006	
	30°	0.05	0.009	0.03	0.008
	50°	0.03	0.006	0.01	0.002
	90°	0.02	0.003	0.02	0.004
20 km/s	0°	0.39	0.086	0.39	0.086
	5°	0.38	0.084	0.34	0.43
	15°	0.38	0.084	0.34	0.075
	30°	0.33	0.072	0.20	0.043
	50°	0.29	0.063	0.08	0.018
	90°	0.23	0.051	0.07	0.16

Table 2.13: Ejecta production for impacts of the 60% impactor on the 6400 km radius target. The mass of ejecta produced by the impact (M_{ej}) is listed normalized to the impactor mass (M_{imp}) and the target mass (M_{target}). Note that there is no table for the impacts of the 40% projectile, since no ejecta resulted from those collisions.

results of O'Keefe and Ahrens [1977b], as in figures 2.28 - 2.30. In all three figures, the dashed lines represent the amount of ejecta, in terms of projectile masses, produced in impacts at velocities from 7.5 to 45 km/s on a semi-infinite target. These simulations did not take into account the effects of gravity. Dotted lines represent the ejecta estimated by Gault et al. [1963] from impact experiments for collisions at 6 km/s. The curve for 45 km/s impacts is as plotted in O'Keefe and Ahrens [1977b]. The points plotted in figure 2.28 correspond to the total amount of ejecta produced by impacts at 5 km/s on the 1700 km target, and 10 and 20 km/s on both targets; only the values from both the normal and the most oblique impacts are plotted. The 5 km/s impacts on the 6400 km target are not plotted, since no ejecta was produced in those cases. For the impacts on the 1700 km target (escape velocity 2.4 km/s), the ejecta production is about as much as would be predicted by O'Keefe and Ahrens for impacts at twice the velocity. For impacts on the 6400 km targets (11 km/s escape velocity), the discrepancy between the two sets of results is greater, and for the 60% impacts, the amount of ejecta is that which would be expected for impacts at 30 to 60 km/s. Our results fit in to the range of ejecta production predicted by Gault for both target sizes. Figure 2.29 shows the results of impacts with the 40% impactor compared with the same curves as in figure 2.28. Since no ejecta was produced for either impacts at 5 km/s, or impacts with this impactor on the 6400 km target, we have points only for the 10 and 20 km/s impacts on the 1700 km target. For this impactor, we see that the amount of ejecta produced is that which would be predicted for impacts at velocities between 7.5 and 15 km/s in the O'Keefe and Ahrens model, and slightly less than that predicted by Gault et al. The oblique impacts at 10 and 20 km/s produce about the same amount of ejecta, suggesting that, for the most oblique impacts, the size of the impactor is a more important factor in determining the amount of ejecta production than the impact velocity.

In comparing our results to those of O'Keefe and Ahrens and Gault et al., there are several complications. Both of the earlier works assume that the target material has strength which must be overcome before fragmentation can occur. Our hydrodynamic code assumes that any material strength will be small compared to the stresses induced by the impact, which is appropriate for impacts on this scale. Since the simulations of O'Keefe and Ahrens are of impacts onto a half-space, it is perhaps more valid to compare their results with ours by comparing the amount of ejecta which is launched on trajectories that take the particles above the plane tangent to the target at the point of impact. (This is the plane pictured in figure 2.1.) Figure 2.30 plots only ejecta meeting this requirement. Here, we find that the amount of material ejected from impacts onto the 1700 km target is in good agreement with the amount predicted by the half-space model of O'Keefe and Ahrens. A normal impact at 20 km/s produced an amount of ejecta that is intermediate to that predicted for impacts at 15 and 30 km/s; a normal impact at 10 km/s ejects as much mass as is predicted for 15 km/s. Oblique impacts produce less ejected mass. Impacts at 5 km/s on the 1700 km target produce no ejected material that travels back above the plane at greater than escape velocity. In the case of the 6400 km targets, the mass of ejecta is still greater than that predicted by the half-space model, but is compatible with the ejecta amounts predicted by Cameron and Benz [1991] and Pongracic [1988].

High amounts of ejecta production were also seen in the work of Cameron and Benz [1991] and are plotted on the same figure. Cameron modeled oblique impacts onto the earth of impactors ranging in mass from 0.14 to 0.25 (51% to 63%) of the target mass, at 11 and 15 km/s. The amount of ejecta produced ranges from 0 to 0.075 projectile masses, which is intermediate to our values of 0 to 0.06 projectile masses for impacts with the 60% impactor at 10 km/s and 0.2 to 0.4 projectile masses for impacts at 20 km/s.

Pongracic modeled impacts at 10, 25, and 50 km/s of a 5 km radius impactor

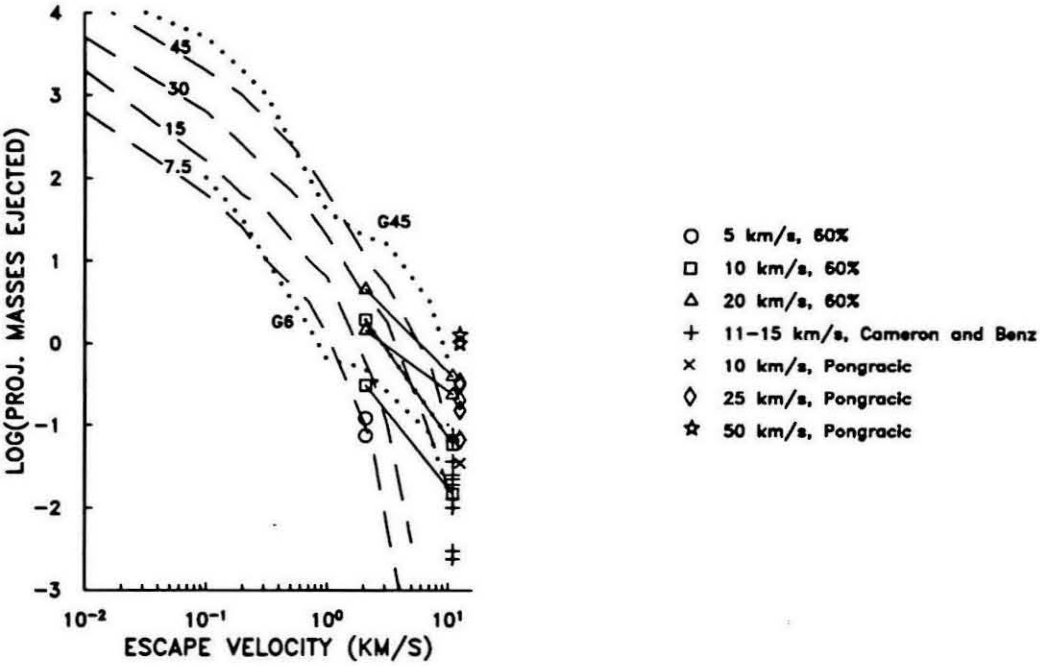

Figure 2.28: Total mass of material ejected from the target, measured as multiples of the projectile mass. All material ejected at greater than escape velocity is plotted, regardless of trajectory. The points plotted for each velocity represent the full range of ejecta production, for all impact angles. The dashed lines are modified from figure 2a of O'Keefe and Ahrens [1977b], and show the amount of ejecta produced by normal impacts at 7.5, 15, 30, and 45 km/s. Dotted lines are from the experiments of Gault et al. [1963].

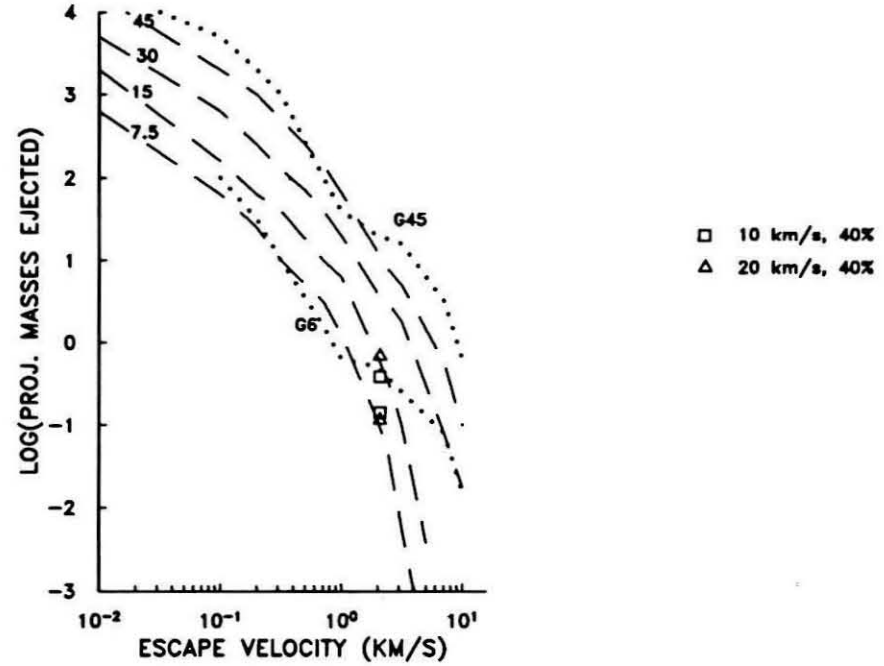

Figure 2.29: Total mass of material ejected from the target, measured as multiples of the projectile mass. The points plotted for each velocity represent the full range of ejecta production, for all impact angles. The oblique impacts at 10 and 20 km/s produce roughly the same (small) amount of ejecta. The dashed and dotted lines are the same as in the previous figure.

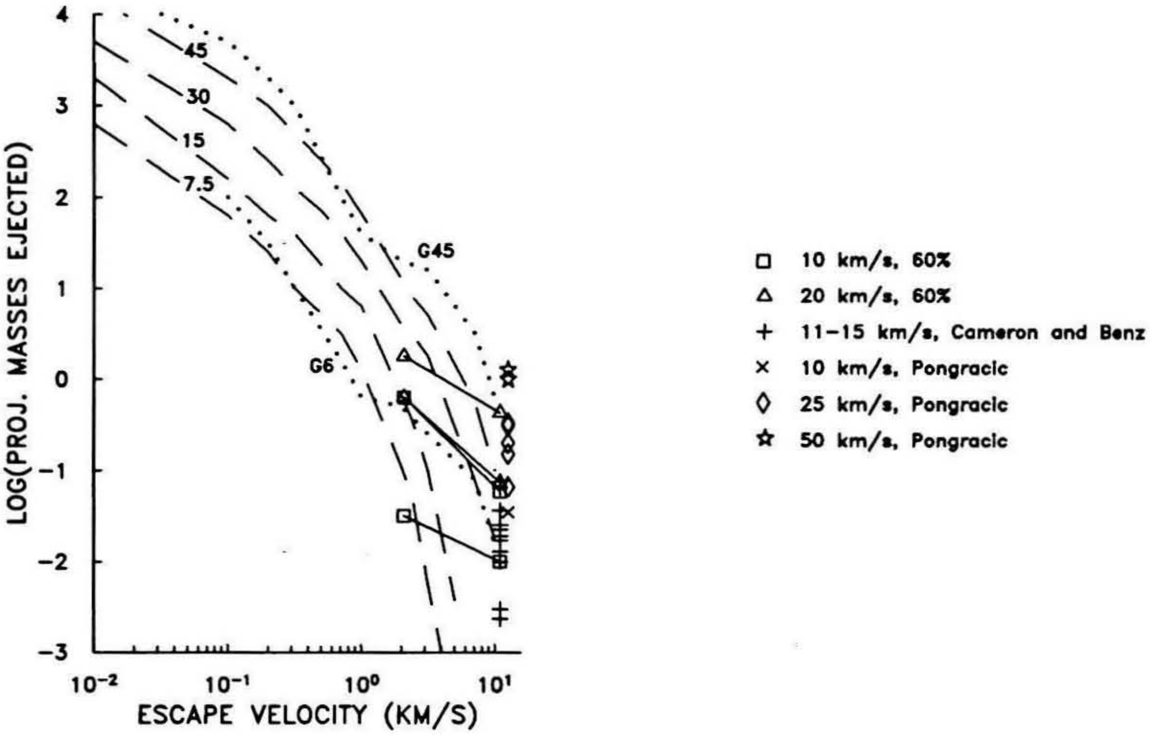

Figure 2.30: Mass of material ejected from the target, measured as multiples of the projectile mass. Only material with trajectories above the plane tangent to the target at the point of impact are considered here. The points plotted for each velocity represent the full range of ejecta production, for all impact angles. The dashed and dotted lines are the same as in figure 2.28.

onto a semi-infinite target at various impact angles. She found ejecta to be produced in the 10 km/s impacts only for the case where the impact angle was 30°, where 0.035 projectile masses were ejected. For the 25 km/s impacts, the amount of ejected material ranged from 0.066 (the most oblique impact) to 0.33 (30°) projectile masses. The fastest impacts produced 1.25 and 0.97 projectile masses of ejecta. These values, though caused by a much smaller impactor, are still close to the ones we find in this study.

In addition to examining the amount of target material ejected in the impact, we may also consider the amount of impactor material that gets accreted to the target, i.e., the material that, after the impact, has a velocity less than that required to escape the target. Table 2.14 shows the figures for all cases of impacts on the 1700 and 6400 km targets. For the larger targets, the 5 km/s impacts occurred at a velocity so low compared to the surface escape velocity that all the impactor material remains gravitationally bound to the target after the impact for both the 40% and the 60% impactors. The same is almost true for the 10 km/s impacts, but a small fraction (up to 7%) of the impactor material leaves the target at greater than escape velocity in the more oblique and larger impacts. For the 20 km/s impacts, the low impact angle cases for the 40% impactor also result in most of the impactor material being accreted to the target, but in the 90° impact, 49% of the impactor is accreted. The 60% impactor at 20 km/s does not leave as much material behind. In the low angle (0° - 30°) impacts, approximately 70% of the impactor is accreted to the target. For the 90° impact, only 30% remains with the target after the impact.

The impacts on the smaller targets result in much less accretion. Even at the relatively low impact velocity of 5 km/s, only 38% of the 40% impactor is accreted to the target. For the 20 km/s impacts, the velocity of the particles is so high that very few of them remain with the target after impact. It is interesting to note that the figures for the 5 km/s impacts on the 1700 km target are similar to those for the

Accretion of projectile mass					
Impact	Impact	6400 km targets		1700 km targets	
velocity	angle	40% impactor	60 % impactor	40% impactor	60%impactor
5 km/s	0°	1	1	0.95	0.74
	5°	1	1	0.95	0.67
	15°	1	1	0.93	0.65
	30°	1	1	0.91	0.49
	50°	1	1	0.66	0.35
	90°	1	1	0.38	0.22
10 km/s	0°	1	0.97	0.63	0.25
	3°	1	0.96	0.60	0.27
	15°	0.99	0.95	0.55	0.24
	30°	0.97	0.96	0.41	0.23
	50°	0.95	0.93	0.23	0.15
	90°	0.94	0.93	0.14	0.08
20 km/s	0°	0.92	0.78	0.32	0
	5°	0.89	0.78	0.39	0
	15°	0.90	0.74	0.33	0
	30°	0.86	0.67	0.18	0
	50°	0.67	0.46	0.06	0
	90°	0.49	0.30	0.04	0

Table 2.14: Mass of impactor accreted to both the 1700 km and the 6400 km targets. The figures are listed as the fraction of the total impactor mass.

20 km/s impacts on the 6400 km target, since in both cases the impact velocity is close to twice the surface escape velocity of the target.

2.5 Discussion

The results presented above show that impacts at the same ratio of impactor to target mass can have greatly different outcomes in terms of the amount of melting, vaporization, and ejecta production, and in the partitioning of the energy in the system. The differences in the ejecta production are the greatest, and will be discussed below. The energy partitioning varies between the impacts on the 1700 km and the 6400 km targets, but the differences are not striking. Perhaps the largest change when moving to the larger targets is that the fraction of energy in the internal energy of the target is higher, implying that the target is more strongly shocked by the larger scale of the collision. This is related to the differences in the amount of melting and vaporization of the target. The melt production is overall quite similar for impacts at 5 and 10 km/s, but the 20 km/s impacts with the 40% impactor melt much more of the target than the 6400 km target. It is difficult to determine whether this would be the case for the 60% impactor, since both targets are nearly completely melted after the impact. The amount of vaporization, however, differs on the two targets. The number of projectile masses vaporized is anywhere from 2 to 20 times as much on the 6400 km targets as on the 1700 km targets.

Ejecta production seems to be much more dependent on the size of the target. In every case, far more material was ejected from the 1700 km target than from the 6400 km target. For instance, impacts with the 40% impactor, which were sufficient to remove half the target material from the 1700 km target after a normal impact at 20 km/s, caused no ejection of material from the 6400 km target. More ejecta was produced than the amount predicted by O'Keefe and Ahrens [1977a], but the results were in reasonable agreement with the findings of Cameron and Benz [1991]. Thus we suggest that impactor size is a significant factor in ejecta production after impacts, and that simple scaling of impact ejecta amounts from small targets to large ones may not hold. Moreover, the relative size of the impactor and the target may also be important. For smaller impactors, the target surface near the point of impact will have less curvature, and material will not be scattered forward to the extent that it is in our simulations of large impacts.

Much work has been done on the fragmentation of targets in the laboratory, and the scaling of the results to apply to impacts of asteroids [e.g., Fujiwara and Tsukamoto 1980, Farinella et al. 1982, Housen and Holsapple 1990, Fujiwara et al. 1989, Davis and Ryan 1990, Housen et al. 1991, and many earlier papers]. The experiments of Fujiwara and Tsukamoto [1980], in which projectiles were fired at basalt targets, found that fragments which were ejected from the surface of the targets have higher velocities than those which originated in the interior, and those which came from the parts of the surface closest to the point of impact point traveled the fastest. This is in general agreement with our results; in our simulations, these are also the particles which are the most strongly shocked. They also performed experiments in which the target was hit obliquely , and found them to be equivalent to normal impacts at a lower specific energy. (The specific energy is the ratio of the kinetic energy of the impactor to the mass of the target). These experiments are, of course, unable to simulate the effects of gravity on the distribution and production of ejecta. Also, the fracture of laboratory-scale targets will be affected by the strength of the target material, which is not an important factor at the scale of our simulations. Housen et al. [1991] have attempted to address the gravity problem by conducting fragmentation experiments under pressure, which would simulate the lithostatic compressive stress in the interior of a large asteroid or planet. They found that the specific energy required to cause catastrophic fragmentation of the target (where more than half of the target mass is ejected) increases with the overpressure applied, and thus would increase with the size of the targets, for large targets where gravity would be significant.

A parameter often used in this literature is the "threshold energy", the specific energy above which catastrophic fragmentation occurs. The value of this parameter is determined from experiments such as those mentioned above, and from scaling arguments, which are used to extrapolate from the small, laboratory scale to the size of the targets of interest, asteroids or planets. Plots of the threshold specific energy as a function of target size, e.g., figure 9 of Fujiwara et al. [1989], would predict that impacts with a specific energy of approximately 1×10^8 erg/g would suffice to cause catastrophic breakup of the 1700 km target, and 1×10^9 erg/g would catastrophically fragment the 6400 km target. But our impacts have specific energies ranging from 7.5×10^9 erg/g for impacts at 5 km/s with the 40% impactor, to 4.4×10^{11} erg/g , for impacts with the 60% impactor at 20 km/s. Thus each of them should have done massive destruction to either target, with the largest remaining fragment being only on the order of 10^{-3} times the mass of the original body. However, we find that, in our simulations, even the largest impacts on the 6400 km target eject only 40% of the target mass, leaving 60% of the target together after the impact, and, for the 1700 km target, only the normal impact at 20 km/s with the 40% impactor and all impacts at 20 km/s with the 60% impactor cause catastrophic fragmentation of the target.

Housen et al. [1991], in their overpressure fragmentation experiments, have revised these estimates to reflect the greater specific energies needed to catastrophically breakup the large bodies. Figures 2.31 and 2.32 are modified from figure 8 of Housen et al. [1991]. Plotted is the threshold energy per unit target mass Q^* required for catastrophic fragmentation plotted against target radius. The dashed lines show other estimates of threshold energy determined by extrapolation of laboratory-scale strength-dominated experiments. Three sets of points are plotted. The points from Fujiwara [1982] are the specific energies estimated to have caused the break up of the parent bodies of the Hirayama families of asteroids Eos, Themis, and Koronis. The squares are from the over-pressure fragmentation experiments of Housen et al., where the target radius is determined by equating the pressure at which the experiment was conducted with the average lithostatic stress in a body. The other points at the upper left of the figure are the ranges of specific energies for the normal impacts on the two targets we used in this study. Figure 2.32 is an expanded version of figure 2.31. The numbers associated with each point designate the amount of target material remaining after the impact. According to the work of Housen et al., it should take a specific energy of approximately 2 x 10^{10} erg/g to catastrophically breakup the 1700 km target. This would imply that the 5 and 10 km/s impacts with the 40% impactors would be too small at specific energies of 7.5 x 10^9 and 1.8 x 10^{10} ergs/g, and the 5 km/s impact with the 60% impactor (specific energy = 2.75 x 10^{10}) would by just large enough, and that all the other impacts would be sufficiently large. The 6400 km targets would require a much large specific energy, approximately 10^{11} ergs/g, for catastrophic breakup. Only the 20 km/s impacts with the 40% impactor (1.2 x 10^{11}) and the 10 and 20 km/s impacts with the 60% impactor (1.1 x 10^{11} and 4.4 x 10^{11}) would suffice; and only the latter case is significantly over the threshold energy. Our results show that catastrophic breakup occurred for the 1700 km target for a normal impact at 20 km/s with the 40% impactor, where 53% of the target was ejected. All other impacts with the smaller impactor on that target created much less ejecta. The 20 km/s impacts with the larger impactor caused catastrophic fragmentation in all but the most oblique impact; lower velocity impacts were not as destructive. For the 6400 km target, as mentioned above, the impacts with the 40% impactor produced no ejecta in any of the cases, and even impacts at 20 km/s with the 60% impactor did not cause more than 9% of the target mass to be ejected. Of course, since the experimental results, even those conducted at pressure, cannot model the effect of gravity in drawing material back to the target, what we are calculating is really the mass of the largest re-accumulated fragment, the amount of material that has not achieved escape velocity. Therefore, we would expect the threshold specific energy required to eject half the mass of the target to be greater than the threshold energies listed above. Still, it appears that these results are not inconsistent with those of Housen et al. [1991].

Another parameter suggested to determine the onset of catastrophic fragmentation in impacts is given in Farinella et al. [1982]. Based on experimental data, they consider the ratio of the impactor to the target mass, and state that catastrophic breakup will occur when this ratio is above the value $\bar{\mu} = 0.938R^{1.316}/V^2$, where R is the radius of the target, and V is the impact velocity. For our cases, we find that for the 1700 km target, $\bar{\mu}$ is 0.25 for 5 km/s impacts, 0.064 for 10 km/s, and 0.016 for 20 km/s. Thus we would expect the 5 km/s impacts to cause catastrophic breakup only for larger impactors than the ones we used; the 10 km/s impacts to cause catastrophic breakup for the 60% impactor, and to be close to breakup for the 40% impactor, and the 20 km/s impacts of both impactors to be highly destructive. For the 6400 km targets, $\bar{\mu}$ is 1.55, 0.388, 0.097 for 5, 10, and 20 km/s impact, respectively. It would thus be impossible to get catastrophic fragmentation from any 5 km/s impact (since $\bar{\mu} > 1$), and our impactors are much too small to get fragmentation from any impact at 10 km/s. The 20 km/s impact with the 60% impactor should cause catastrophic fragmentation. As above, the specific energy for catastrophic breakup seems to be higher in our simulation, but both models are not far off in estimating the amount of ejecta from the large impacts.

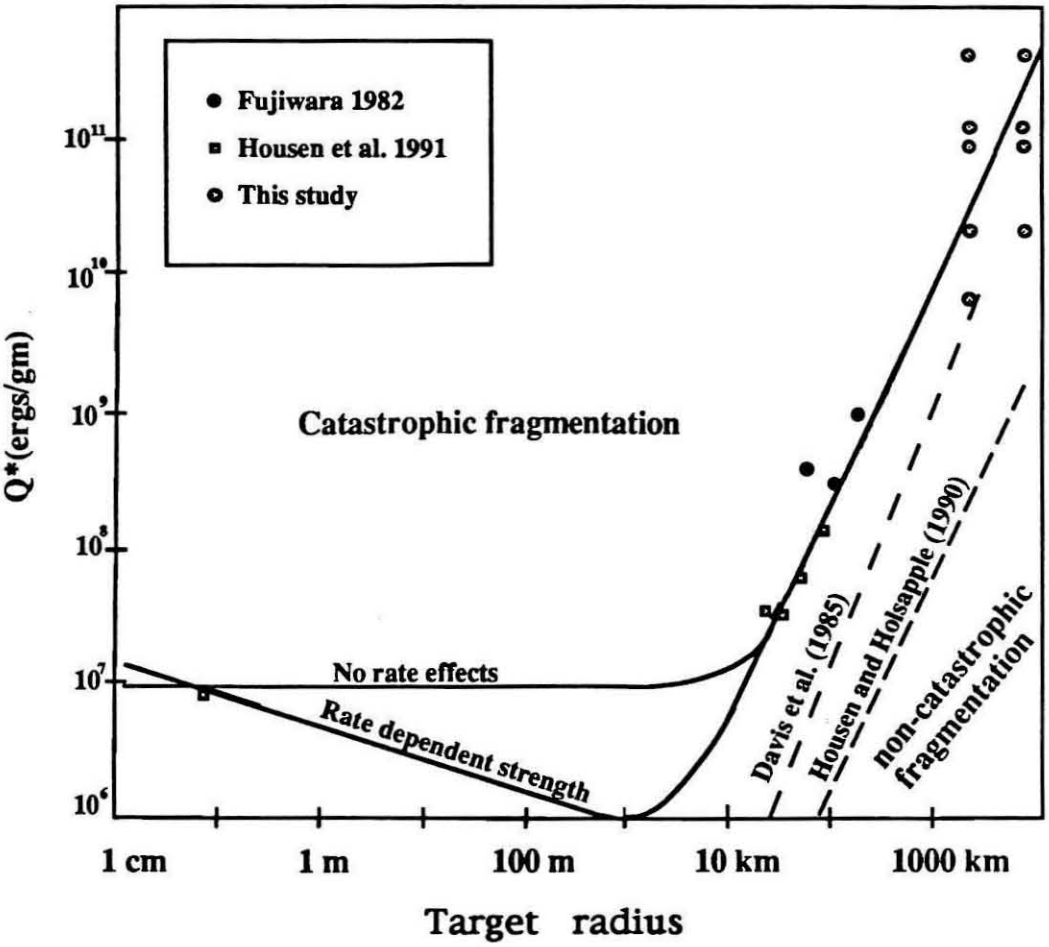

Figure 2.31: Threshold energy required for catastrophic fragmentation as a function of target size. Points above the solid line are in the catastrophic fragmentation regime, where the largest remaining fragment is less than half the mass of the original target. The dashed lines are other estimates of the threshold energy based on extrapolation of strength regime results. The points plotted are identified in the following figure. This figure is modified from figure 8 of Housen et al. [1991].

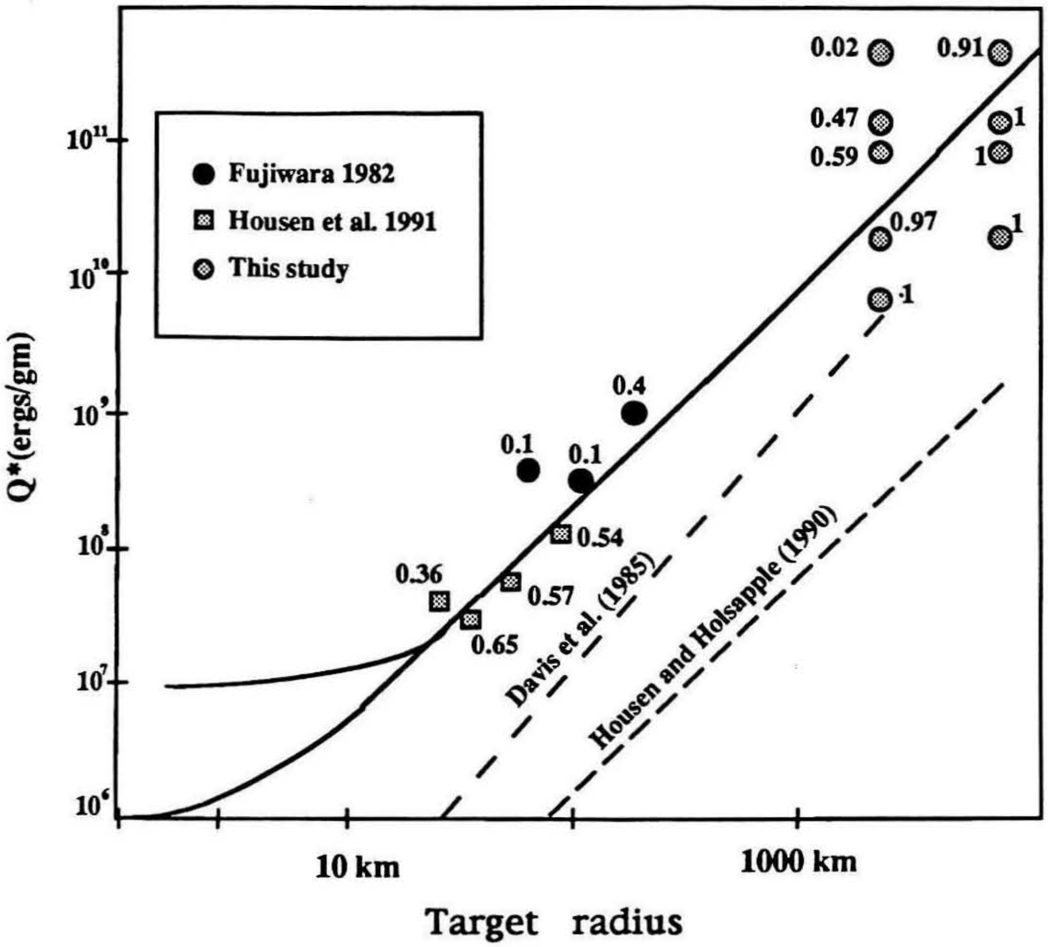

Figure 2.32: Threshold energy for catastrophic fragmentation of larger bodies, expanded from the previous figure. The numbers associated with each point are the fraction of the target remaining after the impact. Larger targets are stronger than would be predicted by the models of Davis et al [1985] and Housen and Holsapple [1990].

40% and 60% the radius of the target (6% and 22% of the mass). We examined the outcome of the impacts to investigate the effects of changing the impactor and target size, and impact angle and velocity on the amount of target material melted, vaporized, and ejected, and the amount of impactor material accreted to the target. We also examined the partitioning of the initial kinetic energy of the impactor into the post-impact internal and kinetic energies of both bodies.

The impacts at 20 km/s were sufficient to melt large fractions of both targets. The 20 km/s impact with the 40% impactor melted more mass on the 1700 km target than on the 6400 km target, but the larger target had more material vaporized. The 60% impactor melted the two targets almost completely at this velocity; again, the larger target had more vaporization. Impacts at 5 and 10 km/s are similar in terms of the amount of melt produced on the different targets with the different impactors when the mass of material melted or vaporized is considered in terms of the number of impactor masses.

Previous work on impacts onto a half space [O'Keefe and Ahrens 1977a, Ahrens et al. 1989] predict that little to none of the initial kinetic energy of the impactor will remain after the impact; the energy will be converted to kinetic and internal energy of the target, and internal energy of the impactor. Our modeling shows this result not to hold for impacts on finite-sized bodies, especially as the impact velocity and impact angle increase. This is because the finite size of the target, and the large size of the impactor relative to the target, ensure that some material can pass beyond the target, and will not be stopped by the surface of the target.

Impacts onto the 1700 km targets produce an order of magnitude more ejecta than do impacts at the same velocity with the same impactors on the large target, due to the lower escape velocity. The large impacts were sufficient to completely destroy the smaller target, but the greatest amount of material ejected from the 6400 km target was only 9% of its mass. The amounts of ejecta produced from the smaller, 1700 km targets are consistent with the values predicted by O'Keefe and Ahrens [1977a] for impacts onto a semi-infinite target. The amount of ejecta produced in impacts on the 6400 km target is significantly larger than predicted by their calculations, but is not inconsistent with the results of Cameron et al. [1991] or Gault et al. [1963]. When compared to the amount of destruction predicted by Housen et al. [1991] or Farinella et al. [1982], the ejecta production of our impacts is low, but not unreasonably so, when the effects of the gravitational field of the target in limiting the amount of material that can escape the target are considered.

Bibliography

Ahrens, T. J. and O'Keefe, J. D. Equations of state and impact-induced shock wave attentuation of the moon, in *Impact and Explosion Cratering,* Roddy, D. J., Pepin, R. O. and Merrill, R. B., eds., Pergamon (New York) 639-656 (1977).

Ahrens, T. J., O'Keefe, J. D. and Lange, M. A. Formation of atmosphere during accretion of the terrestrial planets, in *Origin and Evolution of Planetary and Satellite Atmospheres,* Atreya, S. K., Pollack, J. B. and Matthews, M. S., eds., University of Arizona (Tucson) 328-387 (1989).

Benz, W., Slattery, W. L. and Cameron, A. G. W. The origin of the moon and the single impact hypothesis I, *Icarus* **66**, 515-535 (1986).

Benz, W., Slattery, W. L. and Cameron, A. G. W. The origin of the moon and the single impact hypothesis II, *Icarus* **71**, 30-45 (1987).

Benz, W., Slattery, W. L. and Cameron, A. G. W. Collisional stripping of Mercury's mantle, *Icarus* **74**, 516-528 (1987).

Benz, W., Cameron, A. G. W. and Melosh, H. J. The origin of the moon and the single impact hypothesis III, *Icarus* **81**, 113-131 (1989).

Cameron, A. G. W. and Benz, W. The origin of the moon and the single impact hypothesis IV, *Icarus* **92**, 204-216 (1991).

Davis, D. and Ryan, E. On collisional disruption: experimental results and scaling laws, *Icarus* **83**, 156-182 (1990).

Farinella, P., Paolicchi, P. and Zappala, V. The asteroids as outcomes of catastrophic collisions, *Icarus* **52**, 409-433 (1982).

Fujiwara, A. Complete fragmentation of the parent bodies of Themis, Eos, and Koronis families, *Icarus* **52**, 434-443 (1982).

Fujiwara, A., Cerroni, P., Davis, D., Ryan, E., Di Martino, M., Holsapple, K., and Housen, K. Experiments and scaling laws for catastrophic collisions, in *Asteroids II,* Binzel, R. P., Gehrels, T., and Matthews, M. S. eds., University of Arizona (Tucson) 240-265 (1989).

Fujiwara, A. and Tsukamoto, A. Experimental study on the velocity of fragments in collisional breakup, *Icarus* **44**, 142-153 (1980).

Gault, D. E. Shoemaker, E. M. and Moore, H. J. Spray ejected fomr the lunar surface by meteoroid impact, *NASA TND-1767,* (1963).

Gault, D. E. and Wedekind, J. A. The destuction of tektites by meteoroid impact, *J. Geophys. Res.*, **74**, 6780-6794 (1969).

Gingold, R. A. and Monaghan, J. J. Smoothed particle hydrodynamics: theory and application to non-spherical stars, *Mon. Not. R. Astron. Soc.* **181**, 375-389 (1977).

Gingold, R. A. and Monaghan, J. J. Kernel estimates as a basis for general particle methods in hydrodynamics, *J. Comp. Phys.* **46**, 429-453 (1982).

Housen, K. R. and Holsapple, K. A. On the fragmentation of asteroids and planetary satellites, *Icarus* **84**, 226-253 (1990).

Housen, K. R. Schmidt, R. M. and Holsapple, K. A. Laboratory simulation of large-scale fragmentation events, *Icarus* **94**, 180-190 (1991).

Lucy, L. B. A numerical approach to the testing of the fission hypothesis, *Astron. J.* **82**, 1013-1024 (1977).

Melosh, H. J. Giant impacts and the thermal state of the early earth, in *Origin of the Earth,* Newsom, H. E. and Jones, J. H. eds., Oxford (New York) 69-83 (1990).

Monaghan, J. J. An introduction to SPH, *Comp. Phys. Comm* **48**, 89-96 (1986).

Monaghan, J. J. and Gingold, R. A. Shock simulation by the particle method SPH, *J. Comput. Physics* **52**, 374-389 (1983).

O'Keefe, J. D. and Ahrens, T. J. Impact-induced energy partitioning, melting, and vaporization of terrestrial planets, *Proc. Lunar Plan. Sci. Conf. 8th*, 3357-3374 (1977a).

O'Keefe, J. D. and Ahrens, T. J. Meteorite impact ejecta: dependence of mass and energy lost on planetary escape velocity, *Science* **198**, 1249-1251 (1977b).

Pongracic, H. Numerical modelling of large body impacts, *Ph.D. Thesis*, Monash University (1988).

Thompson, S. L. and Lauson, H. S. *Improvements in the Chart D Radiation-Hydrodynamic Code III. Revised Analytic Equations of State,* Sandia Laboratories Report SC-RR-71 0714 (1984).

Tillotson, J. H. Metallic equations of state for hypervelocity impacts, General Atomic Report GA-3216 (1962).

Wetherill, G. W. Occurrence of giant impacts during the growth of the terrestrial planets, *Science* **228**, 877-879 (1985).

Wood, D. Collapse and fragmentation of thermal gas clouds, *Mon. Not. R. Astron. Soc.* **194**, 201-218 (1977).

Appendix A

Examples of impact runs

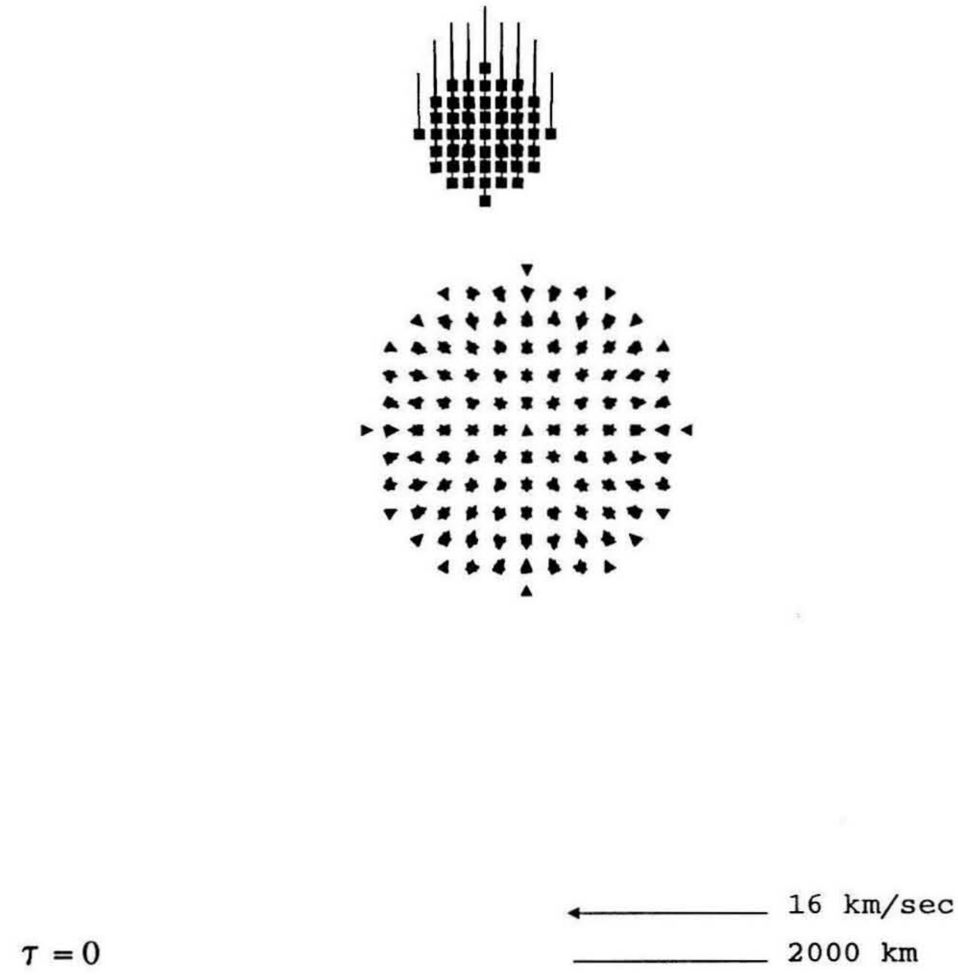

Figure A.1: Impact of the 40% impactor at 15° and 5 km/s on the 1700 km target. Initial configuration: particles are located at the origin of the arrows, and the direction of the arrow head indicates the direction of the particle. All particles are plotted; however, some are hidden behind others. Particles which are essentially stationary are plotted with triangles.

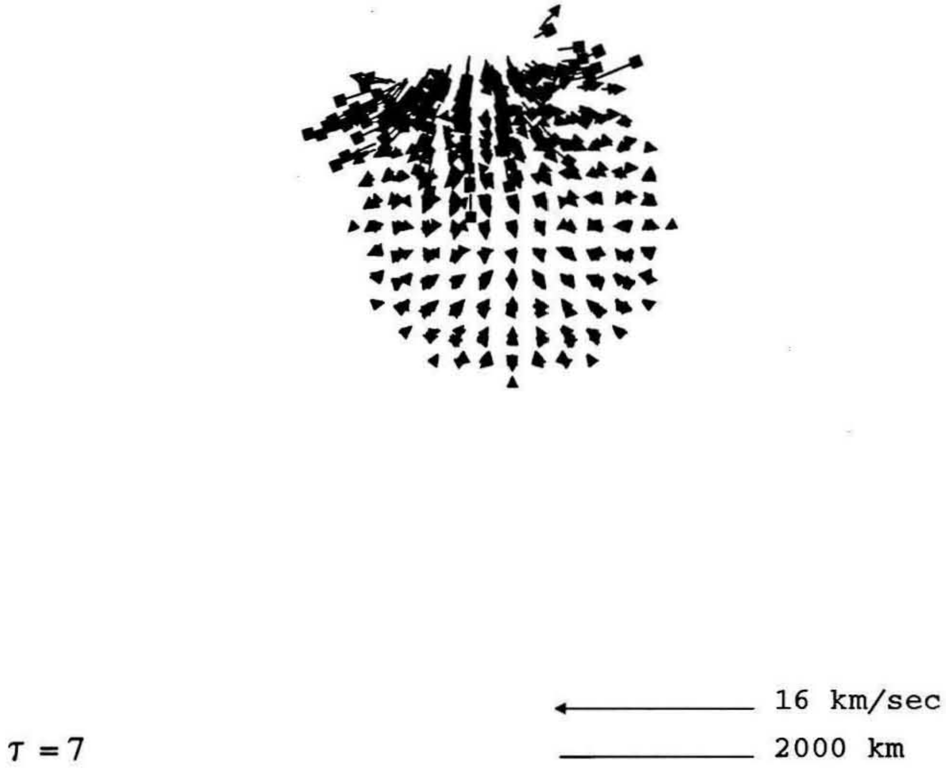

Figure A.2: Impact of the 40% impactor at 15° and 5 km/s on the 1700 km target, at time τ=7.

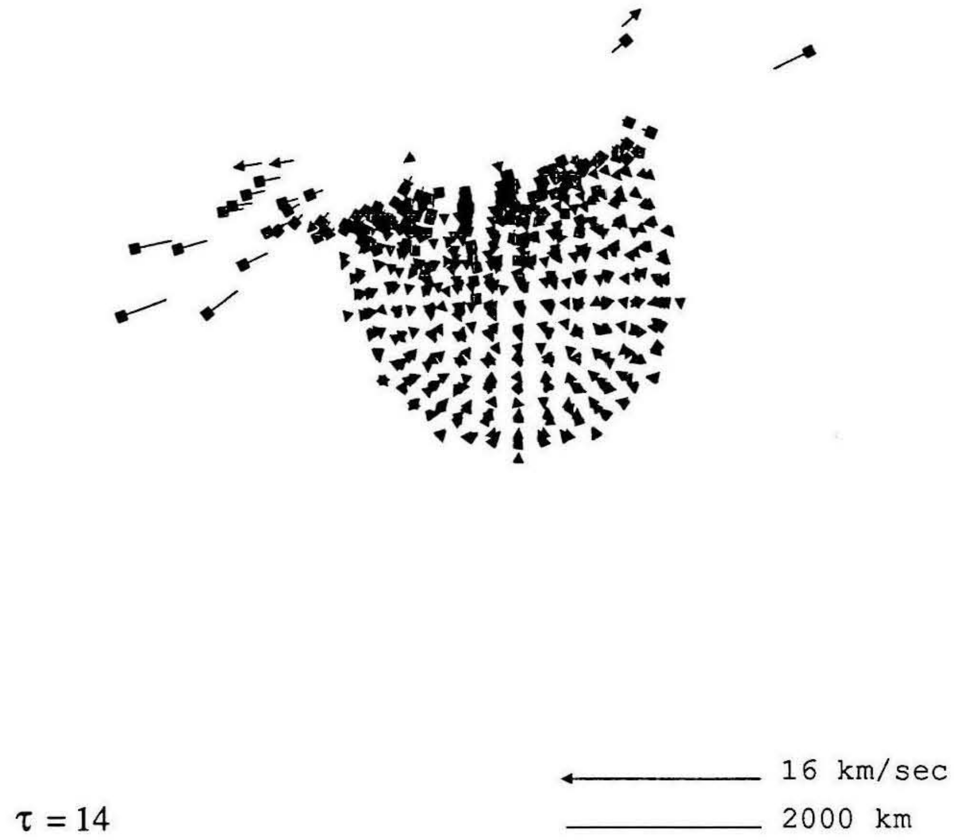

Figure A.3: Impact of the 40% impactor at 15° and 5 km/s on the 1700 km target, at time τ=14.

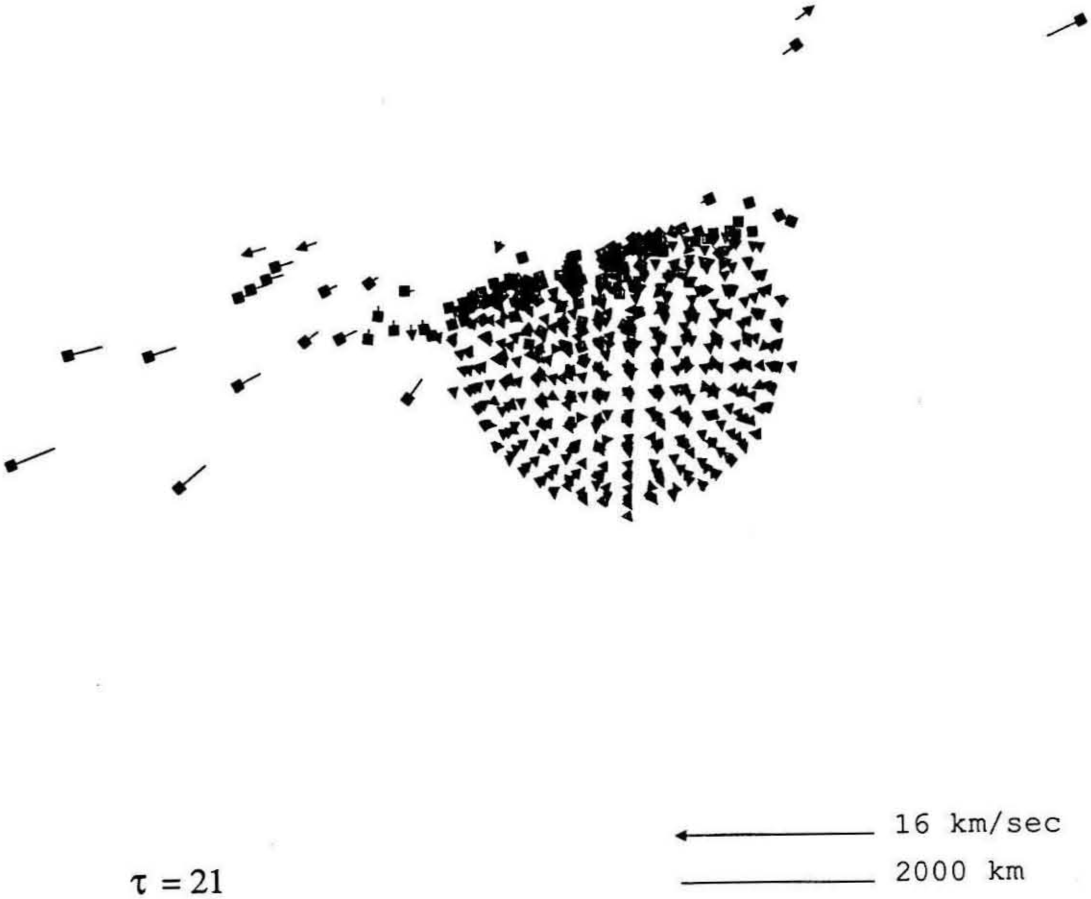

Figure A.4: Impact of the 40% impactor at 15° and 5 km/s on the 1700 km target, at time τ=21.

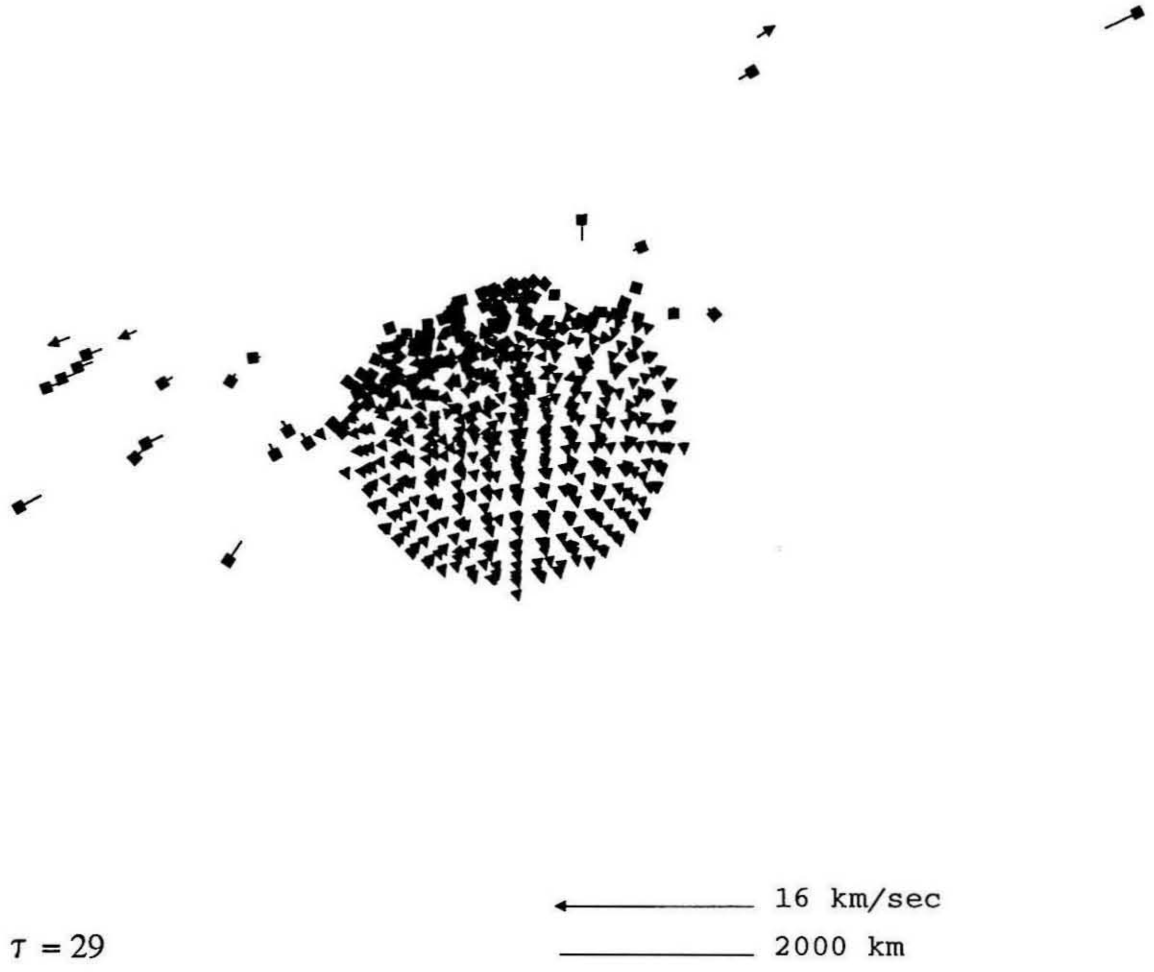

Figure A.5: Impact of the 40% impactor at 15° and 5 km/s on the 1700 km target, at time τ=29.

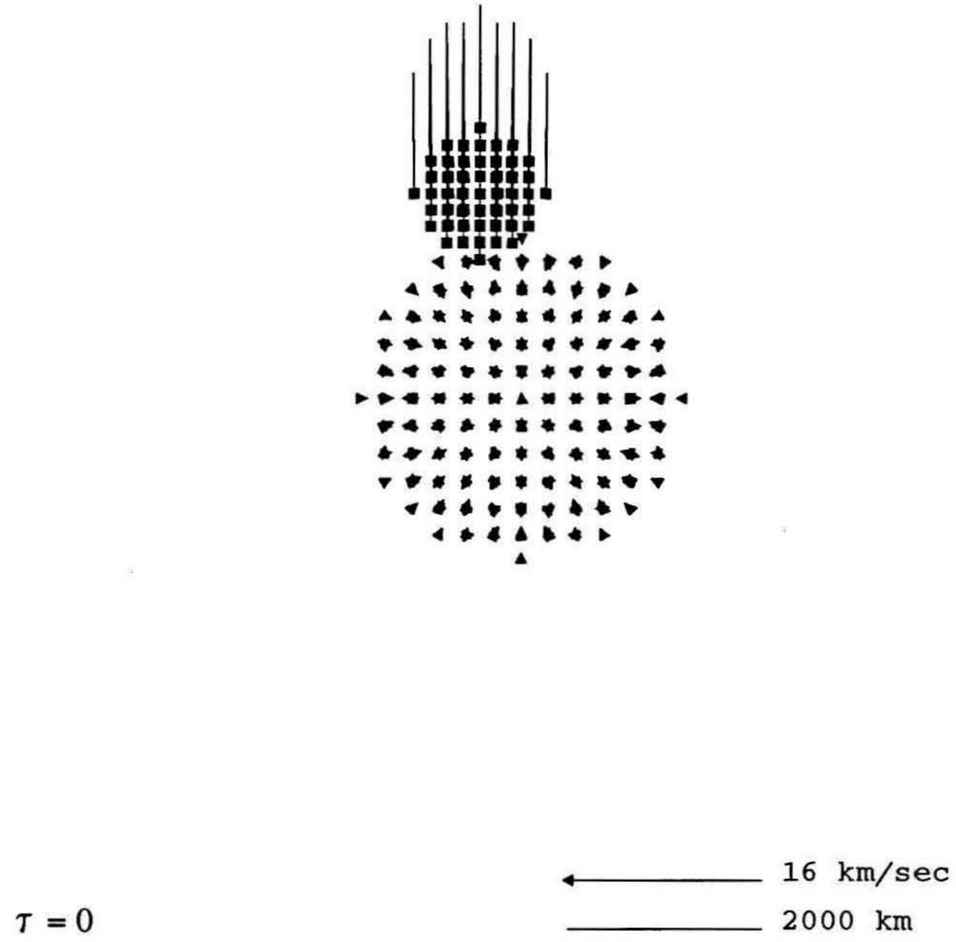

Figure A.6: Impact of the 40% impactor at 15° and 10 km/s on the 1700 km target (initial configuration).

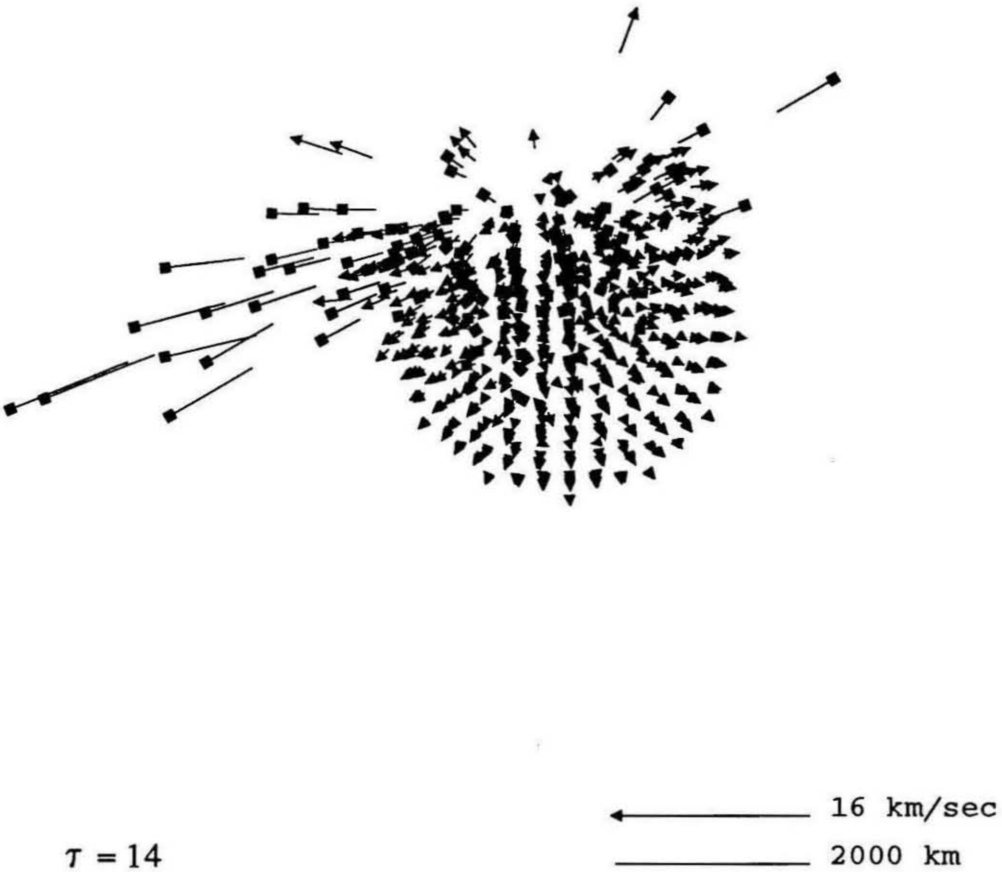

Figure A.7: Impact of the 40% impactor at 15° and 10 km/s on the 1700 km target at time τ=14.

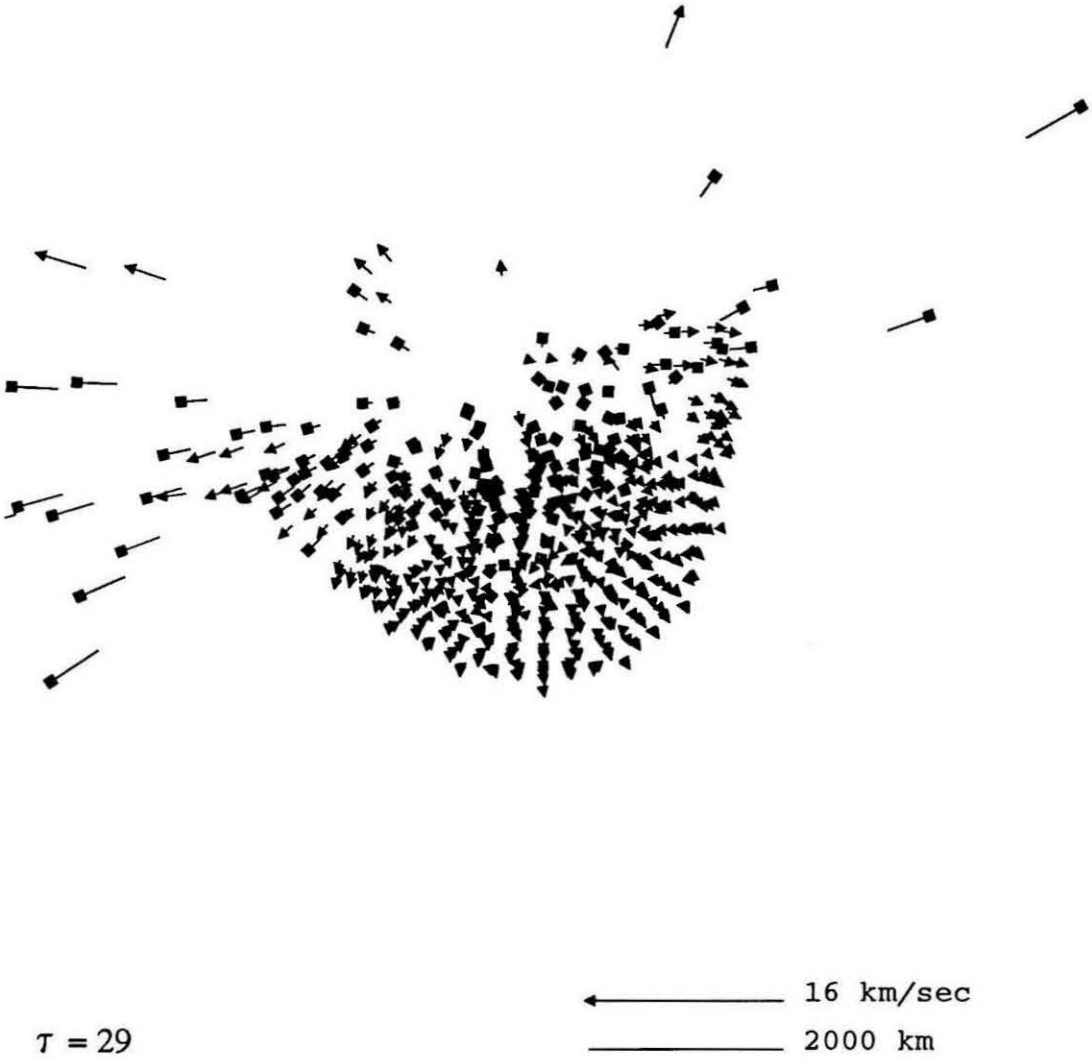

Figure A.8: Impact of the 40% impactor at 15° and 10 km/s on the 1700 km target at time τ=29.

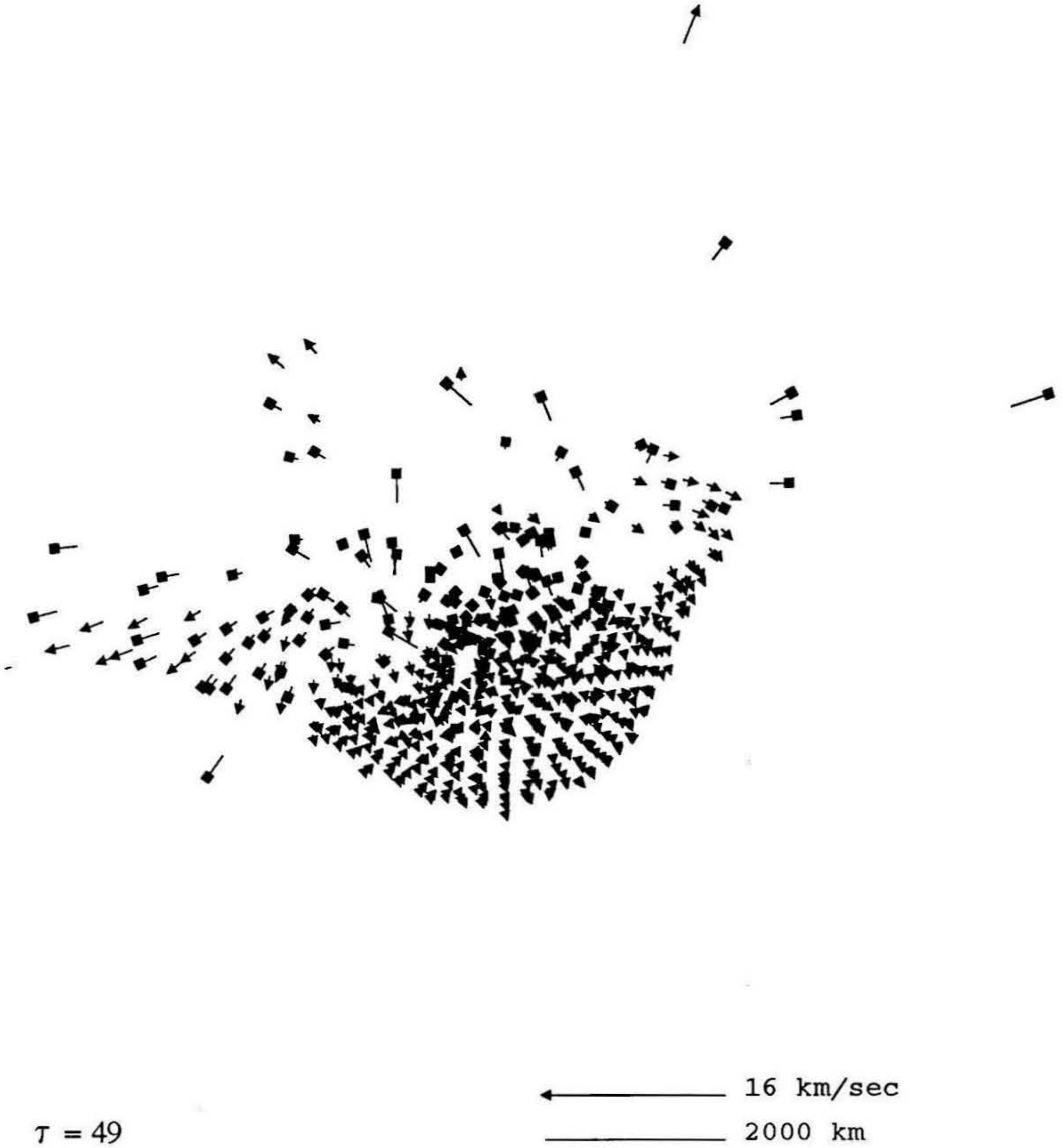

Figure A.9: Impact of the 40% impactor at 15° and 10 km/s on the 1700 km target at time τ=49.

Figure A.10: Impact of the 40% impactor at 15° and 10 km/s on the 1700 km target at time τ=57.

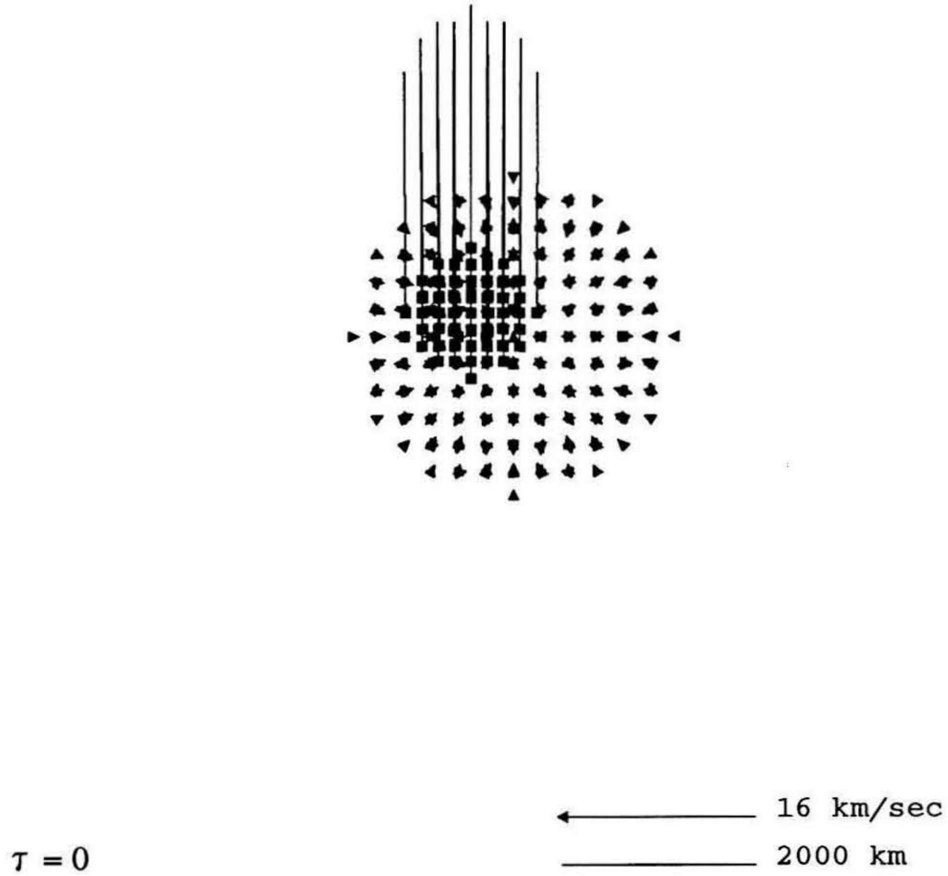

Figure A.11: Impact of the 40% impactor at 15° and 20 km/s on the 1700 km target (initial configuration).

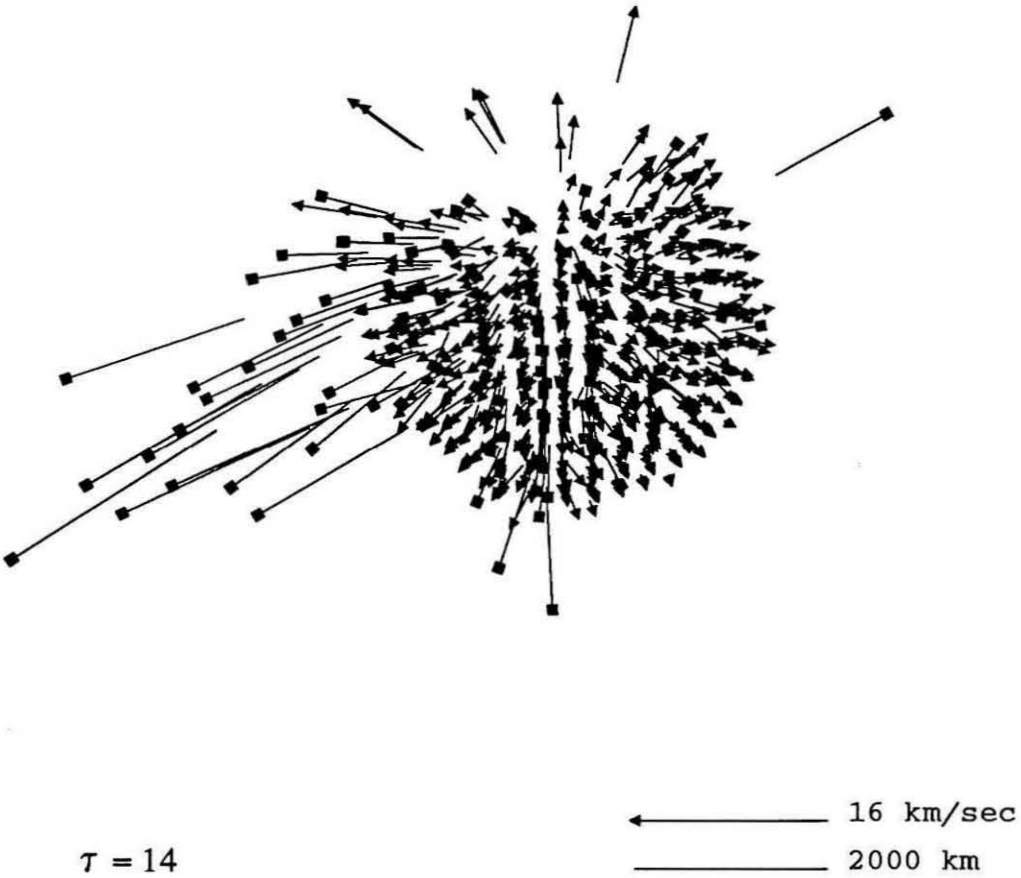

Figure A.12: Impact of the 40% impactor at 15° and 20 km/s on the 1700 km target at time $\tau = 14$.

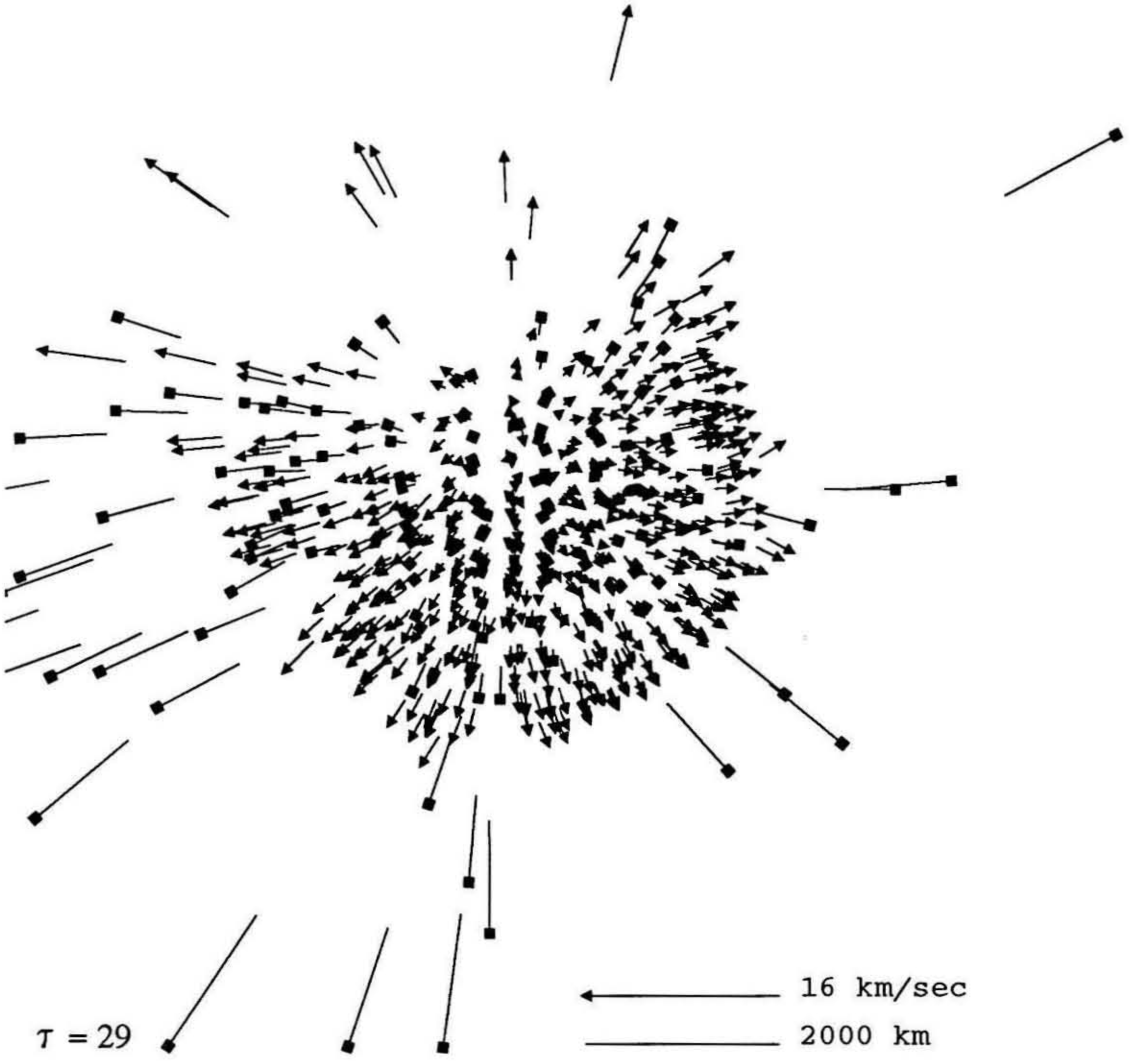

Figure A.13: Impact of the 40% impactor at 15° and 20 km/s on the 1700 km target at time τ=29.

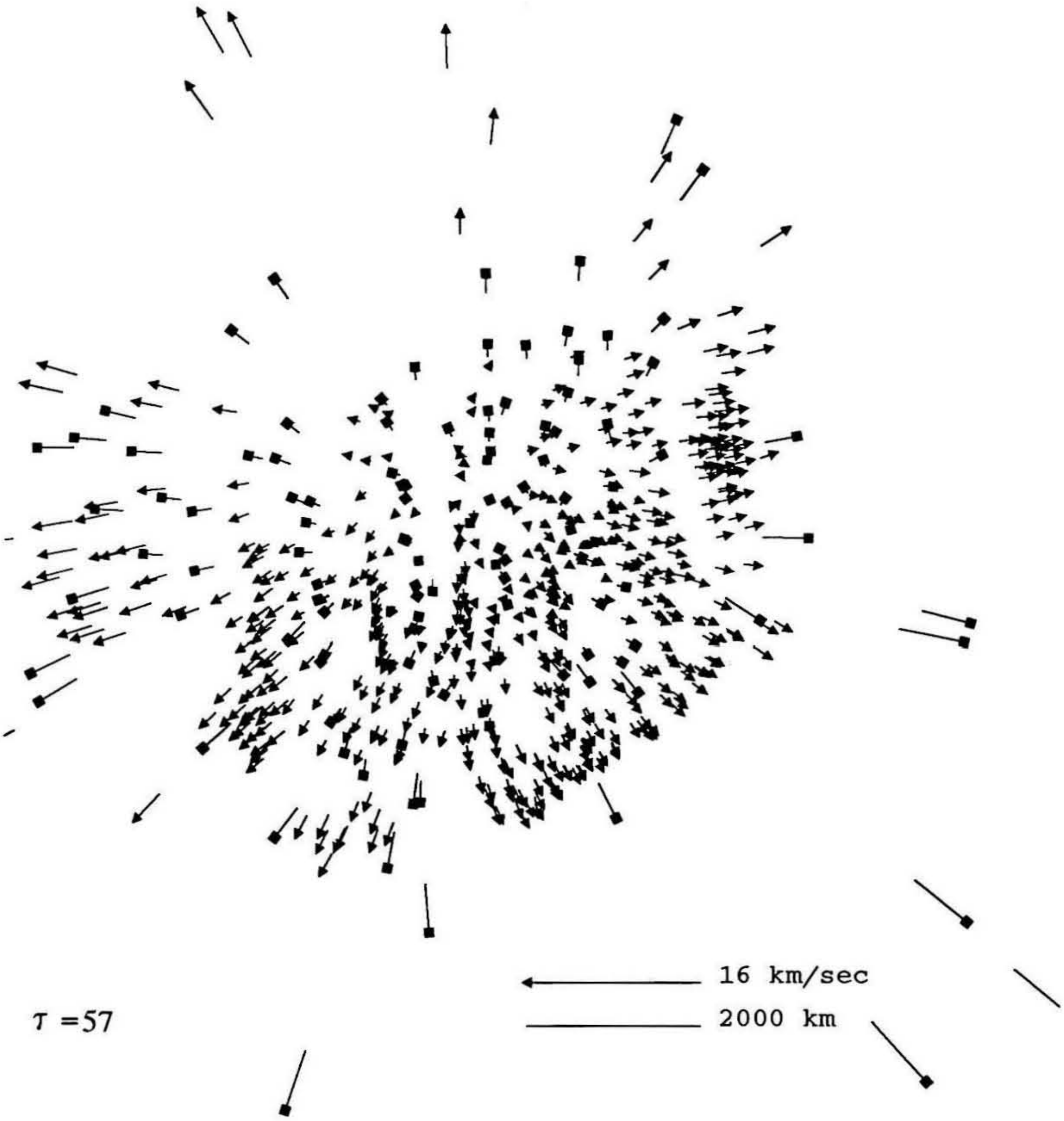

Figure A.14: Impact of the 40% impactor at 15° and 20 km/s on the 1700 km target at time τ=57.

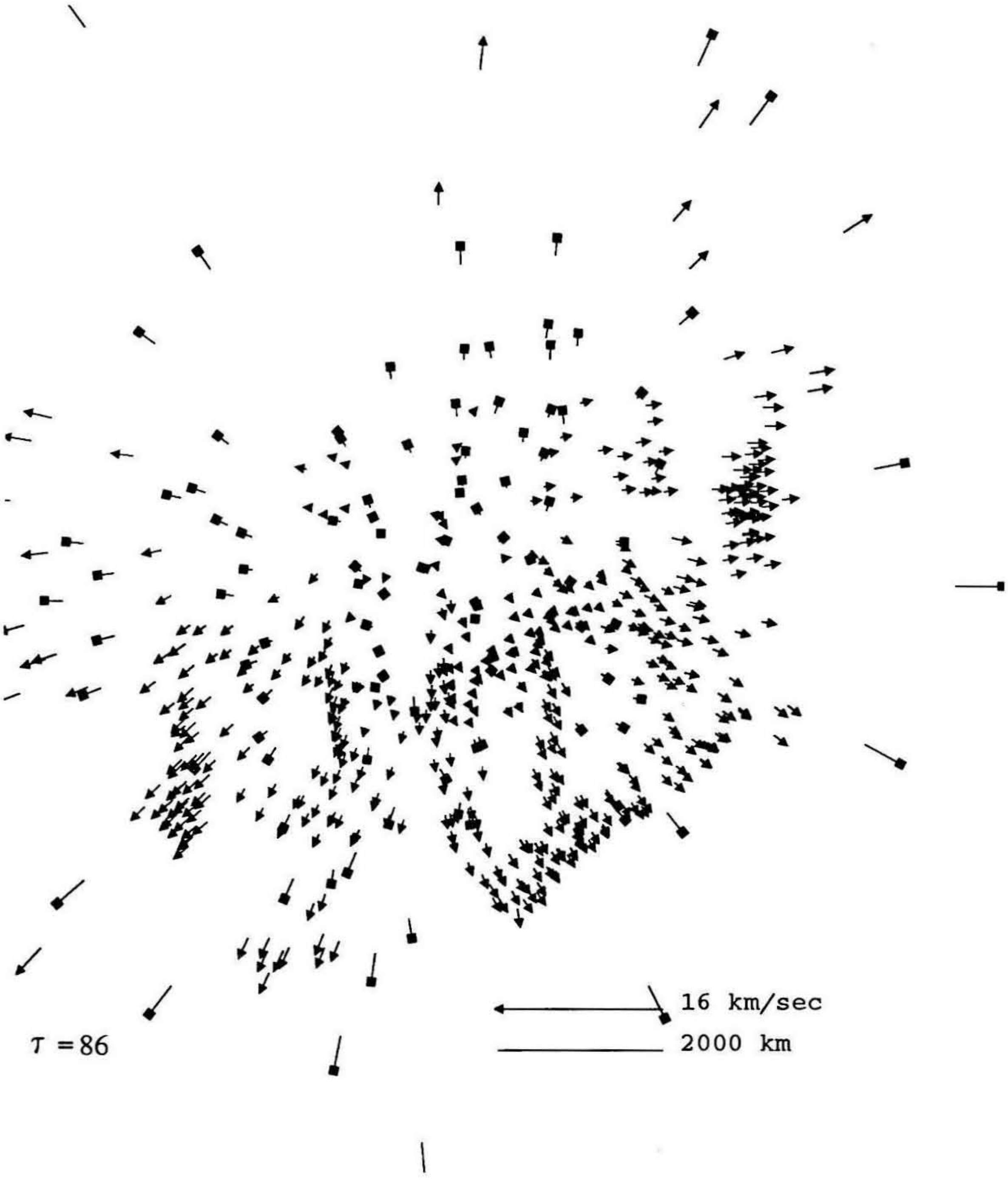

Figure A.15: Impact of the 40% impactor at 15° and 20 km/s on the 1700 km target at time τ=86.

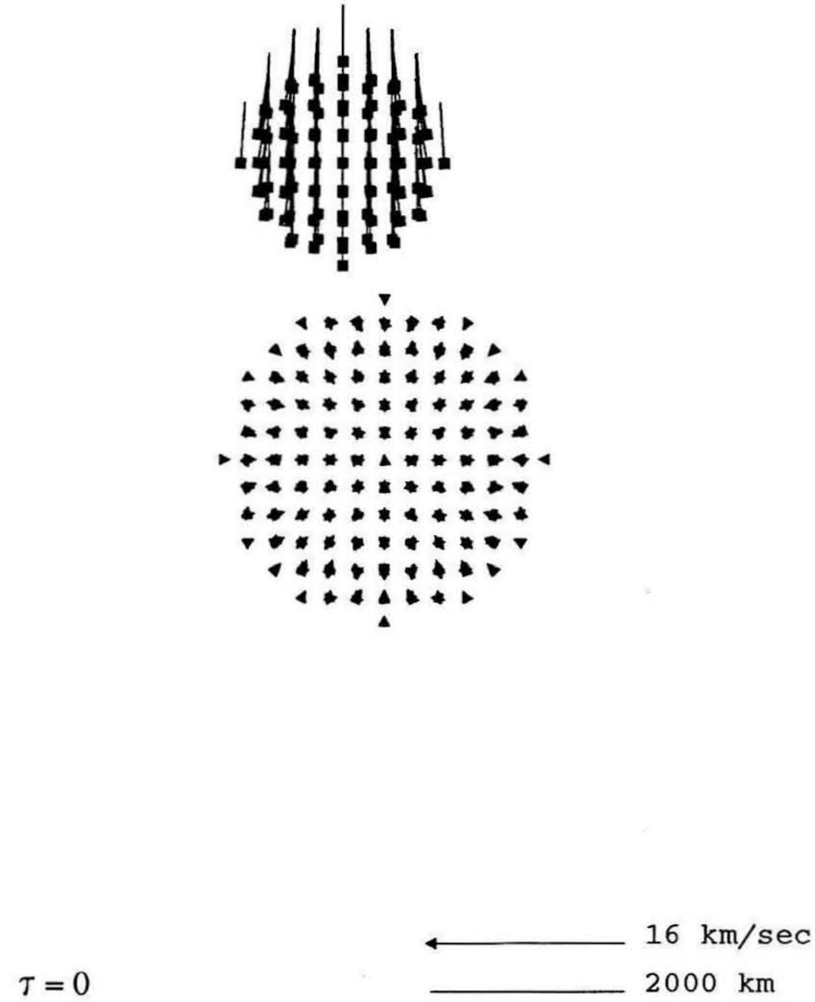

Figure A.16: Impact of the 60% impactor at 15° and 5 km/s on the 1700 km target (initial configuration).

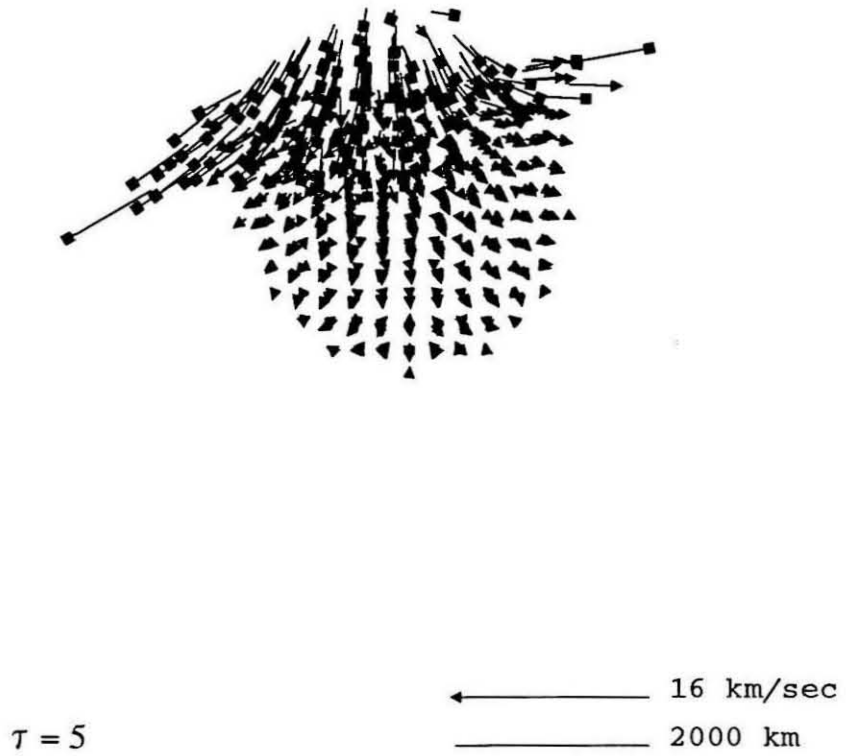

Figure A.17: Impact of the 60% impactor at 15° and 5 km/s on the 1700 km target at time τ=5.

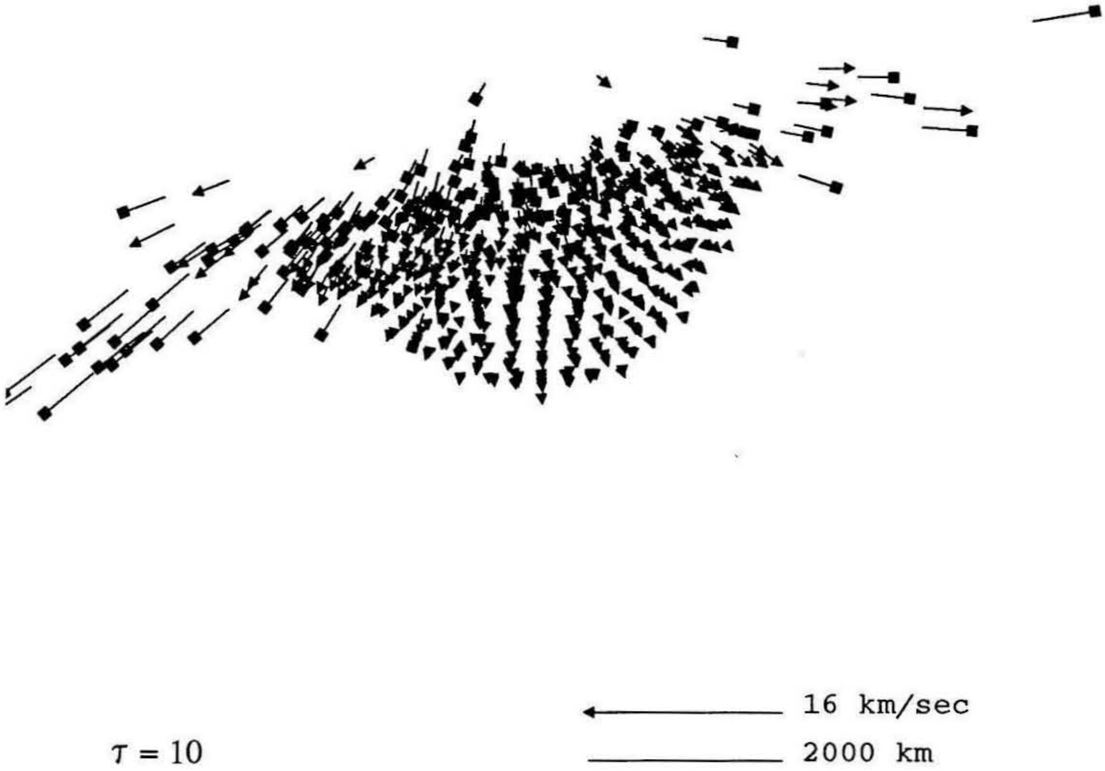

Figure A.18: Impact of the 60% impactor at 15° and 5 km/s on the 1700 km target at time τ=10.

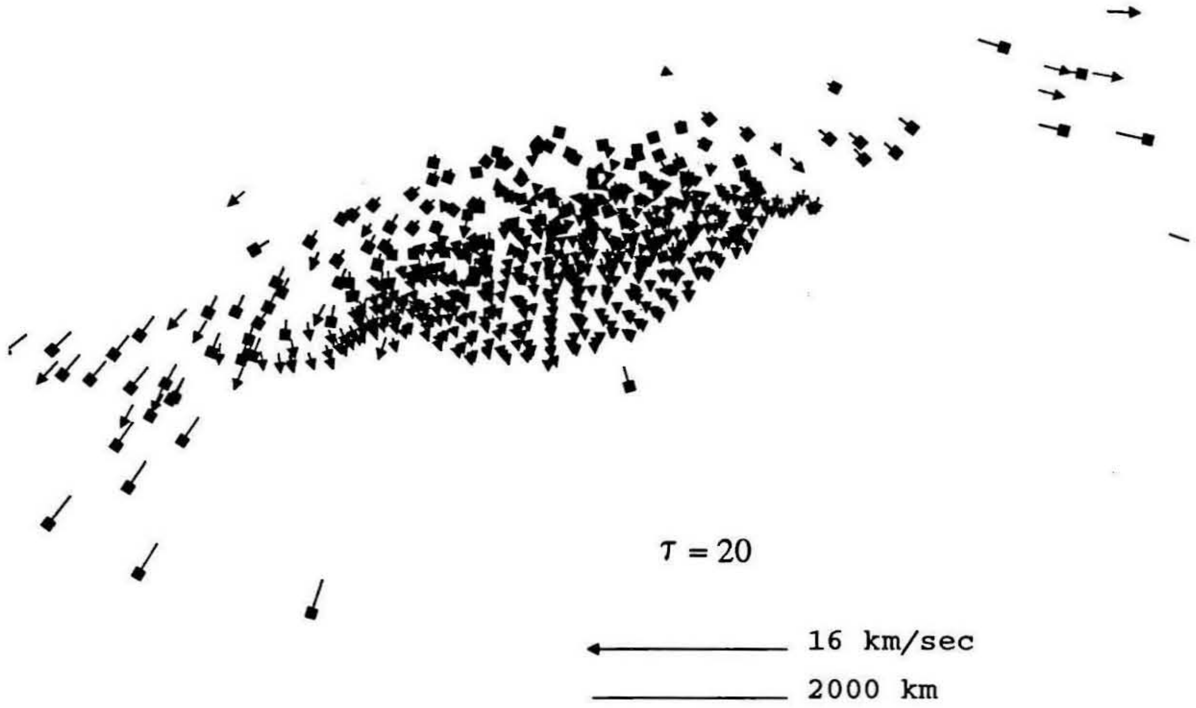

Figure A.19: Impact of the 60% impactor at 15° and 5 km/s on the 1700 km target at time τ=20.

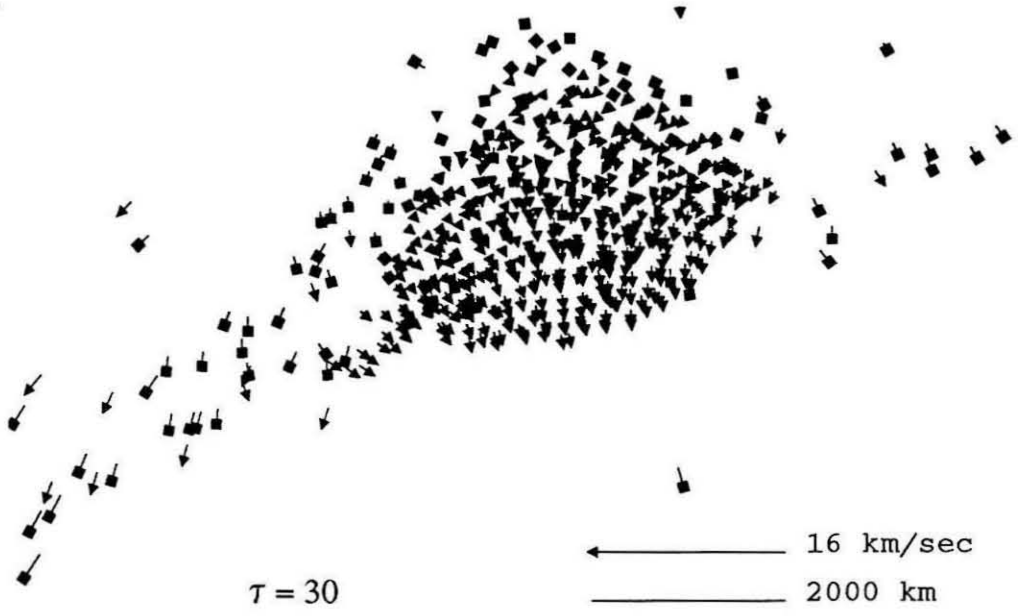

Figure A.20: Impact of the 60% impactor at 15° and 5 km/s on the 1700 km target at time τ=30.

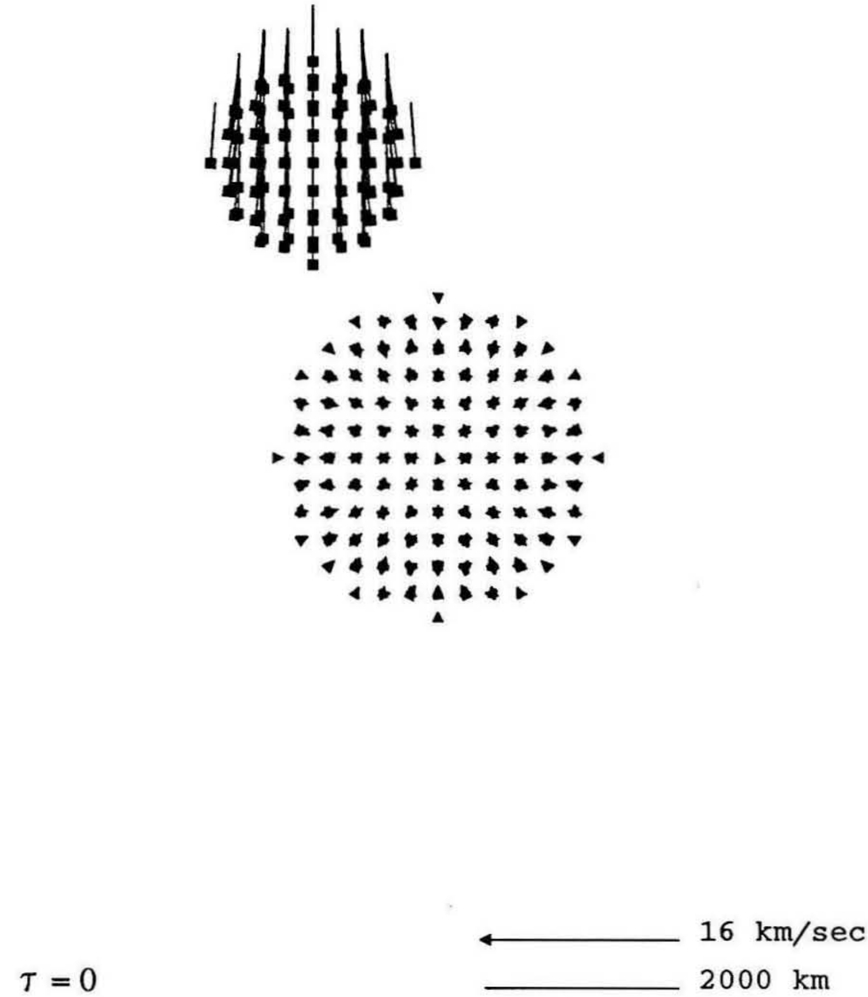

Figure A.21: Impact of the 60% impactor at 50° and 5 km/s on the 1700 km target (initial configuration).

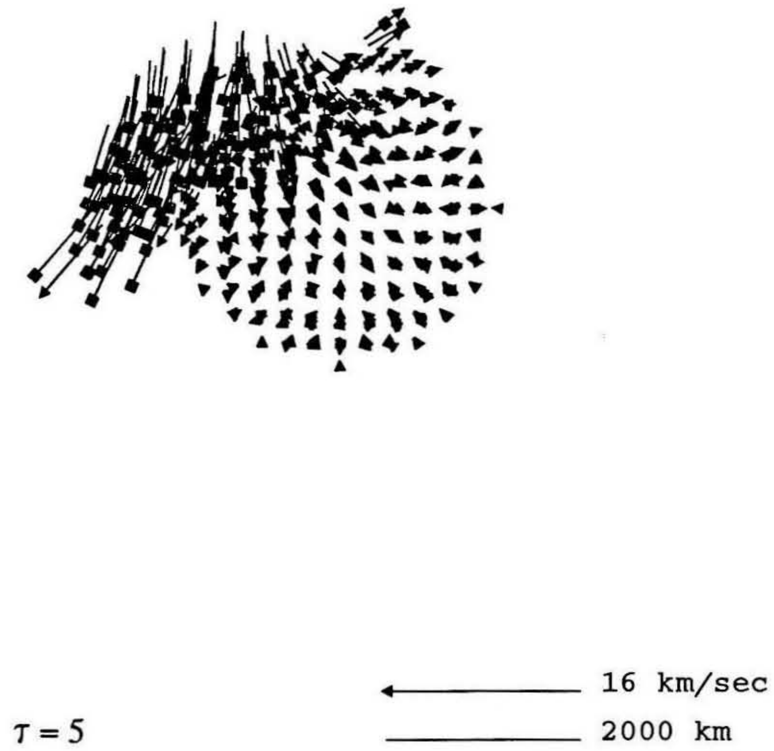

Figure A.22: Impact of the 60% impactor at 50° and 5 km/s on the 1700 km target at time τ=5.

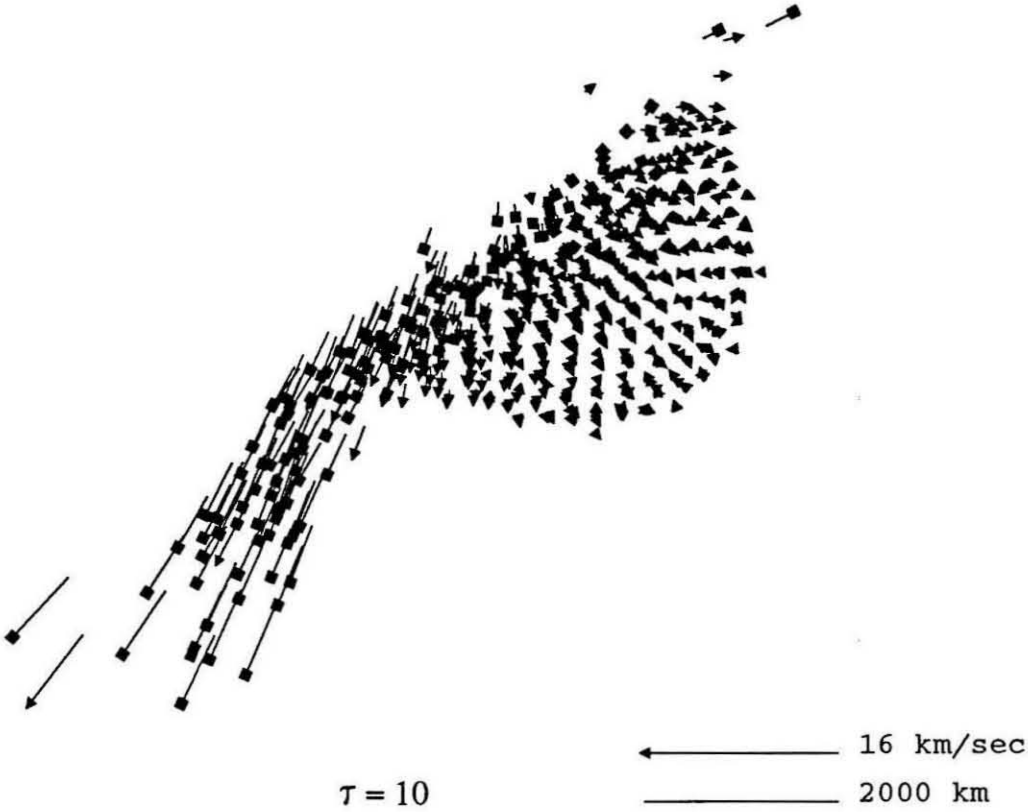

Figure A.23: Impact of the 60% impactor at 50° and 5 km/s on the 1700 km target at time τ=10.

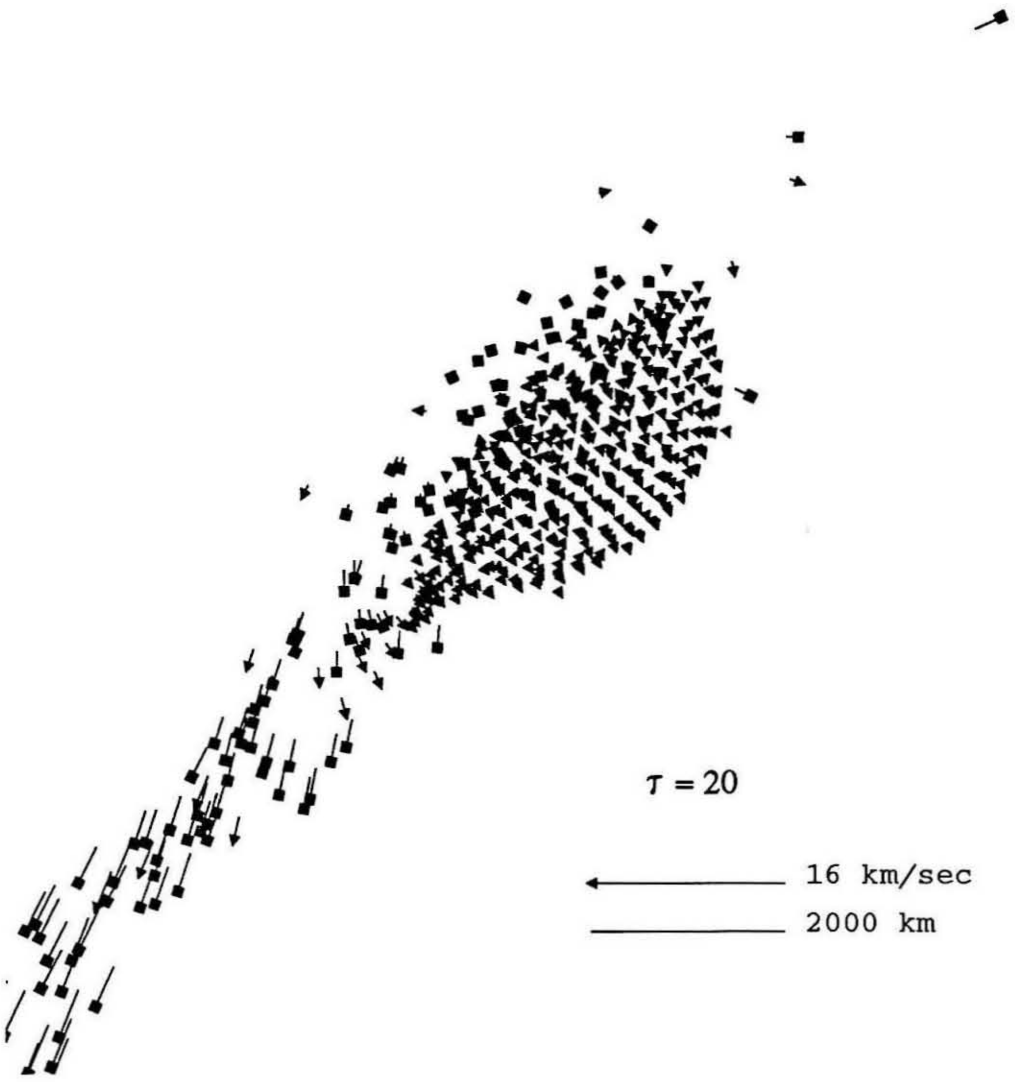

Figure A.24: Impact of the 60% impactor at 50° and 5 km/s on the 1700 km target at time τ=20.

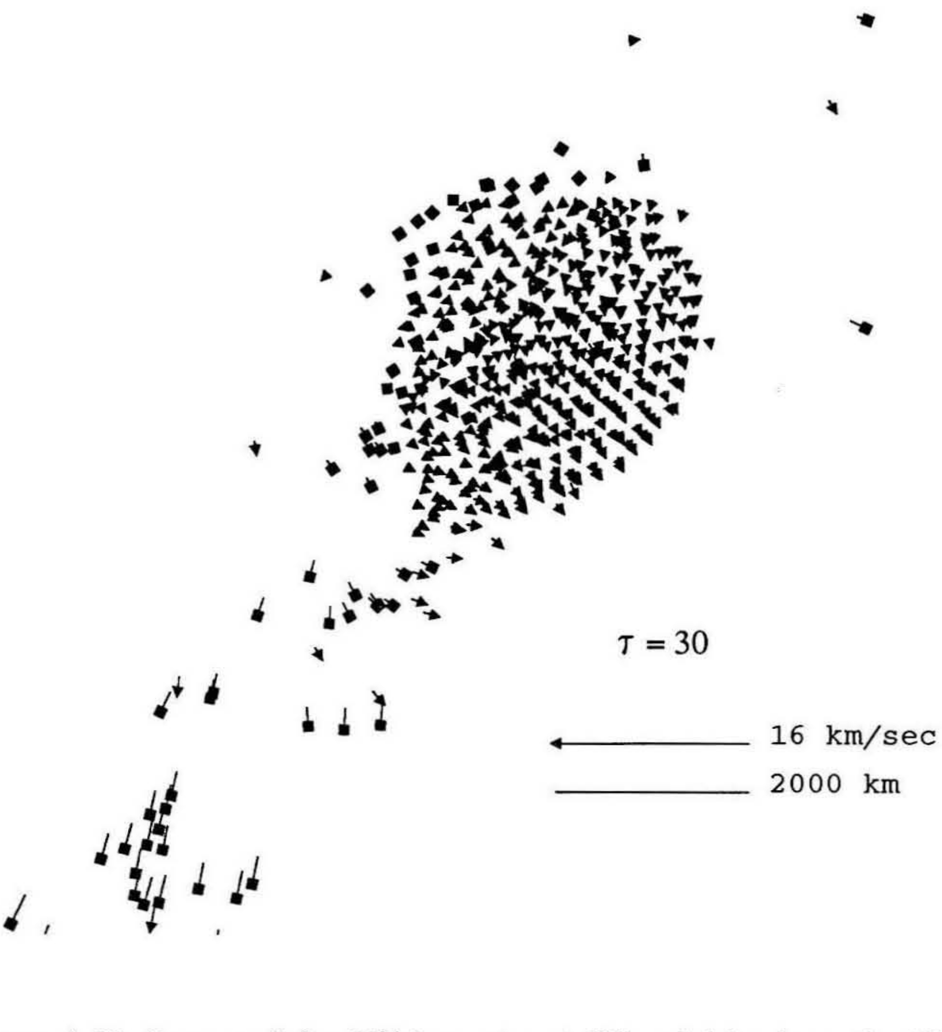

Figure A.25: Impact of the 60% impactor at 50° and 5 km/s on the 1700 km target at time τ=30.

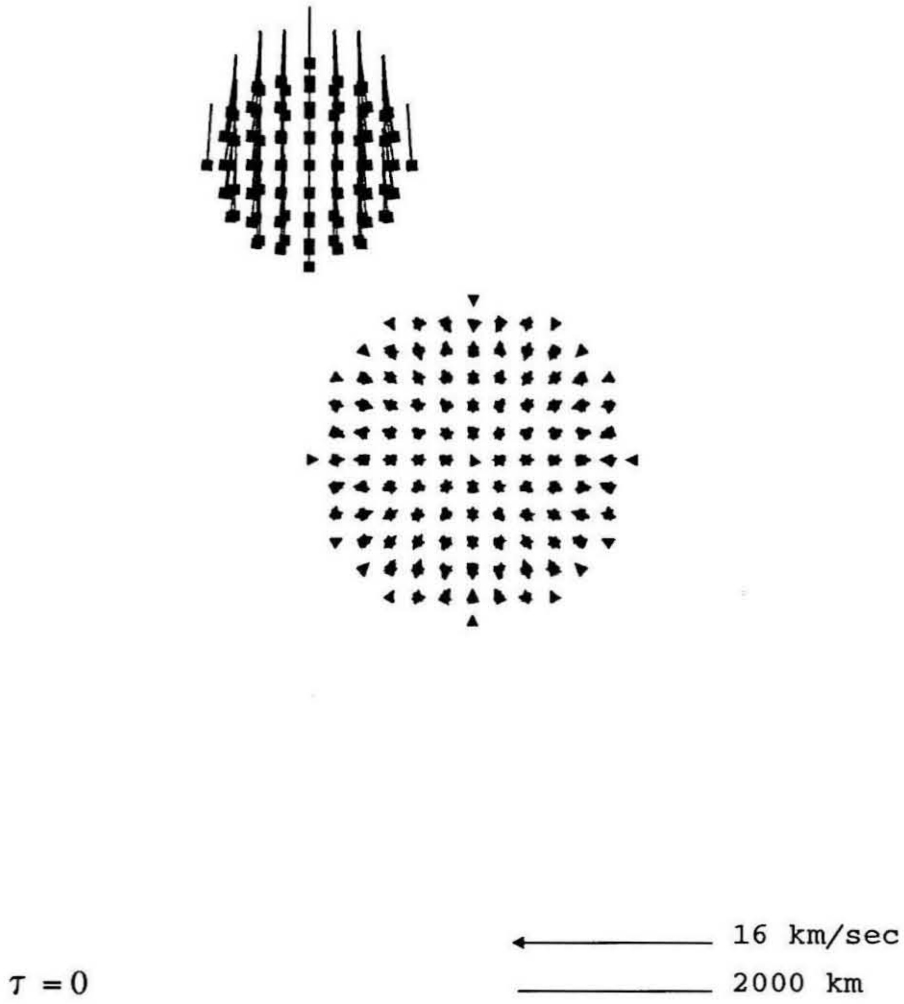

Figure A.26: Impact of the 60% impactor at 90° and 5 km/s on the 1700 km target (initial configuration).

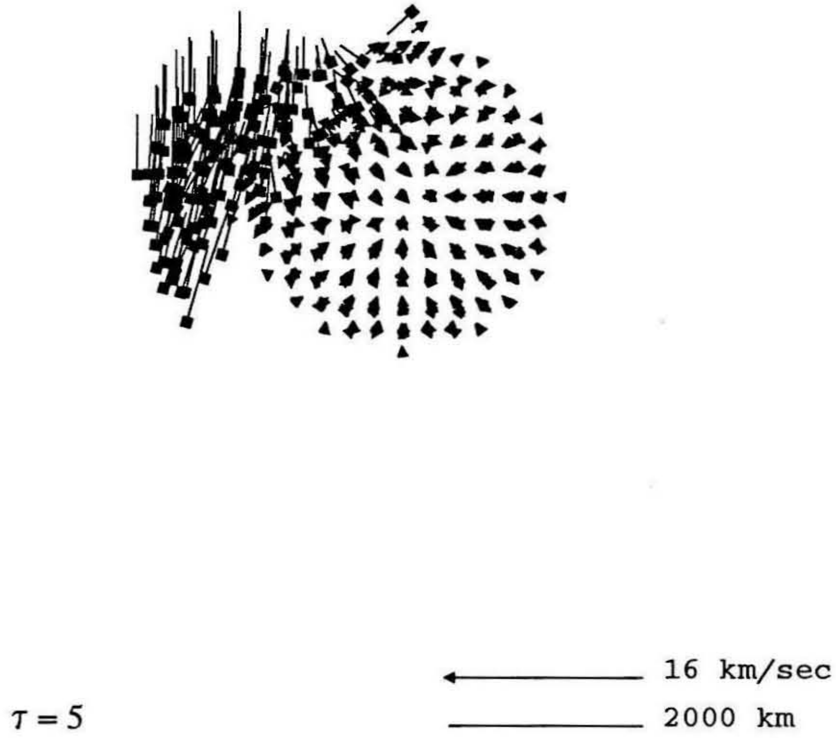

Figure A.27: Impact of the 60% impactor at 90° and 5 km/s on the 1700 km target at time τ=5.

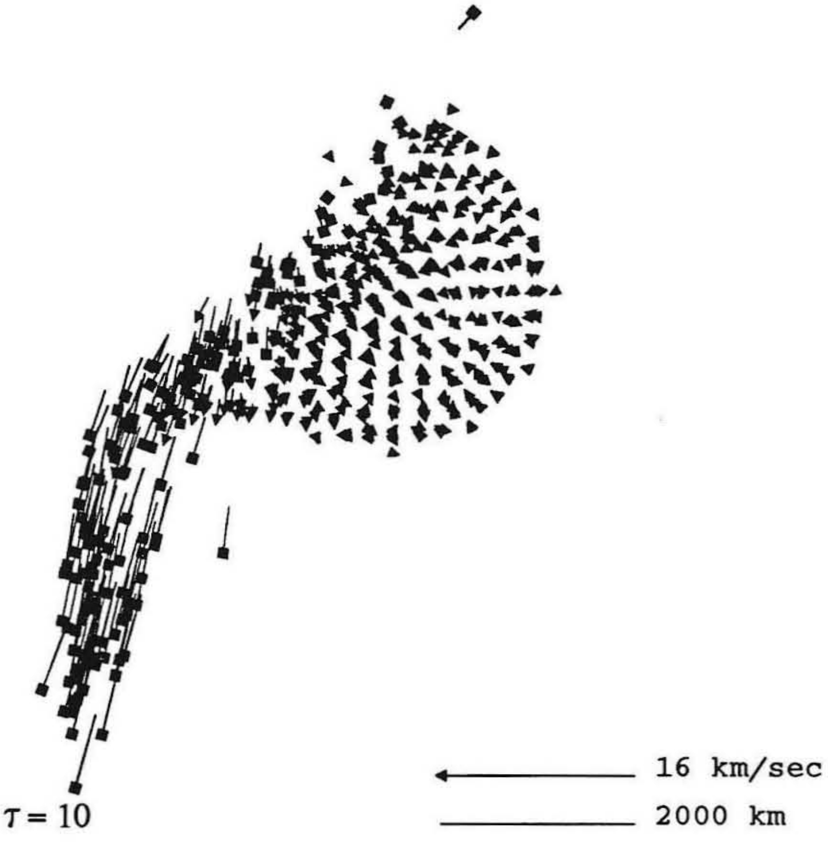

Figure A.28: Impact of the 60% impactor at 90° and 5 km/s on the 1700 km target at time τ=10.

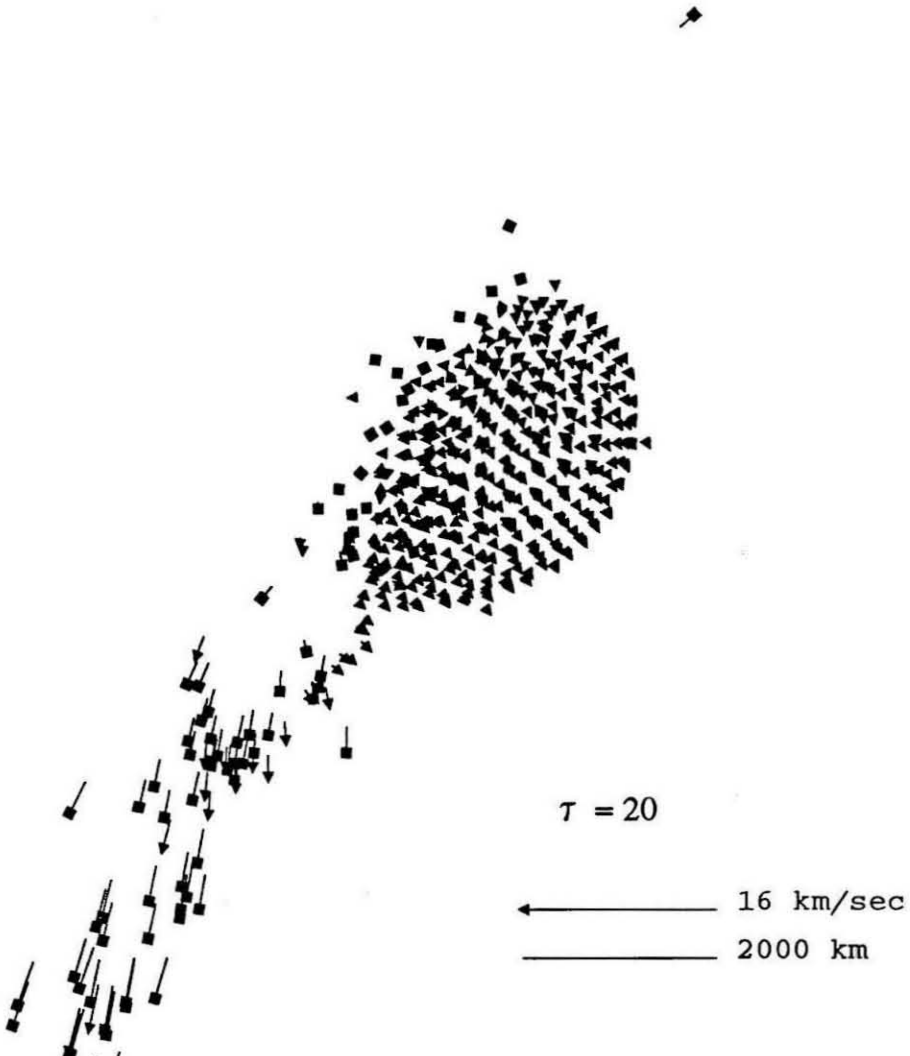

Figure A.29: Impact of the 60% impactor at 90° and 5 km/s on the 1700 km target at time τ=20.

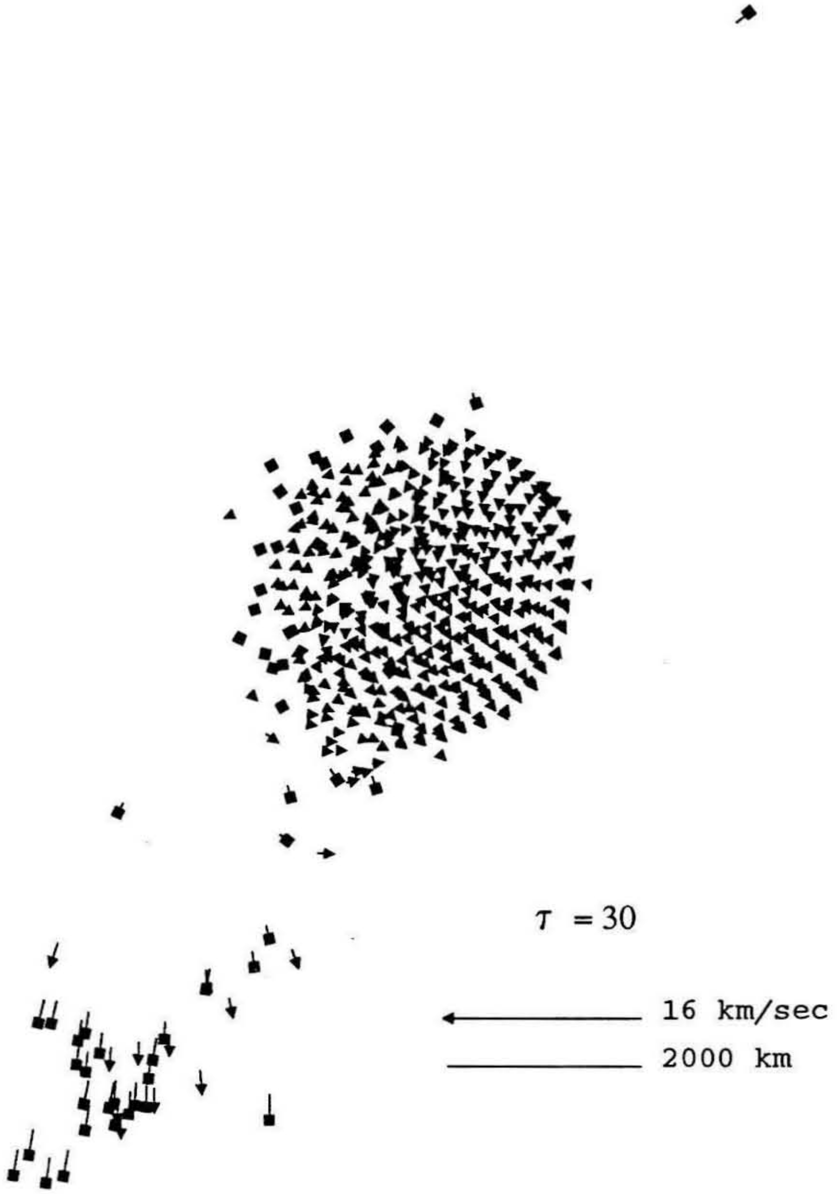

Figure A.30: Impact of the 60% impactor at 90° and 5 km/s on the 1700 km target at time τ=30.

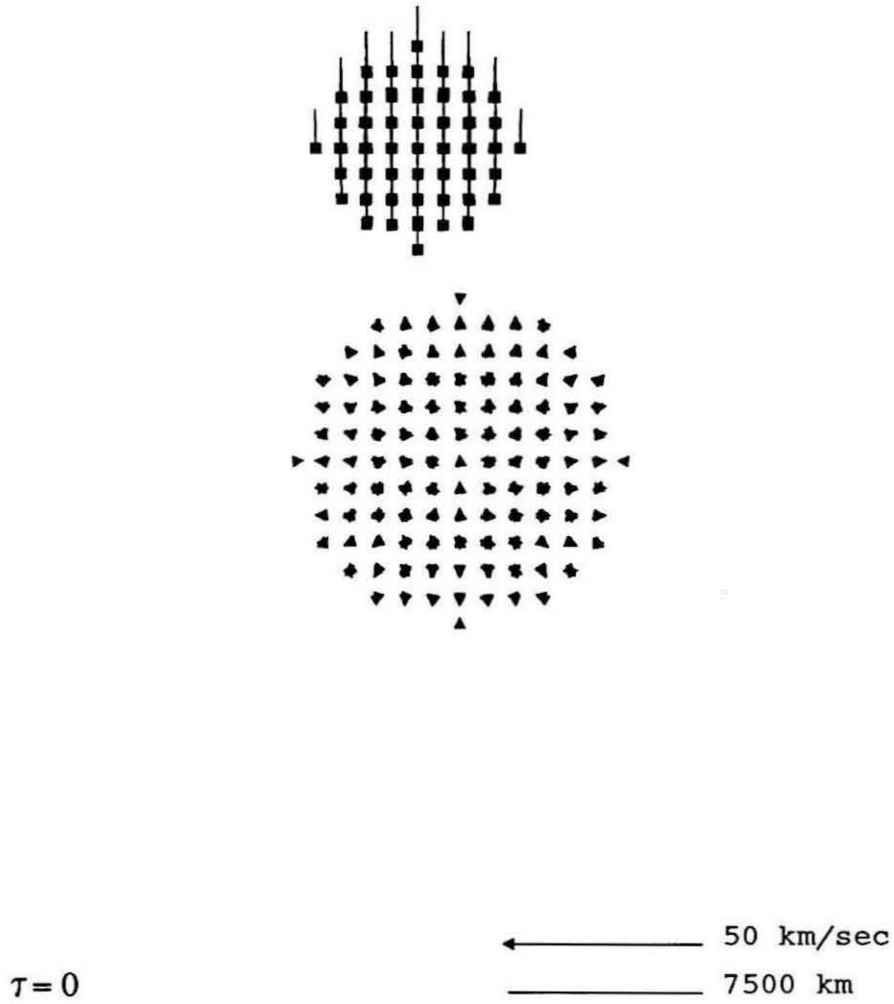

Figure A.31: Impact of the 60% impactor at 15° and 10 km/s on the 6400 km target (initial configuration).

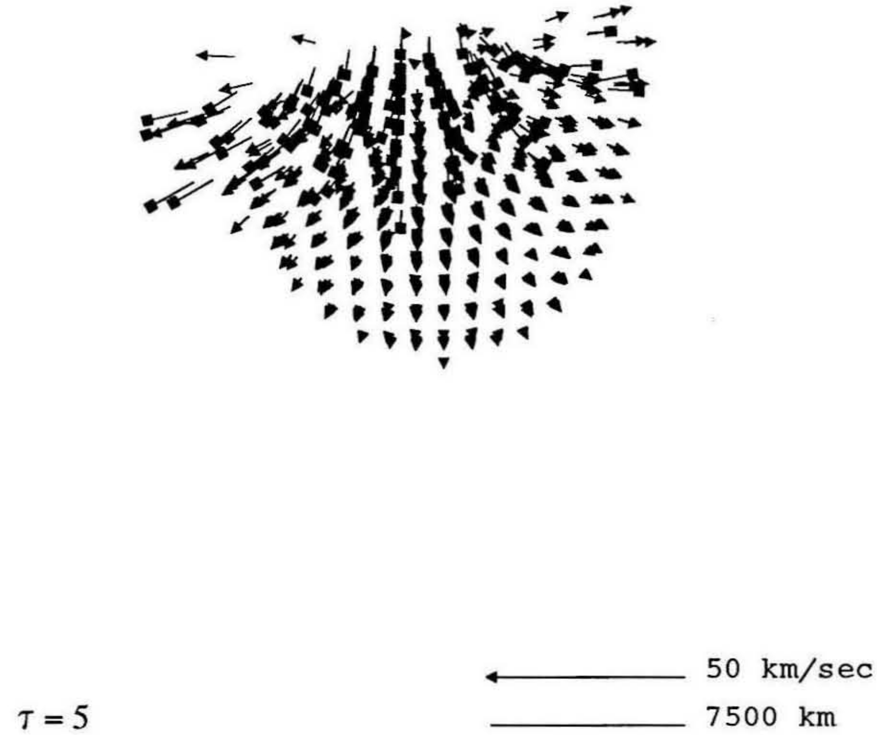

Figure A.32: Impact of the 60% impactor at 15° and 10 km/s on the 6400 km target at time τ=5.

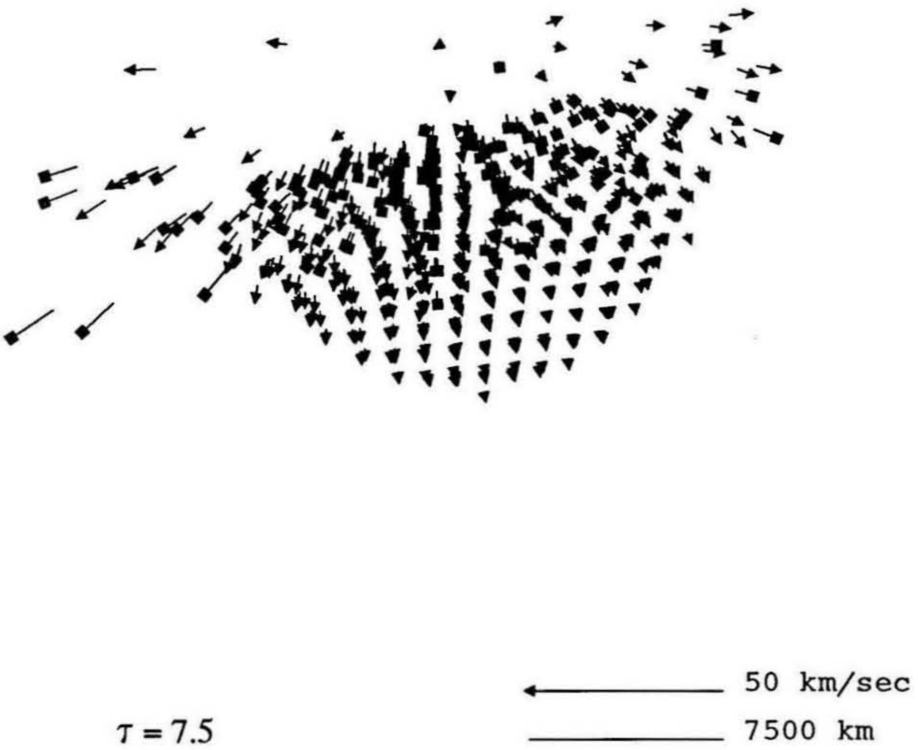

Figure A.33: Impact of the 60% impactor at 15° and 10 km/s on the 6400 km target at time τ=7.5.

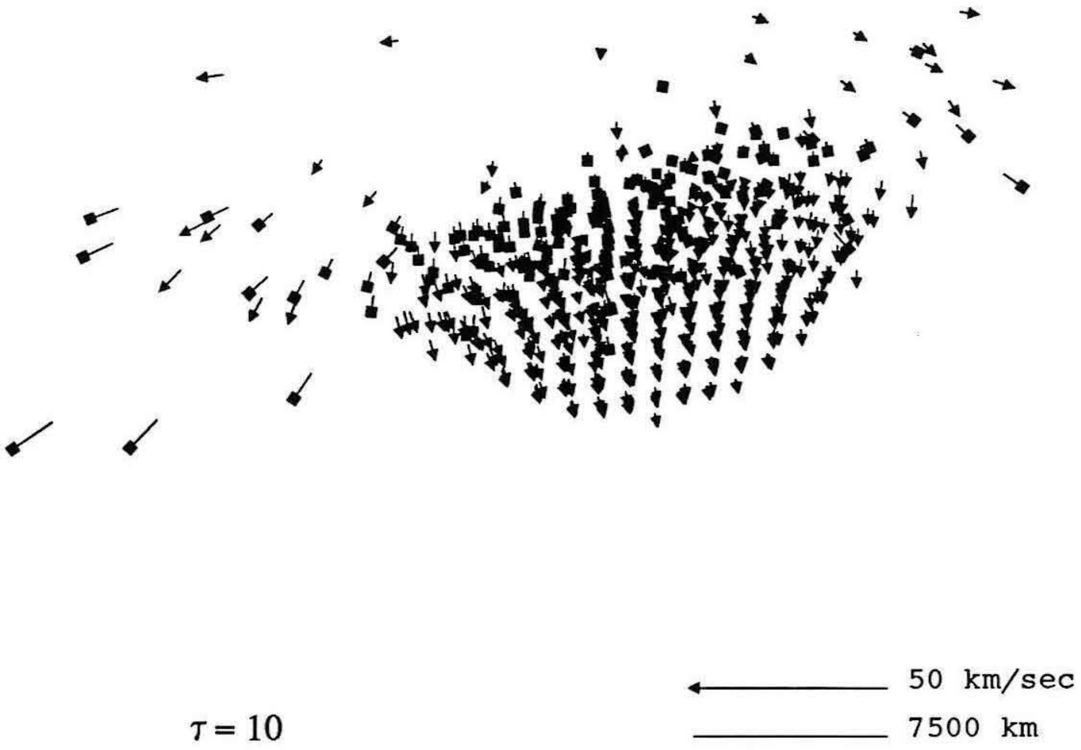

Figure A.34: Impact of the 60% impactor at 15° and 10 km/s on the 6400 km target at time τ=10.

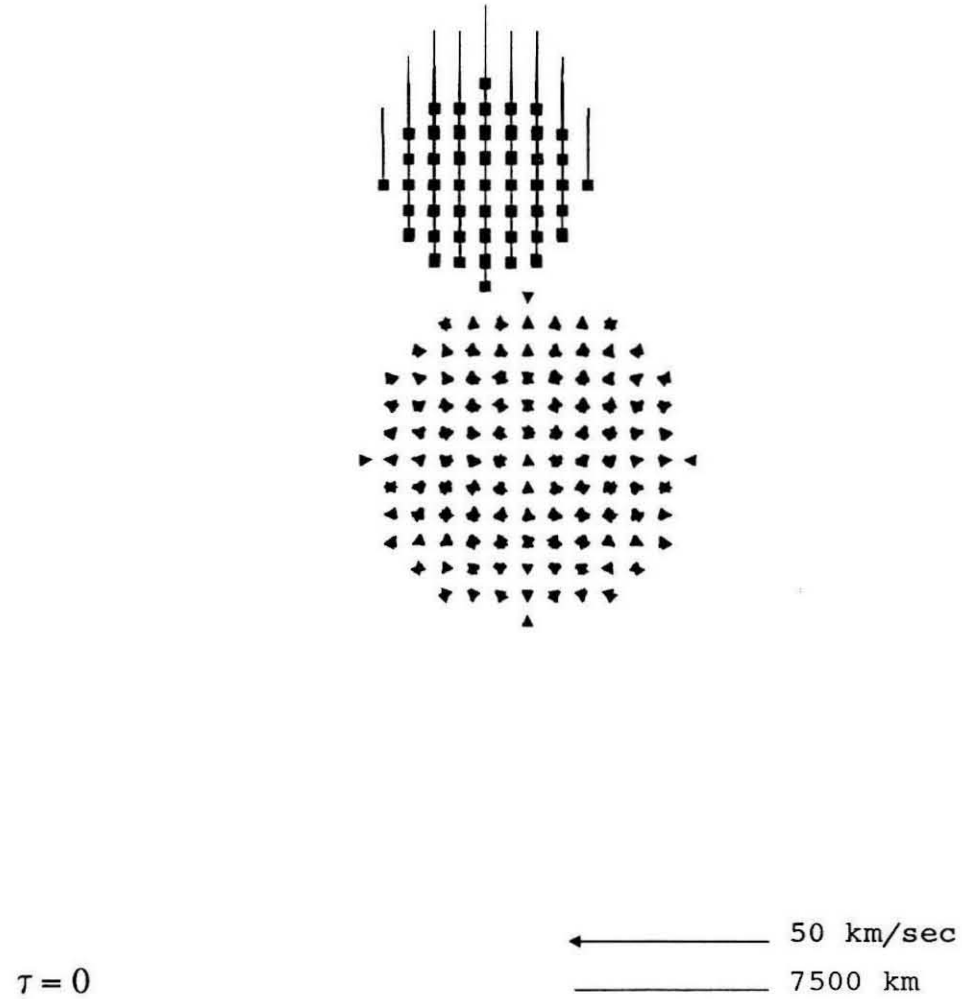

Figure A.35: Impact of the 60% impactor at 15° and 20 km/s on the 6400 km target (initial configuration).

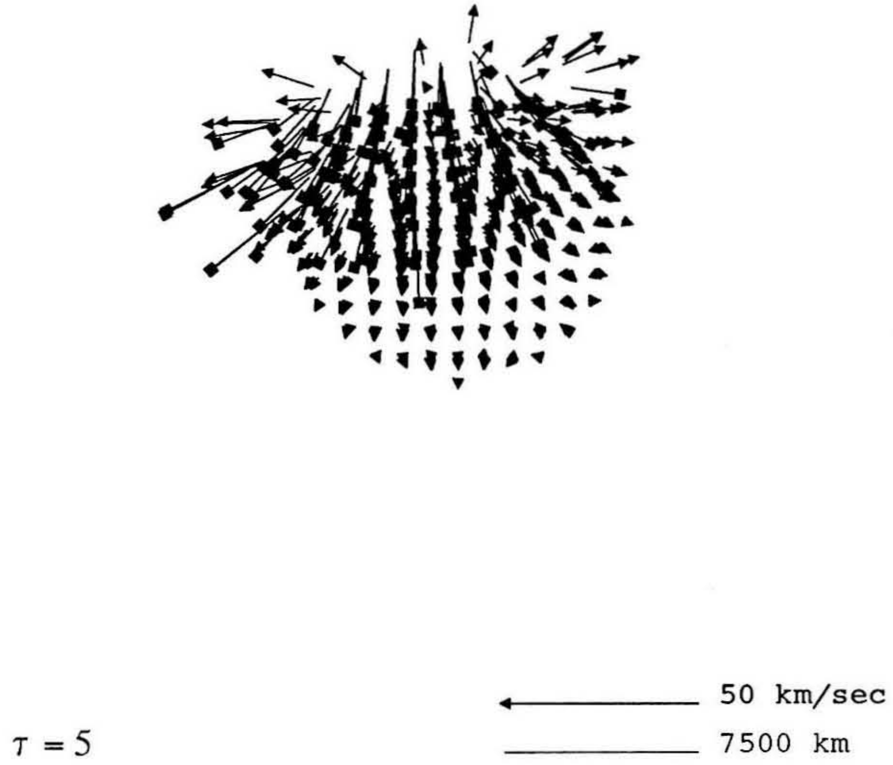

Figure A.36: Impact of the 60% impactor at 15° and 20 km/s on the 6400 km target at time τ=5.

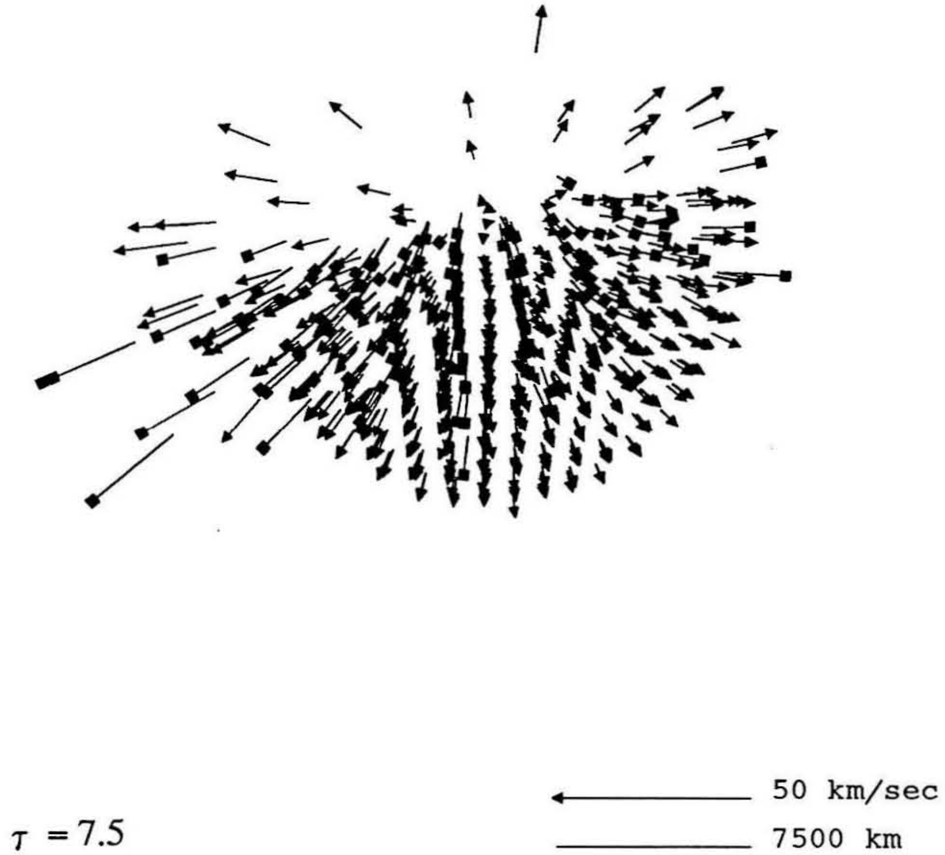

Figure A.37: Impact of the 60% impactor at 15° and 20 km/s on the 6400 km target at time τ=7.5.

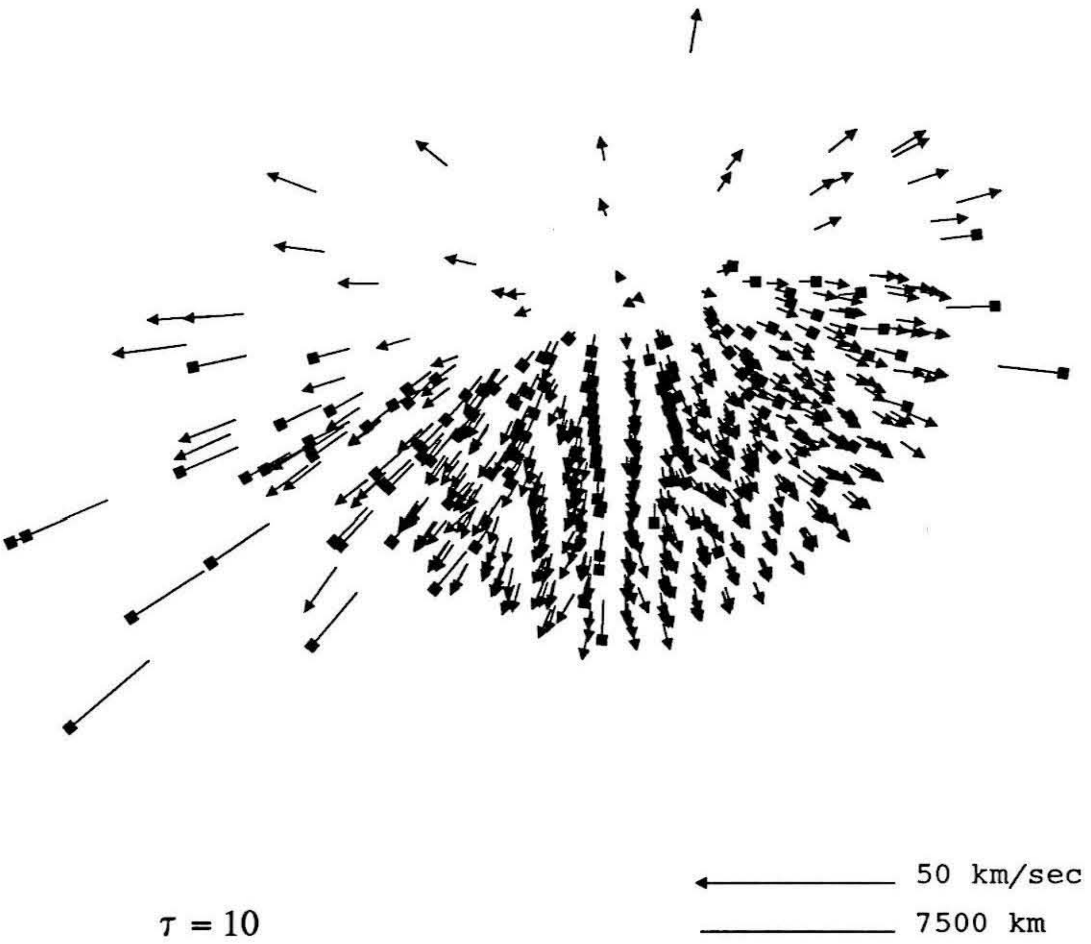

Figure A.38: Impact of the 60% impactor at 15° and 20 km/s on the 6400 km target at time τ=10.

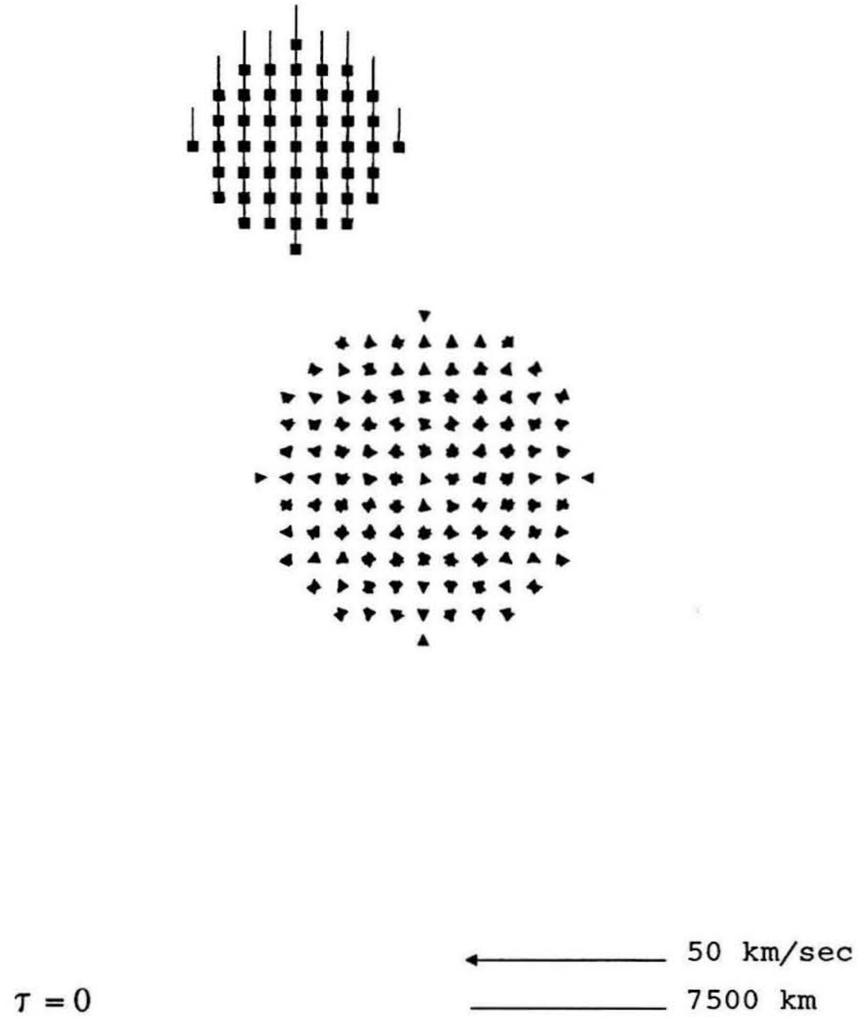

Figure A.39: Impact of the 60% impactor at 50° and 10 km/s on the 6400 km target (initial configuration).

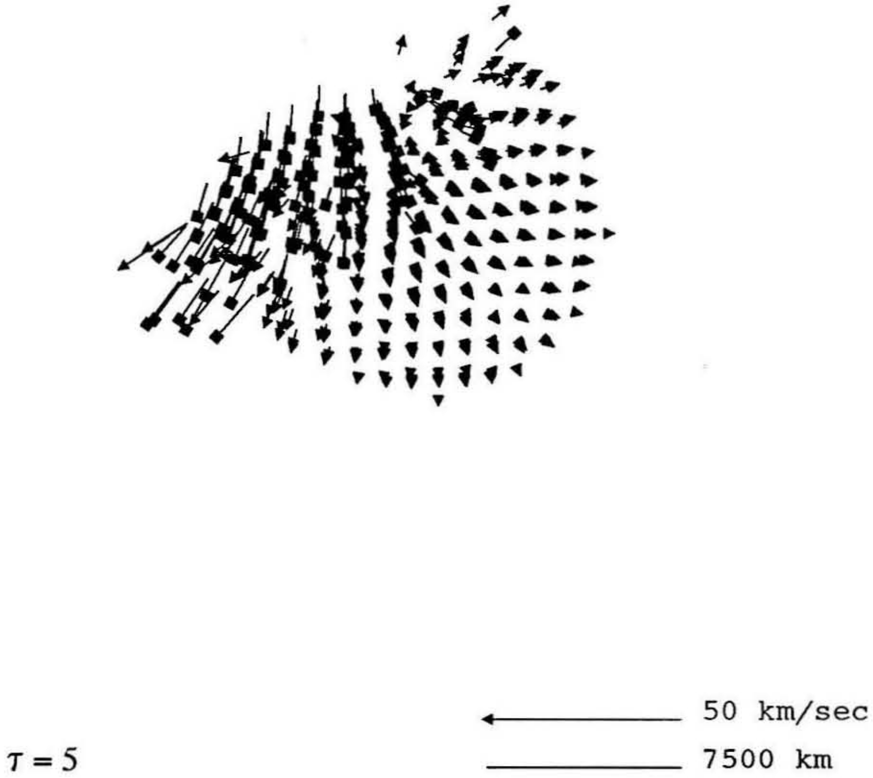

Figure A.40: Impact of the 60% impactor at 50° and 20 km/s on the 6400 km target at time τ=5.

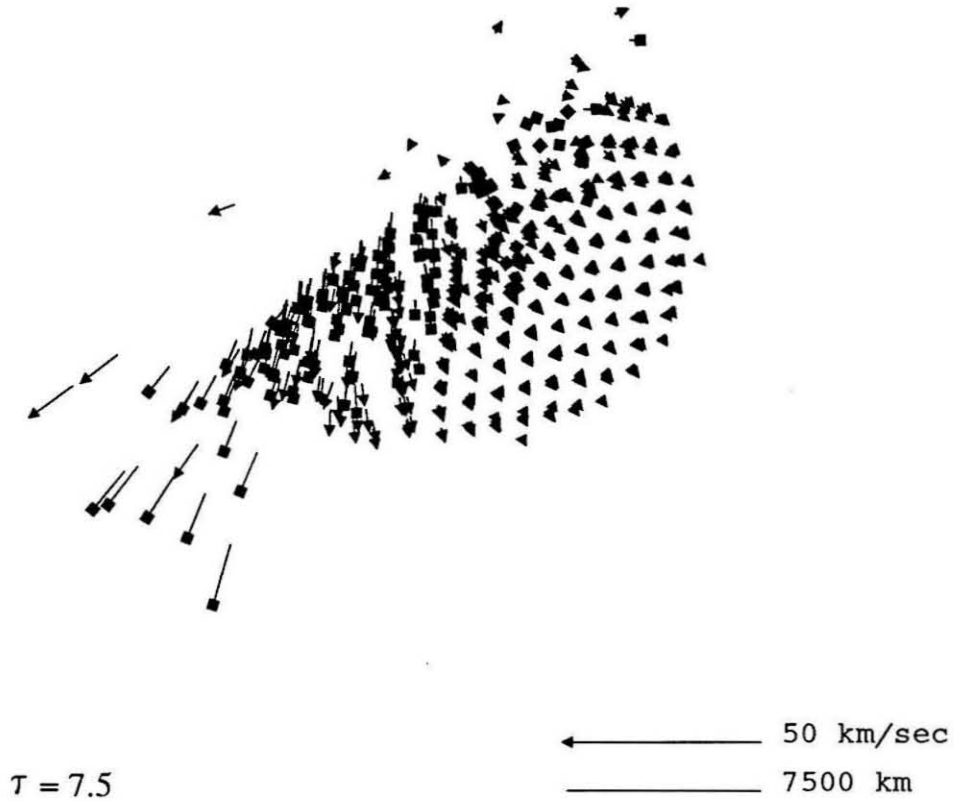

Figure A.41: Impact of the 60% impactor at 50° and 10 km/s on the 6400 km target at time τ=7.5.

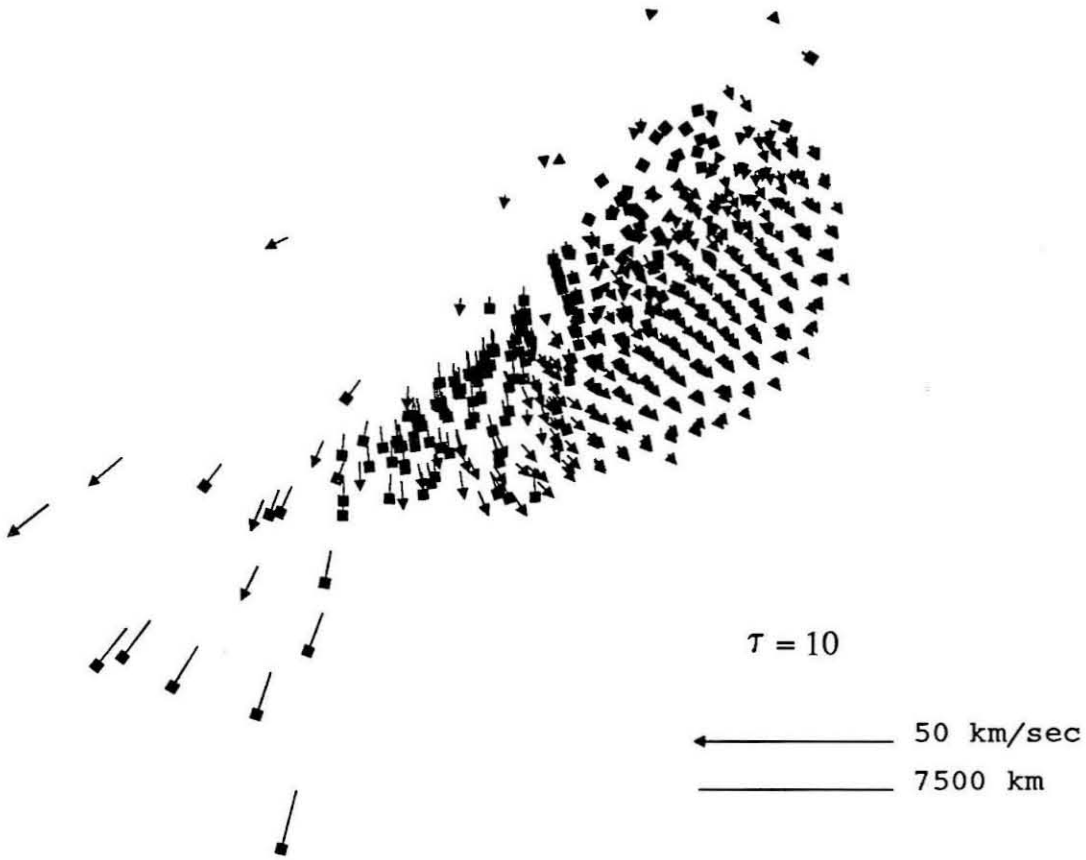

Figure A.42: Impact of the 60% impactor at 50° and 10 km/s on the 6400 km target at time τ=10.

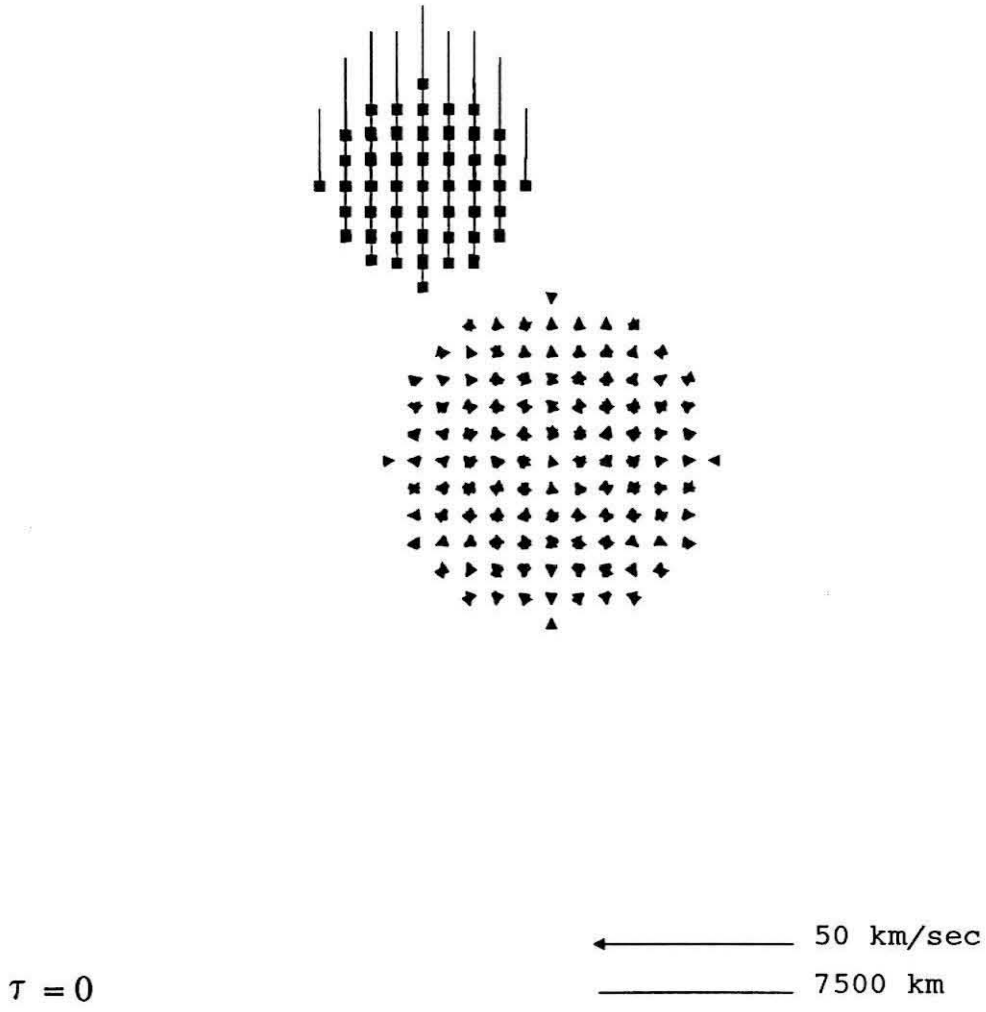

Figure A.43: Impact of the 60% impactor at 50° and 20 km/s on the 6400 km target (initial configuration).

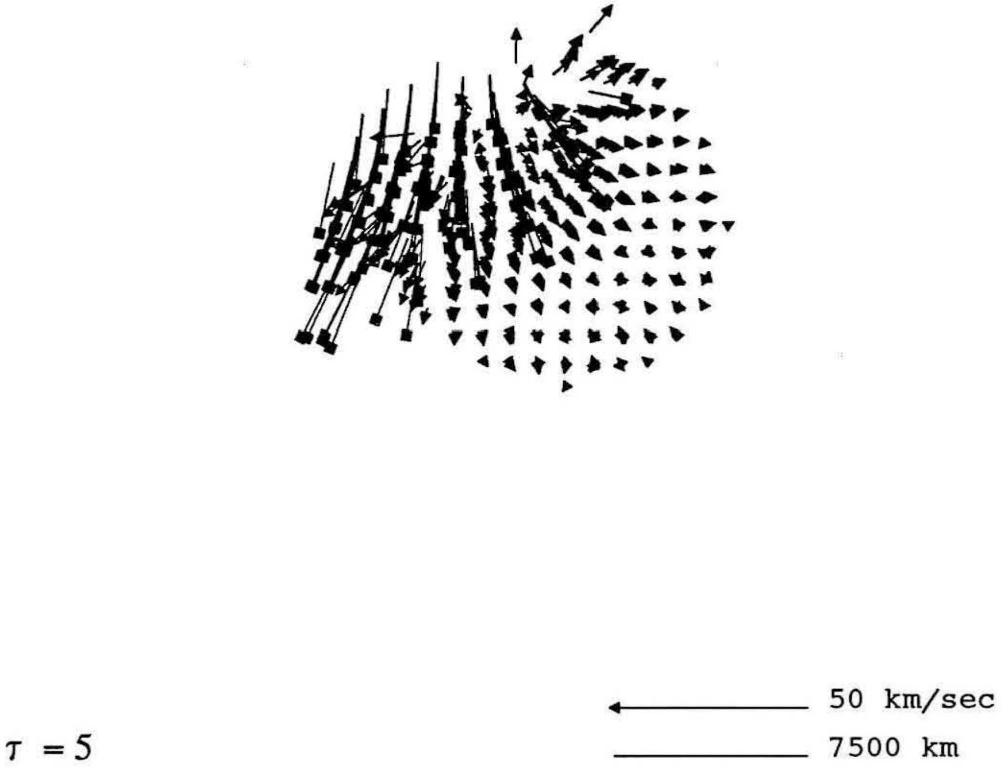

Figure A.44: Impact of the 60% impactor at 50° and 20 km/s on the 6400 km target at time τ=5.

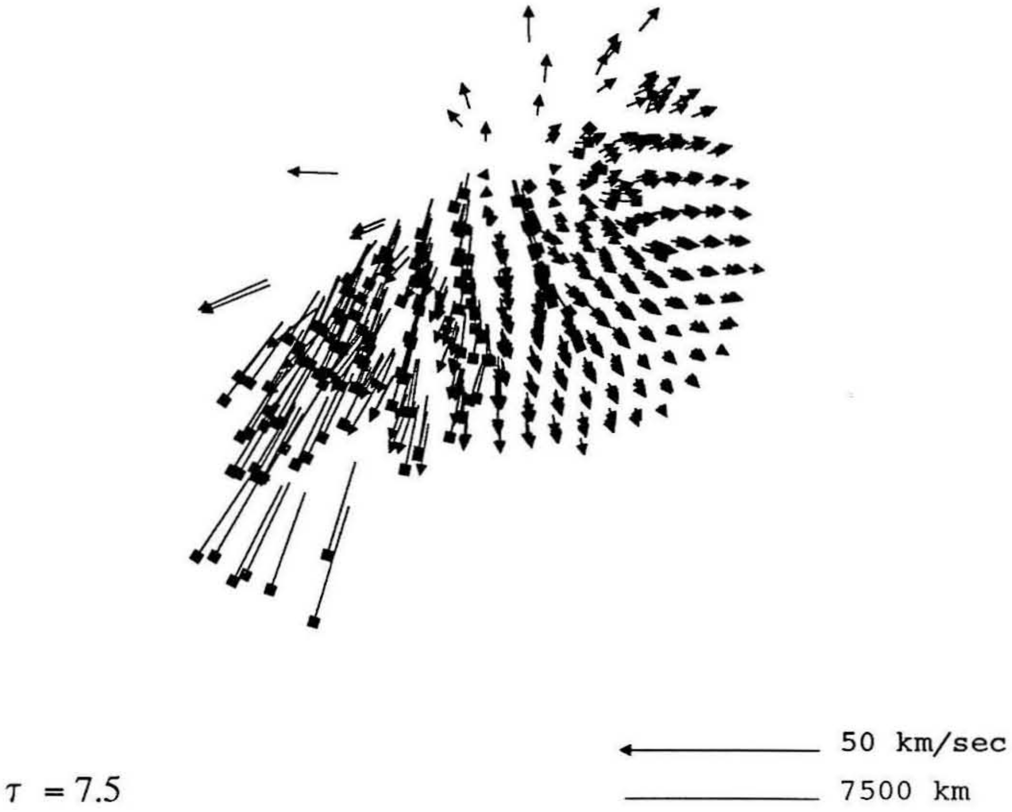

Figure A.45: Impact of the 60% impactor at 50° and 20 km/s on the 6400 km target at time τ=7.5.

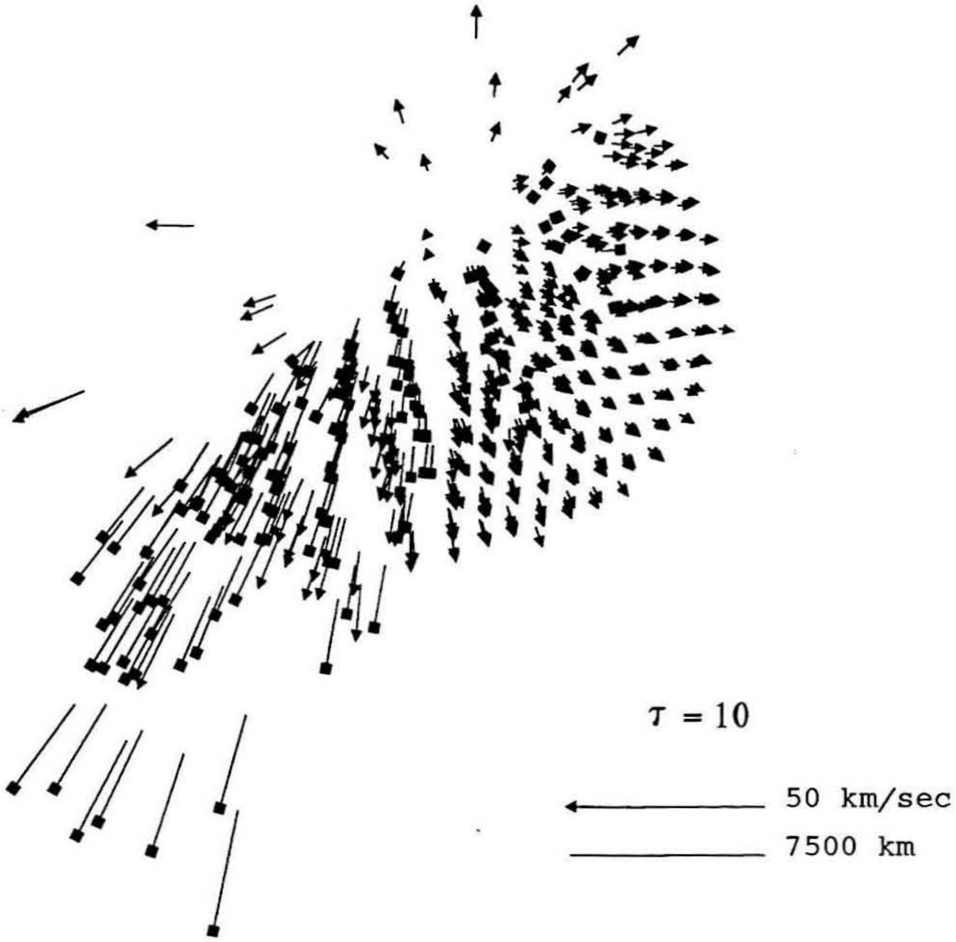

Figure A.46: Impact of the 60% impactor at 50° and 20 km/s on the 6400 km target at time τ=10.

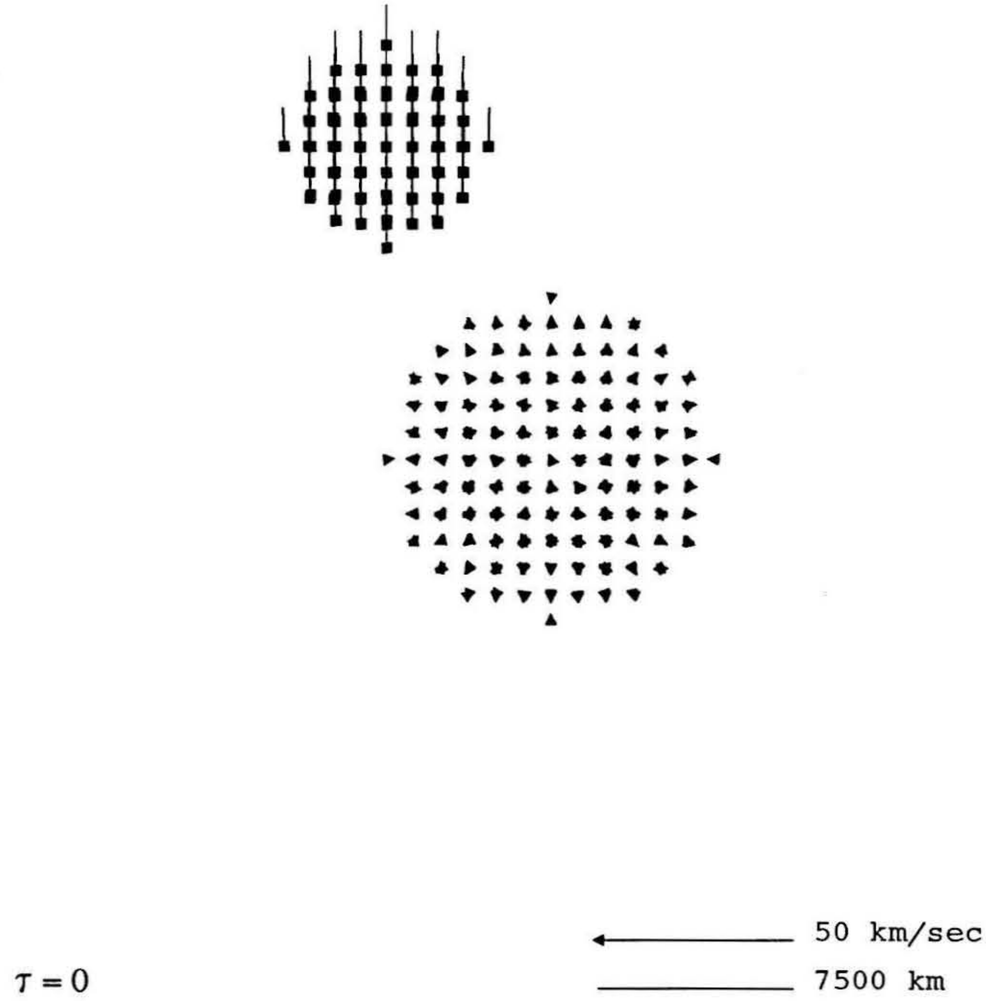

Figure A.47: Impact of the 60% impactor at 90° and 10 km/s on the 6400 km target (initial configuration).

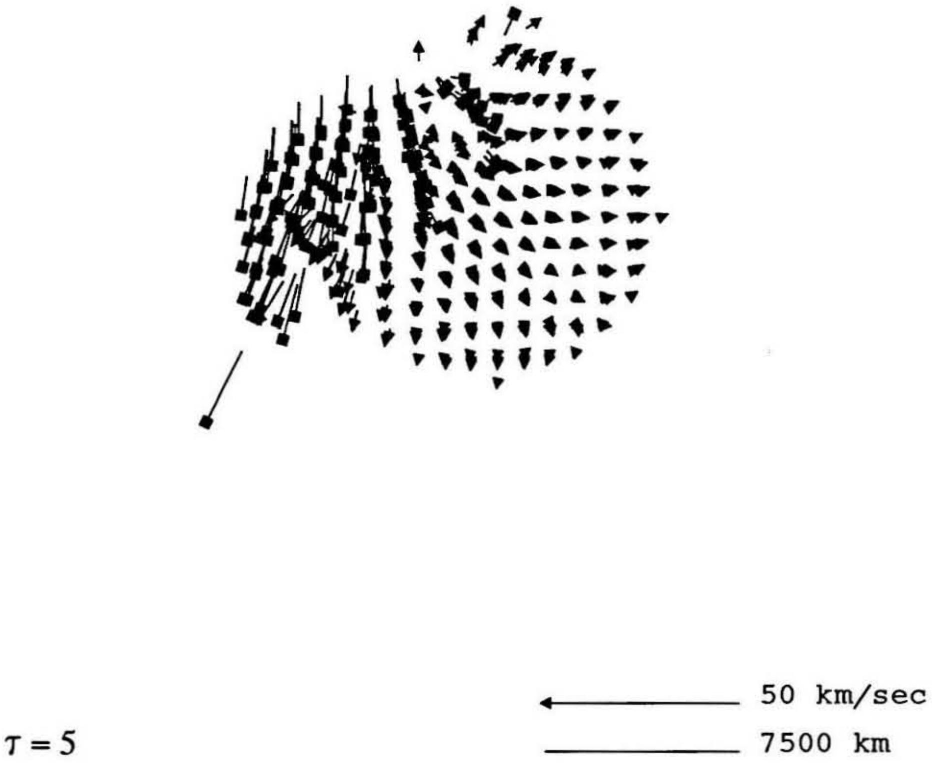

Figure A.48: Impact of the 60% impactor at 90° and 10 km/s on the 6400 km target at time τ=5.

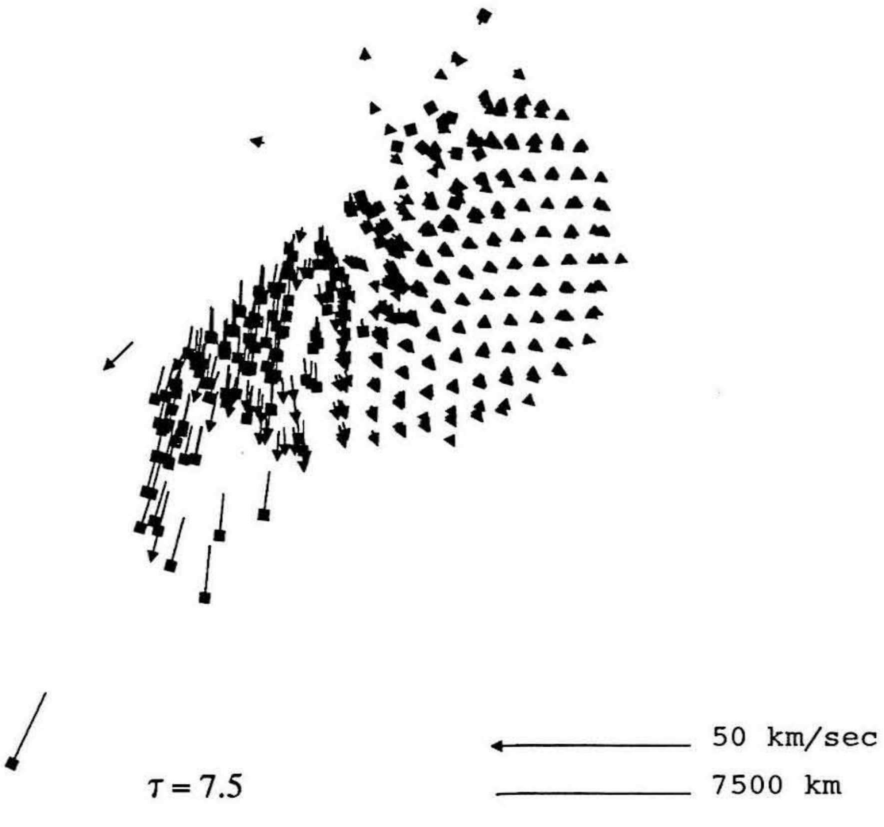

Figure A.49: Impact of the 60% impactor at 90° and 10 km/s on the 6400 km target at time τ=7.5.

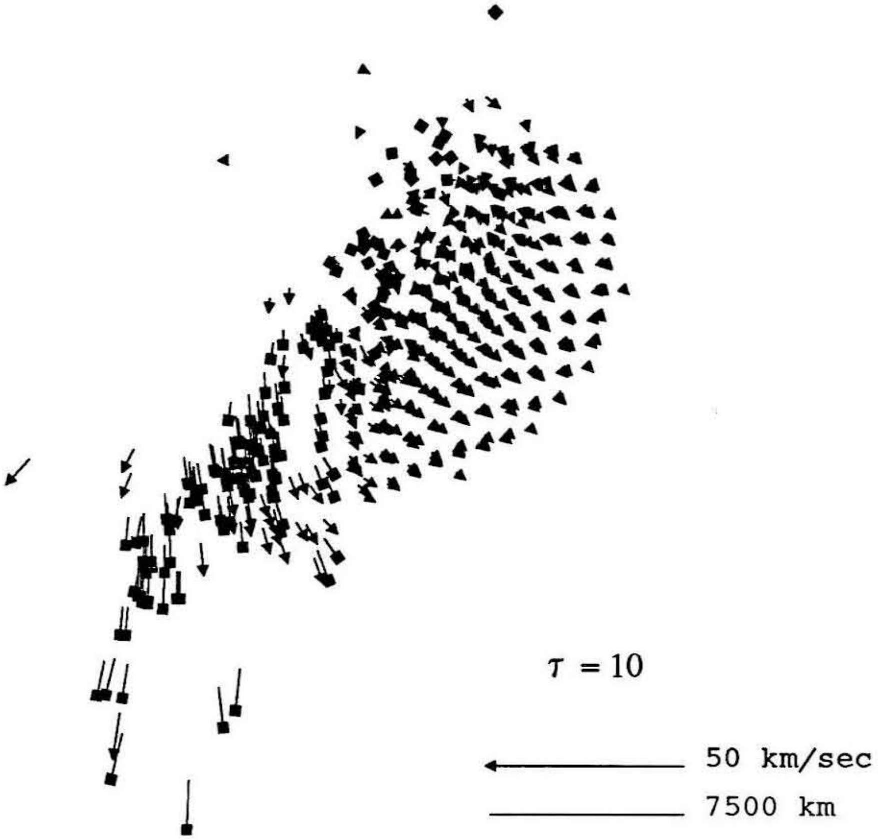

Figure A.50: Impact of the 60% impactor at 90° and 10 km/s on the 6400 km target at time τ=10.

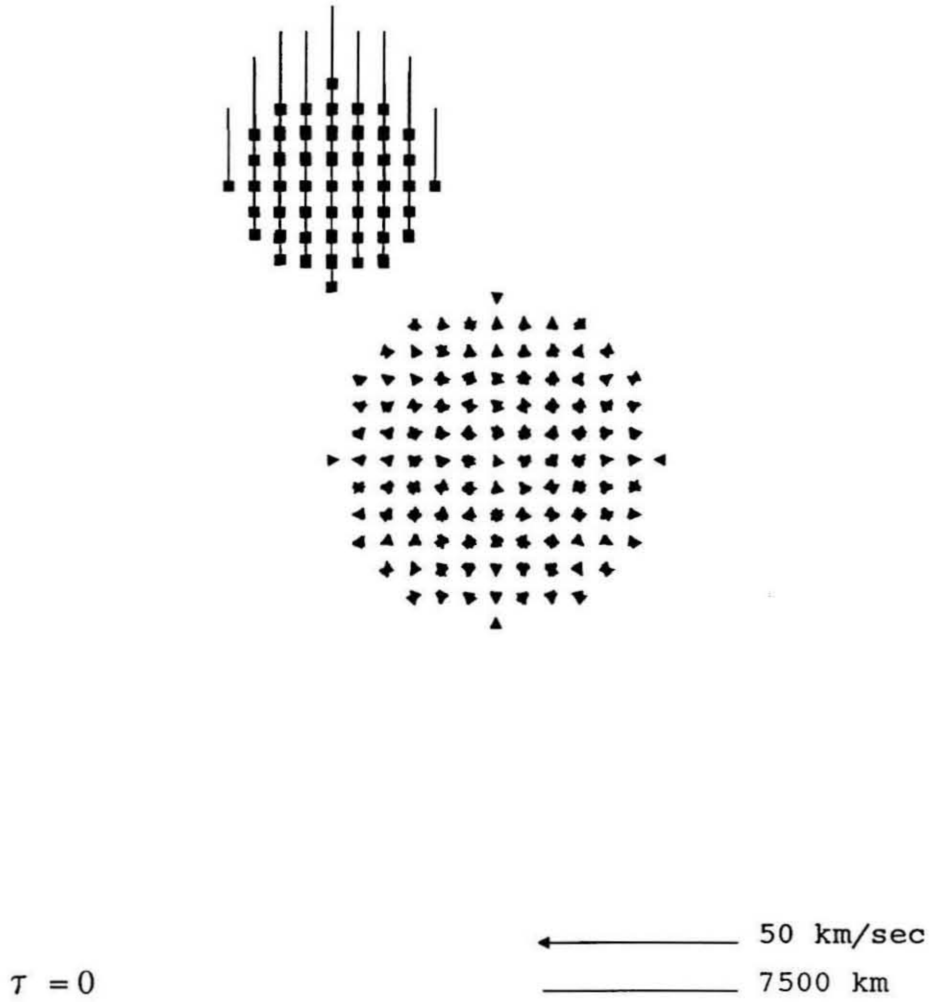

Figure A.51: Impact of the 60% impactor at 90° and 20 km/s on the 6400 km target (initial configuration).

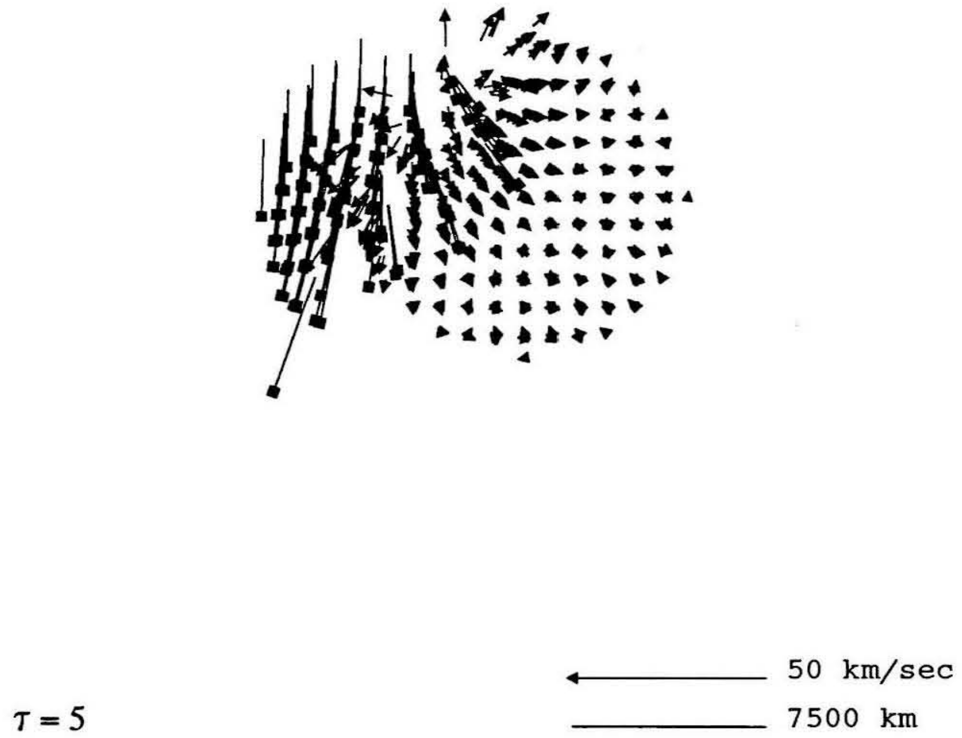

Figure A.52: Impact of the 60% impactor at 90° and 20 km/s on the 6400 km target at time τ=5.

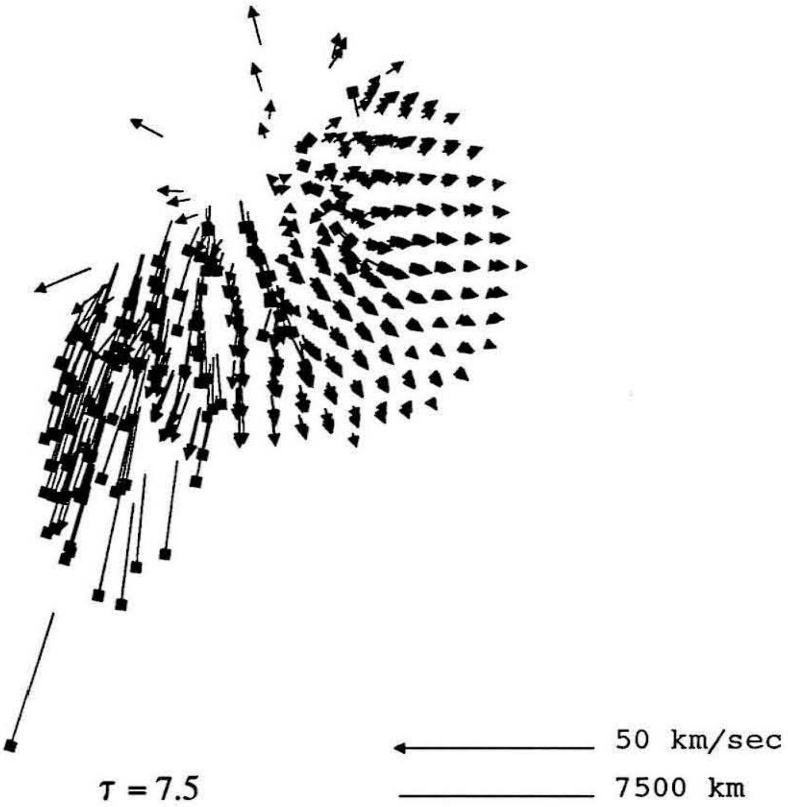

Figure A.53: Impact of the 60% impactor at 90° and 20 km/s on the 6400 km target at time τ=7.5.

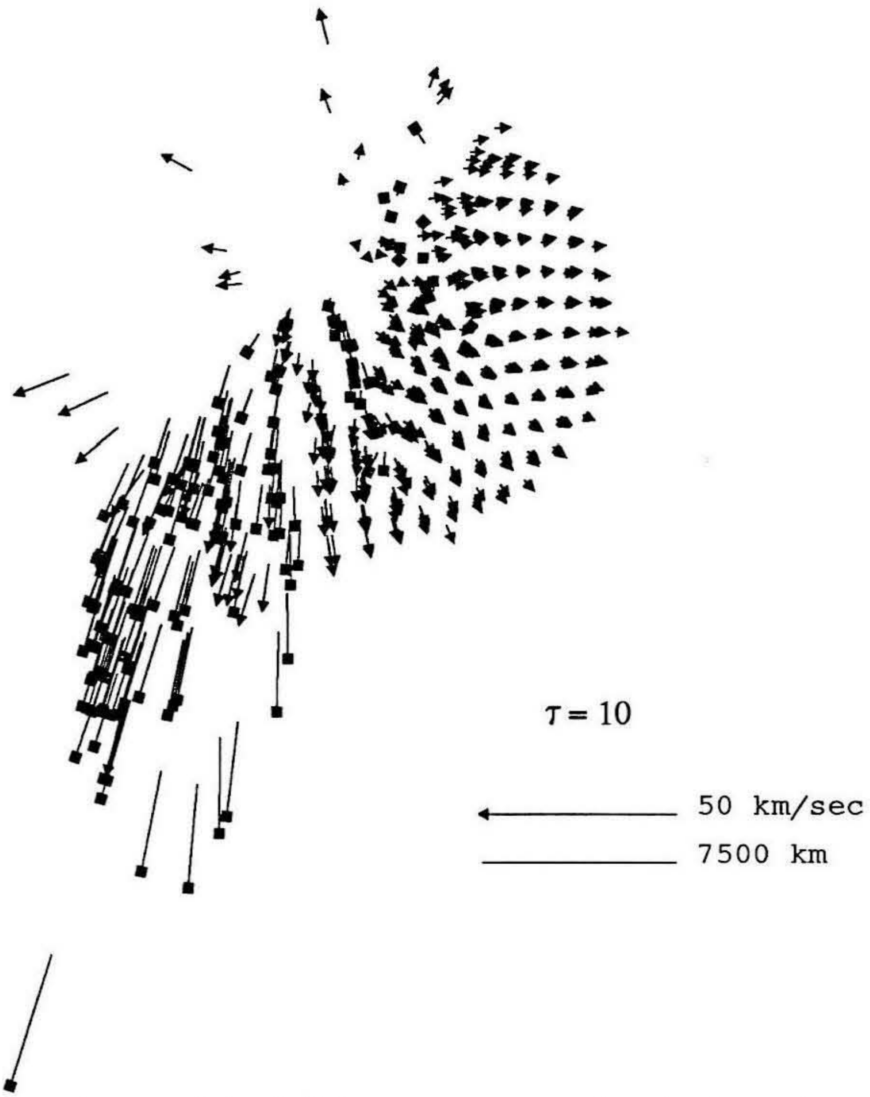

Figure A.54: Impact of the 60% impactor at 90° and 20 km/s on the 6400 km target at time τ=10.

Appendix B

Melt and vapor production tables

Melt production for 1700 km targets 40% impactor						
Impact velocity	Impact angle	Target mass partially melted				
		1%	10%	50%	90%	100%
5 km/s	5°	.043	.043	.038	.037	.037
	15°	.044	.044	.041	.031	.027
	30°	.035	.035	.035	.026	.026
	50°	.032	.032	.023	.022	.022
	90°	.018	.018	.017	.015	.015
10 km/s	0°	.17	.17	.16	.15	.15
	5°	.17	.16	.15	.13	.12
	15°	.15	.15	.14	.12	.12
	30°	.13	.13	.12	.11	.11
	50°	.12	.12	.11	.10	.10
	90°	.07	.07	.07	.06	.06
20 km/s	0°	.63	.62	.56	.51	.51
	5°	.66	.65	.60	.54	.53
	15°	.60	.59	.55	.49	.48
	30°	.51	.49	.45	.40	.39
	50°	.32	.32	.28	.24	.24
	90°	.20	.20	.18	.16	.15

Table B.1: Mass fraction of target material partially melted in impacts of the 40% impactor on the 1700 km target.

Melt production for 1700 km targets 60% impactor						
Impact velocity	Impact angle	Target mass partially melted				
		1%	10%	50%	90%	100%
5 km/s	0°	.23	.23	.22	.20	.20
	5°	.22	.22	.21	.18	.18
	15°	.24	.24	.21	.20	.19
	30°	.20	.20	.19	.17	.17
	50°	.16	.15	.14	.14	.14
	90°	.12	.12	.11	.11	.10
10 km/s	0°	.66	.64	.58	.52	.49
	5°	.67	.66	.61	.56	.56
	15°	.66	.65	.59	.52	.51
	30°	.58	.55	.52	.47	.46
	50°	.43	.43	.40	.37	.36
	90°	.25	.24	.22	.20	.20
20 km/s	0°	1	1	1	1	1
	5°	1	1	.99	.99	.99
	15°	.99	.99	.99	.99	.99
	30°	.99	.99	.99	.98	.98
	50°	.92	.91	.88	.82	.81
	90°	.60	.59	.56	.52	.52

Table B.2: Mass fraction of target material partially melted in impacts of the 60% impactor on the 1700 km target.

Melt production for 6400 km targets 40% impactor						
Impact velocity	Impact angle	Target mass partially melted				
		1%	10%	50%	90%	100%
5 km/s	0°	.081	.076	.063	.061	.061
	5°	.072	.072	.065	.056	.056
	15°	.077	.076	.070	.063	.062
	30°	.066	.066	.062	.052	.050
	50°	.064	.064	.064	.052	.052
	90°	.058	.058	.058	.048	.048
10 km/s	0°	.19	.19	.17	.14	.14
	5°	.17	.17	.16	.14	.14
	15°	.17	.16	.14	.13	.13
	30°	.16	.15	.14	.12	.12
	50°	.13	.13	.12	.11	.11
	90°	.12	.12	.11	.10	.09
20 km/s	0°	.35	.35	.33	.33	.33
	5°	.36	.36	.35	.33	.33
	15°	.33	.33	.32	.31	.31
	30°	.27	.27	.26	.25	.25
	50°	.21	.21	.20	.19	.19
	90°	.13	.13	.13	.11	.11

Table B.3: Mass fraction of target material partially melted in impacts of the 40% impactor on the 6400 km target.

Melt production for 6400 km targets 60% impactor						
Impact velocity	Impact angle	Target mass partially melted				
		1%	10%	50%	90%	100%
5 km/s	0°	.37	.36	.35	.33	.33
	5°	.36	.35	.34	.33	.32
	30°	.36	.36	.34	.33	.33
	50°	.38	.37	.35	.33	.33
	90°	.37	.36	.35	.34	.33
10 km/s	0°	.63	.62	.61	.59	.59
	5°	.63	.63	.62	.59	.59
	15°	.60	.60	.59	.58	.58
	30°	.58	.58	.57	.54	.53
	50°	.52	.52	.50	.48	.48
	90°	.44	.44	.42	.41	.41
20 km/s	0°	.98	.97	.97	.97	.97
	5°	.99	.99	.99	.98	.98
	15°	.98	.98	.97	.96	.96
	30°	.93	.93	.92	.91	.91
	50°	.81	.80	.79	.77	.77
	90°	.66	.65	.63	.61	.61

Table B.4: Mass fraction of target material partially melted in impacts of the 60% impactor on the 6400 km target.

Melt production for 1700 km targets 40% impactor						
Impact velocity	Impact angle	Proj. mass partially melted				
		1%	10%	50%	90%	100%
5 km/s	5°	.72	.72	.62	.61	.61
	15°	.74	.74	.68	.52	.45
	30°	.58	.58	.58	.58	.43
	50°	.54	.54	.38	.36	.36
	90°	.31	.31	.29	.25	.25
10 km/s	0°	2.88	2.88	2.67	2.5	2.5
	5°	2.77	2.7	2.56	2.14	1.95
	15°	2.58	2.56	2.27	2.04	2.03
	30°	2.18	2.18	2.0	1.78	1.75
	50°	2.02	2.02	1.8	1.71	1.63
	90°	1.19	1.19	1.12	1.05	1.05
20 km/s	0°	10.5	10.4	9.3	8.6	8.6
	5°	11.1	10.9	10.0	8.97	8.83
	15°	10.0	9.77	9.12	8.23	8.0
	30°	8.47	8.09	7.5	6.72	6.5
	50°	5.4	5.26	4.7	4.1	4.0
	90°	3.26	3.28	3.06	2.72	2.57

Table B.5: Amount of material partially melted in impacts of the 40% impactor on the 1700 km target, in units of projectile masses.

Melt production for 1700 km targets 60% impactor						
Impact velocity	Impact angle	Proj. mass partially melted				
		1%	10%	50%	90%	100%
5 km/s	0°	1.07	1.04	.98	.92	.91
	5°	1.0	.98	.94	.84	.83
	15°	1.11	1.08	.96	.89	.88
	30°	.90	.89	.85	.76	.75
	50°	.73	.70	.64	.61	.61
	90°	.57	.55	.51	.49	.47
10 km/s	0°	2.99	2.91	2.66	2.36	2.25
	5°	3.04	3.0	2.76	2.55	2.54
	15°	3.0	2.93	2.66	2.36	2.31
	30°	2.61	2.51	2.34	2.12	2.1
	50°	1.97	1.94	1.82	1.69	1.66
	90°	1.12	1.1	1.01	.91	.90
20 km/s	0°	4.55	4.55	4.55	4.55	4.55
	5°	4.55	4.55	4.53	4.51	4.5
	15°	4.52	4.52	4.51	4.49	4.49
	30°	4.54	4.52	4.49	4.46	4.45
	50°	4.19	4.13	3.99	3.72	3.68
	90°	2.71	2.7	2.54	2.38	2.36

Table B.6: Amount of material partially melted in impacts of the 60% impactor on the 1700 km target, in units of projectile masses.

Melt production for 6400 km targets 40% impactor						
Impact velocity	Impact angle	Proj. mass partially melted				
		1%	10%	50%	90%	100%
5 km/s	0°	1.35	1.26	1.05	1.01	1.01
	5°	1.21	1.21	1.08	.94	.94
	15°	1.28	1.26	1.17	1.05	1.03
	30°	1.10	1.10	1.03	.86	.83
	50°	1.06	1.06	1.06	.86	.86
	90°	.97	.97	.97	.79	.79
10 km/s	0°	3.1	3.1	2.8	2.4	2.4
	5°	2.8	2.8	2.65	2.36	2.4
	15°	2.8	2.7	2.6	2.23	2.2
	30°	2.7	2.6	2.4	2.1	2.0
	50°	2.2	2.2	2.1	1.8	1.8
	90°	2.0	1.9	1.9	1.6	1.6
20 km/s	0°	5.9	5.8	5.6	5.5	5.5
	5°	6.0	5.9	5.8	5.4	5.4
	15°	5.6	5.5	5.3	5.1	4.7
	30°	4.5	4.5	4.3	4.1	4.1
	50°	3.5	3.5	3.4	3.2	3.2
	90°	2.2	2.2	2.1	1.9	1.9

Table B.7: Amount of material partially melted in impacts of the 40% impactor on the 6400 km target, in units of projectile masses.

Melt production for 6400 km targets 60% impactor						
Impact velocity	Impact angle	Proj. mass partially melted				
		1%	10%	50%	90%	100%
5 km/s	0°	1.68	1.62	1.59	1.51	1.51
	5°	1.63	1.60	1.57	1.49	1.43
	30°	1.64	1.62	1.6	1.51	1.48
	50°	1.72	1.69	1.59	1.51	1.50
	90°	1.67	1.64	1.58	1.53	1.50
10 km/s	0°	2.84	2.83	2.77	2.7	2.7
	5°	2.87	2.87	2.8	2.7	2.67
	15°	2.72	2.72	2.69	2.63	2.62
	30°	2.64	2.64	2.57	2.44	2.43
	50°	2.37	2.35	2.27	2.18	2.18
	90°	1.99	1.99	1.92	1.86	1.84
20 km/s	0°	4.5	4.4	4.4	4.4	4.4
	5°	4.5	4.5	4.5	4.5	4.5
	15°	4.5	4.5	4.4	4.4	4.4
	30°	4.2	4.2	4.2	4.1	4.1
	50°	3.7	3.7	3.6	3.5	3.5
	90°	3.0	3.0	2.9	2.8	2.8

Table B.8: Amount of material partially melted in impacts of the 60% impactor on the 6400 km target, in units of projectile masses.

Vapor production for 1700 km targets 40% impactor						
Impact velocity	Impact angle	Target mass partially vaporized				
		1%	10%	50%	90%	100%
5 km/s	5°	.001	.001	0	0	0
	15°	.001	.001	0	0	0
	30°	.003	.001	.0	0	0
	50°	.001	0	0	0	0
	90°	.004	.002	0	0	0
10 km/s	0°	.023	.023	.001	.001	0
	5°	.024	.017	.001	0	0
	15°	.018	.015	.001	0	0
	30°	.021	.017	.003	0	0
	50°	.022	.017	.001	0	0
	90°	.013	.012	.004	0	0
20 km/s	0°	.11	.055	.024	.001	.001
	5°	.093	.052	.017	.001	.001
	15°	.11	.07	.015	.007	.007
	30°	.12	.07	.023	.008	.005
	50°	.084	.06	.021	.011	.009
	90°	.058	.034	.013	.004	.004

Table B.9: Mass fraction of target material partially vaporized in impacts of the 40% impactor on the 1700 km target.

Vapor production for 1700 km targets 60% impactor						
Impact velocity	Impact angle	Target mass partially vaporized				
		1%	10%	50%	90%	100%
5 km/s	0°	.057	.04	0	0	0
	5°	.052	.034	.001	0	0
	15°	.064	.04	.001	.001	0
	30°	.054	.036	0	0	0
	50°	.046	.028	.002	0	0
	90°	.026	.019	0	0	0
10 km/s	0°	.18	.14	.04	.01	.01
	5°	.20	.14	.04	.02	.01
	15°	.20	.15	.05	.01	.01
	30°	.17	.11	.04	.02	.01
	50°	.12	.09	.04	.02	.01
	90°	.07	.05	.02	.01	.01
20 km/s	0°	.68	.51	.18	.096	.086
	5°	.73	.61	.20	.063	.055
	15°	.69	.54	.20	.081	.071
	30°	.59	.43	.16	.08	.08
	50°	.39	.31	.12	.06	.06
	90°	.21	.17	.06	.03	.03

Table B.10: Mass fraction of target material partially vaporized in impacts of the 60% impactor on the 1700 km target.

Vapor production for 6400 km targets 40% impactor						
Impact velocity	Impact angle	Target mass partially vaporized				
		1%	10%	50%	90%	100%
5 km/s	0°	.04	.015	.001	.001	.001
	5°	.025	.015	.001	.001	.001
	15°	.017	.017	.004	.001	.001
	30°	.021	.015	.004	.002	0
	50°	.019	.017	.008	.002	.002
	90°	.018	.015	.012	0	0
10 km/s	0°	.041	.041	.01	.001	.001
	5°	.041	.039	.013	.001	.001
	15°	.038	.027	.015	.004	.004
	30°	.041	.028	.015	.006	.004
	50°	.041	.032	.012	.008	.008
	90°	.031	.026	.016	.006	.006
20 km/s	0°	.13	.12	.046	.024	.024
	5°	.14	.099	.044	.027	.025
	15°	.13	.098	.046	.023	.023
	30°	.12	.092	.046	.026	.023
	50°	.084	.064	.034	.026	.017
	90°	.068	.054	.029	.015	.013

Table B.11: Mass fraction of target material partially vaporized in impacts of the 40% impactor on the 6400 km target.

Vapor production for 6400 km targets 60% impactor						
Impact	Impact	Target mass partially vaporized				
velocity	angle	1%	10%	50%	90%	100%
5 km/s	0°	.20	.14	.075	.036	.036
	5°	.18	.12	.077	.028	.025
	30°	.16	.13	.06	.03	.021
	50°	.15	.11	.061	.027	.017
	90°	.14	.11	.055	.02	.02
10 km/s	0°	.33	.21	.065	.042	.041
	5°	.32	.23	.075	.041	.040
	15°	.32	.22	.074	.041	.037
	30°	.29	.18	.061	.039	.037
	50°	.24	.16	.064	.039	.036
	90°	.17	.11	.054	.031	.029
20 km/s	0°	.79	.68	.43	.25	.22
	5°	.79	.69	.42	.26	.23
	15°	.74	.63	.39	.25	.23
	30°	.65	.54	.32	.20	.19
	50°	.50	.42	.24	.16	.14
	90°	.37	.32	.18	.11	.10

Table B.12: Mass fraction of target material partially vaporized in impacts of the 60% impactor on the 6400 km target.

Vapor production for 1700 km targets 40% impactor						
Impact velocity	Impact angle	Proj. mass partially vaporized				
		1%	10%	50%	90%	100%
5 km/s	5°	.018	.018	0	0	0
	15°	.018	.018	0	0	0
	30°	.054	.018	0	0	0
	50°	.016	0	0	0	0
	90°	.072	.036	0	0	0
10 km/s	0°	.38	.38	.018	.018	0
	5°	.40	.29	.018	0	0
	15°	.31	.25	.018	0	0
	30°	.34	.29	.054	0	0
	50°	.36	.29	.018	0	0
	90°	.22	.2	.07	0	0
20 km/s	0°	1.82	.92	.4	.018	.018
	5°	1.55	.86	.29	.018	.018
	15°	1.86	1.14	.25	.11	.11
	30°	1.93	1.14	.38	.13	.09
	50°	1.41	.92	.34	.18	.14
	90°	.97	.56	.22	.07	.07

Table B.13: Amount of target material partially vaporized in impacts of the 40% impactor on the 1700 km target, in terms of number of projectile masses.

Vapor production for 1700 km targets 60% impactor						
Impact velocity	Impact angle	Proj. mass partially vaporized				
		1%	10%	50%	90%	100%
5 km/s	0°	.26	.18	0	0	0
	5°	.24	.15	.005	0	0
	15°	.29	.18	.005	.005	0
	30°	.25	.16	0	0	0
	50°	.21	.13	.01	0	0
	90°	.12	.088	0	0	0
10 km/s	0°	.82	.65	.18	.04	.04
	5°	.93	.66	.18	.07	.04
	15°	.89	.69	.23	.05	.05
	30°	.76	.49	.20	.07	.06
	50°	.55	.41	.19	.07	.06
	90°	.33	.24	.09	.06	.05
20 km/s	0°	3.09	2.34	.84	.44	.4
	5°	3.34	2.77	.90	.29	.25
	15°	3.14	2.46	.90	.37	.32
	30°	2.68	1.96	.73	.35	.35
	50°	1.77	1.41	.55	.29	.28
	90°	.95	.76	.29	.15	.14

Table B.14: Amount of target material partially vaporized in impacts of the 60% impactor on the 1700 km target, in terms of number of projectile masses.

Vapor production for 6400 km targets 40% impactor						
Impact velocity	Impact angle	Proj. mass partially vaporized				
		1%	10%	50%	90%	100%
5 km/s	0°	.67	.25	.018	.018	.018
	5°	.41	.25	.108	.018	.018
	15°	.29	.29	.072	.018	.018
	30°	.34	.25	.072	.036	0
	50°	.32	.29	.13	.036	.026
	90°	.31	.25	.20	0	0
10 km/s	0°	.68	.68	.18	.018	.018
	5°	.68	.65	.22	.018	.018
	15°	.63	.45	.25	.072	.07
	30°	.68	.46	.25	.11	.07
	50°	.68	.54	.20	.13	.13
	90°	.52	.43	.27	.11	.10
20 km/s	0°	2.11	2.03	.77	.40	.4
	5°	2.32	1.66	.74	.45	.42
	15°	2.14	1.64	.77	.38	.38
	30°	2.04	1.53	.77	.43	.43
	50°	1.41	1.06	.56	.43	.29
	90°	1.1	.90	.49	.25	.22

Table B.15: Amount of target material partially vaporized in impacts of the 40% impactor on the 6400 km target, in terms of number of projectile masses.

Vapor production for 6400 km targets 60% impactor						
Impact velocity	Impact angle	Proj. mass partially vaporized				
		1%	10%	50%	90%	100%
5 km/s	0°	.91	.63	.34	.16	.16
	5°	.81	.56	.35	.13	.11
	30°	.74	.57	.27	.13	.09
	50°	.70	.51	.28	.12	.074
	90°	.64	.50	.25	.098	.093
10 km/s	0°	1.51	.96	.29	.19	.19
	5°	1.45	1.03	.34	.19	.18
	15°	1.45	.98	.33	.19	.17
	30°	1.31	.84	.28	.18	.17
	50°	1.09	.72	.29	.18	.16
	90°	.78	.52	.25	.14	.13
20 km/s	0°	3.59	3.07	1.97	1.12	.99
	5°	3.59	3.15	1.93	1.19	1.06
	15°	3.38	2.88	1.79	1.12	1.05
	30°	2.95	2.48	1.47	.93	.85
	50°	2.29	1.92	1.11	.72	.66
	90°	1.68	1.44	.80	.52	.44

Table B.16: Amount of target material partially vaporized in impacts of the 60% impactor on the 6400 km target, in terms of number of projectile masses.

Binned melt production for 1700 km targets 40% impactor						
Impact velocity	Impact angle	Proj. mass partially melted				
		0-10%	10-50%	50-90%	90-100%	100+
5 km/s	5°	0	0.09	0.02	0	0.59
	15°	0	0.05	0.20	0.04	0.43
	30°	0.02	0	0.14	0	0.38
	50°	0	0.16	0.02	0.00	0.33
	90°	0	0.05	0	0	0.18
10 km/s	0°	0.14	0.14	0.09	0.07	2.2
	5°	0.11	0.18	0.41	0.13	1.55
	15°	0.05	0.31	0.20	0	1.73
	30°	0.02	0.18	0.23	0	1.41
	50°	0	0.22	0.13	0.04	1.28
	90°	0	0.11	0.04	0	0.83
20 km/s	0°	0.14	1.08	0.79	0	6.78
	5°	0.36	0.68	1.05	0.13	7.10
	15°	0.47	0.54	1.03	0.18	6.15
	30°	0.45	0.58	0.83	0.18	4.58
	50°	0.22	0.56	0.65	0.02	2.63
	90°	0.02	0.25	0.34	0.09	1.59

Table B.17: Amount of target material partially melted in impacts of the 40% impactor on the 1700 km target. The mass of melted material produced by the impact is listed normalized to the impactor mass (M_{imp}), and is binned according to the amount of partial melting of each particle.

Binned melt production for 1700 km targets 60% impactor						
Impact velocity	Impact angle	Proj. mass partially melted				
		0-10%	10-50%	50-90%	90-100%	100+
5 km/s	0°	0.02	0.06	0.06	0.02	0.65
	5°	0.04	0.04	0.10	0.01	0.60
	15°	0.03	0.13	0.07	0.01	0.60
	30°	0.01	0.04	0.08	0.01	0.50
	50°	0.03	0.06	0.02	0	0.40
	90°	0.02	0.04	0.02	0.01	0.35
10 km/s	0°	0.08	0.25	0.29	0.12	1.48
	5°	0.07	0.25	0.21	0.01	1.60
	15°	0.09	0.27	0.25	0.05	1.42
	30°	0.13	0.16	0.23	0.02	1.35
	50°	0.04	0.12	0.13	0.03	1.11
	90°	0.03	0.08	0.10	0.01	0.57
20 km/s	0°	0	0	0	0	1.45
	5°	0	0.01	0.02	0	1.18
	15°	0	0.01	0.02	0	1.35
	30°	0.01	0.04	0.03	0.01	1.76
	50°	0.06	0.14	0.27	0.04	1.91
	90°	0.02	0.16	0.15	0.02	1.41

Table B.18: Amount of target material partially melted in impacts of the 60% impactor on the 1700 km target. The mass of melted material produced by the impact is listed normalized to the impactor mass (M_{imp}), and is binned according to the amount of partial melting of each particle.

Binned melt production for 6400 km targets 40% impactor						
Impact velocity	Impact angle	Proj. mass partially melted				
		0-10%	10-50%	50-90%	90-100%	100+
5 km/s	0°	0	0	0.09	0	0.41
	5°	0	0.14	0	0	0.56
	15°	0.02	0.09	0.14	0	0.74
	30°	0.04	0.07	0.09	0	0.49
	50°	0.02	0	0.20	0	0.52
	90°	0	0.04	0.13	0	0.52
10 km/s	0°	0	0	0.29	0	1.73
	5°	0.13	0.11	0.29	0	1.60
	15°	0	0.23	0.18	0.02	1.65
	30°	0.07	0.22	0.13	0.02	1.38
	50°	0.04	0.14	0.25	0.04	1.15
	90°	0.13	0.07	0.23	0.07	1.03
20 km/s	0°	0	0.29	0.09	0	3.8
	5°	0.09	0.11	0.36	0	3.7
	15°	0.04	0.25	0.14	0	3.2
	30°	0.05	0.16	0.38	0.13	2.3
	50°	0.07	0.07	0.22	0	1.8
	90°	0.04	0.05	0.18	0	.94

Table B.19: Amount of target material partially melted in impacts of the 40% impactor on the 6400 km target. The mass of melted material produced by the impact is listed normalized to the impactor mass (M_{imp}), and is binned according to the amount of partial melting of each particle.

Binned melt production for 6400 km targets 60% impactor						
Impact velocity	Impact angle	Proj. mass partially melted				
		0-10%	10-50%	50-90%	90-100%	100+
5 km/s	0°	0.06	0.02	0.08	0	0.60
	5°	0.06	0.04	0.06	0.02	0.70
	30°	0.03	0.02	0.09	0	0.75
	50°	0.02	0.03	0.10	0.02	0.73
	90°	0	0.08	0.05	0.02	0.73
10 km/s	0°	0.02	0.12	0.10	0	2.0
	5°	0.04	0.12	0.18	0	2.0
	15°	0.03	0.11	0.10	0	1.9
	30°	0.03	0.07	0.13	0.01	1.5
	50°	0.02	0.09	0.08	0.03	1.5
	90°	0.01	0.07	0.06	0.02	1.4
20 km/s	0°	0.02	0	0.10	0.04	2.0
	5°	0.03	0.02	0.10	0.02	2.1
	15°	0.01	0.08	0.04	0.01	2.1
	30°	0.02	0.07	0.15	0.02	1.8
	50°	0.02	0.09	0.12	0.01	1.6
	90°	0.04	0.06	0.15	0.02	1.6

Table B.20: Amount of target material partially melted in impacts of the 60% impactor on the 6400 km target. The mass of melted material produced by the impact is listed normalized to the impactor mass (M_{imp}), and is binned according to the amount of partial melting of each particle.

Binned vapor production for 1700 km targets 40% impactor						
Impact velocity	Impact angle	Proj. mass partially vaporized				
		0-10%	10-50%	50-90%	90-100%	100+
5 km/s	5°	0	0.02	0	0	0
	15°	0	0.02	0	0	0
	30°	0.04	0.02	0	0	0
	50°	0.02	0	0	0	0
	90°	0.04	0.04	0	0	0
10 km/s	0°	0	0.36	0	0.02	0
	5°	0.11	0.27	0.02	0	0
	15°	0.05	0.23	0.02	0	0
	30°	0.05	0.23	0.05	0	0
	50°	0.07	0.27	0.02	0	0
	90°	0.02	0.13	0.07	0	0
20 km/s	0°	0.90	0.52	0.38	0	0.02
	5°	0.68	0.76	0.27	0	0.02
	15°	0.72	0.88	0.14	0	0.11
	30°	0.79	0.76	0.25	0.04	0.09
	50°	0.49	0.57	0.16	0.04	0.14
	90°	0.41	0.34	0.14	0	0.07

Table B.21: Amount of target material partially vaporized in impacts of the 40% impactor on the 1700 km target. The mass of vaporized material produced by the impact is listed normalized to the impactor mass (M_{imp}), and is binned according to the amount of partial vaporization of each particle.

Binned vapor production for 1700 km targets 60% impactor						
Impact velocity	Impact angle	Proj. mass partially vaporized				
		0-10%	10-50%	50-90%	90-100%	100+
5 km/s	0°	0.08	0.19	0	0	0
	5°	0.08	0.15	0.01	0	0
	15°	0.11	0.18	0	0.01	0
	30°	0.08	0.16	0	0	0
	50°	0.08	0.12	0.01	0	0
	90°	0.03	0.09	0	0	0
10 km/s	0°	0.12	0.47	0.14	0	0.04
	5°	0.27	0.48	0.10	0.03	0.04
	15°	0.21	0.46	0.17	0	0.05
	30°	0.27	0.29	0.13	0.01	0.06
	50°	0.14	0.22	0.12	0.01	0.06
	90°	0.10	0.15	0.03	0.01	0.05
20 km/s	0°	0.75	1.50	0.40	0.04	0.39
	5°	0.57	1.86	0.62	0.03	0.25
	15°	0.68	1.55	0.54	0.04	0.32
	30°	0.72	1.23	0.38	0.01	0.35
	50°	0.36	0.86	0.26	0.01	0.28
	90°	0.19	0.47	0.14	0.01	0.14

Table B.22: Amount of target material partially vaporized in impacts of the 60% impactor on the 1700 km target. The mass of vaporized material produced by the impact is listed normalized to the impactor mass (M_{imp}), and is binned according to the amount of partial vaporization of each particle.

Binned vapor production for 6400 km targets 40% impactor						
Impact velocity	Impact angle	Proj. mass partially vaporized				
		0-10%	10-50%	50-90%	90-100%	100+
5 km/s	0°	0.65	0	0	0	0.02
	5°	0.25	0.11	0	0	0.02
	15°	0.11	0.09	0.05	0	0.02
	30°	0.09	0.18	0.04	0.04	0
	50°	0.09	0.09	0.04	0.04	0.04
	90°	0.09	0.02	0.20	0	0
10 km/s	0°	0	0.67	0	0	0.02
	5°	0.11	0.31	0.20	0	0.02
	15°	0.11	0.29	0.09	0	0.07
	30°	0.22	0.25	0.11	0.04	0.07
	50°	0.14	0.34	0.05	0	0.15
	90°	0.22	0.16	0.04	0.04	0.07
20 km/s	0°	0.14	0.81	0.38	0	0.40
	5°	0.29	0.68	0.29	0.04	0.42
	15°	0.14	0.63	0.40	0	0.38
	30°	0.34	0.76	0.34	0	0.43
	50°	0.34	0.50	0.25	0.02	0.29
	90°	0.04	0.45	0.20	0.04	0.22

Table B.23: Amount of target material partially vaporized in impacts of the 40% impactor on the 6400 km target. The mass of vaporized material produced by the impact is listed normalized to the impactor mass (M_{imp}), and is binned according to the amount of partial vaporization of each particle.

Binned vapor production for 6400 km targets 60% impactor						
Impact velocity	Impact angle	Proj. mass partially vaporized				
		0-10%	10-50%	50-90%	90-100%	100+
5 km/s	0°	0.28	0.29	0.18	0.04	0.12
	5°	0.20	0.21	0.22	0.01	0.11
	30°	0.14	0.32	0.14	0.03	0.07
	50°	0.12	0.29	0.11	0.03	0.07
	90°	0.12	0.24	0.14	0	0.09
10 km/s	0°	0.14	0.25	0.06	0	0.19
	5°	0.13	0.26	0.06	0.01	0.18
	15°	0.10	0.28	0.15	0.02	0.17
	30°	0.24	0.40	0.10	0.01	0.17
	50°	0.22	0.41	0.12	0.01	0.16
	90°	0.09	0.13	0.05	0.01	0.13
20 km/s	0°	0.28	0.54	0.51	0.12	0.99
	5°	0.15	0.54	0.47	0.14	1.10
	15°	0.15	0.59	0.42	0.06	1.05
	30°	0.28	0.65	0.55	0.07	0.85
	50°	0.20	0.53	0.32	0.06	0.66
	90°	0.18	0.30	0.22	0.04	0.44

Table B.24: Amount of target material partially vaporized in impacts of the 60% impactor on the 6400 km target. The mass of vaporized material produced by the impact is listed normalized to the impactor mass (M_{imp}), and is binned according to the amount of partial vaporization of each particle.